

Scanning Tunneling Microscopy as Local Probe of Electron Density, Dynamics, and Transport at Metal Surfaces

*A dissertation submitted to the
SWISS FEDERAL INSTITUTE OF TECHNOLOGY
LAUSANNE*

*for the degree of
Docteur ès Sciences*

*presented by
Lukas Bürgi
Dipl. Phys. ETH Zürich*

*examining board:
Prof Dr K. Kern
Dr D. Eigler
Prof Dr A. Goldmann
Prof Dr L. Zuppiroli*

September 21, 1999

Résumé

Dans cette thèse quelques propriétés électroniques de systèmes à dimensions réduites sont étudiés au moyen de la microscopie et de la spectroscopie à effet tunnel (STM et STS) à basse température. De par sa très haute résolution spatiale, le STM offre la possibilité de sonder les propriétés électroniques à des échelles plus petites que le libre parcours moyen inélastique de l'électron, lorsque les effets quantiques prédominent. Cette thèse est divisée en trois parties.

La première partie concerne les interférences quantiques d'états électroniques s - p de surface sur des surfaces (111) de métaux nobles (Cu, Ag, Au). Les électrons occupant ces états de surface forment un gaz d'électrons libres quasi-bidimensionnel confiné aux premières couches atomiques de la surface du cristal. Ils sont diffusés par le potentiel associé aux défauts de surface, p.ex. des impuretés ou des marches atomiques, et créent des motifs d'interférences quantiques dans la densité d'états locale (LDOS) autour de ces défauts.

La relation de dispersion des états électroniques s - p de surface des trois métaux nobles est évaluée avec une grande précision en mesurant le vecteur d'onde des oscillations de la LDOS au bord d'une marche atomique en fonction de l'énergie de l'électron. Pour la première fois, les déviations de la structure de bandes de l'état de surface du métal noble par rapport à la dispersion parabolique sont observées et caractérisées quantitativement. Les bandes de l'état de surface présentent un aplatissement significatif en direction des bords de la zone de Brillouin de surface.

La longueur de relaxation de phase L_ϕ et la durée de vie inélastique $\tau_\phi = L_\phi/v$ des électrons de l'état de surface s - p des métaux nobles sont étudiées en analysant quantitativement l'amortissement spatial des motifs d'interférences quantiques pour des marches rectilignes. Nous trouvons que les durées de vie inélastiques des électrons "chauds" de l'état de surface sont dominées par la diffusion électron-électron. Ces durées de vie montrent une dépendance en énergie suivant $(E - E_F)^{-2}$ et sont plus courtes que celles prédites par la théorie des liquides de Fermi pour les électrons correspondants du solide massif. Cependant, l'amortissement des motifs d'interférences en fonction de la température est principalement dû à l'élargissement des distributions de Fermi-Dirac de l'échantillon et de la pointe. Pour de basses énergies de l'électron, cet élargissement domine donc l'amortissement dû aux processus inélastiques

intrinsèques, tels que l'interaction électron-électron ou électron-phonon. Néanmoins, nous pouvons déduire des limites inférieures pour la longueur de relaxation de phase du gaz électronique à deux dimensions à l'énergie de Fermi : $L_\phi(E_F) \gtrsim 660$ Å à 77 K et $\gtrsim 160$ Å à 178 K pour Cu(111), et $L_\phi(E_F) \gtrsim 600$ Å à 3.5 K et $\gtrsim 250$ Å à 77 K pour Ag(111). Par contraste avec des techniques intégrales telles que la photo-émission, L_ϕ et τ_ϕ sont mesurés localement. Ceci élimine l'élargissement de lignes dû à la diffusion par des défauts de surface, un phénomène inhérent à toute technique intégrale. Par conséquent, les résultats STM de ce travail fournissent des valeurs absolues de la longueur de relaxation de phase et de la durée de vie inélastique des électrons de l'état de surface.

Par la suite, les électrons bidimensionnels de l'état de surface de Ag(111) sont confinés artificiellement dans des structures quantiques à une dimension, formées par une paire de marches parallèles. La LDOS mesurée dans de telles structures présente un comportement quantique, qui s'explique parfaitement à l'aide d'un modèle de Fabry-Pérot, lequel révèle avec précision la dépendance en énergie de l'amplitude de réflexion et le déphasage de diffusion des différentes marches de Ag(111). Ce modèle de résonateur électronique permettra de quantifier des expériences de diffusion électronique pour des structures tests introduites dans le résonateur.

Basée sur le théorème de Hohenberg-Kohn, nous développons une nouvelle méthode de réponse linéaire qui permet de visualiser directement, avec le STM, le potentiel extérieur ressenti par les électrons de l'état de surface. Cette méthode est appliquée à l'état de surface sur Au(111), où la reconstruction "en chevrons" modifie le potentiel. Les images du potentiel ainsi obtenues sont en excellent accord avec les résultats précédemment publiés.

Les études sur les propriétés de transport des électrons à travers des contacts ponctuels réversibles et bien définis sont présentées en seconde partie. Les contacts sont formés par un ou deux atomes métalliques (Mn ou Gd) entre la pointe STM et un substrat Cu(100). Par contraste avec tous les travaux précédents, aucun réarrangement atomique n'est observé lors de la formation du contact. Ces contacts ponctuels présentent des signes évidents de quantification de la conductance. Dans le cas du Mn, un seul atome métallique suffit à ouvrir entièrement un canal de conduction de conductance $2e^2/h$.

Dans la troisième partie, nous discutons, sur la base de résultats préliminaires réalisés en utilisant une pointe supraconductrice, une approche permettant de rendre le STM sensible à des moments magnétiques aussi petits que quelques magnétons de Bohr. Cette approche tire parti du fait que seules les impuretés magnétiques induisent des changements drastiques dans la bande interdite de la LDOS du supraconducteur.

Abstract

In this thesis several electronic properties of systems with reduced dimensions are investigated using low-temperature scanning tunneling microscopy and spectroscopy (STM and STS). With its very high spatial resolution STM offers a close-up look at electronic properties on length scales shorter than the electron inelastic mean free path, where quantum mechanical effects prevail. In other terms, STM is used here to read fingerprints of quantum mechanics. The thesis is organized in three parts.

The first part deals with quantum interferences in *s-p* derived electronic surface states on noble-metal (111) surfaces (Cu, Ag, Au). These surface-state electrons form a quasi two-dimensional (2D) free electron gas which is confined to the first few atomic layers at the crystal surface. They are scattered by the potential associated with surface defects, e.g. impurity atoms or step edges, leading to quantum interference patterns in the local density of states (LDOS) around these defects.

The dispersion relation of all three noble-metal *s-p* derived surface states was evaluated with high accuracy by measuring the wave vector of the LDOS oscillations at step edges as a function of electron energy. Deviations of the noble-metal surface-state band structure from parabolic dispersion are observed and quantitatively characterized for the first time. The surface state bands show a significant flattening towards the surface Brillouin zone boundary.

The phase-relaxation length L_ϕ and inelastic lifetime $\tau_\phi = L_\phi/v$ of *s-p* derived noble-metal surface-state electrons was investigated by quantitatively studying the spatial decay of quantum interference patterns at straight step edges. The inelastic lifetimes of hot surface-state electrons for both Cu(111) and Ag(111) are found to be dominated by electron-electron scattering. They show a $(E - E_F)^{-2}$ energy dependence and are shorter than predicted by Fermi-liquid theory for the corresponding bulk electrons. The damping of surface-state interference patterns as a function of temperature, however, was found to be mainly due to the broadening of the Fermi-Dirac distributions of sample and tip. At low electron energies this broadening thus dominates damping due to intrinsic inelastic processes like electron-electron or electron-phonon interaction. Nevertheless,

lower limits of the phase-relaxation length at the Fermi energy of the 2D electron gas could be deduced: $L_\phi(E_F) \gtrsim 660 \text{ \AA}$ at 77 K and $\gtrsim 160 \text{ \AA}$ at 178 K for Cu(111), and $L_\phi(E_F) \gtrsim 600 \text{ \AA}$ at 3.5 K and $\gtrsim 250 \text{ \AA}$ at 77 K for Ag(111). In contrast to integral techniques such as photoemission, L_ϕ and τ_ϕ were measured locally. This eliminates residual linewidths due to surface defect scattering found in all integrating techniques. The STM results of this work, therefore, provide absolute values for the phase-relaxation length and inelastic lifetime of surface-state electrons.

The 2D surface-state electrons on Ag(111) were further confined in artificial 1D quantum structures formed by a pair of parallel straight step edges. The measured LDOS in such structures shows a distinct quantum behavior and can perfectly be explained with a simple Fabry–Pérot model which accurately reveals the energy dependent reflection amplitude and scattering phaseshifts of the different kinds of Ag(111) step edges. The model character of the electron resonator provides the possibility of quantitative electron scattering experiments on test structures brought into the resonator.

Furthermore, based on the Hohenberg–Kohn theorem, a new linear-response method to map directly the external potential felt by the surface-state electrons with an STM was developed. It was applied to the surface state on the “herringbone”-reconstructed Au(111) surface. The resulting potential maps are in excellent agreement with previously published results on potential modulations induced by the reconstruction.

Studies on transport of electrons through well-defined and reversible metal-atom point contacts are presented in the second part. The contacts were formed by one or two metal atoms (either Mn or Gd) between the STM tip and a Cu(100) substrate. In contrast to all previous studies no atomic rearrangement was observed upon contact formation. The point contacts show clear signs of conductance quantization. In the case of Mn one single metal atom suffices to open an entire conduction channel with conductance $2e^2/h$.

In the third part a promising approach to make the STM sensitive to surface magnetic moments as small as a few Bohr magnetons by using a superconducting tip material is discussed on the basis of preliminary results. This approach relies on the fact that only magnetic impurities induce drastic changes in the gap region of the LDOS of a superconductor.

Contents

Résumé	i
Abstract	iii
Abbreviations and Common Symbols	vii
1 Introduction: Nano!	1
2 Scanning Tunneling Microscopy	7
2.1 Principles	7
2.2 Experimental	13
2.3 Sample Preparation	20
3 Noble-Metal Surface States	23
3.1 Introduction	23
3.2 Surface-State Band Structure	28
3.3 Deviations from Parabolic Dispersion	42
4 Electron Lifetimes	49
4.1 Introduction	49
4.2 Electron-Electron Interaction	55
4.3 Electron-Phonon Interaction	61
5 Confinement of Surface-State Electrons	71
5.1 Introduction	71
5.2 Fabry–Pérot Model	74
5.3 Ag(111)	79
5.4 Au(111)	87
6 Potential Mapping	89
6.1 Introduction	89

6.2	Linear Response Theory	90
6.3	Reconstruction Induced Potential on Au(111)	94
7	Conduction Through Single Metal Atoms	105
7.1	Quantized Conductance of Ballistic Point Contacts	105
7.2	Vertical Manipulation of Metal Atoms with an STM	111
7.3	Single-Metal-Atom Point Contacts	116
8	Probing Magnetism with STM	125
8.1	Towards Magnetism on the Atomic Scale	125
8.2	Detecting Magnetism with a Superconducting Tip	129
	Bibliography	139
	Curriculum vitae	151
	Remerciements	153

Abbreviations and Common Symbols

ARPES	Angle-Resolved PhotoEmission Spectroscopy
c.f.	closed feedback loop conditions
$e-e$	electron-electron
$e-ph$	electron-phonon
KRIPES	k -Resolved Inverse PhotoEmission Spectroscopy
(L)DOS	(Local) Density Of States
o.f.	open feedback loop conditions
PES	PhotoEmission Spectroscopy
ph	phonon
STM	Scanning Tunneling Microscopy
STS	Scanning Tunneling Spectroscopy
2D	Two-Dimensional
2DEG	Two-Dimensional Electron Gas
UHV	Ultra-High Vacuum
δ	delta function
dI/dV	differential conductance
ΔV	sinusoidal peak-to-peak bias modulation
E	energy with respect to the Fermi energy (if not otherwise stated)
e	protonic charge, $e = 1.6 \cdot 10^{-19}$ C
E_F	equilibrium Fermi energy
$E_{\overline{\Gamma}}$	surface-state band edge
$f(E, T)$	equilibrium Fermi function
G	conductance
J_i	Bessel function of order i

k_B	Boltzmann constant, $k_B = 0.087$ meV/K
L_M	elastic mean free path
L_ϕ	phase-relaxation length
L_0	density of states of a free electron gas, $L_0 = m^*/\pi\hbar^2$
m_e	free electron mass, $m_e = 9.1 \cdot 10^{-31}$ kg
m^*	effective electron mass
n	electron density
ν	bias modulation frequency
φ	coherent reflection phaseshift
r	coherent step reflection amplitude
ρ_b	bulk electron contribution to the density of states at the surface
ρ_s	electronic density of states at the surface
s	tip-sample distance
T	temperature (except in chapter 7, where it stands for the transmission)
Θ	step function
U	external potential energy
τ_ϕ	phase-relaxation time
V	electric potential of sample with respect to tip
W	work function
z	tip height

Chapter 1

Introduction: Nano!

The entire information technology of today relies on the physics of large ensembles of particles. This fact has not been changed by the rapid miniaturization which leads to always more compact storage media and ever faster computer chips. The magnetic particles which constitute a single bit on a computer hard disk are still too large to show any influence of the individual atoms. Also, in the electrical circuits of microchips hundred thousands of electrons are still involved in order to switch the state of a single bit. However, if miniaturization continues at the pace postulated by the pioneer Gordon Moore already in the early seventies, i.e. a doubling of the number of transistors per unit area every 18 months, then an area will inevitably be reached in the years to come, where a *single* atom or electron counts and where pure quantum effects dictate the physics of devices. This will happen e.g. at the point where the dimension of a single transistor becomes comparable to the inelastic mean free path or the de Broglie wavelength of the electrons.

Continuous miniaturization is a demanding issue for research and development. The actual research strategies can be divided into two groups: a “top-down” and a “bottom-up” approach. “Top-down” strategists try to refine conventional lithographic methods. The currently smallest structures on a state-of-the-art lithographically manufactured chip are about $0.25\ \mu\text{m}$ wide. By using UV-light with shorter wavelengths, structures smaller than 100 nm were already obtained by optical lithography in research laboratories. The next step will be X-rays with wavelengths of the order of 1 nanometer. This would allow the fabrication of integrated circuits containing up to a billion of transistors. Electron-beam lithography offers another possibility to refine lithographic methods. The limits of continuous miniaturization using traditional methods are not reached yet. At the beginning of this year several semiconductor companies announced the completion of the smallest storage chip with structures of down to only $0.175\ \mu\text{m}$ width. Linley

Gwennap, editor in chief of “Microprocessor Report”, estimates that Moore’s law will hold for another ten years. Thereafter new solutions must be available, which are to be expected from the “bottom-up” approach.

The “bottom-up” strategy has emerged in the early eighties when some physicists started to tackle the miniaturization problem by studying the very “bottom”, i.e. the smallest structures available. The aim of the “bottom-up” strategy is a thorough understanding of physics on the nanometer (atom) scale in a first step. In a second step this knowledge is applied to tailor useful down-to-atomic-scale devices with specific properties. Nowadays, there exists much interest in “bottom-up” or nanotechnology, and a lot of financial support flows into corresponding research projects, so-called nanoscience.

In his visionary talk “There’s plenty of room at the bottom” Richard Feynman anticipated nanoscience already in 1959 ¹. With unmatched boldness and accuracy Feynman prognosticated a realm of possibilities that look startlingly familiar to today’s researchers - so much so that his talk serves as a catalogue of the themes sounded in nanoscience: “I would like to describe a field, in which little has been done, but in which an enormous amount can be done in principle. The field is not quite the same as others in that it will not tell us much of fundamental physics, but it is more like solid-state physics in the sense that it might tell us much of great interest about the strange phenomena that occur in complex situations. Furthermore, a point that is most important is that it would have an enormous number of technical applications. (...) But I am not afraid to consider the final question as to whether, ultimately - in the great future - we can arrange the atoms the way we want; the very *atoms*, all the way down! (...) When we get to the very, very small world - say circuits of seven atoms - we have a lot of new things that would happen that represent completely new opportunities for design. Atoms on a small scale behave like *nothing* on a large scale, for they satisfy the laws of quantum mechanics. So as we go down and fiddle around with the atoms down there, we are working with different laws, and we can expect to do different things. We can manufacture in different ways. We can use, not just circuits, but some system involving the quantized energy levels, or the interactions of quantized spins, etc ... ”

Much has been accomplished in nanoscience since Feynman prepared the ground. As an example, tantalizing electron tunneling experiments revealed the discrete electronic states and superconducting gap in individual nanometer-scale metal particles [1, 2]. Importantly for the field, in the beginning of the eighties a tool has emerged which is very useful for the purposes of nanoscience: scanning tunneling microscopy (STM). It was

¹The talk was originally published in February 1960 in the Caltech alumni magazine “Engineering and Science”.

with an STM that D. Eigler and E. Schweizer succeeded in arranging “single atoms the way they wanted” for the first time in 1990 [3], just as Feynman prognosticated 30 years before. Not only can STM be used to build the smallest structures atom by atom, but it offers an unprecedented access to local physical properties on the atomic scale. For example, the influence of a *single* magnetic moment on the local properties of a superconductor was addressed with STM [4]. The same was done for a *single* magnetic atom on normal metals, revealing the Kondo effect on an atomic scale [5,6]. In 1998 B. Stipe and coworkers reported on *single-molecule* vibrational spectroscopy by means of inelastic tunneling experiments with an STM [7,8]. These recent successes establish STM as a key-tool to explore the properties of matter on the very “bottom”.

In this thesis we use low-temperature STM to elucidate physical properties of systems with reduced dimensions. The aim of this work is to make valuable contributions to the field of nanoscience.

In a first part, we have investigated several properties of surface-state electrons on noble metals (Chapters 3–6). These surface states constitute a high-density low-mobility two-dimensional electron gas. First of all, electrons in two dimensions (2D) are highly interesting *per se*, i.e. from a fundamental point of view. In recent years big surprises in condensed-matter physics came from two-dimensional systems, e.g. quantum Hall effect and high-temperature superconductivity. Two-dimensional systems mark the borderline between high and low dimensions, as far as localization is concerned: in one dimension, coherent back-scattering always strongly localizes the quantum states of the electrons; in three dimensions, electronic states are spatially extended (the electron “sea” of familiar metals). 2D systems are more complicated in that they may show weak localization. As an illustration of the complexity of the problems in two dimensions, the nature of the zero-temperature conductance of the apparently simple system of a two-dimensional electron fluid moving in a weak random potential still poses basic challenges to our understanding [9]. Secondly, in recent years there has been a renaissance of interest in the physics of surface-state electrons, which it is argued influence a variety of physical and chemical processes at surfaces [10,11]. For example, surface states play an important role in shaping the physisorption potential, which in turn determines chemical properties of surfaces, e.g. catalytic reactivity and dissociation [12–14]. Furthermore, surface states are responsible for long-range (R^{-2}) substrate-mediated adsorbate interactions, which may dominate the bulk-state mediated contribution (R^{-5}) for large adsorbate-adsorbate separation [15]. Also, the contribution from surface states is relevant for the total energy balance of surface reconstructions [10,11]. If there is a strong interaction between electrons and phonons, the 2D surface state can undergo a Peirls (metal-to-

insulator) transition and thereby drive a displacive surface transition [10]. As the result of such a transition a charge density wave establishes on the surface. W(100) and Mo(100) are good examples for systems showing a surface-state charge density wave. Occupied surface states are believed to play a major role in epitaxial growth on metal surfaces, too [14, 16]: depopulation of the surface state is suggested to increase the diffusion barrier on terraces and to lower the activation barrier for interlayer diffusion (Ehrlich–Schwoebel barrier). Since the growth mode (e.g. layer-by-layer or 3D growth) is determined by the delicate balance between intra and interlayer diffusion, it may be tuned by specific depopulation of surface states, e.g. by adding the right surfactant. Even the equilibrium crystal shape may be influenced by surface states, through a surface-state mediated interaction between step edges [17]. Finally, due to the fact that surface states are confined to the first few atomic layers of the crystal, they can serve as a very sensitive probe of surface magnetism, surface reconstruction and subsurface defects [10, 11, 14, 18]. It is clear from the above mentioned examples that surface states may be interesting for applications, e.g. through their influence on dissociation, catalytic reactivity or epitaxial growth.

Miniaturization of electronic circuits has reached a stage where electronic transport through “nanowires” may become technologically relevant soon. We address electron transport through metallic “wires” as narrow as one single atom in the second part of this thesis (Chapter 7). The behavior of such “quantum wires” is dictated by quantum mechanics and is completely different from the behavior of a macroscopic wire. The conductance of the latter follows Ohm’s law, i.e. it is inversely proportional to the length of the wire. The conductance of a “quantum wire”, on the other hand, is (almost) independent of its length, and it is given by an integer multiple of the so-called quantum of conductance, (almost) independent of material properties and shape. Furthermore, even an ideal “quantum wire”, i.e. a wire through which electrons can pass without suffering collisions, shows a finite conductance. This is due to an unavoidable voltage drop at the very contacts of the “quantum wire”. The difference in behavior of narrow and macroscopic wires comes along with the quantization of electronic states which occurs when the width of the wire becomes smaller than the electron mean free path and phase-relaxation length (the so-called ballistic regime).

Part three of the thesis deals with magnetism of nanosized structures (Chapter 8). In particular, we outline a promising approach to make the STM sensitive to magnetic moments as small as a few Bohr magnetons. It is of great importance to have a tool with high spatial resolution and magnetic sensitivity at one’s disposal in order to address the properties of ultrasmall magnetic particles. Although STM-based methods have

successfully been applied to obtain magnetic information from particular systems, none of these has established itself as a routinely used tool to investigate magnetism on the atomic scale. The issue of magnetic behavior of small particles is highly interesting from a fundamental point of view. Prominent size and shape effects govern the magnetism in this small world [19]. Also, some elements that show no ferromagnetism in the bulk are expected to behave differently when their atoms are assembled to very small building blocks, e.g. dimers or trimers, where a ferromagnetic phase may establish [20]. Obviously, profound understanding of the properties of tiny magnetic particles and their mutual interactions is very important for technology, e.g. for data storage devices.

The present work is organized as follows:

Chapter 2 describes the technical background: introduction to principles and theory of scanning tunneling microscopy, experimental set-up and sample preparation.

In Chapter 3 we present measurements revealing the band structure of noble-metal surface states with high precision.

Studies of the damping of quantum interference patterns in Chapter 4 reveal the phase-relaxation length of noble-metal surface-state electrons as a function of energy and temperature. The phase-relaxation length determines the length scale over which pure quantum effects prevail and, therefore, is an important issue with respect to e.g. quantum interference in the surface-state electron gas, substrate-mediated adsorbate interactions, surface-state-mediated step-step interaction which in turn may influence the equilibrium crystal shape, or charge transfer and electronic excitations in surface chemistry [21].

Chapter 5 deals with the confinement of the intrinsically 2D surface-state electrons in artificial 1D quantum structures formed by a pair of atomically parallel step edges on the surface. The confining mechanism determines the degree of depopulation of surface states and hence is relevant for e.g. epitaxial growth or the energetics of surface reconstructions.

A new method to map directly the external potential felt by 2D (surface-state) electrons with an STM is presented in Chapter 6.

In Chapter 7 we discuss measurements of the electrical conductance of single-metal-atom constrictions.

Finally, Chapter 8 deals with a new approach to detect magnetic moments as small as a few Bohr magnetons with an STM.

Chapter 2

Scanning Tunneling Microscopy

This Chapter starts with an introduction to the principles and theory of scanning tunneling microscopy in Section 2.1. The experimental set-up and sample preparation used during this thesis are discussed in Section 2.2 and Section 2.3, respectively.

2.1 Principles

Scanning tunneling microscopy [22], invented by Binnig and Rohrer in 1982 [23,24], is a technique strongly related to classical electron tunneling experiments pioneered in the early sixties by Giaever and coworkers [25]. In both cases the quantity of interest is the current I tunneling between two electrodes biased at a voltage V . The electrodes are separated by a thin insulating medium. The amount of current flowing for a given potential difference V depends on the density of electronic states (DOS) in the electrodes, and thus contains valuable information about the electronic structure of the surfaces of the electrodes. In classical tunnel junctions an oxide was mostly used as insulator, whereas a vacuum gap serves as tunnel barrier in STM. The gap can also consist of “insulating” gaseous and liquid substances, e.g. air or electrolyte. In STM one electrode is tip shaped, i.e. microscopic, and can be positioned relative to the second electrode, contrary to classical tunnel experiments, where two static planar electrodes were used. Thus *STM offers the advantage of performing locally resolved tunneling experiments.*

Figure 2.1(a) shows the schematic of an STM. A tip, normally a sharpened metallic wire, is brought close to the conducting surface of a sample. In ultra-high vacuum (UHV) experiments the sample surface is atomically clean, usually by means of rare gas ion bombardment with subsequent annealing for metals, or by cleaving and subsequent annealing in the case of semiconductors. The lateral tip position (x and y axis), as well as the tip-sample distance s are controlled with picometer precision by means of

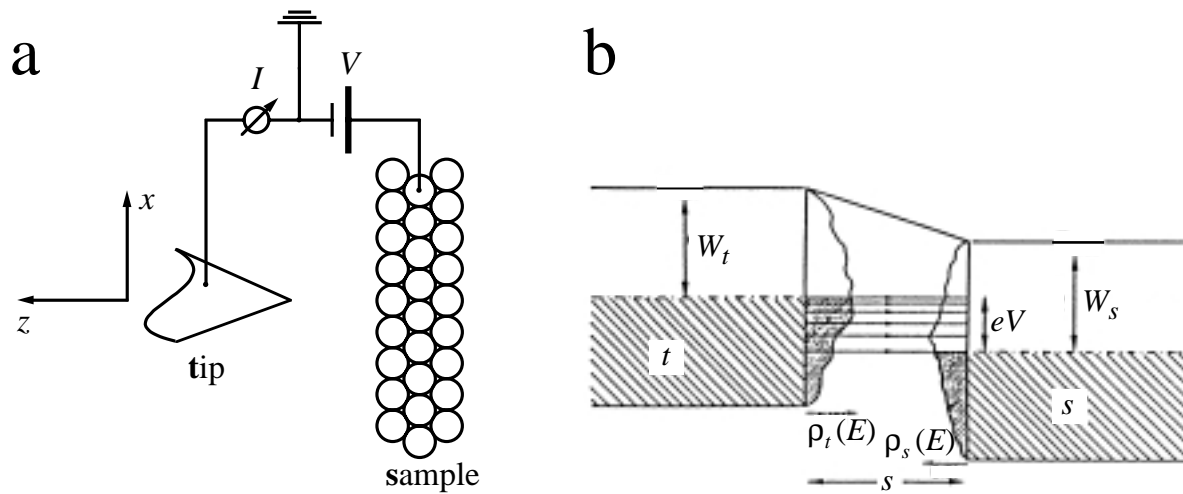


Figure 2.1: (a) Principle of an STM. (b) Corresponding potential energy diagram.

voltage signals applied to piezo-electric materials. If the tip is brought close enough to the sample that the wave functions of the conduction electrons of tip and sample begin to overlap substantially, a measurable tunneling current I can flow between the biased sample (potential V with respect to ground) and the virtually grounded tip (Fig. 2.1(b)). The tip-sample (core-to-core) distance in typical tunneling experiments is about 5 - 10 Å. Since the tunneling current depends exponentially on the tip-sample distance, it mainly flows through the few atoms at the very apex of the tip. Thus the tunneling current is highly localized, leading to the atomic-scale resolution of STM. In the case of a positively biased sample (as in Fig. 2.1(b)) the net current comes from electrons tunneling from occupied states in the tip to unoccupied states of the sample. The current per energy unit, i , is represented by the density of horizontal arrows in Fig. 2.1(b). As can be seen i decreases with decreasing energy since the energetically lower lying states decay faster in the vacuum barrier region. Whereas it is intuitively clear from Fig. 2.1(b) that the tunneling current will depend on the density of occupied and unoccupied states of tip and sample (ρ_s and ρ_t), respectively, the exact calculation of the tunneling current starting from the electronic structures of tip and sample is a difficult task. Compared to classical tunneling experiments the modeling of the tunneling current is further complicated in STM by the fact that the atomic structure and the chemical nature of the tip apex is normally not known.

To interpret our data we followed the widely used transfer Hamiltonian approxima-

tion introduced by Bardeen [26], where the tunneling current is given by [27]:

$$I(V) = 2e \sum_{\mu,\nu} \frac{2\pi}{\hbar} |T_{\mu,\nu}|^2 \delta(E_\mu - eV - E_\nu) \times \\ \left(f(E_\mu - eV, T) [1 - f(E_\nu, T)] - f(E_\nu, T) [1 - f(E_\mu - eV, T)] \right). \quad (2.1)$$

Here the summation goes over all quantum states μ and ν of the unperturbed sample and tip, respectively, f is the Fermi–Dirac distribution function¹, T is the temperature and $T_{\mu,\nu}$ is given by

$$T_{\mu,\nu} = -\frac{\hbar^2}{2m_e} \int_{\Sigma} d\mathbf{S} (\Psi_\nu^* \nabla \Psi_\mu - \Psi_\mu \nabla \Psi_\nu^*), \quad (2.2)$$

which must be evaluated over a surface Σ within the barrier region and with the wave functions of the unperturbed sample and tip, Ψ_μ and Ψ_ν , respectively. The $T_{\mu,\nu}$ matrix elements depend roughly exponentially on the barrier width s and they depend also on the electron momentum parallel to the surface, $p_{||}$. The larger $p_{||}$ the less energy is in the motion perpendicular to the surface, E_z , and thus the faster the vacuum tail of the wave functions decay. Therefore, electrons of total energy E with little parallel momentum tunnel with a higher probability than electrons of the same total energy E with large $p_{||}$. By analyzing the expression in Eq. (2.1) qualitatively, Hörmandinger stressed another general property of the derivative dI/dV of the tunneling current [28]: $dI/dV(V)$ is a signal related to the unoccupied sample LDOS for $eV \gg \hbar\sqrt{2W_t}/(s\sqrt{m_e})$, to the tip LDOS for $eV \ll -\hbar\sqrt{2W_t}/(s\sqrt{m_e})$ and it is a good measure of the sample LDOS for relatively low voltages $-\hbar\sqrt{2W_t}/(s\sqrt{m_e}) \ll eV \ll \hbar\sqrt{2W_t}/(s\sqrt{m_e})$. Here W_s and W_t are the work functions of sample and tip, respectively.

To get beyond qualitative properties of the tunneling current one has to find good approximations for the matrix elements $T_{\mu,\nu}$. A common approximation in STM theory is the s -wave approximation for tip wave functions introduced by Tersoff and Hamann [29], leading to the following expression for the tunneling current [30,31]

$$I(V, T, x, y, s) \propto \int_{-\infty}^{\infty} dE \rho_s(E, x, y) \rho_t(E - eV) \times \\ \mathcal{T}(E, V, s) [f(E - eV, T) - f(E, T)], \quad (2.3)$$

where ρ_t is the DOS of the tip, x and y characterize the lateral position on the sample and s the distance between tip and sample measured from a virtual plane passing through the uppermost atoms. ρ_s is the LDOS of the sample in this virtual plane. An often used

¹Energies are given with respect to the Fermi level if not otherwise stated.

expression for the tunneling transmission factor $\mathcal{T}(E, V, s)$ disregards the $p_{||}$ dependence of $T_{\mu,\nu}$ and reads [31]:

$$\mathcal{T}(E, V, s) = \exp \left(-2s \sqrt{\frac{m_e}{\hbar^2}} \sqrt{W_s + W_t - 2E + eV} \right). \quad (2.4)$$

Although this is a crude simplification, the expressions in Eqs. (2.3) and (2.4) contain the essential and are a good starting point for qualitative and under certain conditions quantitative discussions. In our discussion of surface-state electrons in the following Chapters we will at some points use a more accurate transmission factor, which takes into account the $p_{||}$ dependence of $T_{\mu,\nu}$ for surface-state electrons [28]. For low bias voltages the bias and energy dependence of the transmission factor in Eq. (2.4) can be disregarded, leading to the following simplified expression for the current:

$$I(V, T, x, y, s) \propto e^{-2s \sqrt{\frac{m_e}{\hbar^2}} \sqrt{2\overline{W}}} \int_{-\infty}^{\infty} dE \rho_s(E, x, y) \rho_t(E - eV) g(E, V, T), \quad (2.5)$$

where $2\overline{W} = W_s + W_t$ and $g(E, V, T) = f(E - eV, T) - f(E, T)$. If in addition the measurements are performed at low temperatures, the Fermi functions in Eq. (2.5) can be approximated by Θ (step) functions², i.e.

$$I(V, x, y, s) \propto e^{-2s \sqrt{\frac{m_e}{\hbar^2}} \sqrt{2\overline{W}}} \int_0^{eV} dE \rho_s(E, x, y) \rho_t(E - eV). \quad (2.6)$$

Guided by this simplified expression for the tunneling current we will discuss in the following the two main applications of STM, *constant-current imaging* and *scanning tunneling spectroscopy* [22].

Constant-current imaging

In constant-current imaging the tunneling current I is compared to a preset current value I_0 . The difference signal $\Delta I = I - I_0$ is fed back to the voltage applied to the z -piezo so that the tip-sample distance is adjusted in order to minimize ΔI [32]. The surface is then scanned by the tip and the voltage applied to the z -piezo in order to keep the current constant is recorded. One thus obtains a so-called topograph $z(x, y)|_{I,V}$, where

$$z(x, y)|_{I,V} = s(x, y)|_{I,V} + t(x, y). \quad (2.7)$$

² $f(E, 0) = \Theta(-E)$

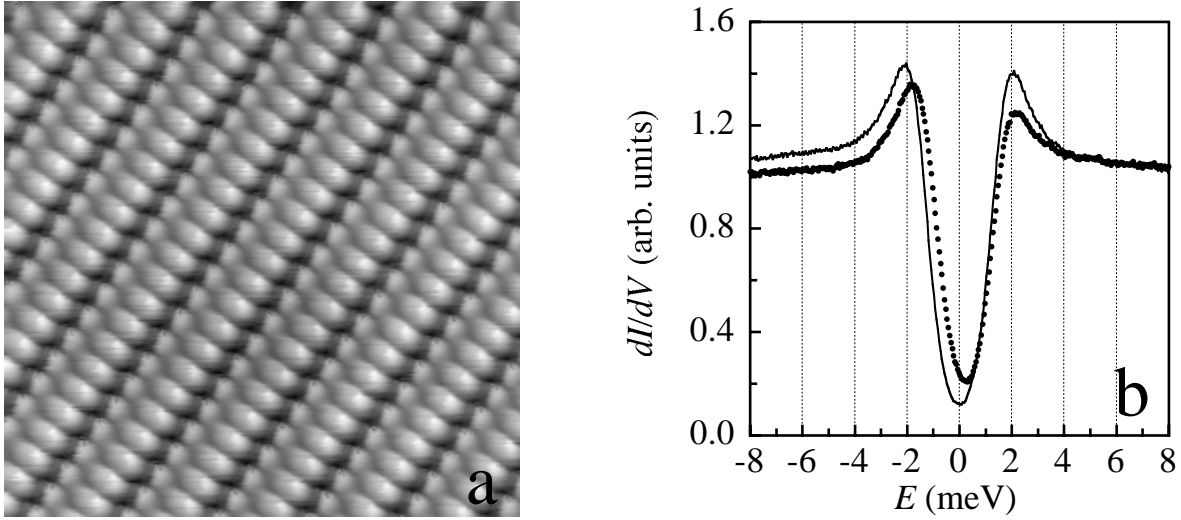


Figure 2.2: (a) $52 \text{ \AA} \times 52 \text{ \AA}$ constant-current image of a Au(110) surface showing the 2×1 missing row reconstruction with atomic resolution. Note that atoms at the bottom of the missing row are resolved as well. The white and black levels are separated by 0.9 \AA (raw data, $V = 0.2 \text{ V}$, $I = 2.3 \text{ nA}$, $T = 4.9 \text{ K}$). (b) Scanning tunneling spectra taken at 3.8 K on a bare spot on Nb(110) (full line) and on top of a Mn atom on the same surface (dots). They clearly show the BCS density of states of the sample. The spectra are reproduced from Ref. [4].

Here $t(x, y)$ characterizes the topography of the surface, i.e. a virtual plane passing through the surface atom nuclei. In the ideal case, where $\Delta I = 0$, $s(x, y)|_{I, V}$ is given by (see Eq. (2.5))

$$s(x, y)|_{I, V} = \text{const} + \frac{1}{2\sqrt{\frac{m_e}{\hbar^2}}\sqrt{2\overline{W}}} \ln \left(\frac{\int_{-\infty}^{\infty} dE \rho_s(E, x, y) \rho_t(E - eV) g(E, V, T)}{\int_{-\infty}^{\infty} dE \bar{\rho}_s(E) \rho_t(E - eV) g(E, V, T)} \right) \\ \approx s_0 + \frac{1}{2\sqrt{\frac{m_e}{\hbar^2}}\sqrt{2\overline{W}}} \frac{\int_{-\infty}^{\infty} dE \Delta\rho_s(E, x, y) \rho_t(E - eV) g(E, V, T)}{\int_{-\infty}^{\infty} dE \bar{\rho}_s(E) \rho_t(E - eV) g(E, V, T)}, \quad (2.8)$$

where $\bar{\rho}_s(E)$ is the spatial average of $\rho_s(E, x, y)$, s_0 a constant and $\Delta\rho_s(E, x, y) = \rho_s(E, x, y) - \bar{\rho}_s(E)$ is assumed to be a small quantity for the last linear approximation. The term topograph is misleading in the sense that, except for some special cases, $z(x, y)|_{I, V}$ is not directly an image of the positions of the atomic nuclei but rather a surface of constant local density of states (LDOS) of the sample (Eq. (2.8)). Thus it contains not only information on topography but also on electronic structure, and *one has to be careful in interpreting $z(x, y)|_{I, V}$ images in terms of surface topography.*

Only in special cases $z(x, y)|_{I, V}$ reflects the surface geometry. For example, the density of states on two clean adjacent terraces separated by a monoatomic step edge is the very same and $z(x, y)|_{I, V}$ on the upper terrace distinguishes itself from $z(x, y)|_{I, V}$ on the lower terrace by the height of a monoatomic step. Therefore, one can say that

the height difference between two terraces is reflecting the topology. A second, less straightforward example of topography related imaging is “atom imaging”. It is clear that $\rho_s(E, x, y)$ shows the periodicity of the surface lattice, and thus the integral in Eq. (2.8) will show the same periodicity implying that also $z(x, y)|_{I,V}$ will have the very same periodicity. As seen in Fig. 2.2(a) this periodicity can easily be resolved in STM. This is the so-called atomic resolution.

On the other hand there are very clear examples of electronic structure induced variations of $z(x, y)|_{I,V}$. As an example we would like to mention the standing wave patterns in constant-current images taken at low bias voltages on noble-metal (111) surfaces (see following Chapters). They are due to interference effects in the surface-state electron gas [33]. Actually, at low bias values and low temperatures Eq. (2.8) can be approximated by

$$s(x, y)|_{I,V} \approx s_0 + \frac{1}{2\sqrt{\frac{m_e}{\hbar^2}}\sqrt{2W}} \frac{\Delta\rho_s(E_F, x, y)}{\bar{\rho}_s(E_F)}, \quad (2.9)$$

i.e. at low bias voltages $z(x, y)|_{I,V}$ is a measure of $\rho_s(E_F, x, y)$, and thus the standing wave patterns of Ref. [33] directly reflect Friedel-type oscillations in the density of states at the Fermi level and have nothing to do with surface topology.

Scanning Tunneling Spectroscopy

In scanning tunneling spectroscopy (STS) one measures I - V curves or equivalently dI/dV - V curves at a fixed location and (normally) fixed tip-sample distance s , much like in classical electron tunneling experiments. The advantage of STM is the *high spatial resolution*. If we assume that in the bias range of interest the tip density of states is much less structured than ρ_s , one derives from Eq. (2.6)

$$dI/dV(V, x, y) \propto \rho_s(eV, x, y). \quad (2.10)$$

The assumption can be justified whenever there are sharp features in the sample DOS, e.g. if spectra are taken on single atoms or molecules with strong resonances. *dI/dV spectra contain valuable information about the local electronic structure of the sample* in general and, under certain circumstances, are directly proportional to the surface local density of states (see Eq. (2.10)). As an example, Fig. 2.2(b) depicts spectra taken on a classical superconductor, niobium, showing the energy gap as expected from BCS theory [34].

In STM one always has to be aware of the effects that the high current densities ($\approx 10^{10}$ A/m²) and the high contact fields ($\approx |W_s - eV - W_t|/e s \approx 10^9$ V/m) could

have on the experiment. In the case of an *elastic* tunnel junction the local heating in tip and sample can be estimated to cause a temperature enhancement smaller than 1 K [35], and thus can be disregarded in most experiments. The electric field on the other hand can severely influence physical properties [36–38], and one thus always has to discuss its influence on the particular experiment. One way to do this is to repeat the very same measurement with different tip-sample distances. By varying tip-sample distance for otherwise unchanged parameters one varies the strength of the electric field, and can thus check its influence on the experiment.

Concluding this Section, STM and STS opened up a fascinating access to *local* surface properties. Major advantages are the very high spatial resolution (atomic-scale), a sub-millivolt energy resolution in STS (see Fig. 2.2(b)) and the access of electronic states below and above the Fermi level ³. In addition STM is very sensitive to surface impurities, since every disturbance of the lattice periodicity is directly imaged in $z(x, y)|_{I,V}$. Thus, by choosing surface spots with very little density of impurities, impurity effects can be minimized (avoided). Via single atom manipulation, STM can also be used as a tool to fabricate nanostructures at will, and thus gives access to new phases of matter [3].

2.2 Experimental

All measurements presented in this thesis have been performed with a low-temperature UHV scanning tunneling microscope. The results for Chapters 7 and 8 have been acquired in the laboratory of D. Eigler at IBM Almaden with a 4 K-UHV STM [3,39]. A set-up which is very similar to Don Eigler’s is carefully described in Ref. [35]. The measurements presented in Chapters 3, 4, 5 and 6 have been performed with a custom-built 4 K-5 T STM operating in UHV, which is extensively described in Ref. [40], and which we briefly describe in the following.

The motivation for building the set-up currently under operation at the Federal Institute of Technology in Lausanne was the *combination of growing (metallic) nanostructures via self-organization [41] with the advantages of a highly stable low-temperature STM*. For these purposes low-temperature STM has two advantages: firstly, thermally activated processes such as diffusion are hindered and thus the kinetically grown nanostructures are quenched even though they may be far from thermodynamic equilibrium. Secondly, due to the suppression of thermally activated junction instabilities, the tunnel

³Compare this to photoemission and inverse photoemission, where only occupied and unoccupied states are accessible, respectively.

junction is much more stable at low temperatures leading to a better signal-to-noise ratio in the tunneling current. This in addition with strongly reduced thermal broadening at 4 K (Eq. (2.5)) ensures very high resolution in tunneling spectroscopy, which is necessary for the investigation of physical properties of such nanostructures.

The UHV-chamber (see Fig. 2.3) is designed such that samples can be prepared on a temperature controlled manipulator (40 K - 1000 K), thus enabling the self-organization of low-dimensional structures via kinetically controlled growth. The base pressure of the UHV system described here is at $\approx 8 \cdot 10^{-11}$ mbar ($\approx 3 \cdot 10^{-10}$ mbar) when the cryostat is at 4.2 K (300 K). The standard UHV preparation and analysis tools are concentrically arranged in the sample preparation plane (Fig. 2.3): differentially pumped sputter gun (IQE 12/38 from SPECS), two electron beam evaporators (EFM from Omicron) and an Auger spectrometer with cylindrical mirror analyzer (CMA 150 from Omicron). A rotational feedthrough allows the orientation of the sample. A filament is used to heat the sample up to 1000 K by electron bombardment. The single crystal samples are hat shaped and clamped on their brim into a sandwich Mo sample holder. Two sapphire spacers between Mo and crystal provide the electrical insulation necessary to apply the bias voltage V to the sample in the STM. The sapphire is also thermally insulating at high T , enabling fast and clean flashes for sample preparation. At low T the thermal conductivity of sapphire (along the C-axis) reaches that of clean Cu, thus providing efficient sample cooling, too. The sample holder further has chromel/constantan thermocouple contacts with their spring loaded counter parts in the sample manipulator. Precise temperature measurement is achieved by contacting the thermocouple wires to different sides of the single crystal ensuring that the thermocouple hot junction is located at the crystal.

After preparation of the substrate and growth of the desired surface structures the sample holder is transferred into the microscope with a wobble stick. We were seeking for isothermal sample transfer in order to preserve metastable growth structures. To achieve this we isolated the parts that are in touch with the sample holder (2 CuBe-bars and a central steel-bayonet joint, together building a fork) by Teflon spacers from the wobble stick housing. Their thermal mass is small compared to the sample holder and thus the temperature raise while transferring cold samples to the STM is minimized (the CuBe-fork can additionally be pre-cooled for this purpose). Up to 3 samples can be held in UHV in a storage system which is also served by the wobble stick. New samples can be introduced into the UHV system through a load-lock.

The STM is located in the center of a superconducting split-pair magnet operating at 4.2 K and providing magnetic fields of up to 5 T perpendicular to the sample surface.

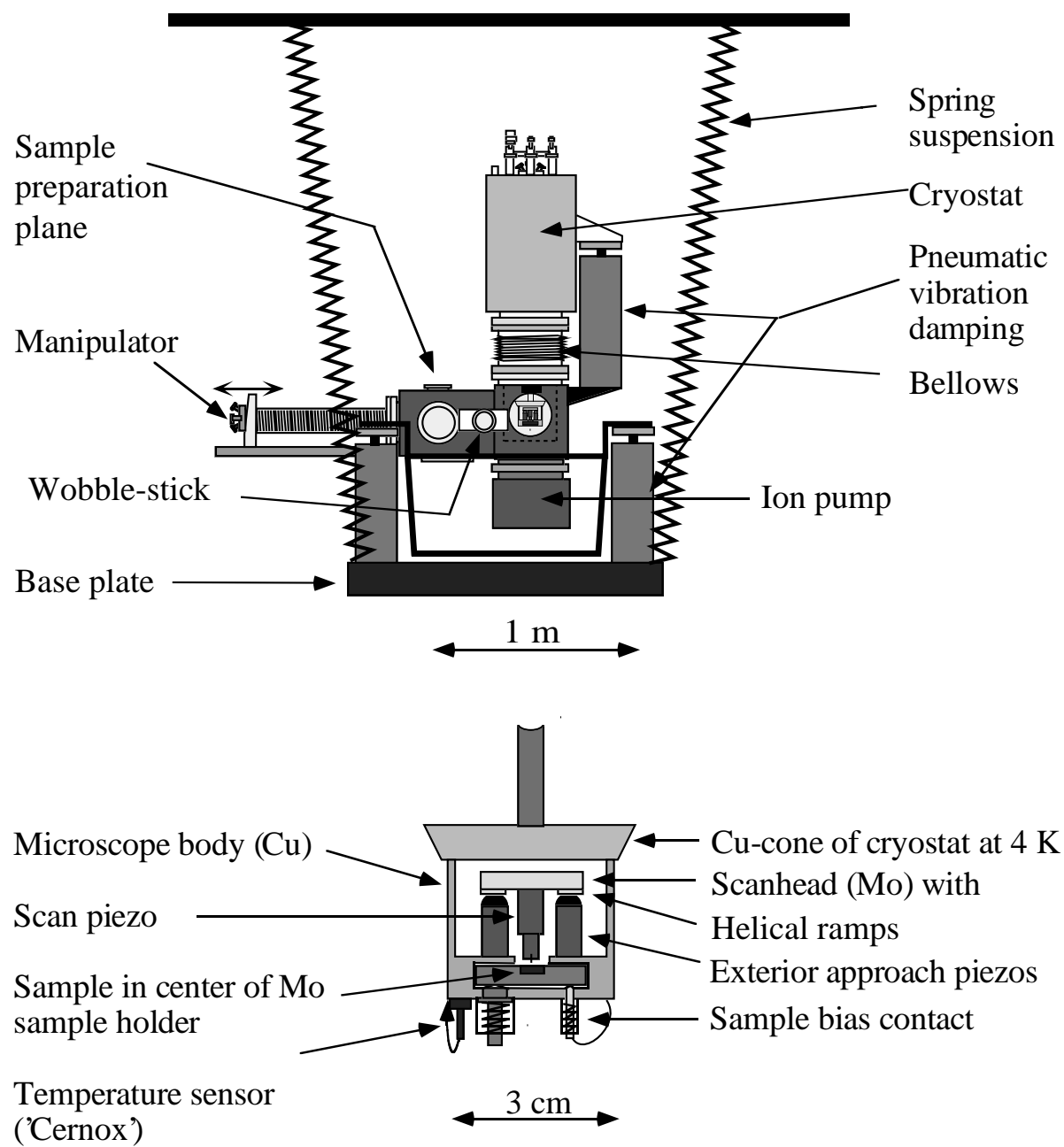


Figure 2.3: Sketch of the UHV-chamber and the 4K-5T scanning tunneling microscope.

The split coil geometry of the magnet allows access to the STM via 4 bores ($\varnothing = 50$ mm) arranged horizontally at 90° to each other. Sample transfer is performed through one of the bores while a second bore is used to watch the transfer from the side with a CCD-camera. Through the third bore we are currently trying to dose small metal coverages from a current heated filament onto the sample when placed in the STM. The remaining bore can be used for instance to irradiate the tunnel junction with a laser beam. For low-temperature STM operation the bores are shielded against room temperature radiation by a 77 K sliding door. Furthermore, the view bore is shielded with a sapphire window which is anchored at 4.2 K and the two remaining bores have been reduced to the necessary diameter of 10 mm and thus irradiation on the microscope body from 77 K is minimized. Thermal contact of the sample to the microscope body is achieved by sliding the sample holder into a drawer with spring loaded teflon cones firmly pressing it towards the top against a polished Cu surface (Fig. 2.3). Accordingly, the temperature of STM and sample are with 4.9 K close to that of liquid He, as measured by a “Cernox” metal-film thermometer mounted very close to the sample. The coarse tip approach is achieved with the inertial rotation [42] of a Mo disk ($\varnothing = 28$ mm) residing on 3 ruby balls glued to 3 piezo feet ($\varnothing = 6.65$ mm) pointing to the top. The Mo disk provides the helical ramps with a height difference of 0.5 mm. The disk carries in its center the central scan piezo which itself carries the tip within a tube. Thus, the beetle design [43] has been splitted (see Fig. 2.3) to provide good thermal contact to the sample while maintaining the convenient coarse approach and lateral displacement accomplished by the inertial motion of the Mo disk on the ruby balls. To achieve reliable operation of the sliding motion down to 4 K, the surface of the Mo ramps was carefully polished. We have characterized the stiffness of the microscope (i.e. its resonance frequencies) with the method described in Ref. [44]. We find the lowest resonance frequency around 1.5 kHz, which is comparatively high for beetle-type systems. We believe that this is due to the fact that the relatively heavy Mo disk shows the so-called “rattling” resonances at higher frequencies than conventional disks made from Al for example [40]. With a low-lying resonance frequency of 1.5 kHz our beetle STM is by far not the stiffest design one can imagine, but for low scanning frequencies (> 10 ms per line scan) the stability is very satisfactory and the disadvantages due to the relatively low resonance frequencies are compensated by the ease of coarse approach and lateral mm-scale displacements. The microscope body itself is thermally and mechanically coupled to the cryostat by a copper cone-shaped disk which is firmly pressed by springs in the transfer rod against its counterpart located in the cryostat. We employed indium to improve the thermal contact at the cone. The He bath cryostat together with the magnet were designed by

Oxford Instruments. The cryostat is mounted on a CF-300 flange and contains 40 l He. A 25 l liquid N₂ bath shields against room temperature radiation. During measurements the bubbling due to the boil-off of liquid nitrogen in the shield is avoided by solidification with a rotary pump located in the basement of the building. The boiling of He proved to have no effect on the measurements.

Despite the advantage of having good thermal contact to the He bath, our choice to mount the STM rigidly to the cryostat requires rather careful vibrational damping. The low frequency vibrations of the building are efficiently damped by arranging three harmonic oscillators in series. The first consists in a spring suspension of the base plate from the ceiling. The second harmonic oscillator is realized by a set of four commercial pneumatic damping elements (Newport) suspending the UHV chamber with respect to the base plate. The last damping stage is a set of three such elements supporting the cryostat with respect to the chamber. There is a CF-300 bellows (38 membranes) between cryostat and chamber. The lowest resonance frequency of the overall suspension is $\nu_0 \approx 0.3$ Hz. High frequency vibrations, as acoustic noise, are efficiently damped by encapsulation of the UHV system into a sound proof cubicle, which constitutes a Faraday cage at the same time. The measurements are performed while turning off all mechanical pumps and every power supply in the cubicle. The power supply of the ion pump and the STM electronics (SPM 2000, RHK-technology) are situated outside the cubicle.

The tunneling current has been measured on top of the cryostat, since current amplification at low temperatures and in high magnetic fields seemed to be too delicate⁴. We used a two-stage home-built current amplifier consisting of a pre-amplifier with 10^7 Ω gain at a bandwidth of 100 kHz and a post-amplifier of alternatively 1, 10, or 100 gain. The post-amplifier has two output channels, one of which can be additionally filtered with 10, 3, 1, or 0.3 kHz bandwidth (fourth order active Bessel filter). The filtered output is fed to the feedback of the STM electronics, whereas the lock-in is connected to the unfiltered post-amplifier output. Thus, by choosing a bias modulation frequency above the bandwidth of the feedback signal, a closed feedback loop dI/dV lock-in signal can be measured at a tip-sample distance which is not influenced by the modulation (see below). The instrument is designed to have a spectroscopic energy resolution of better than 100 μ V. Thus grounding was done very carefully and all signal lines to the microscope (bias voltage, all piezo connections, tunneling current) are filtered with radio frequency tight filters directly on top of the cryostat (see Table 2.1). With a further

⁴Measuring the current directly on the low-temperature stage has two advantages: firstly, Johnson noise is strongly reduced at 4 K, and secondly, the length of the current signal line can be kept short, minimizing capacitive cross-talk to ground.

	Filter type	C (nF)	R (Ω)	ν_{RC} (kHz)
Bias voltage	9050-100-0008	750	20	10.6
Current	54-862-002	0.1		
z -piezo	9050-100-0011	150	100	10.6
x and y -piezos	9050-100-0011	150	350	3.0
Outer piezos	51-703-001	1.5	20	5300

Table 2.1: EMI filters used for the different signal lines, fabricated by Spectrum Control Inc. C is the capacity of the RF filter with respect to ground and R is a resistance that was put in series with the RF filter, leading to an additional RC low-pass filter of bandwidth ν_{RC} .

home-built device the bias voltage supplied by the RHK electronics (± 10 V, 16 bits) can be low-pass filtered with 3 k, 1 k, 100 or 10 Hz bandwidth (fourth order active Bessel filter) and be divided by 1, 10 or 100. The division is necessary to have enough bias bit resolution when performing spectra tempting to resolve sub-millivolt features. It is also in this device that the bias modulation from the lock-in is added to the bias voltage. This is done after the filter and right before the division of the signal by 1, 10 or 100, thus allowing for a highly stable sub-millivolt modulation of the bias voltage at any frequency up to 10 kHz. Altogether, our bias voltage and the virtual ground of the tip (pre-amplifier) are highly stable.

To reduce heat flux to the microscope all the signal lines are carefully anchored to 4.2 K. Since the scan head (Mo disk and center piezo) is relatively poorly coupled to the He bath, it is crucial to anchor all connections to the central piezo with special care. The virtual ground (tip connection) and the z -piezo connection have therefore been anchored to Cu blocks which are electrically isolated but thermally very well contacted to the copper cone (which is at a temperature of 4.2 K) by thin glued sapphire plates [40].

Scanning tunneling *spectra*, i.e. dI/dV as a function of V , have been recorded with lock-in technique under open feedback loop conditions (o.f.). Thus, the tip was held at fixed lateral position and tip-sample distance while acquiring the spectrum. A sinusoidal bias modulation ΔV (peak-to-peak) of frequency ν has been added to the bias voltage V . The current was fed into the lock-in and the dI/dV output has been recorded while the bias voltage was ramped linearly from preset lower to upper bias values. In the other spectroscopic mode, so-called dI/dV imaging, $dI/dV(x, y)|_V$ was acquired simultaneously with the constant-current image by lock-in technique under closed feedback loop conditions (c.f.). In this case the modulation frequency was chosen above the bandwidth of the feedback of typically 2 - 3 kHz. Thus $z(x, y)|_{I, V}$ does not

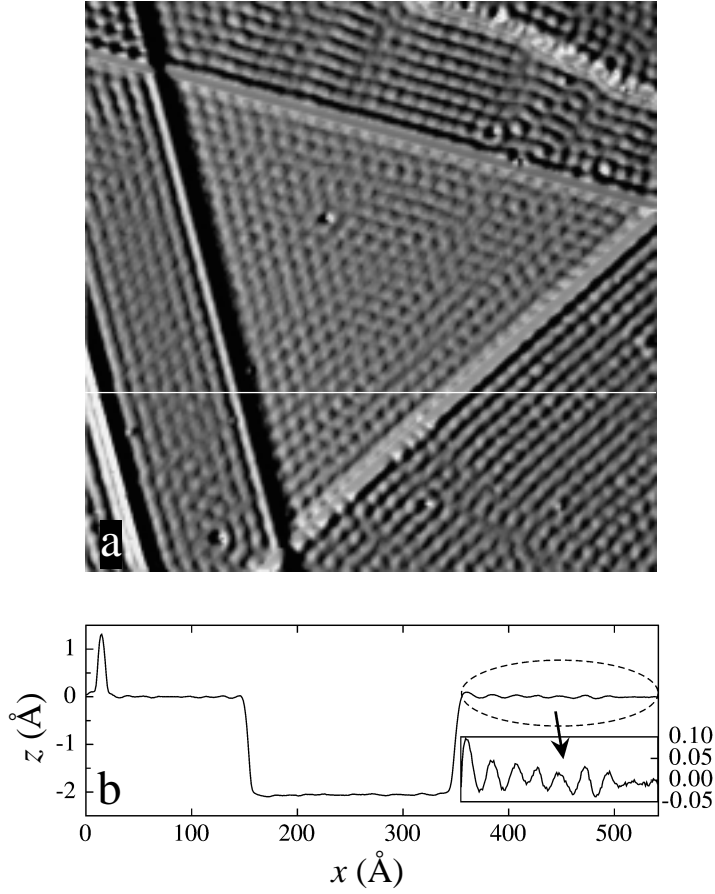


Figure 2.4: (a) Constant-current STM topograph showing quantum interference of surface-state electrons on a Cu(111) surface (raw data). The step structure has been created by indenting the tip at a place nearby. The image area of $545 \text{ Å} \times 545 \text{ Å}$ exhibits three terrace levels and an atomic chain on the lower left hand side (see also line scan (b) taken along the white line in (a)). The gray levels correspond to illumination of the surface from the left hand side. The image was acquired at $V = 1.0 \text{ mV}$ and thus approximately shows the $\text{LDOS}(x, y)$ at E_F ($I = 1.1 \text{ nA}$, $T = 4.9 \text{ K}$).

follow the bias modulation induced current modulations. When one aims to interpret dI/dV images performed in this manner quantitatively, one has to be aware of the fact that the electronic structure of the sample does not only enter through $\rho_s(E, x, y)$ in Eq. (2.6), and thus dI/dV , but also through the tip-sample distance $s(x, y)|_{I, V}$ which itself depends on $\rho_s(E, x, y)$ as seen in Eq. (2.8) [45, 46] (see also Chapter 4).

The temperature of the microscope can simply be varied by removing liquid helium from the cryostat giving rise to a temperature increase of the microscope over days, thus enabling drift-free STM-measurements at well defined temperatures up to 300 K. A minimum microscope temperature of 3.5 K can be attained by pumping the liquid He reservoir in the cryostat. At 4.9 K, the lateral drift of our STM is better than 1 Å/min

and the stability along the z -direction is of the order of $5/1000$ Å. Thus atomic resolution is routinely obtained (Fig. 2.2(a)) and, more demanding, quantum interference patterns of scattered surface-state electrons are readily resolved in $z(x, y)|_{I,V}$ -topographs (see Fig. 2.4). The vertical stability is also crucial for the resolution achievable in dI/dV spectra recorded with open feedback loop. The stability of our system is not at all influenced by the presence of the magnetic field and it is possible to record STM data on the very same surface spot at different values of the magnetic field.

The measurements presented in Chapters 3, 4, 5 and 6 have all been performed with an electrochemically etched (K^+OH^-) polycrystalline *tungsten* tip. The tip could be prepared in-situ by field-emission, Ar^+ ion sputtering or controlled indentation into metal samples. Field-emission was done by applying a voltage of typically -500 V to the tip while bringing it close to the grounded sample. The distance between tip and sample was then adjusted in order to have a current flow of typically 10 μA . By letting $\approx 10^{-5}$ mbar Ar^+ in the chamber during field-emission, the tip could be sputtered. The onset of sputtering could be observed in a sudden increase in emission current due to the contribution of the positively charged ions flowing to the tip. In the following we will sometimes use the term “different tips”, which refers to one and the same macroscopic tip with a different microscopic tip apex prepared with one of the methods described above.

2.3 Sample Preparation

Cu(111), Ag(111), Au(111)

The experiments described in Chapters 3, 4, 5 and 6 have been performed on noble-metal (111) surfaces: Cu(111), Ag(111) or Au(111). The three crystals are hat shaped with a circular surface of 7 mm in diameter and a total thickness of 3 mm. They were supplied by MaTeck with an orientational misfit of better than 0.1° and mechanically polished (grain size < 30 nm). The samples were cleaned under UHV conditions by sequential cycles of Ar^+ sputtering at 300 K and subsequent annealing. We typically used a 0.5 μA ion beam of 700 eV energy and an incidence angle of 45° for sputtering. One sputter cycle typically lasted 30 min. Annealing was performed during 10 min at a temperature given in Table 2.2. The pressure while annealing was always below $1 \cdot 10^{-9}$ mbar. Usually an impurity depletion layer was created by annealing to temperatures exceeding the usual final temperatures by about $50 - 100$ K for some cycles and only for the final preparation cycles the temperatures given in Table 2.2 were chosen again. This procedure resulted

	Cu(111)	Ag(111)	Au(111)
T (K)	820	870	800

Table 2.2: Annealing temperatures.

in atomically clean and flat surfaces with regions showing terraces of more than 2000 Å width. For all three surfaces we observed a coverage of less than ≈ 0.05 % of a monolayer (ML) impurities. We were not able to determine the chemical identity of these impurities since our Auger spectrometer only detects residual impurities in coverages larger than ≈ 1 %.

Cu(100), Nb(110)

For the experiments presented in Chapters 7 and 8 Cu(100) and Nb(110) crystals were used. Cu(100) has been prepared by repeated cycles of 1 kV Ar⁺ ion sputtering during about 5 min followed by annealing to 900 K and showed a surface quality comparable to the (111) crystals described before. The Nb(110) was cleaned by numerous sputter-anneal cycles. Sputtering was performed as for Cu(100). The annealing temperature has been decreased from 1000 K to 800 K with increasing number of cycles in order to produce an impurity depletion layer at the surface. The quality of the Nb surface is not comparable to noble-metal surfaces, but showed an acceptable terrace defect density for the purpose of the experiments described in Chapter 8. The main surface impurity on Nb was oxygen, which is imaged as a dip in STM topographs.

Chapter 3

Noble-Metal Surface States

In this Chapter the band structure of the *s-p* derived surface-state electrons on noble-metal (111) surfaces is discussed. An overview over the field is presented in Section 3.1. In Section 3.2 we show STS measurements which allow the determination of the dispersion relation for these surface state electrons. Finally, in Section 3.3 we discuss the deviations of the surface state bands from isotropic parabolic behavior.

3.1 Introduction

One usually distinguishes between three different types of electronic one-particle states in a solid. The first class of states, the so-called bulk states, are extended over the whole sample. Surface states, on the other hand, are localized close to the surface, i.e. the envelope of their probability amplitude decays exponentially into the bulk as well as into the vacuum region (see Fig. 3.1). They thus do not propagate perpendicularly to the surface and in this sense form a two-dimensional electron gas. Thirdly, surface resonances are extended states with an enhanced probability amplitude at the surface. The total number of bulk states in a real sample is comparable to the number of atoms, i.e. $\approx 10^{23}$, whereas the number of surface states is of the order of the number of surface atoms of the sample, i.e. $\approx 10^{15}$. Thus there are about 10^8 bulk states per surface state in a macroscopic sample, i.e. surface states can be completely neglected when one is interested in bulk properties. However, surface properties can be influenced strongly by surface states, since they may contribute a considerable fraction to the local density of states at and directly in front of the surface (see Chapter 1).

In an idealized, infinite crystal complex Bloch wave vectors are forbidden, since the corresponding wave functions grow exponentially and can thus not be normalized. But if one considers a semi-infinite crystal, exponentially growing solutions of the Schrödinger

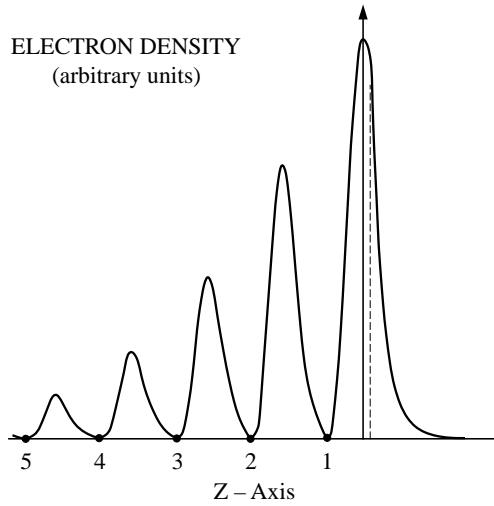


Figure 3.1: Probability density ρ of a surface-state electron. z denotes the direction perpendicular to the surface, 2 - 5 the atomic layers below the surface layer 1. (Figure from Ref. [47].)

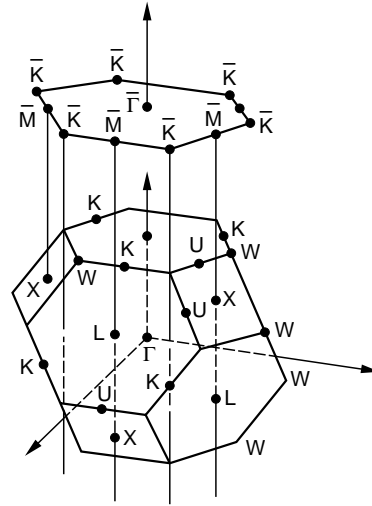


Figure 3.2: First Brillouin zone for an fcc lattice and the corresponding surface Brillouin zone (SBZ) for the (111) surface. The distance $\bar{\Gamma}\bar{K}$ is given by $4\pi/3a$, where a is the next neighbor distance. (Figure from Ref. [48].)

equation can be matched to exponentially decaying vacuum tails at the surface boundary. The breaking of the translational symmetry perpendicular to the surface is thus at the origin of surface states. Since the two-dimensional translational symmetry parallel to the surface persists, electronic states of semi-infinite crystals, and in particular surface states, can be characterized by the Bloch wave vector \mathbf{k}_{\parallel} . It shows that surface-state bands $E(\mathbf{k}_{\parallel})$ always lie in projected bulk band gaps, i.e. in regions of $(E, \mathbf{k}_{\parallel})$ space where no bulk states with the particular energy E and parallel wave vector \mathbf{k}_{\parallel} exist¹. When a crossing of a surface-state band with projected bulk states occurs, the surface state evolves into a surface resonance.

A good introduction to the theory of surface-state electrons and the historical development of “surface-state science” is given in Ref. [50]. Here we content ourselves with a very brief overview. Studying a one-dimensional semi-infinite Kronig–Penney model with surface potential, Tamm predicted the existence of surface states in 1932 [51]. Shockley took another approach and studied how surface states originate from the atomic levels by varying the lattice constant from infinity to a finite value [52]. He found that surface states develop in inverted bulk band gaps which form when the over-

¹Starting from the bulk bands $E(\mathbf{k}_{\parallel}, k_{\perp})$ of the infinite crystal the projected bulk band structures are obtained by plotting $E(\mathbf{k}_{\parallel})$ for all values of k_{\perp} , i.e. one disregards the wave vector perpendicular to the surface altogether [49].

lap of the atomic orbitals is large enough that band crossing occurs. After Shockley published his work in 1939, the general trend in the literature was to distinguish between Shockley and Tamm surface states, reflecting the different approaches. Tamm states are referred to as states being entirely due to the change in potential in the outermost cells of the crystal, whose atoms are far enough apart, so that no band crossing occurs. On the other hand, Shockley states are usually defined as the states obtained when a periodic potential is symmetrically terminated at the surfaces and the atoms are sufficiently close together that band crossing is possible ².

Experimental interest in surface states arose only in the late 1940's when, motivated by the development of semiconductor devices like transistors, many laboratories started to study all types of phenomena occurring at crystal surfaces and at metal-metal or metal-semiconductor interfaces. The first experimental evidence for the existence of surface states at semiconductor surfaces came in 1947 [54–57]. In the case of metals it was only 35 years after their prediction by Tamm that surface states were observed experimentally in 1967 [58, 59]. In the latter two decades research in electronic structure of surfaces has become a rapidly developing field. Most important for the progress in the field was the improvement of photoemission experiments and in particular angle-resolved photoemission (ARPES) in the early 70's [60], which gives access to both E and \mathbf{k}_{\parallel} and thus the electronic structure of the surface. Since the measurements presented in this Chapter and Chapters 4, 5 and 6 of this thesis have been performed on surface states of noble-metal (111) surfaces, we focus on these systems.

All three noble metals, copper, silver and gold, show a bulk band gap in their Γ L projected bulk band structure in the SBZ center around $\bar{\Gamma}$ (see Figs. 3.2 and 3.3). This so-called L gap is the result of an s - p band crossing in these materials. Thus all requirements for a Shockley type surface state are met, and an s - p derived Shockley-type surface state at $\bar{\Gamma}$ is indeed present at the surfaces of all three noble metals. There are actually further surface states on the (111) surfaces of these metals, e.g. an s - d derived Shockley-type surface state at $\bar{\Gamma}$ and a d derived Tamm state with negative effective mass at \bar{M} ([62–64] and Refs. therein), but their band edges are far above or below the Fermi level (> 2 eV), and they are not (easily) accessible to STM. Thus the s - p derived surface state is the system of choice in STM studies.

The s - p Shockley states on noble-metal surfaces have been extensively studied by angle-resolved photoemission [61–71] and k -resolved inverse photoemission spectroscopy (KRIPES) [72–75]. The picture that emerges from these experiments is that of a free

²This classification may be confusing and several author's recommend to refrain from making this distinction [53].

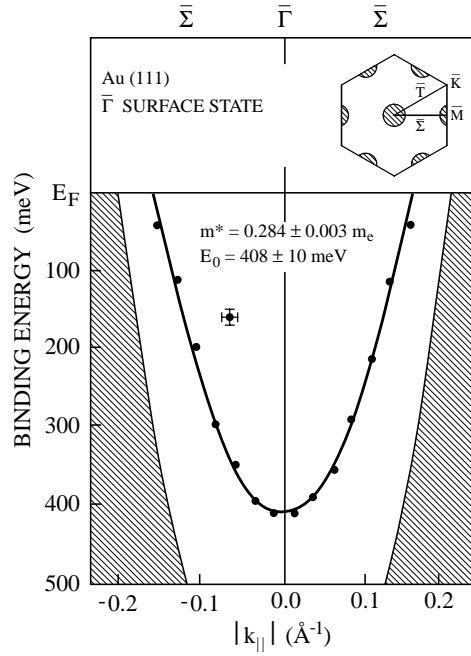


Figure 3.3: Electronic band structure of the (111) surface of Au(111) along the high symmetry line $\bar{\Gamma}\bar{M}$. There exist bulk states in the hatched regions of $(E, \mathbf{k}_{||})$ space. Clearly visible is the L bulk band gap, resulting from the crossing of s and p bands (white region). It is in this gap that the $\bar{\Gamma}$ s - p derived Shockley-type surface state exists. Its dispersion is parabolic with a positive effective mass m^* . The inset in the upper right corner shows the necks of the bulk Fermi surface. Hatched regions in the inset are regions where no bulk states exist at the Fermi level. (Reproduced from Ref. [61].)

quasi two-dimensional electron gas (see Fig. 3.3), i.e. the surface-state dispersion is *parabolic* and *isotropic* in the center of the SBZ ($k_{||} \lesssim 0.2 \text{ \AA}^{-1}$):

$$E = E_{\bar{\Gamma}} + \frac{\hbar^2}{2m^*} k_{||}^2. \quad (3.1)$$

Here $E_{\bar{\Gamma}}$ is the surface-state band edge energy and the effective mass m^* is positive in all three cases. However, for Cu, Ag as well as for Au, m^* is considerably smaller than m_e due to the presence of the crystal potential (see Table 3.1). The localization of the surface-state electrons perpendicular to the surface was determined in a very nice experiment by Hsieh *et al.* [67], who found a decay length into the bulk of the probability density for the Ag(111) surface state of about 6 interlayer spacings, i.e. 14 Å. On the other hand, the relatively small m^* indicates a complete delocalization of the surface-state electrons in the plane³. The density of states of a free 2D electron gas is a constant

³ $1/m^*$ scales with the overlap integral in a simple tight-binding model.

	$E_{\bar{\Gamma}}$ (meV)	m^*/m_e	k_F (\AA^{-1})	T (K)	Method	Ref.
Cu(111)	-400	0.42	0.21	300	ARPES	[65]
	-390	0.46	0.22	300	ARPES	[61]
	-440	0.38	0.21	4	STM	[28, 76]
	-390	0.40	0.20	300	ARPES	[70]
Ag(111)	-120	0.53	0.13	300	ARPES	[61]
	-60	0.44	0.084	65	ARPES	[69]
	-65	0.42	0.085	50	STM	[46]
	-65	0.40	0.083	5	STM	[77], Section 3.2
Au(111)	-410	0.28	0.17	300	ARPES	[61]
		0.15		300	STM	[28, 78]
	-440			300	ARPES	[69]
	-417	0.25	0.17	300	ARPES	[71]
	-520	0.26		4	STM	[79]
	-510	0.27	0.17	5	STM	Section 3.2

Table 3.1: Experimental values for the band edge energy $E_{\bar{\Gamma}}$, effective mass m^* and Fermi wave vector k_F for $\bar{\Gamma}$ s - p derived surface states on noble-metal (111) surfaces.

above the onset at $E_{\bar{\Gamma}}$,

$$\rho_{2D}(E) = L_0 \Theta(E - E_{\bar{\Gamma}}) = \frac{m^*}{\pi \hbar^2} \Theta(E - E_{\bar{\Gamma}}) \quad (3.2)$$

and the total density n_0 of the surface-state electron gas is given by ($E_{\bar{\Gamma}} < E_F$)

$$n_0 = |E_{\bar{\Gamma}}| \frac{m^*}{\pi \hbar^2}. \quad (3.3)$$

For the surface states on noble metals n_0 is of the order of 10^{13} cm^{-2} and they constitute rather high-density 2D electron gases (2DEGs). For comparison, the carrier density in a typical 2DEG present at interfaces of semiconductor heterojunctions is of the order of $5 \cdot 10^{11} \text{ cm}^{-2}$ [80].

Starting in 1991 with the work by Davis *et al.* [81], STM has frequently been used to investigate noble-metal surface states [28, 33, 46, 76–78, 82–92]. Electrons in the two-dimensional surface states are subjected to scattering at surface imperfections such as steps and point defects leading to periodic spatial oscillations of the electronic local density of states. The standing LDOS-waves are the analogue to the well known Friedel oscillations of the total charge density [93–95]. The LDOS-oscillations at surfaces can be understood as interference of the electron wave traveling towards the scattering defect with the back-scattered one. The resulting quantum mechanical interference patterns

can be spatially resolved in scanning tunneling microscopy/spectroscopy [33, 76, 78, 82]. The STM acquires a quantity roughly proportional to the surface LDOS in spectroscopic $dI/dV(E, x, y)|_s$ maps [28] (see Eq. (2.10)), whereas it displays the integral of the LDOS from E_F to $(E_F + eV)$ in conventional $z(x, y)|_{I,V}$ topographs (Eq. (2.8)). Standing electron waves have been reported in both imaging modes. These STM images of the spatial distribution of the LDOS around defects enabled an unprecedented direct access to several surface electronic properties. The dispersion relation $E(k_{||})$ of the 2D electron gas has been determined by means of STM [28, 46, 76–78] with an accuracy comparable to state-of-the-art angle-resolved photoelectron spectroscopy studies [61, 69, 70]. The advantage of STM in measuring the dispersion relation is the access to electronic states both below and above E_F . Mapping of the 2D Fermi contour of surface states was achieved through the Fourier transform of STM topographs taken at very low bias voltage [87, 96, 97]. Finally, stationary solutions of the Schrödinger equation in 2D were visualized for particular geometries of the scattering potential [33, 82, 88, 91] (see Chapter 5).

3.2 Surface-State Band Structure

The way surface-state electrons influence STM measurements will now be discussed in detail. First of all, we recall that the density of states of the free surface-state electrons is constant above the surface-state band edge $E_{\overline{\Gamma}}$ (Eq. (3.2)), and thus the surface density of states in absence of surface defects as steps and impurities is given by

$$\rho_s(E) = \rho_b(E) + L_0 \Theta(E - E_{\overline{\Gamma}}), \quad (3.4)$$

where $\rho_b(E)$ is the contribution of the bulk states. (For the moment states in the very center of the SBZ are considered, where the dispersion is parabolic [28, 46, 61, 69, 76–78]). From Eq. (3.4) one expects a step-like feature in scanning tunneling spectra (Eq. (2.10)). Figure 3.4 shows an STS spectrum taken on a clean wide Ag(111) terrace where interference effects due to impurity or step scattering can be neglected and thus $\rho_s(E)$ is given by Eq. (3.4). Since for this spectrum $e|V| \ll \overline{W}$ the transmission factor (Eq. (2.4)) can be assumed constant and dI/dV is a direct measure of $\rho_s(E)$ [28]. We assume a constant $\rho_b(E) = \rho_b$ and $\rho_t(E) = \rho_t$ in this narrow energy window. The sharp feature at -65 meV in Fig. 3.4 can thus directly be interpreted in terms of the surface-state band edge, i.e. $E_{\overline{\Gamma}} = -65$ meV for Ag(111). Above -65 meV dI/dV is almost constant. This confirms the assumption of a constant ρ_b and ρ_t . The relative contribution of the surface state to the surface density of states as measured by STS can be estimated from spectra as shown in Fig. 3.4, e.g. for Ag(111) $L_0/(L_0 + \rho_b) \approx 0.64$.

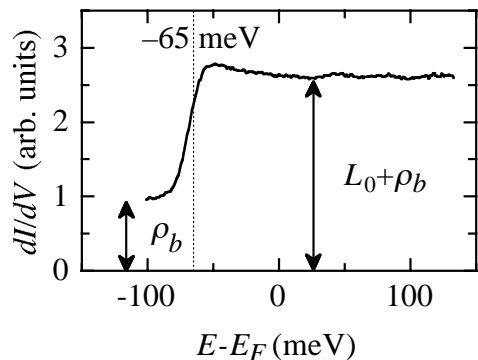


Figure 3.4: Spectrum taken in the center of a clean wide Ag(111) terrace showing the onset of the surface state at -65 meV ($T = 4.9$ K, o.f., $\Delta V = 28$ mV, $\nu \approx 1$ kHz, stabilizing conditions: $V_{st} = 91$ mV, $I = 1$ nA).

The contribution of surface-state electrons to the LDOS detected by the STM is about twice that of electrons from bulk states in the case of Ag(111). As outlined in Section 2.1 STM roughly measures the sample density of states at the tip apex [29–31] and it is clear from Fig. 3.4 that the surface state contributes a considerable fraction to the DOS in front of these noble-metal (111) surfaces⁴. This of course has consequences on various physical properties as described in Chapter 1. The feature in STS spectra would be the only manifestation of surface states, if the crystal surface was perfect, i.e. if there were no structural defects as step edges and no chemical defects as foreign surface and sub-surface atoms. But even the best prepared surface shows residual impurities (0.05 %) and step edges separating terraces of the order of some 1000 Å width. The periodic potential experienced by the surface-state electrons can be considerably altered at and in close proximity to defects and this naturally leads to scattering. In other terms, such impurities and step edges can act as static scatterers [80], i.e. electrons in the 2D surface state may be reflected elastically by such defects and thus interference effects may alter the DOS around surface defects. Figure 3.5 shows a dI/dV image taken at a Cu(111) step edge recorded simultaneously with the corresponding constant-current image (page 18). According to Eq. (2.10) the clearly visible spatial oscillations in Fig. 3.5(a) are due to spatial oscillations in the LDOS of the sample at the energy $E = eV = 600$ meV. The straight step edge leads to a planar wave pattern in the LDOS whereas the point defect in the lower left creates circular standing waves. Note the interference effects in the region between the point defect and the step edge. The oscillations in the LDOS close to defects are due to interference effects in the 2D electron gas of the surface-state electrons, analogous to Friedel oscillations in the total electron density [93]. It is clear from Fig. 3.5 that every static scatterer on the surface can be identified by the corresponding interference pattern. Thus STM offers the possibility to estimate the *elastic mean free path* of surface-state electrons, i.e. the distance an electron can travel without encountering a static scatterer, L_m , by evaluating the mean distance between

⁴Note that the bulk-state density decays faster into the vacuum than the surface-state density, since surface-state electrons have a smaller average in-plane momentum.

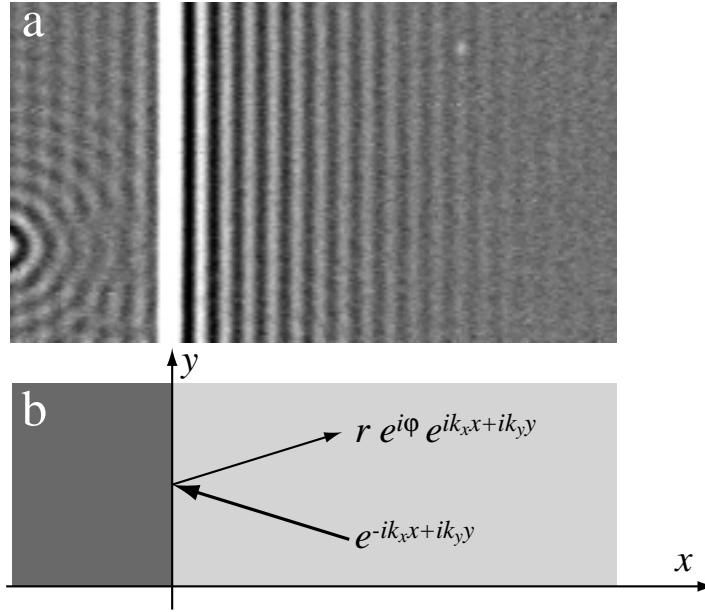


Figure 3.5: (a) $247 \text{ \AA} \times 138 \text{ \AA}$ dI/dV image at a straight Cu(111) step edge. The step edge itself is imaged as a white stripe and the upper terrace is on the right hand side. To the very left a surface impurity is visible. LDOS oscillations at the step edge and impurity atom are clearly visible ($T = 4.9 \text{ K}$, c.f., $\Delta V = 101 \text{ mV}$, $\nu = 5.7 \text{ kHz}$, stabilizing conditions: $V = 600 \text{ mV}$, $I = 3 \text{ nA}$). (b) Corresponding scattering schematics.

such static scatterers. For our samples, with an impurity density of about 0.05 %, we find a global L_m of some 100 \AA . The mobility of the surface-state electrons, defined by $\mu = eL_m/\hbar k_F$, can thus be estimated to $\mu \approx 10^2 \text{ cm}^2/\text{Vs}$ [80]. For comparison, the mobility in a semiconductor 2DEG can be larger than $10^6 \text{ cm}^2/\text{Vs}$.

Since k_F^{3D} of the bulk electrons in the noble metals addressed here is with about 1.2 \AA^{-1} considerably larger than k_F^{2D} of the surface-state electrons ($k_F^{2D} = 0.21 \text{ \AA}^{-1}$, $k_F^{2D} = 0.083 \text{ \AA}^{-1}$ and $k_F^{2D} = 0.17 \text{ \AA}^{-1}$ for Cu, Ag and Au respectively, see Table 3.1), and since the Thomas–Fermi screening length is inversely proportional to k_F [98, 99], screening on this surfaces is dominated by bulk electrons. The Coulomb electric field of an electron in a surface state is thus efficiently screened by bulk electrons and a second surface-state electron will hardly feel the presence of other surface-state electrons except through the Pauli principle. In other words, the Coulomb repulsion between electrons in the 2D gas is likely to play a minor role. We will see later on in this Section and in Chapter 6 that treating noble-metal surface-state electrons as uncharged particles is a very good approximation.

The Friedel-type oscillations in the LDOS at a straight step edge are readily calculated in the following model. Let us consider a *free non-interacting* 2D electron gas with

dispersion given by Eq. (3.1). By convention, the x axis is chosen perpendicular to the step edge, i.e. x denotes the distance from the step (Fig. 3.5(b)). Since we do not know anything about the step potential and to stay as general as possible, we model the step edge as a plane wave reflector with a coherent reflection amplitude $r(k_x)$ and a reflection phaseshift $\varphi(k_x)$, which both may depend on the energy which is in the electron motion perpendicular to the step. For coherent (elastic) processes the electron energy is conserved and since the straight step problem is invariant under translations along y , k_y is conserved during the process, i.e. $k'_y = k_y$ ⁵. From energy and parallel momentum conservation it directly follows that $k'_x = -k_x$. Thus the incoming plane wave $e^{-ik_x x + ik_y y}$ has to be superimposed coherently by the reflected plane wave $r(k_x)e^{i\varphi(k_x)}e^{ik_x x + ik_y y}$, i.e. the wave function has the form

$$\Psi_{E,k_y}(x, y) = (e^{-ik_x x} + r(k_x)e^{i\varphi(k_x)}e^{ik_x x})e^{ik_y y}, \quad (3.5)$$

where $k_x = \sqrt{2m^*(E - E_{\overline{\Gamma}})/\hbar^2 - k_y^2}$. Electrons are not only reflected at the step edge but may be transmitted into the surface states on the adjacent terrace (with probability $t^2(k_x)$) or, since the 2D electron gas may be coupled to the bulk electrons at the step edge, they may be absorbed at the step (with probability $a^2(k_x)$). Absorption then means scattering from surface into bulk states. For simplicity we disregard the possible k_y dependence of $a^2(k_x)$ and will reason later on that this does not change the final result for the LDOS at the step. Particle conservation implies $r^2(k_x) + t^2(k_x) + a^2(k_x) = 1$. Since there is no net flux of electrons from surface states into bulk states, as much electrons must be emitted into surface states as are absorbed by bulk states, i.e. $a^2 = e^2$, where a^2 and e^2 are the k_x - k_y -averaged probabilities for absorption and emission. We further assume that the probability distribution for emission is the very same as for absorption, implying in this case $a^2(k_x) = e^2(k_x)$ (also this does not alter the final result, as seen below). The number N of electrons per unit area at location (x, y) with energy less than E is given by *incoherent* summation over $|\Psi_{E,k_y}(x, y)|^2$ of Eq. (3.5), the transmitted

⁵We neglect the discrete nature of the translation symmetry and thus Bragg reflection [45], which is a good approximation since typical π/k_y are much larger than next-nearest atom distances.

electrons from the left hand side and the emitted electrons:

$$\begin{aligned}
N(E, x) &= 2 \int_0^{k_E} \frac{dk_x}{2\pi} \int_{-\sqrt{k_E^2 - k_x^2}}^{\sqrt{k_E^2 - k_x^2}} \frac{dk_y}{2\pi} \left(\left(1 + r^2(k_x) + 2r(k_x) \cos(2k_x x + \varphi(k_x)) \right) + \right. \\
&\quad \left. + t^2(k_x) + e^2(k_x) \right) \\
&= \frac{2}{\pi} \int_0^{k_E} \frac{dk_x}{2\pi} \left(2 + 2r(k_x) \cos(2k_x x + \varphi(k_x)) \right) \sqrt{k_E^2 - k_x^2}. \tag{3.6}
\end{aligned}$$

Here the factor 2 comes from the assumed spin degeneracy and we have used $t^2(k_x) + e^2(k_x) = 1 - r^2(k_x)$. k_E is given by

$$k_E = \sqrt{2m^*(E - E_{\bar{\Gamma}})/\hbar^2}. \tag{3.7}$$

The LDOS at the step edge is then readily calculated from Eq. (3.6):

$$\begin{aligned}
\rho_{\text{step}}(E, x) &= \frac{\partial}{\partial E} N(E, x) \\
&= \frac{2}{\pi} L_0 \int_0^{k_E} dk_x \frac{1 + r(k_x) \cos(2k_x x + \varphi(k_x))}{\sqrt{k_E^2 - k_x^2}}. \tag{3.8}
\end{aligned}$$

For Ag(111) the phaseshift $\varphi(k_x)$ has experimentally been shown to lie close to $-\pi$ independent of k_x [91]. Furthermore, numerical integration of Eq. (3.8) showed, that the results for an arbitrary $\varphi(k_x)$ distinguishes itself from the result for $\varphi(k_x) = -\pi$ mainly by a mere x -translation of the order of $(\varphi + \pi)/k_E$. For these two reasons we set $\varphi(k_x) = -\pi$ in the following. Under these conditions and with a reasonable k_x dependence of $r(k_x)$ [45, 91] one finds

$$\rho_{\text{step}}(E, x) \approx L_0 (1 - r(k_E) J_0(2k_E x)), \tag{3.9}$$

where J_0 is the Bessel function of order zero. The relation is exact in the case of an energy independent reflection amplitude. The oscillations seen in Fig. 3.5 can thus be understood in terms of the oscillating part of Eq. (3.9), i.e. the $J_0(2k_E x)$ term. The asymptotic behavior of $J_0(u)$ is $\sqrt{2/\pi u} \cos(u - \pi/4)$, and thus, in a 2D electron gas, there is an intrinsic $1/\sqrt{x}$ decay of the Friedel-type LDOS oscillations at a step edge⁶. This decay for $D > 1$ comes from the fact that all k_x values from 0 up to k_E contribute to the LDOS at fixed energy E . A decay of the interference patterns in Fig. 3.5 is clearly seen. But it is not *a priori* clear that this measured decay is governed by the intrinsic $1/\sqrt{x}$

⁶An intrinsic decay of the LDOS oscillations is absent in 1D, but even more pronounced in 3D.

decay, since additional inelastic processes on the terrace may alter the decay behavior as discussed in Chapter 4. The LDOS in Eq. (3.9) asymptotically approaches the constant value L_0 far away from the step, justifying the assumptions made on $a^2(k_x)$ and $e^2(k_x)$.

Starting from ρ_{step} in Eq. (3.9) the current close to a step edge for bias voltages $e|V| \ll \overline{W}$ is given by Eq. (2.5) where $\rho_s(E, x, y)$ has to be replaced by the sum of $\rho_{\text{step}}(E, x)$ and a constant bulk contribution ρ_b . We assume a constant tip DOS in the narrow energy intervals of interest. The current can then be written

$$I(V, T, x, s) \propto e^{-2s\sqrt{\frac{m_e}{\hbar^2}}\sqrt{2\overline{W}}} \left(\int_{-\infty}^{\infty} dE \left(\rho_b + \rho_{\text{step}}(E, x) \right) f(E - eV, T) \right. \\ \left. - \int_{-\infty}^{\infty} dE \left(\rho_b + \rho_{\text{step}}(E, x) \right) f(E, T) \right), \quad (3.10)$$

Following Adawi [100] the temperature effect due to the broadening of the Fermi function in the integrands of Eq. (3.10) can be approximated by performing the integration at $T = 0$ K and by multiplying the oscillating parts of the resulting functions with $\xi_{k_E}/\sinh \xi_{k_E}$, where

$$\xi_{k_E} = x \frac{2\pi m^*}{\hbar^2} \frac{k_B T}{k_E}, \quad (3.11)$$

and the energy E for the evaluation of k_E has to be chosen at the cut-off of the Fermi function, i.e. $E_F + eV$ and E_F for the first term and second term in Eq. (3.10), respectively. The integrations at $T = 0$ K are readily evaluated and one obtains the following expression for the tunneling current close to a step edge

$$I(V, T, x, s) \propto e^{-2s\sqrt{\frac{m_e}{\hbar^2}}\sqrt{2\overline{W}}} \left(eV(L_0 + \rho_b) - rL_0 \frac{\hbar^2}{2m^*} \frac{1}{x} \right. \\ \left. \times \left(\frac{\xi_{k_{eV}}}{\sinh \xi_{k_{eV}}} k_{eV} J_1(2k_{eV}x) - \frac{\xi_{k_F}}{\sinh \xi_{k_F}} k_F J_1(2k_Fx) \right) \right). \quad (3.12)$$

Here J_1 is the first order Bessel function. We have assumed that the step reflection amplitude r is the same for all k_x wave vectors contributing to $I(V, T, x, s)$, which is a good approximation when $e|V| \ll |E_F|$. For low bias voltages the effective reflection amplitude r is given by $r(k_F)$. Numerical solution of the integral in Eq. (2.5) with ρ_{step} from Eq. (3.9) shows that the ‘‘Adawi’’ approximation in Eq. (3.12) is very accurate. By inverting Eq. (3.12) the constant-current tip-sample distance at a step edge is obtained

(see also Eq. (2.8)):

$$\begin{aligned}
s(x)|_{I,V} = & \frac{1}{2\sqrt{\frac{m_e}{\hbar^2}}\sqrt{2\overline{W}}} \ln \left(1 - r \frac{1}{eV} \frac{L_0}{\rho_b + L_0} \frac{\hbar^2}{2m^*} \frac{1}{x} \right. \\
& \times \left(\frac{\xi_{k_{eV}}}{\sinh \xi_{k_{eV}}} k_{eV} J_1(2k_{eV}x) - \frac{\xi_{k_F}}{\sinh \xi_{k_F}} k_F J_1(2k_Fx) \right) \\
& \left. + s_0 \right). \tag{3.13}
\end{aligned}$$

Since for $u \gg 1$ $J_1(u)$ behaves as $\sqrt{2/\pi u} \cos(u - 3\pi/4)$, $s(x)$ asymptotically falls off like $1/x^{\frac{3}{2}}$ at zero temperature, i.e. faster than the corresponding LDOS. This is due to the wave vector spread in the integral over the LDOS. It is seen in Eq. (3.13) that the amplitude of the oscillations scales with k_{eV}/eV , meaning that the higher the tunneling bias, the smaller is the amplitude of the interference patterns. Furthermore, the wave vector spread leads to a damping of the interference patterns which is more pronounced for larger bias values (see Chapter 4). Altogether, the effect of the LDOS oscillations on $s(x)|_{I,V}$ are more pronounced at low bias values and are almost not visible at higher biases, where the wave vector spread washes out the interference effects in $s(x)|_{I,V}$.

To demonstrate the validity of our $s(x)|_{I,V}$ model we present in Fig. 3.6(a) the fit by Eq. (3.13) to a topographic linescan taken perpendicularly to a monatomic Ag(111) step. For Ag(111) the electron wave vectors k_{eV} , k_F and the effective mass m^* are known from the dispersion (Table 3.1). The ratio $L_0/(\rho_b + L_0) = 0.64$ has been estimated from dI/dV data on a clean terrace (see Fig. 3.4). Furthermore, by ramping z and measuring the tunneling current I (Eq. (2.6)) we have determined the apparent barrier height $\overline{W} = (3.1 \pm 0.1)$ eV for Ag(111) [101]. Except from the reflection amplitudes r_{desc} and r_{asc} for the descending and ascending side of the step, respectively, all parameters entering Eq. (3.13) are thus known. The good agreement between model and experiment is evident. From our fit we obtain quite different reflection amplitudes r on the upper and on the lower terrace. For electrons being reflected by the ascending step r_{asc} is 1.8 ± 0.4 times smaller than for those approaching a descending step. These r -values represent the reflection amplitude at the Fermi level, $r(k_F)$, since the linescan has been taken at low bias. The linescan in Fig. 3.6(b) has been performed at a bias voltage of 100 mV. It clearly shows the beating of the Bessel functions at $k_{100 \text{ meV}}$ and k_F (see Eq. (3.13)). The oscillations and beating in $z(x)$ down to amplitudes of $1/1000 \text{ \AA}$ are perfectly described by Eq. (3.13). Note the difference in amplitude of the oscillations in Fig. 3.6(a) and (b). At 10 mV the amplitude of the oscillations are almost a factor of 10 larger than at 100 mV, confirming that the wave vector spread washes out the coherence effects.

LDOS oscillations as seen in Fig. 3.5 reveal information about the wave vector k_E

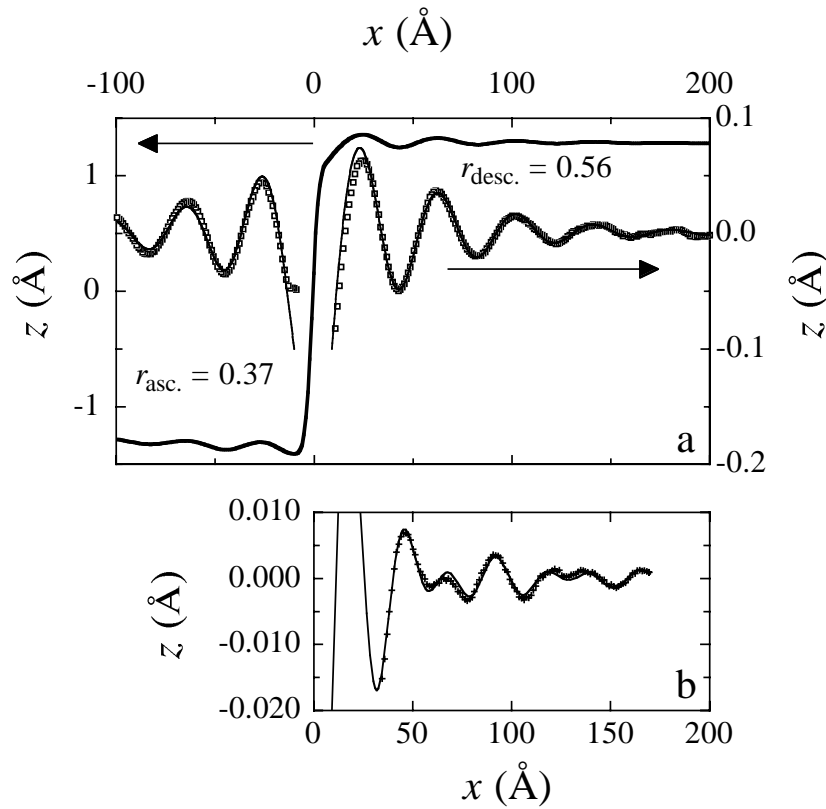


Figure 3.6: Constant-current linescan taken across a Ag(111) step **(a)** at $V = 10$ mV and $T = 77.3$ K, **(b)** at $V = 100$ mV and $T = 3.5$ K ($I = 1.0$ nA in (a) and (b)). The solid lines are fits using Eq. (3.13) (see text). The agreement between experiment and model is striking; also pronounced beating effects appearing at larger bias voltage as in (b) are perfectly reproduced. The only free fit parameters in (a) are the two reflection amplitudes r_{desc} and r_{asc} for descending and ascending steps.

of electrons with energy E . This is very welcome in STM, since STM is not intrinsically sensitive to the wave vector. In this sense LDOS oscillations open up an access to the surface-state band structure, i.e. the dispersion relation can be acquired. In order to measure the dispersion relation of a surface state with STS, it suffices to take a single linescan perpendicular to a straight substrate step, and to measure a conductance map $dI/dV(E, x)$, while moving the STM tip on this linescan. Technically, the conductance map is acquired by taking $dI/dV(E)|_x$ spectra at every fourth topographic pixel x of the linescan under open feedback loop conditions (page 18). The idea is to acquire these spectra at a constant distance from the atomic nuclei in the surface layer, i.e. at constant s . If one succeeds in keeping s constant, then the only contribution to spatial variations in $dI/dV(E)|_x$ comes from the surface density of states $\rho_s(E, x)$, as seen in Eq. (2.5). In order to keep s constant we stabilized the tip height in constant-current mode, $s(x)|_{I, V_{\text{st}}}$, at relatively large bias ($V_{\text{st}} > 300$ meV) where the LDOS induced oscillations in $s(x)|_{I, V_{\text{st}}}$ are very weak as discussed above (see also Eq. (3.13)). We

checked the procedure numerically by introducing the expressions for $s(x)|_{I,V_{\text{st}}}$ with $s_0 = 5 \text{ \AA}$ from Eq. (3.13) and $\rho_s(E, x) = \rho_{\text{step}}(E, x)$ from Eq. (3.9) with typical surface-state parameters (Table 3.1) in Eqs. (2.3) and (2.4) and calculated the resulting $dI/dV(E = eV, x)$ (assuming a constant tip DOS). The simulation shows that $dI/dV(E, x)$ acquired under these conditions is an excellent measure of $\rho_{\text{step}}(E, x)$ for $|E| \lesssim 400 \text{ meV}$ and if V_{st} is larger than about 100 meV [28]. Hence, by measuring $dI/dV(E, x)$ as described, the convolution between standing waves in the tip height $s(x)$ of the constant-current linescan and those in dI/dV spectra can completely be avoided [28, 46, 76].

Ag(111)

The result of the $dI/dV(E, x)$ measurement perpendicular to a Ag(111) step edge is shown in Fig. 3.7. The upper graph displays the constant-current linescan on which the tip was moved while taking the $dI/dV(E)|_x$ spectra. As can be seen, at the stabilizing bias voltage of $V_{\text{st}} = 0.3 \text{ V}$ the tip-surface distance is almost not influenced by standing waves (only in the immediate vicinity of the step) and the tip closely follows the real topography. The $dI/dV(E, x)$ data are represented by graylevels as a function of the distance from the step edge x in abscissa and energy E in ordinate. First of all one recognizes a rather sharp transition from black (low LDOS values) at energies below -65 meV to white (high LDOS) above. This is just the onset of the surface state as already discussed in Fig. 3.4. Furthermore, the density plot in Fig. 3.7 nicely illustrates the dispersion of the Ag(111) surface state. From top to bottom the wavelength of the standing waves in the LDOS increases for energies approaching E_F until it diverges at the band edge at $E_F = -65 \text{ meV}$. As stated above the experimental $dI/dV(E, x)$ in Fig. 3.7 can directly be interpreted in terms of the sample LDOS $\rho_{\text{step}}(E, x)$. The lower graph of Fig. 3.7 shows a constant energy cut of the $dI/dV(E, x)$ plot, which is accurately fitted by Eq. (3.9). *The fact that the LDOS oscillations in these surface states are perfectly described by the simplest model neglecting Coulomb interaction strongly supports what has been stated above: s - p derived noble-metal surface-state electrons are screened by the underlying bulk electrons* (see also Fig. 3.6 and Refs. [28, 33, 46, 76, 77, 82, 83, 91, 92]). If there was no such screening, the surface-state electron density would be completely different from what is observed (see Chapter 6). It would show a Thomas–Fermi screening behavior of the positive charge accumulated in the depletion region close to the scatterer [98, 99], superposed by Friedel oscillations with amplitudes that are much weaker than in the non-interacting case. By fitting $dI/dV(x)|_E$ at various energies we obtain the wave number for each energy, and thus the dispersion relation of the Ag(111) s - p derived Shockley-type surface state. The fits actually are performed

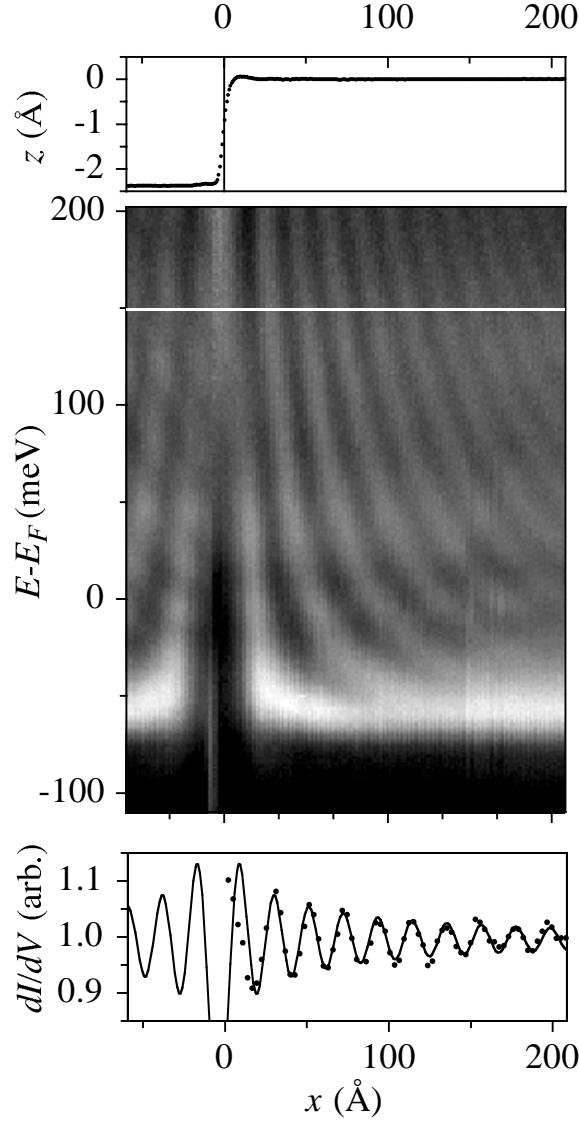


Figure 3.7: Plot of the differential conductance dI/dV of Ag(111) as a function of the lateral distance from the step x and of bias energy $E = eV$ with respect to E_F . The upper graph shows the constant-current linescan ($V_{st} = 0.3$ V, $I = 2.0$ nA) on which the STM-tip was moved while taking the $dI/dV(V)$ -spectra. The lower graph is a cut of the dI/dV plot taken along the white line at $E = 148$ meV (dots). The full line depicts a fit by Eq. (3.9) ($T = 4.9$ K, o.f., $\Delta V = 10$ mV, $\nu \approx 1$ kHz).

with four parameters: wave vector k_E , proportionality factor, background term and step edge position x_0 . The latter coincides with the midheight points of the step edge, confirming a phaseshift φ of $-\pi$. The result of the k_E fits is displayed as $E(k_{||})$ in Fig. 3.8. Our data are in excellent agreement with previously published results derived from photoelectron spectroscopy [69] and STS [46] (see also Table 3.1). The state is free-electron-like in the vicinity of $\bar{\Gamma}$, the effective mass determined from a quadratic fit

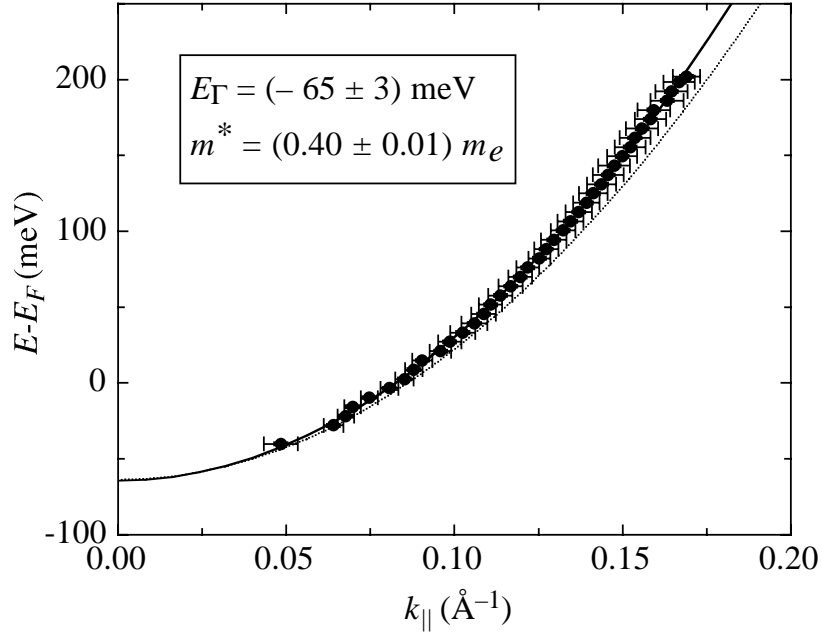


Figure 3.8: Dispersion relation of the Ag(111) s - p derived surface state. The solid line is a quadratic fit to our STM data and the dotted line shows results from photoemission data at 65 K [69] ($T = 4.9$ K).

is $m^* = (0.40 \pm 0.01) m_e$ and the band edge is located at $E_{\bar{\Gamma}} = (-65 \pm 3)$ meV with respect to E_F ($k_F = 0.083 \text{ \AA}^{-1}$, $\lambda_F = 76 \text{ \AA}$). In our experiments we have found no significant temperature dependence of $E(k_{\parallel})$ between 5 K and 77 K [69].

Au(111)

In contrast to the unreconstructed close-packed surfaces of copper and silver, the Au(111) surface exhibits the well-known $22 \times \sqrt{3}$ “herringbone” reconstruction ([102] and Refs. therein). Figure 3.9 shows a typical constant-current image of the Au(111) surface. The reconstruction pattern is due to a stress induced contraction along the $\langle 1\bar{1}0 \rangle$ direction (the lines perpendicular to the ridges). In one part of the reconstruction unit cell the surface atoms occupy hcp sites, while in the adjacent part they occupy fcc sites. The hcp region is with 25 \AA noticeably narrower than the 38 \AA wide fcc region. The ridges are formed by surface atoms occupying bridge sites between the fcc and hcp regions. A longer range structure, consisting of rotated uniaxial domains, arises to establish long range isotropic stress release [102]. Chen *et al.* showed that the reconstruction acts as a superlattice for the s - p derived surface-state electrons [79]. Their data is compatible with an extended Kronig–Penney model, where the hcp region of the reconstruction provides a broad, shallow electronic well that is approxi-

mately 25 meV deeper than the fcc region. As outlined in Chapter 6 we have taken a completely different approach to investigate the influence of the reconstruction on the surface-state electron potential landscape, which essentially yields the same results as Ref. [79]. Due to the superlattice the Au(111) s - p derived surface-state band structure should exhibit deviations from free behavior, e.g. one expects band gaps at wave vectors characterizing the superlattice, in analogy to a 1D Kronig–Penney model [103].

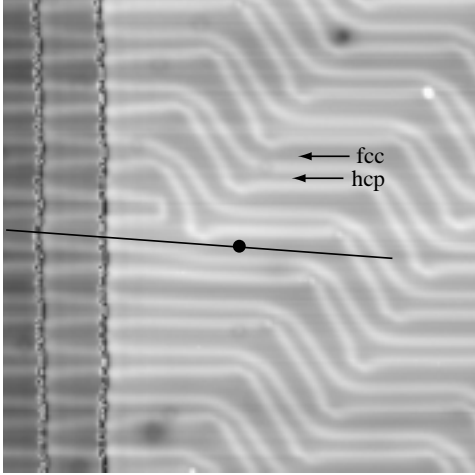


Figure 3.9: 600 Å×600 Å constant-current image of the Au(111) surface, showing the “herringbone” reconstruction with alternating fcc and hcp stacking regions. The dI/dV data of Fig. 3.10 have been taken in the fcc region along the indicated line. The dot depicts the location at which the spectrum in the inset of Fig. 3.11 has been taken.

The assumptions made for the formalism derived above in Eqs. (3.9), (3.12) and (3.13) are thus in principle not fulfilled. But since the potential modulation ΔU due to the superlattice is minor (of the order of some 10 meV) we expect the effects to be small, at least for energies far above $E_{\bar{\Gamma}}$, i.e. $(E - E_{\bar{\Gamma}})/\Delta U \gg 1$. For this reason we have determined the dispersion relation for the Au(111) s - p derived Shockley-type surface state at $\bar{\Gamma}$ using the formalism for free electrons. A differential conductance map at a straight step edge on Au(111) has been acquired in the very same way as for Ag(111) (page 35). The result of a $dI/dV(E, x)$ measurement taken along the line depicted in Fig. 3.9 is shown in Fig. 3.10. The $dI/dV(E, x)$ map has been acquired perpendicularly to the step edges and in an fcc region. A relatively high stabilizing voltage of 0.9 V is used again, to ensure a constant tip-sample distance (see upper graph in Fig. 3.10). The reconstruction ridges are clearly seen at about 300 Å and 330 Å in the constant-current linescan (compare to Fig. 3.9). On the wide terrace, one recognizes a similar LDOS behavior as in Fig. 3.7 for Ag(111), i.e. the interference pattern due to the presence of a *single* step edge. The dispersion relation for the s - p surface state on Au(111) has been determined by fitting this part of the density map with ρ_{step} from Eq. (3.9), much as for Ag(111). The result, $E(k_{\parallel})$, is depicted in Fig. 3.11. Between the two steps and on the left side of the left hand step of Fig. 3.10 the differential conductance map, i.e. the surface LDOS, shows a washed-out peaked structure. This structure in the dI/dV map is due to the confinement of electrons between two step edges [82, 86, 91], and will be extensively discussed in Chap-

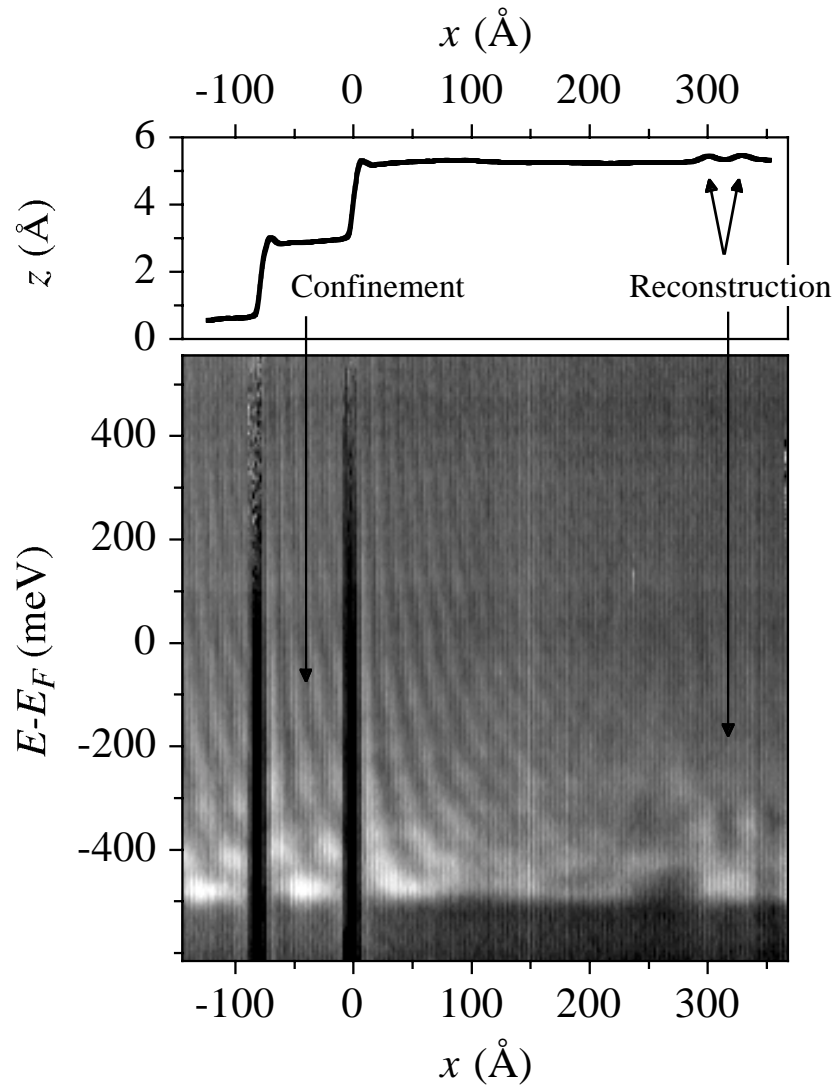


Figure 3.10: Plot of the differential conductance taken in an fcc region of Au(111) along the line depicted in Fig. 3.9. dI/dV is plotted as a function of the lateral distance from the step x and of bias energy $E = eV$ with respect to E_F . The upper graph shows the constant-current linescan ($V_{\text{st}} = 0.9$ V, $I = 2.0$ nA) on which the STM-tip was moved while taking the $dI/dV(V)$ -spectra ($T = 4.9$ K, o.f., $\Delta V = 20$ mV, $\nu = 1.8$ kHz).

ter 5. Furthermore, there is a faint structure in the LDOS close to and directly above the hcp region located around 315 Å. Clearly recognizable are a broad peak around -470 meV and two maxima around -380 meV. These structures in dI/dV are induced by a potential modulation associated with the reconstruction and will be discussed in Chapter 6.

As seen in Fig. 3.11 the dispersion determined with our model for free electrons deviates considerably from parabolic behavior at energies below -300 meV. In a Kronig-Penney model we expect the energy bands to converge to a parabola characterized by the effective mass of the corresponding free electrons for energies $(E - E_{\text{T}})/\Delta U \gg 1$ [103].

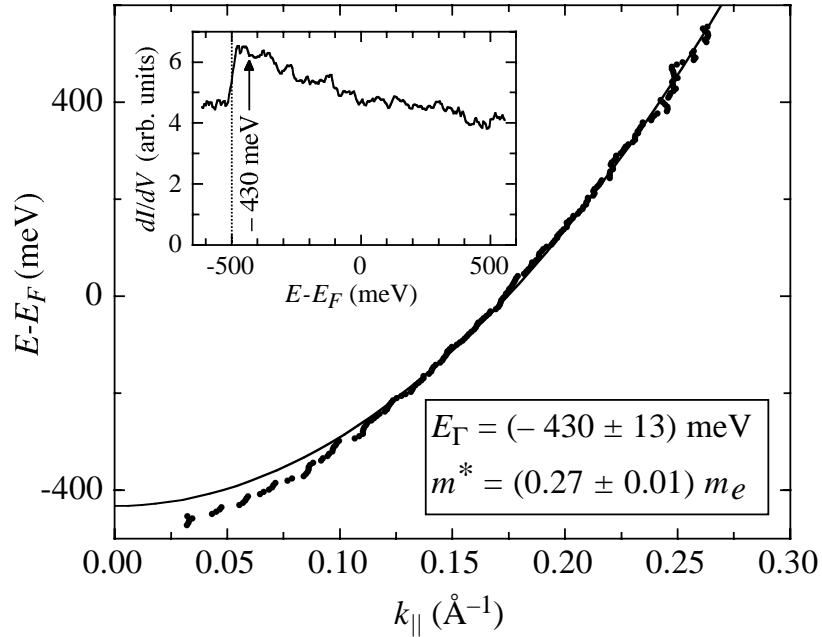


Figure 3.11: Dispersion relation of the Au(111) s - p derived surface state. The solid line is a quadratic fit to our STM data (see text). The spectrum shown in the inset has been taken at the location marked with a dot in Fig. 3.9, i.e. in an fcc region away from step edges ($T = 4.9$ K).

Of course, this parabola is shifted with respect to the band of the free electrons by an energy corresponding to the spatial average of the Kronig–Penney potential. Thus, fitting our data points at energies larger than -300 meV with a parabola should yield a good measure for the effective mass and it is not surprising that the deduced value of $m^* = (0.27 \pm 0.01) m_e$ compares very well with previous experiments (Table 3.1, note that m^* has been shown to be temperature independent [69]). However, as outlined above, the “band edge” value $E_{\Gamma} = (-430 \pm 13)$ meV determined by the parabolic fit is not a true band edge and has no physical meaning, since there are electronic surface states with energies well below $E_{\Gamma} = -430$ meV, as seen in the spectrum in the inset of Fig. 3.11. The onset in this spectrum and thus the band edge of the Au(111) s - p surface state is around -510 meV, in good agreement with low-temperature STS [79] and photoemission [69] results. The deviations from a parabola at low energies are due to the fact that the electrons on Au(111) are subjected to a complicated but rather shallow potential landscape. We would like to emphasize that the model for free electrons we used to determine k_E is only correct for higher energies and the fitted k_E have no physical meaning for energies $\lesssim -300$ meV.

Altogether, the electronic structure of the s - p surface state on Au(111) deviates noticeably from a parabolic band in the center of the SBZ, in contrast to Cu(111) and

Ag(111). This is due to the “herringbone” reconstruction of the Au(111) surface and its influence on surface state electrons. We have been able to determine the effective mass of corresponding free 2D electrons, i.e. electrons with the very same properties as the Au(111) surface-state electrons but which are not subjected to the reconstruction induced potential. The natural way to think of the Au(111) surface state is that free electrons with an effective mass as determined here are brought into the reconstruction potential landscape, leading to a complicated bandstructure. For the characterization of the latter, more elaborate models are needed than discussed here, treating the low-energy states correctly.

Finally, we expected to observe additional interference effects in the LDOS patterns around scatterers due to the large spin splitting observed for the Au(111) *s-p* surface state [71]. This spin orbit coupling induced spin splitting leads to two possible k_{\parallel} vectors at fixed energy, k_{\parallel}^{\uparrow} and $k_{\parallel}^{\downarrow}$, where $k_{\parallel}^{\uparrow} - k_{\parallel}^{\downarrow} = 0.023 \text{ \AA}$. Thus one would expect beating effects on a length scale of the order of 270 \AA , which should be seen for example in a splitting of the Fermi contour in the Fourier transform of large ($\gg 270 \text{ \AA}$) constant-current images taken at low biases [87,89]. But despite the fact that we have been able to acquire a large amount of valuable data (large scale topographs showing nice interference patterns), we have not seen any effect of the spin splitting in our measurements on Au(111). We have no satisfactory explanation why this splitting does not manifest itself in STM.

3.3 Deviations from Parabolic Dispersion

So far we have seen that the *s-p* derived Shockley-type surface states on Cu(111), Ag(111) and with some restrictions also Au(111) form an isotropic and parabolic band, i.e. behave like free electrons in the very center of the SBZ. However, it is well known that in the presence of a periodic potential electronic bands flatten towards the SBZ boundary [98,103]. Therefore the question arises, to what extent these surface-state bands deviate from an isotropic paraboloid further out in the Brillouin zone.

Since the *s-p* derived noble-metal surface states have a band edge $E_{\overline{\Gamma}}$ lying very close to the Fermi energy E_F (Table 3.1), the ARPES studies are inherently limited to the very center of the SBZ, and thus unable to detect any deviations from the quasi-free-electron picture of the surface-state band structure. The dispersion of the unoccupied part of the surface states became accessible through *k*-resolved inverse photoemission spectroscopy. Although the KRIPES dispersions available for the surface states in question show no significant deviation from parabolic behavior either [72,73,75], the deduced values for m^* depend on the energy/momentum interval used for fitting the parabolic

dispersion to the experimental data. Furthermore, the values are usually larger than the corresponding ARPES values and differ from one group to another [72, 75]. The interval dependence was interpreted in terms of the expected flattening of the dispersion towards the SBZ boundary [73]. The STM studies in Refs [46, 76–79], on the other hand, were all restricted to \mathbf{k}_{\parallel} -vectors in the very center of the SBZ ($k_{\parallel} < 0.2 \bar{\Gamma}\bar{\text{M}}$), and thus no deviation of the dispersion relations from a parabolic behavior could be detected. Altogether, it is not clear from the existing literature to what extent the bands of these surface states (resonances) deviate from the parabolic free-electron-like behavior. Actually, the surface-state bands (probably) cross the bulk continuum and thus evolve into surface resonances above E_F [72–75]. We do not distinguish between surface states and resonances here and will refer to both of them as surface states.

In this Section we present measurements of $E(k_{\parallel})$ along $\bar{\Gamma}\bar{\text{M}}$ over an *extended range of the SBZ* ($0 < k_{\parallel} < 0.6 \bar{\Gamma}\bar{\text{M}}$), in contrast to previous STM studies. To do so we have analyzed the Friedel-type oscillations in dI/dV images (see page 18) at descending straight step edges on Cu(111) and Ag(111) (Fig. 3.5). In principle it is possible to investigate the dispersion relation via elegant dI/dV mapping as described in Section 3.2 over the whole k_{\parallel} range accessible to STM. But since the step reflection amplitude $r(k)$ decreases with increasing k [45, 91], the amplitude of the LDOS oscillations becomes so small for energies $E > 500$ meV that they can not be resolved in dI/dV maps shown in Section 3.2. Therefore, dI/dV imaging under closed feedback loop conditions has been chosen to investigate $E(k_{\parallel})$ for larger k_{\parallel} , since it facilitates, e.g. by lateral averaging, to enhance the signal-to-noise ratio as compared to dI/dV mapping.

Figure 3.12 shows typical $dI/dV(x)|_V$ data perpendicular to descending $\langle 1\bar{1}0 \rangle$ -oriented monatomic steps of a Cu(111) surface. Such linescans are obtained from dI/dV images similar to Fig. 3.5 as follows: the dI/dV images are slightly rotated to align the step edge vertically, and then we have averaged the dI/dV data over several linescans. To do the measurements we have chosen surface spots bare of impurities. As seen in Fig. 3.12 we have been able to observe the dI/dV (LDOS) oscillations over many periods, and thus our measurements are very sensitive to the wave vector. Note the different oscillation periods for different energies: the higher the energy, the shorter is the wavelength, as expected.

Since we are interested in deviations of the surface-state band structure from free-like behavior, we can not *a priori* use ρ_{step} from Eq. (3.9) to interpret our data, since ρ_{step} has been calculated under the assumption that the surface-state electrons are free. Here, we therefore consider a 2D electron gas with a more general dispersion given by $E'(q_x, q_y)$, where (q_x, q_y) characterize the 2D Bloch wave vectors. Since the x -axis is by definition

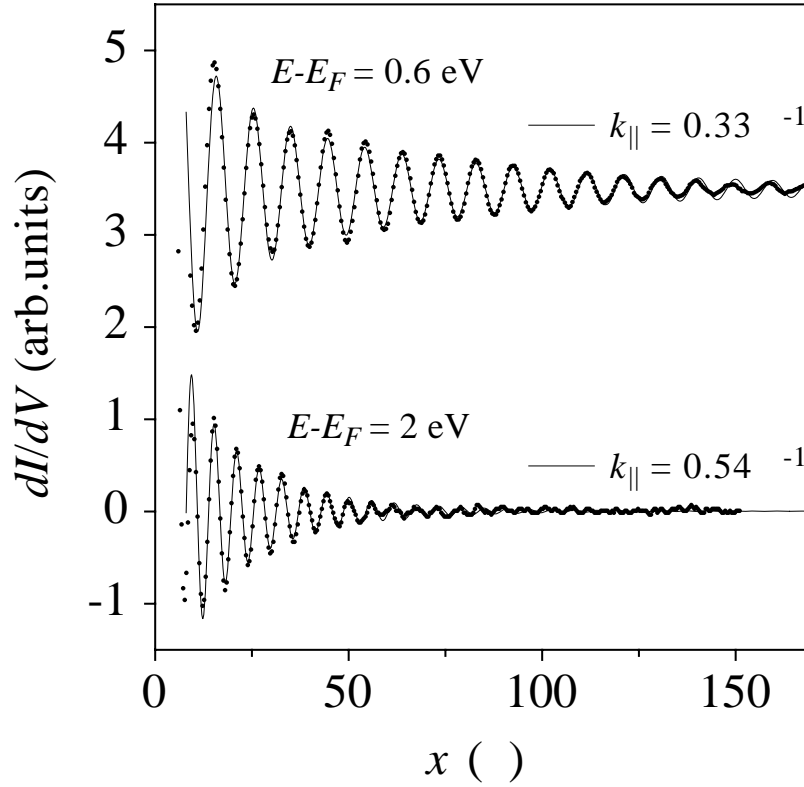


Figure 3.12: Typical dI/dV data perpendicular to a straight descending Cu(111) step obtained by averaging over several linescans. The data at 0.6 eV and 2 eV were taken with a stabilizing current of 3 nA and 10 nA and a ΔV of 101 mV and 156 mV, respectively. The solid lines depict the fits with Eq. (3.15) ($T = 4.9$ K, c.f., $\nu = 5.72$ kHz).

perpendicular to the $\langle 1\bar{1}0 \rangle$ step direction, q_x is along $\bar{\Gamma} \bar{M}$ (see Fig. 3.13(a)). The only assumption we make is that $E'(q_x, 0) \leq E'(q_x, q_y)$ for all (q_x, q_y) which is certainly fulfilled for our systems and the SBZ region of interest [61, 65, 68–70, 72, 73, 75, 104]. Following the derivation of ρ_{step} in Eq. (3.8) one can state that in the case of the more general dispersion $E'(q_x, q_y)$ the sample LDOS at a step edge has the form

$$\rho_s(E, x) = \rho_b + \int_0^{k_x} dq_x \left(1 - r(q_x) \cos(2q_x x) \right) w(q_x, k_x), \quad (3.14)$$

where we assume that the lateral variations of the bulk LDOS ρ_b can be neglected, k_x is given by $E'(k_x, 0) = E$, and $w(q_x, k_x)$ is a weight function depending on the exact form of the crystal potential, i.e. the dispersion relation $E'(q_x, q_y)$. For 2D electron gases not too different from free electrons and k_x not too close to the SBZ boundary $w(q_x, k_x)$ is strongly peaked at $q_x = k_x$, e.g. for free electrons $w^0(q_x, k_x) = 2m^*/(\pi^2 \hbar^2 \sqrt{k_x^2 - q_x^2})$. Thus, due to this property of $w(q_x, k_x)$, $\rho_s(x)|_E$ from Eq. (3.14) is oscillatory with period π/k_x independent of the exact form of $w(q_x, k_x)$. In other words, since we assumed that

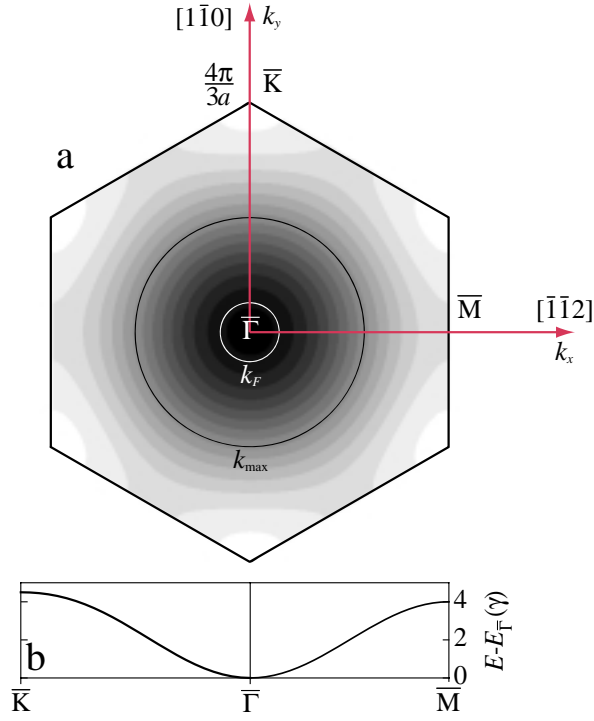


Figure 3.13: (a) First SBZ of an fcc (111) surface. The tight-binding dispersion relation from Eq. (3.17) is plotted in grayscales. The inner white circle (k_F) depicts the surface-state Fermi contour for Cu(111). All our measurements have been limited to the area enclosed by the black circle (k_{\max}), where the tight-binding dispersion can be considered isotropic. (b) Tight-binding surface-state band along high symmetry lines of the SBZ.

$E'(q_x, 0) \leq E'(q_x, q_y)$ the maximal q_x vector contributing to the LDOS oscillations is k_x and since $w(q_x, k_x)$ has an abrupt cut-off at k_x , the LDOS oscillations are dominated by the wave vector k_x . Because we are only interested in the oscillation period here (i.e. wave vector) we therefore do not have to take care of the exact form of $w(q_x, k_x)$ and can safely choose the free-like $w^0(q_x, k_x)$ to interpret our data. This is further supported by the fact that the deviations of the dispersion relation from free-electron-like behavior turn out to be small (see below). With the free-like $w^0(q_x, k_x)$ one comes back to $\rho_s(E, x) = \rho_b + \rho_{step}(E, x)$ with $\rho_{step}(E, x)$ from Eq. (3.9).

Furthermore, as shown in Section 4.2, *closed feedback loop* $dI/dV(x)|_V$ data can directly be interpreted in terms of the LDOS of the sample under the conditions: $0.3 \text{ V} < V < 3.5 \text{ V}$, $x > \pi/k_x$, low temperatures. For these reasons we can write (Eq. (3.9))

$$dI/dV(x)|_V = A - B e^{-\frac{|x|}{\ell}} J_0(2k_x x), \quad (3.15)$$

where A and B are constants, ℓ is an effective mean free path, and k_x is related to V by $E'(k_x, 0) = eV$. The $e^{-\frac{|x|}{\ell}}$ term accounts for inelastic processes and the bias modulation ΔV , both of which damp the dI/dV oscillations with increasing distance

from the step. This term is extensively discussed in Section 4.2 [92]. We only emphasize here, that neither the bias modulation nor inelastic processes alter the oscillation period (i.e. k_x) [92]!

Figure 3.12 depicts fits of our dI/dV data with Eq (3.15). By fitting similar Ag and Cu dI/dV data taken at different energies we obtain $k_x(E)$, and thus the dispersion relation along $\bar{\Gamma}-\bar{M}$ shown in Fig. 3.14. The data points in Fig. 3.14 are averaged over several independent data sets measured at different $\langle 1\bar{1}0 \rangle$ -oriented steps, with different tips and different tunneling impedances. The absence of an influence of the latter on our measurement has been checked by measuring $k_{||}$ at fixed bias and a stabilizing current that has been varied by a factor of 100 around the usual values. Thus, the presence of the tip, i.e. the tip induced electric field or tip-surface interactions, does not influence the measured wave vectors. The largest contribution to the error in $k_{||}$ (not shown in Fig. 3.14) comes from the uncertainty in the STM piezo calibration of about 5 %. We have not been able to measure the dispersion relation beyond energies of about 3.5 eV since the decrease in the step reflection amplitude with increasing energy leads to a decrease in the LDOS oscillation amplitudes. Anyway, tunneling experiments are limited to energies smaller than the work function of typically 3.5 eV-5 eV since the tunneling barrier breaks down when eV approaches the value of the work function.

It becomes clear from Fig. 3.14 that the measured dispersion relations for the Cu as well as for the Ag surface state (resonance) deviate from the free-electron-like behavior. The dashed lines depict the parabola corresponding to low-temperature values of the band edge energies $E_{\bar{\Gamma}}$ and effective masses m^* determined previously with ARPES and STM measurements in the SBZ center: $E_{\bar{\Gamma}} = -420$ meV, $m^* = 0.40 m_e$ and $E_{\bar{\Gamma}} = -65$ meV, $m^* = 0.40 m_e$ for Cu and Ag, respectively (Table 3.1). With increasing wave vector the dispersion bends away from the free-electron-like parabola and flattens when getting closer to the \bar{M} -point, as expected. In the case of silver we can detect an inflexion point.

There exists some theoretical work on the band structure of noble-metal (111) surfaces [47, 105, 106]. But we are not aware of any calculation giving results over the extended $k_{||}$ -range studied here. Therefore, we discuss our data with simple general models. First of all the nearly free electron approximation, i.e. electrons in a weak periodic 2D potential, can not explain effective masses smaller than m_e , and thus has to be discarded. Since our m^* -values are considerably smaller than m_e we expect the crystal potential to be rather strong. Therefore, we compare the measurements with a simple tight-binding model [107, 108]. Following Eq. (2.21) of Ref. [107] the dispersion of the surface state, present in this model under certain conditions (see Ref. [107]), is

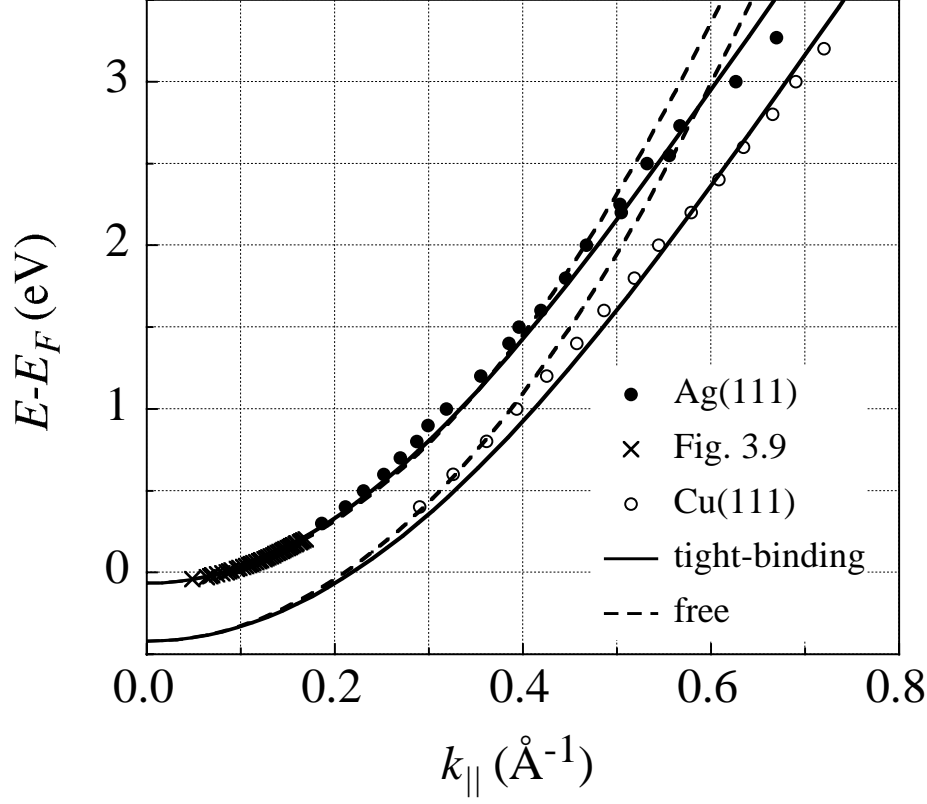


Figure 3.14: Dispersion relation of the $\bar{\Gamma}$ s - p derived surface states on Cu(111) and Ag(111) along the $\bar{\Gamma}$ \bar{M} line ($T = 4.9$ K).

given by

$$E(k_x, k_y) = W(k_x, k_y) + U_0 + \frac{T^2(k_x, k_y)}{U_0}, \quad (3.16)$$

where U_0 is the one-center surface perturbation matrix element and $W(k_x, k_y)$, $T(k_x, k_y)$ are matrix elements as defined following Eq. (2.14) in Ref. [107]. These matrix elements are readily calculated for a (111) surface of an fcc crystal leading to the following surface-state dispersion:

$$E(k_x, k_y) = E_{\bar{\Gamma}} + \gamma \left(3 - \cos(k_y a) - 2 \cos\left(\frac{k_y a}{2}\right) \cos\left(\frac{\sqrt{3} k_x a}{2}\right) \right), \quad (3.17)$$

where a is the next nearest neighbor distance (2.56 \AA and 2.89 \AA for Cu and Ag, respectively), $E_{\bar{\Gamma}} = E_0 + U_0 + 3E_1(2 + 3E_1/U_0)$ and $\gamma = -2E_1(1 + E_1/U_0)$. Here E_0 and E_1 are the one-center and the nearest-neighbor matrix elements, respectively, as defined in Ref. [107]. In Fig. 3.13 we have plotted the dispersion relation from Eq. (3.17) in the first SBZ. (The white and the black level are separated by $\frac{9}{2}\gamma$.) It is evident that this dispersion can be considered isotropic for the wave vectors accessible to our measurements. The surface-state band width of our model is $\frac{9}{2}\gamma$ and the corresponding

surface DOS shows a logarithmic van Hove singularity at $E = E_{\bar{\Gamma}} + 4\gamma$, where the dispersion goes through the saddle points at \bar{M} (Fig. 3.15).

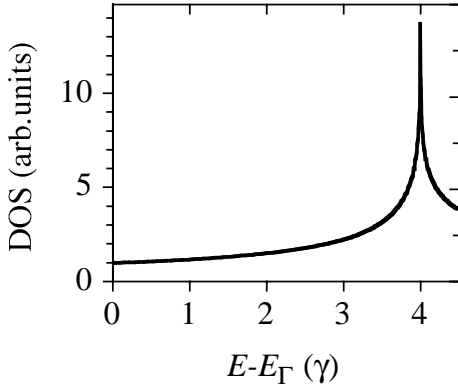


Figure 3.15: Density of states for the surface state in the tight-binding model with dispersion given by Eq. (3.17).

$\bar{\Gamma}$ -point yields effective masses of $m^* = 0.42 m_e$ and $m^* = 0.37 m_e$ for Cu and Ag, respectively, in agreement with previous results (Table 3.1). Although the tight-binding model explains the essential trends in our data, there are deficiencies of the model, e.g. the inflexion in the Ag data is not reproduced. Therefore it would be interesting to compare our data with *ab initio* calculations of noble-metal *s-p* surface-state band structures.

Concluding this Section, we have for the first time experimentally and quantitatively characterized noble-metal surface-state band structures beyond the free-electron-like approximation.

Since the band edge energy $E_{\bar{\Gamma}}$ is precisely known (-420 meV and -65 meV for Cu and Ag, respectively) we are left with a single unknown parameter, namely γ . The full lines in Fig. 3.14 depict the least-square fits with Eq. (3.17). We find γ -values of 1.6 eV and 1.8 eV for Ag and Cu, respectively. The surface-state band widths can thus be estimated to 7 eV and 8 eV implying that possible van Hove singularities would lie outside the STM-accessible range. The tight-binding fits are satisfactory, and obviously reproduce the flattening of the dispersion. In addition, the Taylor expansion of these fits around the

Chapter 4

Electron Lifetimes

In this Chapter we report on a novel approach to measure the electron phase-relaxation length and femtosecond lifetimes at surfaces. We have studied the spatial decay of quantum interference patterns in the LDOS of s - p derived surface-state electrons on Cu(111) and Ag(111) with the STM. The characteristic decay length of the LDOS oscillations is influenced by the finite lifetime, and thus reveals information about inelastic scattering in the 2D electron gas. After an introduction in Section 4.1, energy dependent lifetime measurements of hot electrons are presented in Section 4.2 and interpreted in terms of electron-electron scattering. The temperature dependent lifetime measurements of low-energy quasiparticles discussed in Section 4.3 give insight into the interaction of these 2D electrons with phonons.

4.1 Introduction

The phase-relaxation length L_ϕ , i.e. the distance a quasiparticle can propagate without losing its phase memory, is a key quantity in solid state physics. Quantum mechanical interference phenomena can only prevail if L_ϕ is larger than any other relevant length scale [80]. Examples include Aharonov–Bohm oscillations, quantum Hall effect, Friedel oscillations and localization. With respect to surface physics L_ϕ , or equivalently the lifetime τ_ϕ of the quasiparticle ¹, is of particular interest, since it governs the dynamics of charge transfer and electronic excitations in surface chemistry [21]. Also, a sufficiently long L_ϕ is a prerequisite for the standing waves discussed in Chapter 3 to appear.

Collisions of an electron with static scatterers, i.e. scatterers with no internal degree of freedom, do not influence the phase coherence [80]. On the other hand, L_ϕ is reduced by inelastic scattering processes like electron-phonon (e - ph) or electron-electron (e - e)

¹If $L_M > L_\phi$, then $\tau_\phi = L_\phi/v$ where v is the group velocity of the electron [80].

interaction. To familiarize with the order of magnitude of typical lifetimes in metals, we discuss the e - e and e - ph scattering rates of a quasiparticle of energy $E - E_F$ with respect to the Fermi sea in simple models. Fermi liquid theory (FLT) for a 3D free electron gas predicts the following energy dependence of the e - e lifetime at $T = 0$ K ($E - E_F \ll E_0$) [109, 110]:

$$\tau_{e-e}(E) = \tau_0 \left(\frac{E_0}{E - E_F} \right)^2, \quad \tau_0 = \frac{64}{\pi^2 \sqrt{3} \pi} \sqrt{\frac{m_e}{n e^2}}, \quad (4.1)$$

where n is the density of the electron gas and E_0 the width of the band. e - e processes at low excitation energies are dominated by electron-hole pair creation, and the inverse quadratic excess energy dependence basically relies on a phase space argument, i.e. the larger the initial excess energy $E - E_F$ the more final states with an additional electron-hole pair are accessible [98]. In FLT the temperature dependence of τ_{e-e} is given by

$$\tau_{e-e}(T) = \tau_0 \left(\frac{E_0}{\pi k_B T} \right)^2. \quad (4.2)$$

The e - ph scattering rate can be estimated within a Debye model [70, 111]:

$$\begin{aligned} \frac{\hbar}{\tau_{e-ph}(E, T)} = & 2\pi\hbar \int_0^{\omega_D} d\omega' \lambda \cdot \left(\frac{\omega'}{\omega_D} \right)^2 \left(1 - f(E - \hbar\omega', T) + \right. \\ & \left. 2 b(\hbar\omega', T) + f(E + \hbar\omega', T) \right). \end{aligned} \quad (4.3)$$

Here ω_D is the Debye frequency, λ the electron-phonon mass enhancement parameter and $b(E, T)$ the Bose-Einstein distribution function². One readily shows that

$$\frac{\hbar}{\tau_{e-ph}(E_F, T)} = 2\pi\lambda k_B T \quad (4.4)$$

when $k_B T \gg \hbar\omega_D$. For any E and T the integral in Eq. (4.3) has to be calculated numerically. Figure 4.1 shows the calculated lifetimes for bulk Cu. The e - ph scattering rate is independent of energy as long as $E - E_F > \hbar\omega_D$ (dashed line in Fig. 4.1(a)). It is clear from Fig. 4.1 that for Cu bulk electrons e - e scattering dominates e - ph scattering at low temperatures and excess energies larger than ≈ 0.5 eV, whereas at energies very close to the Fermi level inelastic scattering is dominated by e - ph processes at all temperatures of interest.

Elegant experiments have been performed to determine L_ϕ of ballistic electrons in low-density high-mobility two-dimensional electron gases present at the interfaces of semiconductor heterostructures. In particular, the excess energy and temperature dependence of L_ϕ in GaAs/AlGaAs heterostructures has been measured by Yacoby *et*

²Remember that energies are always with respect to E_F .

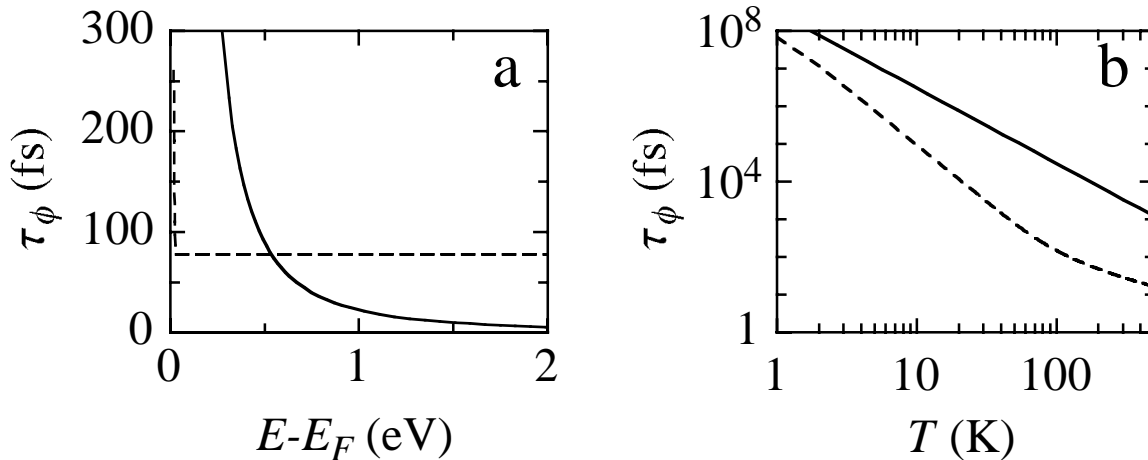


Figure 4.1: e - e (full line) and e - ph (dashed line) lifetimes as calculated using 3D Fermi liquid theory (Eqs. (4.1) and (4.2)) and a Debye model (Eq. (4.3)), respectively, for Cu parameters: $\tau_0 = 0.46$ fs, $E_0 = 7$ eV, $\omega_D = 27$ meV, $\lambda = 0.15$ [98, 111]. **(a)** Lifetime at $T = 0$ K as a function of excess energy of the quasiparticle with respect to the Fermi sea. **(b)** Temperature dependence of the lifetimes for particles at the Fermi level (double logarithmic plot).

al. [112] and Murphy *et al.* [113], respectively, where the main contribution to L_ϕ could be attributed to electron-electron (e - e) scattering, in striking agreement with Fermi liquid theory for a 2DEG [114, 115]. Another access to electron and hole lifetimes (and hence to L_ϕ) has become possible through electron spectroscopic methods on single-crystal metal surfaces [64, 116]. In particular the photohole lifetimes of noble-metal surface states have been investigated with high-resolution angle-resolved photoemission, revealing Lorentzian line shapes [61, 63, 64, 70, 116, 117], whose full peak widths at half maximum (FWHM) Γ give access to the lifetime via $\Gamma = \hbar/\tau_\phi$. Although the phonon contribution to copper surface-state lifetimes has been successfully determined with ARPES [63, 70], the assignment of ARPES-linewidths to true quasiparticle lifetimes is complicated by non-lifetime effects [66, 104], e.g. due to impurities, and hence the absolute values of ARPES-lifetimes have to be considered as lower limits [70]. Furthermore, recent femtosecond time-resolved two-photon photoemission (2PPE) experiments opened up a new path to measure excess energy dependent lifetimes of hot bulk quasiparticles for metals and semimetals [118–126]. But due to cascade and depopulation effects the interpretation of 2PPE spectra is a difficult task, and up to now it does not seem to be clarified why different groups report lifetimes which vary by up to a factor of 4 for the very same system [120, 124].

In the field of STM many authors have qualitatively discussed a possible contribution of quasiparticle and electron-phonon interactions to the damping of interference patterns

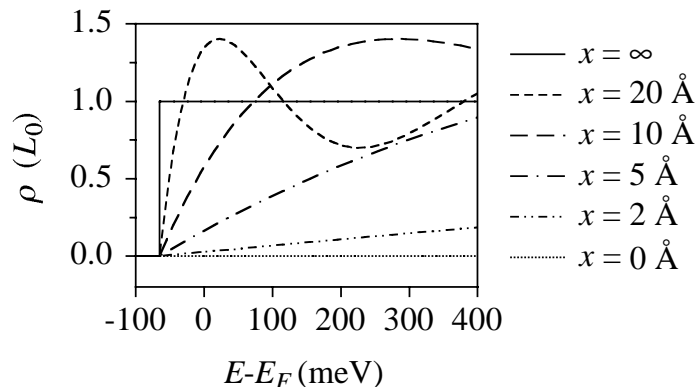


Figure 4.2: DOS at different distances from a straight step edge modeled as infinite square barrier (Ag(111) parameters: $E_{\overline{\Gamma}} = -65$ meV, $m^* = 0.4 m_e$).

and to spectroscopic linewidth [33,76,78,82,83,88,127]. Especially, Crampin and Bryant emphasized the importance of quasiparticle interactions to interpret the spectroscopic linewidth of confined electrons in quantum corrals [128]. However, it was only recently that Li *et al.* used STM to determine the lifetime of excited holes at the band edge of the Ag(111) surface state quantitatively [90,129]. Similar to ARPES Li *et al.* have investigated the linewidth of the surface-state onset in tunneling spectra (see Fig. 3.4). The advantage over ARPES is the capability to choose a surface spot bare of impurities, and hence non-lifetime effects are reduced. But with the method used by Li *et al.*, L_ϕ of excited holes can be studied at only one energy ($E_{\overline{\Gamma}}$), which constitutes a major limitation. In Ref. [129] Li *et al.* state that “the width of the surface-state onset provides a local measure of surface-state lifetimes”. However, this is only correct if static scatterers are absent. Interference effects due to the presence of such scatterers can lead to a substantial broadening of the surface-state onset, which is a pure non-lifetime effect. This is illustrated in Fig. 4.2, where the LDOS in the presence of a straight step edge, $\rho(E) = L_0 (1 - J_0(2k_E x))$ (Eq. (3.9) with step reflection amplitude $r = 1$ for simplicity), is plotted for different distances x from the step. Far away from the scatterer the onset is indeed infinitely sharp due to the absence of inelastic processes. But close to the step edge the onset is substantially broadened because of interference effects. Note that in our case of $r = 1$ there is no contribution from the surface state at $x = 0$, due to the fact that all surface-state wave functions have to vanish at the (hard wall) step edge location. The reduction of the LDOS at and close to scattering centers [76,85,129] is thus imposed by the potential of the scatterer and can be understood in the framework of the simplest model.

In this Chapter we present a new approach to measure lifetimes of surface-state and

surface-resonance electrons *locally* with an STM. (As in Section 3.3, the term surface states shall include surface resonances for the following.) To do so we have studied the decay of LDOS interference patterns of surface-state electrons scattering off descending straight step edges, which is influenced by the loss of coherence and hence by L_ϕ . The major interest to do lifetime measurements with an STM comes from the fact that STM offers a complete control over impurities, i.e. surface spots bare of defects can be chosen for the lifetime measurements, and thus *non-lifetime effects*, embarrassing all integral techniques like ARPES and KRIPES, may be *completely avoided*.

So far we included only possible loss of coherence during scattering at the step edge itself (via $r(k_E)$) in our model for the LDOS at step edges (Eq. (3.8)), but completely disregarded inelastic processes on the terrace. The latter processes include e - e and e - ph scattering. Not including them in the model was justified, since the measurements discussed in Section 3.2 have been performed at low temperature and low energies ($E - E_F < 0.5$ eV), where L_{e-e} and L_{e-ph} are much larger than the intrinsic LDOS decay length (see below for estimates of the order of L_ϕ in this regime). Figure 4.3 illustrates electron scattering processes at step edges without and with inelastic processes on the terrace. In the absence of inelastic processes on the terrace an electron wave packet of wave vector $(-k_x, k_y)$ will be reflected partially by the step edge into a state characterized by (k_x, k_y) and will interfere coherently with the incoming wave packet, leading to the well known interference patterns. At the step edge itself we allowed for inelastic processes which further reduce the step reflection amplitude $r(k_x)$. Since these processes are located at the step edge, an electron starting at distance x from the step will come back to this distance with a probability that is independent of x . Thus, inelastic processes *at steps* lead to an overall reduction of the LDOS oscillation amplitude, but not to damping (Eq. (3.9)). If we take inelastic processes on the terrace into account, then the electron may be scattered out of its state into another quantum state (q_x, q_y) somewhere on its way from distance x to the step or from the step to distance x again. Since this is an inelastic process, the energy of state (q_x, q_y) is different from the energy of (k_x, k_y) , e.g. the process involves absorption or emission of a phonon. If we assume that the system is homogeneous, then an inelastic process occurs with a constant probability $d\ell/L_\phi$ per length unit $d\ell$, i.e. the probability that the electron is in the same quantum state after a distance ℓ is $e^{-\ell/L_\phi}$. The distance an electron wave packet in state $(-k_x, k_y)$ has to travel starting from distance x , going to the step and then back to distance x , where it can interfere with the incoming $(-k_x, k_y)$, is given by $2xk_E/k_x$, where $k_E^2 = k_x^2 + k_y^2$. The probability that the electron in state $(-k_x, k_y)$ gets back to distance x in state (k_x, k_y) is reduced by a factor $\exp(-2\frac{k_E x}{k_x L_\phi})$, and therefore, under inclusion of inelastic processes,

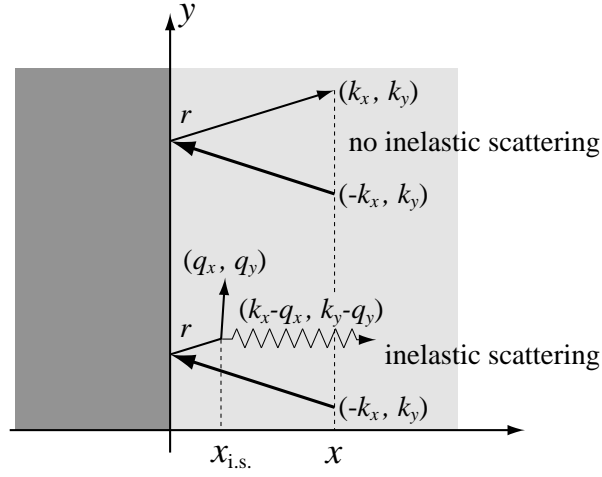


Figure 4.3: Schematics of electron reflection at a straight step edge, without (top) and with inelastic scattering (bottom) at the location $x_{\text{i.s.}}$. Possible inelastic processes include e - ph (as sketched) and e - e scattering.

the LDOS of the 2D electron gas at a step edge in Eq. (3.8) reads:

$$\rho_{\text{step}}(E, x) = \frac{2}{\pi} L_0 \int_0^{k_E} dk_x \frac{1 - r(k_x) e^{-2 \frac{k_E x}{k_x L_\phi}} \cos(2k_x x)}{\sqrt{k_E^2 - k_x^2}}. \quad (4.5)$$

Again, numerical integration of Eq. (4.5) shows that for $x > \pi/k_E$ and a reasonable k_x dependence of $r(k_x)$ [45, 91], $\rho_{\text{step}}(E, x)$ can very well be approximated by

$$\rho_{\text{step}}(E, x) \approx L_0 \left(1 - r(k_E) e^{-2 \frac{x}{L_\phi}} J_0(2k_E x) \right). \quad (4.6)$$

As seen in Eq. (4.6) inelastic processes on the terrace lead to an additional damping of the LDOS interference patterns. By quantitatively studying the decay of these interference patterns at straight step edges with STM, one can investigate inelastic processes like e - e and e - ph scattering. We emphasize that L_ϕ as defined here (and elsewhere [130]) does not account for coherence loss at scattering centers themselves. Hence, our measured lifetime directly reflects the lifetime of surface-state electrons on an ideal surface free of any defects.

Theoretical lifetimes usually refer to one single quasiparticle added to the Fermi sphere (ground state) [109]. Photoelectron spectroscopic methods are far from this idealized situation since many quasiparticles are usually excited with the photon (electron) pulse, leading to a highly non-equilibrium quasiparticle distribution. STM, on the contrary, comes close to the theoretical scenario. To illustrate this statement let us use the picture put forward by Heller *et al.* [131]: at positive bias voltages (similar arguments can be made for negative bias) electrons tunnel from the tip to the sample surface. On

the sample this electron wave travels away from the tip. If it encounters scattering centers like steps or impurities, it may be scattered and return to the tip, where it will interfere constructively or destructively with the amplitude leaving the tip. The electron can be injected at a well defined energy eV above the Fermi surface by choosing the appropriate bias voltage V . In this picture it gets clear, that with the STM tip one injects electrons, whose properties can be probed by the very same tip. Since at typical tunneling currents of 1 nA an electron is injected about every 0.16 ns and since typical lifetimes of these surface-state electrons are in the fs range (see below), only one *single* quasiparticle is probed at a time. Altogether, STM offers in principle the experimental realization of the simple picture used in theory, where one single quasiparticle is added to the Fermi sphere.

4.2 Electron-Electron Interaction

To learn about e - e interaction of s - p derived surface-state electrons on noble metals we have studied the decay of quantum interference patterns at step edges as a function of the quasiparticle excess energy (Fig. 4.1). With a simple model we have been able to extract $L_\phi(E)$ from dI/dV scans acquired under closed feedback loop conditions at step edges for the Shockley type surface states on Ag(111) and Cu(111). We present the first experimental energy dependent lifetime study for surface-state electrons.

Figure 4.4 shows a constant-current image of a Cu(111) step edge at $V = 1.4$ V in (a) and the *closed feedback* dI/dV image taken simultaneously in (b) (see page 18). Again, Friedel-type oscillations in the LDOS are responsible for the clearly visible spatial oscillations in Figure 4.4(b). For our experiment we have chosen straight step edges with a defect free area larger than $250 \text{ \AA} \times 250 \text{ \AA}$ on the adjacent upper terrace (Fig. 4.4). By doing so we are sure that the local elastic mean free path L_m is considerably larger than the measured L_ϕ [80], and thus the LDOS oscillations at the step are not influenced by other static scattering centers. In order to evaluate the decay of the standing waves at straight step edges as shown in Fig. 4.4 the dI/dV images have been slightly rotated to align the step edge vertically, and then we have averaged the dI/dV data over several line scans. Typical averaged dI/dV data are presented in Fig. 4.5(a). To interpret this data we start with the general expression for the tunneling current I in Eq. (2.3). The tip LDOS ρ_t is assumed to be constant which is justified since we are only interested in lateral variations of dI/dV . We use the transmission factor [28]

$$\mathcal{T}(E, V, s) = e^{-s\sqrt{2m_e/\hbar^2} \left(\sqrt{W_t - E + eV} + \sqrt{-E(1 - m^*/m_e) - m^*/m_e E_T + W_s} \right)}, \quad (4.7)$$

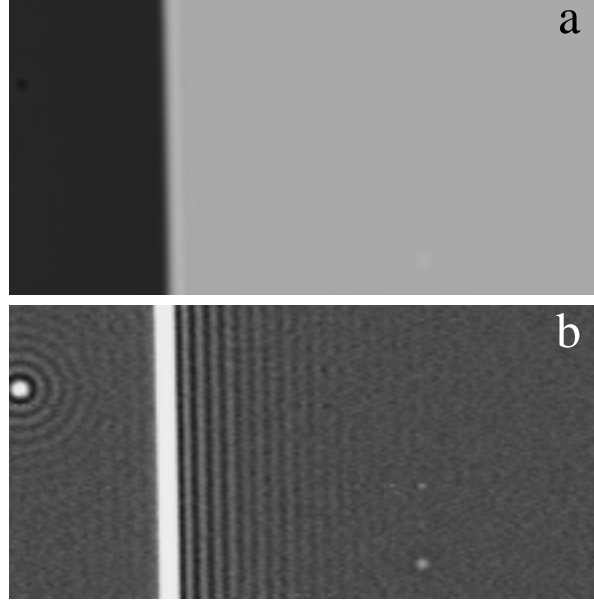


Figure 4.4: (a) Constant-current image of a Cu(111) step edge: $280 \text{ \AA} \times 138 \text{ \AA}$, $V = 1.4 \text{ V}$, $I = 7 \text{ nA}$. (b) dI/dV image taken simultaneously with (a). Standing wave patterns at static scatterers as steps and impurities are clearly visible ($T = 4.9 \text{ K}$, c.f., $\Delta V = 135 \text{ mV}$, $\nu = 5.72 \text{ kHz}$).

which respects the $p_{||}$ dependence of the vacuum barrier penetration of surface-state wave functions (see Section 2.1)³. The work function of the sample, W_s , can be considered as a constant for our purposes since we have found its reduction at steps due to the Smoluchowski effect to be localized to $\pm 3 \text{ \AA}$ around the step edge [132]. For $\rho_s(E, x)$ in Eq. (2.3) we use $\rho_b + \rho_{\text{step}}(E, x)$ from Eq. (4.6), appropriate for a straight step edge in presence of inelastic processes. Since we are only interested in spatial variations of dI/dV the bulk contribution to the surface DOS, ρ_b , is assumed to be constant.

In the following we prove that \mathcal{T} can be assumed constant for our purposes due to the facts, that firstly, at relatively large bias voltages the constant-current tip sample distance $s(x)|_{I,V}$ is not influenced by the LDOS oscillations, and secondly, the energy dependence of $\mathcal{T}(E, V, s)$ can be neglected since the energies entering in dI/dV all lie in the window of the lock-in bias modulation $e\Delta V$ which is much smaller than \overline{W} . With Eqs. (2.3), (4.6) and (4.7) we have calculated dI/dV numerically, using the constant-current tip sample distance $5 \text{ \AA} + s(x)|_{I,V}$ of Eq. (3.13), and typical 5 K parameters for the Cu(111) and Ag(111) surface states (Table 3.1). By doing so we simulate the dI/dV imaging mode under *closed feedback* loop conditions. The result of such a calculation is depicted in Fig. 4.5(b) (dots) and compared with the result obtained by setting the

³Since these states are 2D, $p_{||}$ is completely characterized by E and it enters implicitly in \mathcal{T} via E .

transmission factor \mathcal{T} constant (full line). From plots as shown in Fig. 4.5(b) it is clear that the energy and gap width dependence of the transmission factor of Eq. (4.7) is neither responsible for a faster decay of the oscillations in dI/dV at steps nor does it change the oscillation period and phase (at least not in the bias regime of 0.3 V–3.5 V). For the sake of a faster fit procedure we thus can safely set the transmission factor $\mathcal{T} = \text{const}$, which is an excellent approximation for $x > \pi/k_E$ and 0.3 V < V < 3.5 V. Under these circumstances the integral in Eq. (2.3) with $\rho_b + \rho_{\text{step}}(E, x)$ from Eq. (4.6) can be analytically solved, and the laterally varying part of the current, I^\sim , is given by (see Eq. (3.12)):

$$I^\sim(V, T, x) \propto -\frac{1}{x} e^{-2\frac{x}{L_\phi}} \left(\frac{\xi_{k_{eV}}}{\sinh \xi_{k_{eV}}} k_{eV} J_1(2k_{eV}x) - \frac{\xi_{k_F}}{\sinh \xi_{k_F}} k_F J_1(2k_Fx) \right). \quad (4.8)$$

Please note that for lower bias values the assumption of a constant transmission factor is not correct and the closed feedback $dI/dV(x)|_V$ can not directly be interpreted in terms of the LDOS [46]. An open feedback loop approach has to be chosen to measure ρ_s for low biases as described in Section 3.2 [28, 77, 78]. Since we have measured our dI/dV data with a non-negligible lock-in bias modulation ΔV (peak-to-peak) we do not fit our data with the analytical derivative of Eq. (4.8) but with its lock-in derivative given by

$$dI/dV(V, \Delta V) \propto \int_0^{2\pi} \sin t \cdot I(V + \frac{\Delta V}{2} \sin t) dt, \quad (4.9)$$

where Eq. (4.8) has to be inserted for the current I . Note that in the limit of $\Delta V \rightarrow 0$ the lock-in output of Eq. (4.9) coincides with the real derivative. By using Eqs. (4.8) and (4.9) to fit our data we take *fully account of modulation and temperature effects*. The bias modulation actually leads to an apparent decay in dI/dV beyond the one present in the LDOS pattern. The decay length $L_{\Delta V}$ of this additional dI/dV decay is of the order of

$$L_{\Delta V} \sim \frac{\hbar^2 k_{eV}}{m^* e \Delta V}. \quad (4.10)$$

(The energy spread of $e\Delta V$ leads to a corresponding wave vector spread Δk which then leads to a decay on a length scale of $1/\Delta k$). $L_{\Delta V}$ can be considerable in our experiments and it is therefore of great importance that we account for this effect with Eq. (4.9). If we just evaluated the apparent decay in dI/dV , $L_{dI/dV}$, we would underestimate the real phase-relaxation length, since $L_{dI/dV}^{-1} = L_\phi^{-1} + L_{\Delta V}^{-1}$.

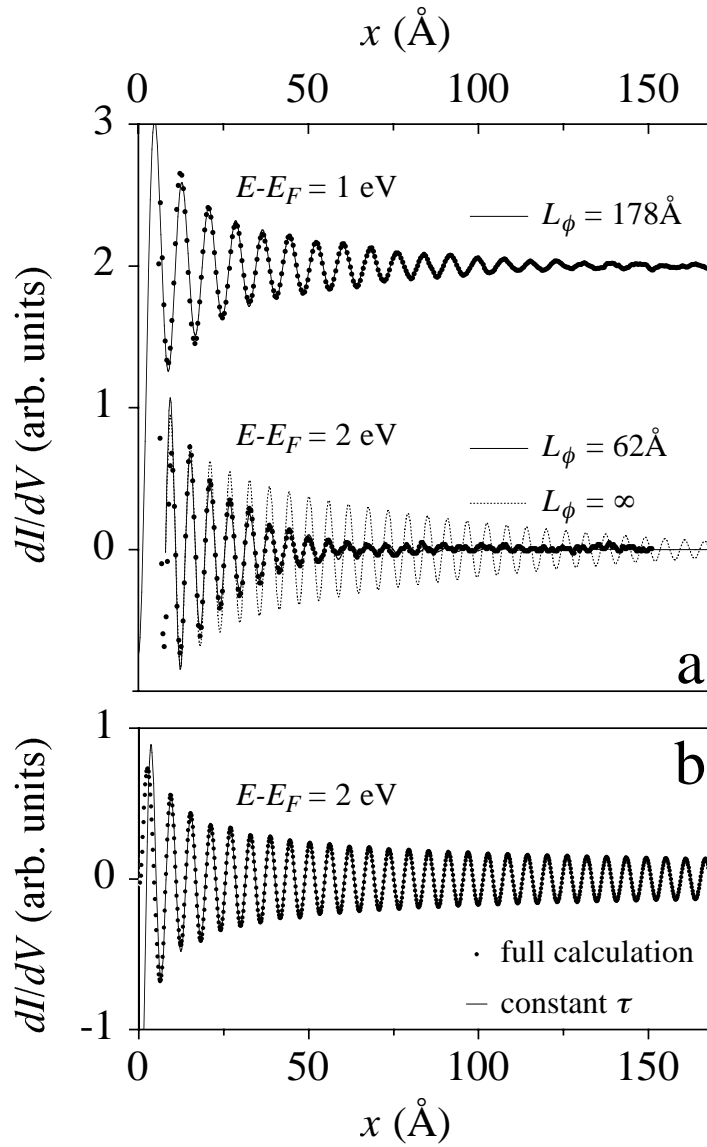


Figure 4.5: (a) Typical dI/dV data perpendicular to a descending Cu(111) step obtained by averaging over several line scans of a dI/dV image as shown in Fig. 4.4(b). The data at 1 eV and 2 eV were taken with a stabilizing current of 5 nA and 10 nA and a ΔV of 119 mV and 156 mV, respectively. The solid lines depict the fits with Eqs. (4.8) and (4.9). The significance of the deduced L_ϕ is demonstrated by the dashed line: neglecting inelastic processes by setting $L_\phi = \infty$ leads to a much slower decay rate than observed ($T = 4.9$ K, c.f., $\nu = 5.72$ kHz). (b) Comparison between the full calculation of dI/dV with Eqs. (2.3), (4.6) and (4.7) and the result obtained by setting \mathcal{T} constant ($T \rightarrow 0$, $L_\phi \rightarrow \infty$, typical Cu(111) parameters: $W_s = W_t = 4.5$ eV, $r = 0.5$ [45]).

Using Eqs. (4.8) and (4.9) to fit our dI/dV line scans, we are left with four fit parameters: L_ϕ , k_{eV} , the step edge location and an overall proportionality factor. Remember that the latter fully accounts for loss of coherence during the scattering process at the step edge itself ($r(k_x)$ in Eq. (4.5)) whereas the decay L_ϕ is only influenced by

inelastic processes on the terrace, e.g. e - e or e - ph interaction. Fits to measured dI/dV data for Cu(111) are depicted in Fig. 4.5(a) for two different bias values (i.e. injection energies). The fit range has been limited to $x > 3\pi/2k$ to ensure the validity of our approximations. The agreement between fits and data is excellent and the relevance of L_ϕ is demonstrated by plotting the calculated dI/dV oscillations for $L_\phi = \infty$. By fitting dI/dV data taken at different bias voltages V (i.e. energies eV) for Ag(111) and Cu(111) we obtain the dispersion relation $k_{E=eV}$ (Section 3.3), and the energy dependent phase-relaxation length $L_\phi(E)$ for Cu(111) and Ag(111), respectively.

To compare our results with theory, APS, and 2PPE measurements we have converted the measured L_ϕ into lifetimes τ_ϕ via $\tau_\phi = L_\phi/v$, where v is the group velocity of the quasiparticles at the particular energy, $v = \hbar k_{eV}/m^*$. This conversion is correct since locally $L_\phi \ll L_m$ in our case (see Section 3.2) [80]. The measured $\tau_\phi(E)$ values are shown in Fig. 4.6 for Cu(111) and Ag(111). The points in Fig. 4.6 have been determined by averaging over data sets obtained with different tips, at different step edges and different fit ranges. The fit range and bias modulation dependence of our τ_ϕ data is minor, which confirms the validity of our model. The error bars are due to a slight tip dependence of our measurement and a 5 % uncertainty in the STM piezo calibration. Actually, the absolute values of the lifetimes have been found to depend slightly on the tip, whereas the energy dependence of τ_ϕ is unaffected. This might be explained by the fact that tips are not radially symmetric and thus may collect surface-state electrons having different in-plane incidence angles $\alpha = \arccos(k_x/k_{eV})$ with different probabilities. Thus, the integrand in Eq. (4.5) would have to be multiplied with a probability function $f(k_x/k_{eV})$. It turns out that a monotonically increasing (decreasing) $f(k_x/k_{eV})$ leads to a slower (faster) decay of ρ_{step} . We point out that the absence of an influence of the tunneling impedance on our measurement has been carefully checked by measuring L_ϕ at fixed bias and a stabilizing current that has been varied by two orders of magnitude around the usual values. Thus, we believe that the presence of the tip, i.e. the tip induced electric field or tip-surface interactions, does not influence the measured decay lengths.

Note that with our technique we avoid depopulation and cascade effects present in 2PPE and we probe only one excited electron at a time. Since electron-phonon lifetimes (typically 70 fs at 5 K) are essentially independent of the quasiparticle energy for the energies of interest and exceed our measured lifetimes considerably (Fig. 4.1), we attribute the inelastic quasiparticle scattering rate τ_ϕ^{-1} to e - e interaction, e.g. electron-hole pair creation and plasmon excitation. Although surface-state electrons are bound to two dimensions they coexist with the underlying bulk electrons, and this opens up

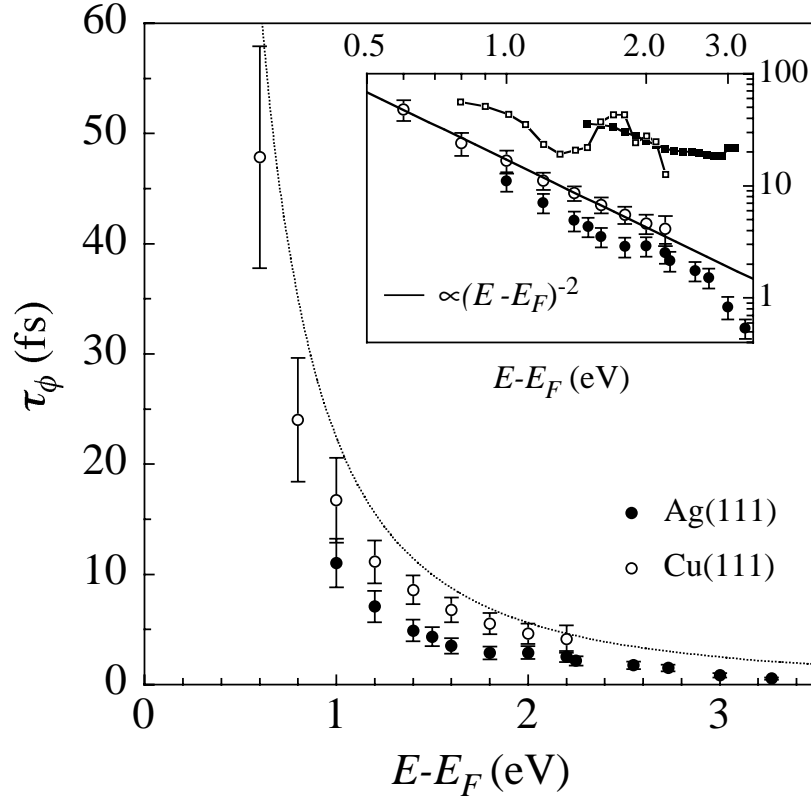


Figure 4.6: Lifetimes of s - p surface-state electrons as a function of excess energy determined as described in the text ($T = 4.9$ K). The dotted line depicts the lifetimes predicted by 3D FLT for Cu (Eq. (4.1)): $\tau_{\text{FLT}} = 22.4 \text{ fs eV}^2 (E - E_F)^{-2}$. The inset shows the same data on a double logarithmic scale. The best inverse quadratic fit to the Cu data (full line) yields $\tau = 17.1 \text{ fs eV}^2 (E - E_F)^{-2}$. The filled and open squares in the inset depict 2PPE data of Cu(111) bulk electron lifetimes measured by Ogawa *et al.* [124] and Knoesel *et al.* [126], respectively.

fully 3D decay channels, e.g. the e - e interaction is not restricted to the 2D electron gas itself but may have contributions from the bulk electrons. We outlined in Chapter 3, and we will come back to this point in Chapter 6, that the surface-state electrons are efficiently screened by underlying bulk electrons, and one therefore expects that the bulk electron contribution to the e - e interaction of hot s - p surface-state quasiparticles with the Fermi sphere is considerable. As can be seen in Fig. 4.6 our results for the surface-state lifetimes indeed lie close to the $\tau_0 (E - E_F)^{-2}$ law predicted by 3D FLT for electron-hole pair creation (Eq. (4.1))⁴: fits to our data yield $\tau_0^{\text{Ag}} = 10.4 \text{ fs eV}^2$ and $\tau_0^{\text{Cu}} = 17.1 \text{ fs eV}^2$, as compared to 16.5 fs eV^2 and 22.4 fs eV^2 expected from FLT with Ag and Cu *bulk* parameters, respectively (see Fig. 4.6). This suggests that

⁴The energies of interest are well below the threshold for plasmon creation in Ag and Cu [103, 133].

our measured *phase-relaxation times of surface-state quasiparticles are mainly governed by inelastic e - e scattering of the hot quasiparticle with 3D bulk electrons in the Fermi sphere*. The picture that emerges is one in which every s - p noble-metal surface-state electron is surrounded towards the bulk side by a cloud of *bulk* holes which screen the Coulomb field of the 2D electron and which govern the e - e interaction of the surface-state electron. However, our surface-state lifetimes in Fig. 4.6 are slightly (but significantly) smaller than the lifetimes predicted in FLT for corresponding bulk electrons. Should we compare our data with more realistic models including the real band structure and exchange [134], which, for noble metals, consistently predict larger lifetimes than FLT⁵, the deviation of our data from theory would even be larger. In addition, recent 2PPE experiments confirm this trend towards larger bulk electron lifetimes for Cu(111) (filled and open squares in the inset of Fig. 4.6). Therefore, the question arises why the surface-state electron lifetimes resulting from our experiment are reduced with respect to bulk electron lifetimes. Calculations performed by Echenique *et al.* show that for the energies of interest the in-plane e - e interaction, i.e. e - e interaction between 2D surface-state electrons, is at the origin of this effect [135]. Further theoretical modeling will be helpful to interpret our results in detail. Especially, the deviations of the τ_ϕ data of Ag(111) above 2 eV from the quadratic behavior of FLT should be related to the real band structure including d bands.

To conclude this Section, we would like to emphasize the possibility to study bulk quasiparticle lifetimes with STM much as described here, since bulk electrons create as well standing wave patterns at structural defects on and below surfaces [89,136].

4.3 Electron-Phonon Interaction

The general aim of this Section is to fully understand and model the thermal damping of interference patterns in 2D free electron gases. We present temperature dependent dI/dV and low-bias constant-current measurements for s - p derived surface-state electrons on noble metals in the temperature range 3.5 K - 178 K. Although temperature dependent damping has been discussed earlier [78,83], we consider this Section valuable since it is more *quantitative* than the earlier studies. In particular, we have performed these quantitative temperature dependent decay studies to learn about electron-phonon processes in noble-metal surface states, which dominate the electron decay rate at low

⁵Including exchange terms leads to a larger mean distance between electrons and thus an enhancement of e - e lifetimes. Including d bands (i.e. the real band structure) introduces additional screening which increases the lifetimes as well.

excitation energy (Fig. 4.1).

Our investigation of the temperature induced spatial damping of standing waves is mostly based on constant-current line scans $z(x)|_{I,V}$ taken perpendicularly to straight steps at low bias voltages. Such topographic data in the vicinity of a step are represented in Fig. 3.6. Although they are less directly related to the LDOS than dI/dV -profiles used to investigate e - e interaction in Section 4.2 (e.g. Fig. 4.5), higher resolution can generally be obtained in topographic data. Since e - ph damping involves much larger L_ϕ values compared to e - e damping of electrons at large bias voltages $V > 1$ V (Fig. 4.1), we need a better resolution here than the resolution that was necessary to learn about e - e processes in Section 4.2. Experimental results presented in this Section have been obtained by averaging over several line scans which were recorded on the same surface spot, i.e. without y -displacement of the tip while scanning in x -direction. Note the resolution of $\approx 1/1000$ Å of such $z(x)$ -data (Fig. 3.6(b)).

To interpret our constant-current line scans we include inelastic scattering processes in the formalism leading to Eq. (3.13). Introducing $\rho_{\text{step}}(E, x)$ from Eq. (4.6) into Eq. (3.10) and going through the calculation sketched in Section 3.2 leads to the following expression for the constant-current tip-sample distance at a straight step edge in presence of inelastic processes:

$$\begin{aligned}
 s(x)|_{I,V} = & \frac{1}{2\sqrt{\frac{m_e}{\hbar^2}}\sqrt{2\overline{W}}} \ln \left(1 - r \frac{1}{eV} \frac{L_0}{\rho_b + L_0} \frac{\hbar^2}{2m^*} \frac{1}{x} e^{-2\frac{x}{L_\phi}} \right. \\
 & \times \left(\frac{\xi_{k_{eV}}}{\sinh \xi_{k_{eV}}} k_{eV} J_1(2k_{eV}x) - \frac{\xi_{k_F}}{\sinh \xi_{k_F}} k_F J_1(2k_Fx) \right) \\
 & \left. + s_0 \right) .
 \end{aligned} \tag{4.11}$$

By using Eq. (3.10) as starting point, we neglected the energy and bias voltage dependence of the transmission factor. Numerical solution of the integral in Eq. (2.3) with $\rho_{\text{step}}(E, x)$ from Eq. (4.6), $\mathcal{T}(E, V, s)$ from Eq. (4.7) and parameters in the range of those used in our experiment yield, that neglecting the energy and bias dependence of $\mathcal{T}(E, V, s)$ is very well justified in the low-bias regime which is the subject of our interest here (V typically 10 mV). Using Eq. (4.11) we have three free parameters for fitting, namely the effective step reflection amplitude r , L_ϕ and the step location. k_{eV} is known from the dispersion relations, \overline{W} from apparent barrier height measurements and $L_0/(\rho_b + L_0)$ from spectra on clean terraces (see Section 3.2).

According to Eq. (4.11) the damping of quantum interference patterns as measured in constant-current mode of STM is caused by a combination of *inelastic scattering processes* (e^{-2x/L_ϕ}), *Fermi-Dirac broadening* ($\xi_{k_{eV}}/\sinh \xi_{k_{eV}}$) and *beating* due to the fact that k vectors from k_F up to k_{eV} contribute to the current and thus to $s(x)|_{I,V}$

($1/eV$ and $1/x$). To compare the damping strength of these different contributions we define, in addition to $L_\phi/2$ for inelastic processes, the following characteristic apparent damping constants. The expression of Fermi-Dirac broadening $\xi_k/\sinh \xi_k$ takes on the value $1/e$ at $\xi_k \approx 2.7$, this defines (see Eq. (3.11))

$$L_{\text{FD}} \approx 2.7 \frac{\hbar^2}{2\pi m^*} \frac{k_{eV}}{k_B T}. \quad (4.12)$$

The beating or wave vector spread due to summing over k vectors from k_F up to k_{eV} leads to a damping over the characteristic length $L_V \approx 1/\Delta k$ with $\Delta k = k_{eV} - k_F = \sqrt{2m^*/\hbar^2} (\sqrt{eV - E_F} - \sqrt{-E_F})$, or for small V , $\Delta k = \frac{m^* eV}{\hbar^2 k_F}$. Depending on the chosen conditions (V, T) one of these three damping lengths is shortest and dominates the decay. Since we are interested in $e-ph$ processes we would like to extract L_ϕ from our data, and therefore we aim to measure in a regime where $L_\phi < L_{\text{FD}}, L_V$. Contrary to L_ϕ and L_{FD} , L_V is temperature independent and by measuring at very low bias voltages L_V is virtually infinite and thus constitutes no major obstacle. The situation is different for L_{FD} . Both L_{FD} and L_ϕ decrease with increasing temperature and L_ϕ will dominate the damping only if $e-ph$ coupling is strong enough, e.g. in the simple Debye model $\lambda \gtrsim 1/2.7 \approx 0.37$ ⁶.

The validity of $s(x)|_{I,V}$ of Eq. (4.11) was already demonstrated in Fig. 3.6(a). The dominant damping is due to L_{FD} in this case ($L_\phi = \infty$ for the fit). The line scan in Fig. 3.6(b) has been taken at a bias voltage of 100 mV. At these conditions L_V prevails. The line scan shows the beating of the Bessel functions with wave vectors $k_{100 \text{ meV}}$ and k_F .

Ag(111)

In Fig. 4.7(a) line scans taken at $V = 10$ mV from 3.5 K to 77.3 K on a Ag(111) terrace adjacent to a descending step are presented. The spatial damping of the standing waves with increasing T is clearly visible. The line scans in Fig. 4.7(a) have been fitted by Eq. (4.11) for $x \geq 30$ Å and by putting $L_\phi = \infty$. The data and the fitted function coincide almost perfectly, except in the immediate vicinity of the step edge where the model is not valid. The spatial damping is dominated by L_{FD} at high T , and by L_V at low temperatures. It is clear from the fits that $L_\phi/2 > L_{\text{FD}}, L_V$ in the experiment. The fit parameter $r_{\text{desc}} = 0.56 \pm 0.06$ does not vary significantly with temperature and is in good agreement with reflection amplitudes determined in independent experiments (Fig. 5.9).

⁶ L_{e-ph} is always larger than its high-temperature extrapolation [70], i.e. $L_{e-ph} \geq \hbar^2 k_{eV} / 2\pi m^* \lambda k_B T$ (Eq. (4.4)). Asking for L_{e-ph} to be smaller than L_{FD} from Eq. (4.12) leads to the condition $\lambda \geq 1/2.7$.

Since the effective damping length L_{FD} due to Fermi-Dirac broadening is inversely proportional to T , at temperatures larger than 100 K, constant-current line scans taken at low bias voltage across a Ag(111) step show too few oscillations for a significant fit procedure (Fig. 4.7(a)). However, since $L_{\text{FD}} \propto k_{\text{eV}}$ (Eq. (4.12)) this problem can be circumvented by measuring quantities like dI/dV or dz/dV with lock-in technique at larger bias voltage. At larger bias values dI/dV rather than constant-current line scans are used since $L_{\Delta V}$ from Eq. (4.10) is generally much smaller than L_V . Fig. 4.7(b) shows dI/dV data across a step at $T = 126$ K, acquired as described in Section 4.2. These data are perfectly fitted by Eqs. (4.8) and (4.9) and $L_\phi = \infty$. Thus, also at 126 K $L_\phi/2 > L_{\text{FD}}$

Within our model the temperature dependent damping of the standing waves of the s - p surface state on Ag(111) is very well described by the Fermi-Dirac broadening alone. Therefore we can only give lower limits for the phase-relaxation length L_ϕ . For Ag(111) surface-state electrons L_ϕ is estimated to be $L_\phi(E_F) \gtrsim 600$ Å at 3.5 K and $L_\phi(E_F) \gtrsim 250$ Å at 77 K. These limits are obtained by reducing L_ϕ in the fit function, Eq. (4.11), until a significant deviation from the experimental data is observed.

Cu(111)

The s - p surface state on Cu(111) shows a k_F that is larger than for Ag(111) (Table 3.1). Therefore, for a given temperature, $L_{\text{FD}}(E_F)$ is larger on Cu(111) than on Ag(111) (Eq. (4.12)). At the Fermi energy Fermi-Dirac broadening is hence expected to play a smaller role for Cu(111) than for Ag(111). This explains why we can clearly observe standing waves in low-bias constant-current images on Cu(111) up to room temperature, whereas on Ag(111) no waves are observable at 300 K in such images (see also Ref. [137] for standing waves at 300 K on Cu). Furthermore, beating effects (i.e. L_V) should also be smaller for Cu(111) due to its steeper dispersion in the vicinity of E_F . Our results of the temperature induced spatial damping on the Cu(111) surface represented in Fig. 4.8 are as for Ag(111) fully reproduced by Eq. (4.11) assuming $L_\phi = \infty$. Again, there is perfect agreement between model and experiment and the observed apparent coherence loss can entirely be explained in the framework of Fermi-Dirac broadening. As in the case of Ag(111) the lower limits of L_ϕ for Cu(111) are obtained by reducing L_ϕ in the fit function Eq. (4.11) until a significant deviation from the data is observed. The estimates are $L_\phi(E_F) \gtrsim 660$ Å at 77 K and $\gtrsim 160$ Å at 178 K (see Fig. 4.9).

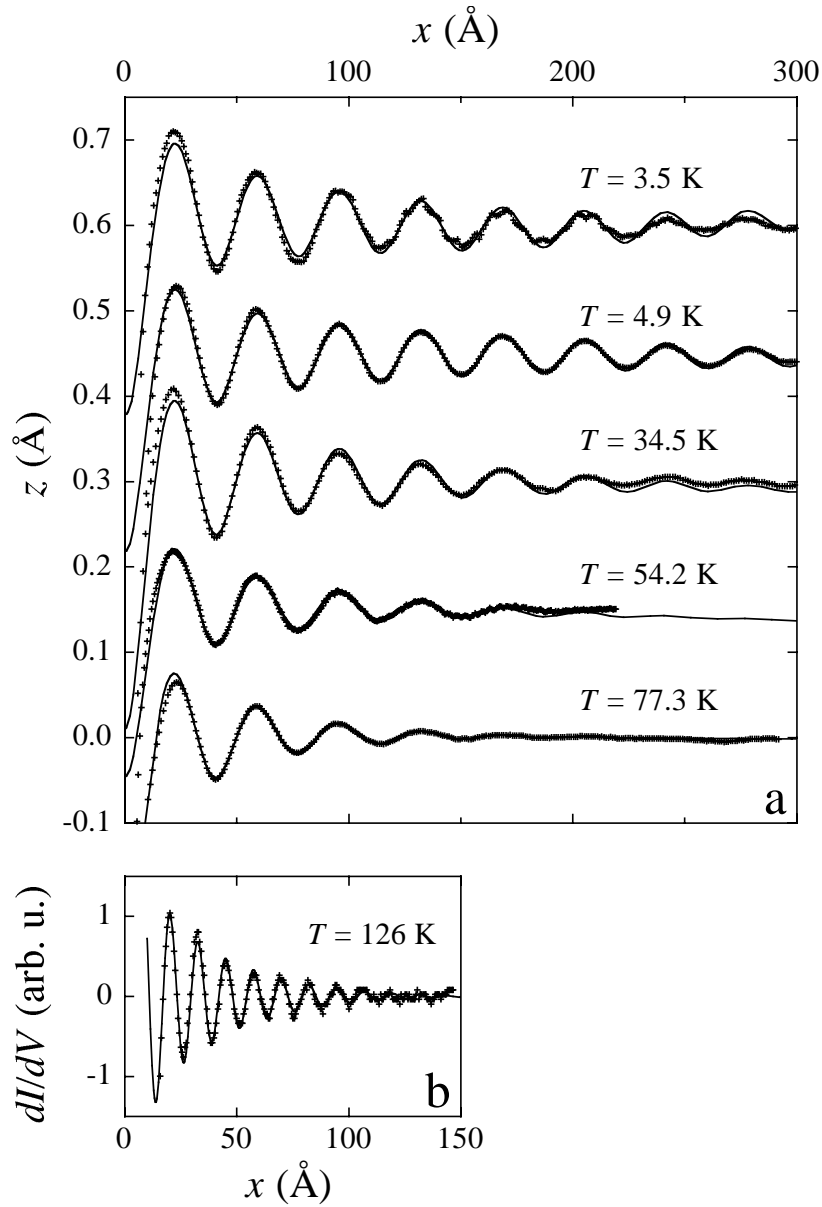


Figure 4.7: (a) Ag(111) constant-current line scans taken on a terrace adjacent to a descending step ($V = 10$ mV, $I = 1.0$ nA). The data have been displaced vertically for clarity. (b) dI/dV data taken across a step at $V = 403$ mV, $I = 4.3$ nA, and $T = 126$ K ($\Delta V = 79$ mV, c.f., $\nu = 5.37$ kHz). The solid lines are fits using Eq. (4.11) in (a), and Eqs. (4.8) and (4.9) for dI/dV in (b), with the reflectivity r and the step location being the only fit parameters (L_ϕ was set to infinity, see text).

Discussion

Photoemission lines originating from surface states are preferred candidates for electron lifetime studies since surface states have no dispersion with respect to \mathbf{k}_\perp . Hence the instrumental final state uncertainty in that quantity does not lead to broadening, and the linewidth Γ gives direct access to the lifetime broadening of the initial state [64].

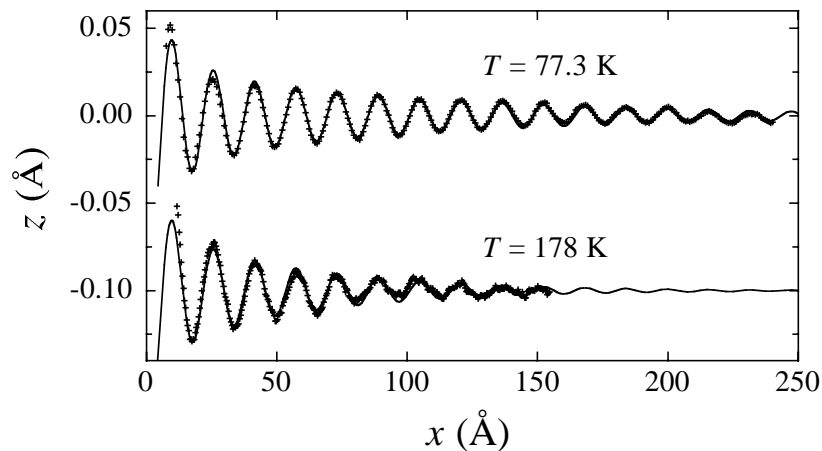


Figure 4.8: Cu(111) constant-current line scans taken at $V = 10$ mV on a terrace adjacent to a descending step. The data have been displaced vertically for clarity ($I = 0.4$ nA at 77.3 K, $I = 0.1$ nA at 178 K). The solid lines are fits using Eq. (4.11) (L_ϕ was set to infinity, see text).

The currently most accurate photoemission studies of surface-state linewidths have been reported by McDougall *et al.* [70] and Matzdorf *et al.* [63] for Cu(111), and by Paniago *et al.* [69] for Ag(111). From the T dependence of Γ , McDougall *et al.* could derive the electron-phonon interaction strength of the s - p derived surface state on Cu(111) ($\Gamma_{e-ph} = 2\pi\lambda k_B T$, Eq. (4.4)). Their result of $\lambda = 0.14 \pm 0.02$ was experimentally confirmed by Matzdorf *et al.* [63] and agrees well with theory ($\lambda = 0.15 \pm 0.03$) [111]. Despite the remarkable success of high-resolution photoemission to infer λ from $d\Gamma/dT$, the *absolute linewidths* Γ reported so far are all far above the theoretical predictions. This deficiency of PES is well known; it could be attributed to broadening by scattering at substrate imperfections [63, 66, 138]. In agreement with this interpretation, Li *et al.* report in a recent STS study on Ag(111) an unprecedented small Γ value from local measurements on surface areas that were bare of defects [90].

We compare inverse lifetimes derived from STS and ARPES with our measurements of the decay of standing waves in Figure 4.9. For the sake of comparison we converted all quantities in $L_\phi = v_F \tau_\phi = v_F \hbar / \Gamma$, where v_F is the group velocity of the electrons at our measuring energy E_F . From the width of the onset of the Ag(111) surface state in tunneling spectra taken at 5 K, Li *et al.* derived $\tau_\phi(E_{\bar{\Gamma}}) = 67 \pm 8$ fs corresponding to $L_\phi^{\text{STS}} = v_F \tau_\phi(E_{\bar{\Gamma}}) \approx 160$ Å [90]. It is evident from Fig. 4.9 that this result gives too large decay rates as compared to our Ag(111) data taken at E_F and 4.9 K. The shorter lifetime observed at $\bar{\Gamma}$ is probably partly due to the fact that the electron-phonon linewidth levels off at low temperature at the $\bar{\Gamma}$ point [70], and partly due to e - e interaction, which of course is enhanced at the $\bar{\Gamma}$ point as compared to E_F . It is also seen that our lower

bound of $L_\phi(E_F) = 600 \text{ \AA}$ is conservative, presumably $L_\phi(E_F)$ is much larger. Our L_ϕ value presents the largest lifetime measured so far for the Ag(111) surface state. It corresponds to a peak width of $\Gamma(E_F, 3.5 \text{ K}) = \frac{\hbar^2 k_F}{m^* L_\phi} \lesssim 2.6 \text{ meV}$, which should be very difficult to resolve in ARPES.

In the Debye model the phase-relaxation length due to electron-phonon interaction close to E_F is described by $L_{e-ph}(E_F, T) = v_F / \tau_{e-ph}(E_F, T)$, where $\tau_{e-ph}(E_F, T)$ is obtained through numerical integration of Eq. (4.3) with λ being the only free parameter⁷. Since there is only one parameter, an absolute measurement of $L_\phi(E_F)$ at a single T yields an estimate of λ . We have used the Debye model of Eq. (4.3) to derive such estimates from our $L_\phi(E_F)$ values. For Ag ($\hbar\omega_D^{\text{Ag}} = 19 \text{ meV}$ [98]) we derive $\lambda_{\text{Ag}} \lesssim 0.27$ from $L_\phi(E_F, 77.3 \text{ K}) \gtrsim 250 \text{ \AA}$. This conservative upper limit for the electron-phonon mass enhancement factor is in agreement with the bulk value of $\lambda_{\text{Ag}} = 0.13 \pm 0.04$ given by Grimwall [111].

The currently lowest intrinsic linewidth measured by PES for the $\bar{\Gamma}$ surface state on Cu(111) is $\Gamma(E_{\bar{\Gamma}}, 77 \text{ K}) = 36 \text{ meV}$ [70]. By deducing the difference of electron-phonon and electron-electron linewidths between $E_{\bar{\Gamma}}$ and E_F of $\Delta\Gamma = 8 \text{ meV} + 5 \text{ meV} = 13 \text{ meV}$ (values inferred from the Debye model in Eq. (4.3) for $\lambda = 0.14$ and from Eq. (4.1)), we estimate the resulting ARPES linewidth at E_F to be about $\Gamma(E_F, 77 \text{ K}) = 23 \text{ meV}$, respectively, $L_\phi^{\text{PES}}(E_F, 77 \text{ K}) \approx 170 \text{ \AA}$. Figure 4.9 shows that this coherence length again is considerably too short compared to the observed decay length of the standing waves. Our lower bound of $L_\phi(E_F, 77 \text{ K}) = 660 \text{ \AA}$ yields a linewidth of $\Gamma(E_F, 77 \text{ K}) = 6 \text{ meV}$. From this upper bound of $\Gamma(E_F, 77 \text{ K})$, and consistently from our measurement at 178 K ($\Gamma(E_F, 178 \text{ K}) \lesssim 26 \text{ meV}$), we derive an upper limit of $\lambda_{\text{Cu}} \lesssim 0.34$ using the Debye model of Eq. (4.3) with $\hbar\omega_D^{\text{Cu}} = 27 \text{ meV}$. Again this is a conservative estimate which is in accordance with $\lambda = 0.14$ measured with ARPES [63, 70].

One evident reason why we measure much larger coherence lengths than can possibly be obtained with photoelectron spectroscopy is that we determine L_ϕ *locally* at terrace stripes perpendicular to steps that are bare of any adsorbates or other steps on the length scale of L_ϕ . From large scale observations of the surface morphology it is clear, however, that every crystal presents surface areas where the average terrace width is below our L_ϕ values. Also, at a lot of surface spots the density of chemical defects is above $1/L_\phi^2$, for L_ϕ in the range discussed here. Every integrating technique will be embarrassed by the steps and point defects since surface-state electrons strongly couple to the bulk at these sites, i.e. are scattered out of the surface state (Chapter 5). This leads to an apparent

⁷In this model we assume that the surface state electrons couple to phonons in the same way as bulk electrons do. Furthermore, surface phonons are not considered.

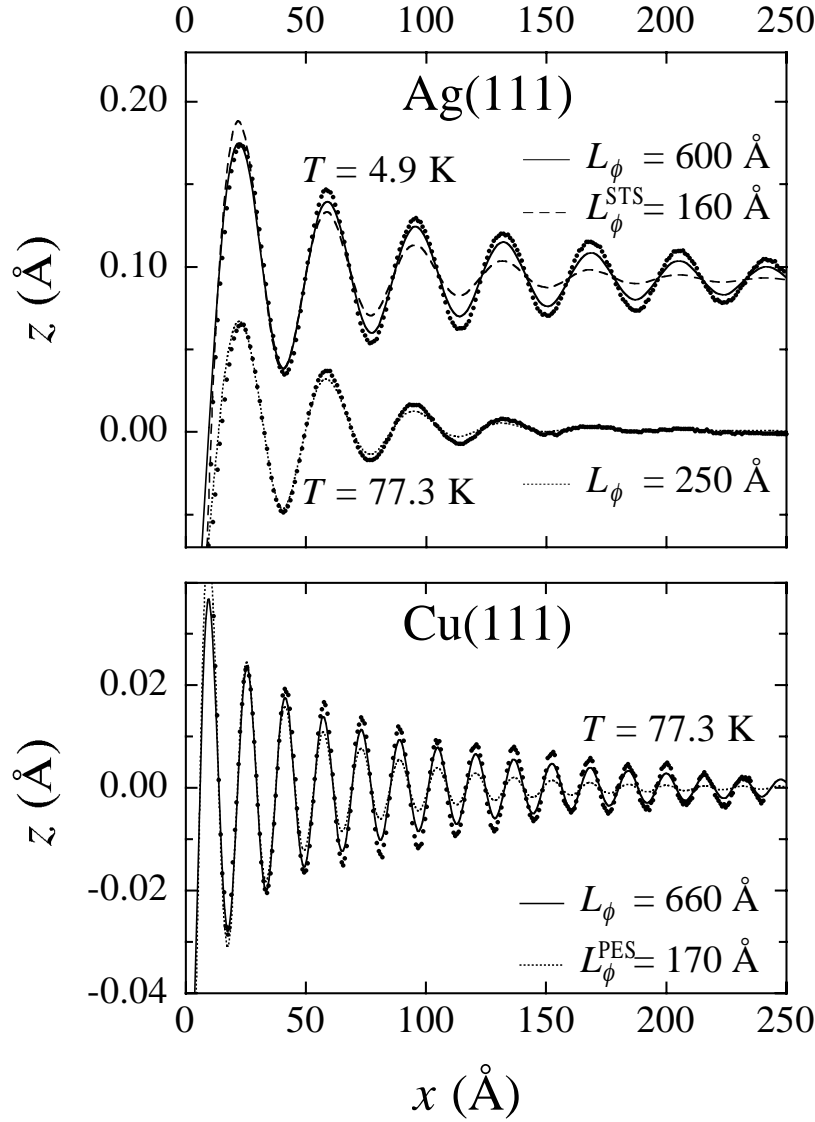


Figure 4.9: Decay of standing waves as determined in experiment for Ag(111) and Cu(111) compared to results from Eq. (4.11) employing various values for the phase coherence length L_ϕ . It is clearly seen that the values deduced in former STS and ARPES studies are too small compared to our experimental result. (For a detailed discussion of, and references to L_ϕ^{STS} and L_ϕ^{PES} see text.)

reduction of the integral L_ϕ as seen in PES. We therefore believe that the "offset" of $\Gamma(0 \text{ K}) \approx 20 - 30 \text{ meV}$ characterizing high-resolution PES peaks is mainly due to structural defects such as steps [63, 70]. This assignment is supported by differences of up to 10 meV in the linewidth "offset" between different research groups, whereas there is good agreement on $d\Gamma/dT$ [63, 70]. The influence of sputter defects on the linewidth Γ was employed to extrapolate to "intrinsic" linewidths expected from PES of perfectly ordered surfaces [138]. The resulting "intrinsic" values, e.g., of $\Gamma(E_{\bar{\Gamma}}, 0 \text{ K}) \leq 21 \pm 5 \text{ meV}$

for Cu(111), still contain phonon excitation at 0 K and electron-electron interactions.

The alternative approach to look at STS peak widths eliminates the defect problem, however, the analysis in terms of lifetimes demands elaborate modeling. We note that our STS peak widths (see Fig. 3.4) are comparable to the ones reported by Li *et al.* [90], hence we would infer similar estimates on τ from regarding $\Gamma(E_{\overline{\Gamma}}, 5 \text{ K})$ in our STS spectra. Compared to a peak width analysis our access to the e - ph part of τ_ϕ via measuring L_ϕ from the decay of standing waves has two advantages, i) it is based on a straightforward analytical model that has been tested experimentally, and ii) since we measure at E_F , our L_ϕ values are not reduced by electron-electron scattering and therefore provide a more direct access to λ .

To conclude this Section, we point out that in contrast to integral measurements such as photoemission we measure the phase-relaxation length L_ϕ *locally*. This eliminates residual linewidths due to surface defect scattering embarrassing integrating techniques. Our STM-results therefore provide currently the best absolute estimates of L_ϕ , respectively inelastic lifetime $\tau_\phi = L_\phi/v_F$ for the s - p surface states on Cu(111) and Ag(111). In principle, by the technique described in this Section, STM constitutes a powerful method to study e - ph interactions at surfaces. Since e - ph interaction in Cu and Ag with mass enhancement parameters of $\lambda_{\text{Cu}} = 0.15$ and $\lambda_{\text{Ag}} = 0.13$ is relatively weak [111], the technique is embarrassed by the fact that $L_{\text{FD}} < L_{e-ph}$, and therefore we have not been able to determine an absolute value of the e - ph interaction strength in these systems, but only an upper limit. In future studies, by choosing systems with an e - ph mass enhancement parameter $\lambda \gtrsim 0.4$, STM could be used to *quantify* electron-phonon interactions at surfaces. Metallic elements with relatively large e - ph interaction include [111]: Be [139, 140], Al, Ti, V, Nb, Ta, Mo, W, Re, Ir, Pd, Pb, Sn.

Chapter 5

Confinement of Surface-State Electrons

s-p derived surface-state electrons on noble-metal surfaces have been confined in symmetric and asymmetric Fabry–Pérot resonators formed by two atomically parallel step edges. The local density of states in the resonators has been measured and can perfectly be explained with a simple Fabry–Pérot model (Section 5.2). As described in Section 5.3 the energy dependent reflection amplitudes and scattering phaseshifts of the different kind of Ag(111) step edges have been determined with high accuracy. The model character of the resonators opens up quantitative electron scattering experiments at test-structures brought into the resonator. In Section 5.4 the confinement of *s-p* surface-state electrons in Fabry–Pérot structures on Au(111) is discussed qualitatively.

5.1 Introduction

Quantum interference of electrons in low-dimensional structures has attracted much interest in recent years. Elegant methods have been developed to probe the quantum-mechanical probability density distribution of electrons in semiconductor heterostructures [141, 142], in metal heterostructures [130] and in Shockley-type surface states of metals [67, 76, 78, 81]. In particular, the real space visualization of the local density of states of surface-state electrons by means of STM/STS has created a lot of excitement [33, 82]. As outlined in Chapters 3 and 4 surface-state electrons are scattered by single adsorbates, impurities and surface defects. Therefore, these can be used as building blocks for the formation of multiple scattering structures, e.g. quantum corrals may be assembled from adsorbates [33], in which surface-state electrons are (partially) confined, leading to tantalizing interference patterns in their LDOS [33, 81, 82, 88, 91, 129, 131].

Such confining structures have been employed to illustrate solutions of the Schrödinger equation [33] and attempts were made to visualize quantum chaos [131].

The LDOS of such quantum structures depends on the confining potential, i.e. the reflection properties of the boundaries. Therefore, by carefully studying the LDOS, one is able to learn about potential changes induced by adsorbates or steps. The first to study the changes in potential energy due to the presence of a step edge for s - p derived surface-state electrons on noble metals were Davis *et al.* [81] followed by Hasegawa *et al.* [78]. Their results indicate that steps are not very efficient reflectors. However, both of them treated steps as real hard wall or δ -potentials, and thus the absorption processes at step edges due to bulk coupling were completely disregarded. Later on, Crommie *et al.* published their beautiful results on confinement in circular quantum corrals formed by arranging single Fe adatoms on Cu(111) by atom manipulation with the STM tip [33]. The location of the peaks in the DOS of the corral could very well be explained with a simple hard wall model. However, this simple model, with infinitely sharp DOS peaks at energies corresponding to the eigenstates, does not at all account for the measured linewidth which are of the order of 100 meV. The experiments by Crommie *et al.* inspired subsequent theoretical work [127,128,131,143]. Heller *et al.* could explain the finite width quantitatively in the framework of a multiple scattering theory, which accounts for absorption of surface-state electrons at the Fe scatterers in addition to transmission of surface-state electrons out of the corral [131]. Heller *et al.* found that only a fraction of about 25 % of the surface-state electrons is reflected at the boundaries, whereas 50 % is absorbed into bulk states. Simultaneously Crampin *et al.* calculated the level broadening in such quantum structures, considering substrate band structure effects [127]. In agreement with Ref. [131] Crampin *et al.* find a substantial level broadening due to scattering into bulk states at the boundaries. But they emphasize the necessity to introduce an additional broadening mechanism which dominates for the lowest levels, where the broadening due to bulk scattering gets negligible. In a further publication Crampin and Bryant were able to quantify this further broadening by introducing e - e and e - ph interaction in their model [128], which greatly improved the level of agreement between theory and experiment. On Cu(111) broadening due to e - e interaction for low-lying surface states may be considerable, since the band edge E_F lies more than 400 meV below the Fermi level (see Section 4.2). It was suggested that e - e broadening could be minimized by choosing Ag(111) as substrate, since on silver the band edge lies close to the Fermi energy [127].

Challenges in surface-state electron confinement are the quantification and possibly improvement of the scattering properties of the confining structures [45, 131], and the

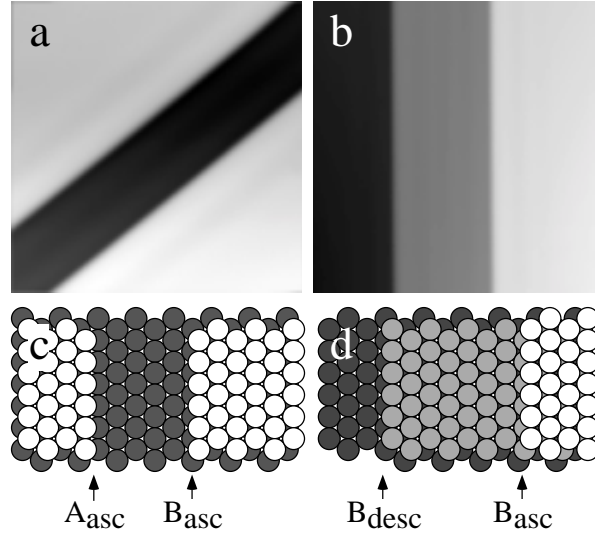


Figure 5.1: Constant-current images ($V = 100$ mV, $I = 1$ nA) show (a) a 56 Å wide symmetric resonator (215 Å \times 215 Å) and (b) a 104 Å wide asymmetric resonator (311 Å \times 311 Å). Hard sphere models for symmetric and asymmetric resonators are sketched in (c) and (d), respectively ($T = 4.9$ K).

construction of quantum resonators which could be used to study electronic properties of nanosized structures introduced into them, much as in optics. The most obvious choice for such a resonator is a set of two perfectly straight and parallel steps. This simplest geometry enables the description of the LDOS in the resonator through analogy with a Fabry–Pérot Etalon known from optics [144]. Electron scattering at parallel step arrangements has been investigated earlier [81, 82, 86], however, steps were treated as real hard-wall or δ -potentials, and hence the absorption processes at step edges due to bulk coupling were not treated correctly.

Here we present measurements of the LDOS in symmetric and asymmetric quantum resonators consisting of pairs of ascending and ascending/descending close-packed steps on Ag(111) and Au(111). The simplicity of the chosen geometry allows for straightforward modeling in the framework of a Fabry–Pérot model. This model establishes a direct correlation of the LDOS of the s - p derived surface-state in the resonator with the step reflection amplitude, r , and scattering phase, φ . The model reveals the different role of φ and r on peak positions and peak broadening of the quantized states and enables the *determination of the full scattering properties of the different kinds of monatomic steps*. We present the first measurements of the energy dependence of the reflection amplitude.

Fig. 5.1 illustrates our Fabry–Pérot quantum resonators bound by $\langle 1\bar{1}0 \rangle$ -oriented monatomic and *straight* steps. The *symmetric* resonator (Figs. 5.1(a) and (c)) consists

of two ascending steps, out of which one is of type A ($\{100\}$ -facet) and the other one necessarily of type B ($\{111\}$ -facet). The *asymmetric* resonator (Figs. 5.1(b) and (d)) is formed by one ascending and one descending step, i.e. either by ($A_{\text{desc}}, A_{\text{asc}}$) or ($B_{\text{desc}}, B_{\text{asc}}$) steps. The latter is illustrated in Fig. 5.1(d).

Before discussing the LDOS measurements of the parallel step quantum structures quantitatively for Ag(111) in Section 5.3 and qualitatively for Au(111) in Section 5.4, the Fabry–Pérot model used to interpret our data is presented in the next Section.

5.2 Fabry–Pérot Model

Following the ideas outlined in Section 3.2 we model the parallel step resonators by two parallel semi-transparent electron reflectors with *coherent* (k_x dependent) reflection amplitudes r_ℓ , r_r , and coherent (k_x dependent) reflection phaseshifts φ_ℓ , φ_r , where ℓ and r denote the left and right-hand step, respectively (Fig. 5.2). A similar ansatz was recently used to interpret beautiful ARPS experiments for the quantum-well system Ag/Fe(100), where the electrons are confined between the Ag surface and the Ag/Fe interface, much like photons in a Fabry–Pérot Etalon [130]. In principle the locations of the reflectors can be chosen at will.

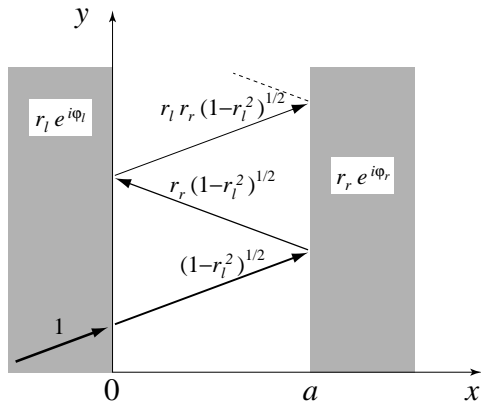


Figure 5.2: Plane parallel electron reflectors are used to model the resonators. The amplitudes of a multiply reflected wave packet impinging from the left are indicated.

But the phaseshifts depend on the choice and there usually is one particular choice of reflector positions for which the energy dependence of the phaseshifts can be minimized¹. Our finding in Section 3.2 that the LDOS patterns at a step edge are consistent with a phaseshift of $-\pi$ with respect to the midheight point in the constant-current line scan in addition with the results of Li *et al.* in Ref. [88] leads us to the following definition: *the mirrors are located at the midheight points in the constant-current line scan of the step* (Figs 5.6(a) and 5.8(a)). Since the measurements presented in this Chapter are restricted to energies close to the Fermi level, the electrons can be assumed

¹For example, in the case of perfect resonators, i.e. an infinite square potential, it is favorable to position the reflectors right at the edges of the potential well. For this choice the phaseshifts are $-\pi$ independent of energy.

free and non-interacting and their dispersion is given by Eq. (3.1) (Chapter 3). In addition, e - e and e - ph phase-relaxation length for these electrons are large (Chapter 4) and, as will be argued later in this Chapter, e - e and e - ph interaction can thus safely be neglected. Since we model the step edges as straight and infinitely extended reflectors there is a translation symmetry along y , i.e. k_y is a good quantum number.

To calculate the wave functions in the resonator, which are characterized by (k_x, k_y) where $k_x = \sqrt{2m^*(E - E_F)/\hbar^2 - k_y^2}$ (Eq. (3.1)), we have to add up all (multiply) scattered waves coherently (Fig. 5.2):

$$\begin{aligned}
\Psi_{k_x > 0, k_y}(x, y) &= \sqrt{1 - r_\ell^2} e^{ik_y y} (e^{ik_x x} + r_r e^{i\varphi_r} e^{2ik_x a} e^{-ik_x x} + \\
&\quad r_\ell e^{i\varphi_\ell} r_r e^{i\varphi_r} e^{2ik_x a} e^{ik_x x} + \dots) \\
&= \sqrt{1 - r_\ell^2} e^{ik_y y} \frac{1}{1 - r_\ell r_r e^{i(\varphi_\ell + \varphi_r)} e^{2ik_x a}} (e^{ik_x x} + r_r e^{i\varphi_r} e^{2ik_x a} e^{-ik_x x}) \\
\Psi_{k_x < 0, k_y}(x, y) &= \sqrt{1 - r_r^2} e^{ik_y y} (e^{ik_x x} + r_\ell e^{i\varphi_\ell} e^{-ik_x x} + r_r e^{i\varphi_r} r_\ell e^{i\varphi_\ell} e^{-2ik_x a} e^{ik_x x} + \dots) \\
&= \sqrt{1 - r_r^2} e^{ik_y y} \frac{1}{1 - r_\ell r_r e^{i(\varphi_\ell + \varphi_r)} e^{-2ik_x a}} (e^{ik_x x} + r_\ell e^{i\varphi_\ell} e^{-ik_x x}). \quad (5.1)
\end{aligned}$$

Here a is the width of the resonator. By choosing the normalization factor $\sqrt{1 - r_{\ell,r}^2}$ instead of the transmission amplitude $\sqrt{1 - r_{\ell,r}^2} - A$, where A is the absorption probability, we take into account inelastic processes at step edges in the correct way (see discussion of special case $r_\ell, r_r \rightarrow 0$ below). The LDOS in the resonator

$$\rho_{\text{FP}}(E, x, y) = \rho_b + \frac{\partial}{\partial E} \left(2 \int_0^{k_E} \frac{dk_x}{2\pi} \int_{-\sqrt{k_E^2 - k_x^2}}^{\sqrt{k_E^2 - k_x^2}} \frac{dk_y}{2\pi} (|\Psi_{k_x, k_y}(x, y)|^2 + |\Psi_{-k_x, k_y}(x, y)|^2) \right) \quad (5.2)$$

is then readily calculated with the wave functions of Eq. (5.1) to yield:

$$\begin{aligned}
\rho_{\text{FP}}(E, x) &= \rho_b + \frac{L_0}{\pi} \int_0^{k_E} dk_x \frac{1}{\sqrt{k_E^2 - k_x^2}} \frac{1}{1 + r_\ell^2 r_r^2 - 2r_\ell r_r \cos(2k_x a + \varphi_\ell + \varphi_r)} \\
&\quad \cdot \left((1 - r_\ell^2) [1 + r_r^2 + 2r_r \cos(2k_x(x - a) - \varphi_r)] + \right. \\
&\quad \left. (1 - r_r^2) [1 + r_\ell^2 + 2r_\ell \cos(2k_x x + \varphi_\ell)] \right). \quad (5.3)
\end{aligned}$$

In the limit of vanishing coherent reflection coefficients, $r_{\ell,r} \rightarrow 0$, $\rho_{\text{FP}}(E, x)$ reduces to the well known constant LDOS L_0 for a free 2D electron gas². Note that this holds even in the case of absorption at step edges and thus the normalization used for Eq. (5.1) is

² $\int_0^{k_E} dk_x (k_E^2 - k_x^2)^{-1/2} = \pi/2$.

correct. Another special case of Eq. (5.3) is the hard wall potential, i.e. $r_{\ell,r} \rightarrow 1$ and $\varphi_{\ell,r} \rightarrow -\pi$. Using

$$\lim_{r \rightarrow 1} \frac{1 - r^2}{1 + r^4 - 2r^2 \cos(2k_x a)} = \frac{\pi}{2a} \sum_{n=-\infty}^{\infty} \delta(k_x - n \frac{\pi}{a}) \quad (5.4)$$

one obtains

$$\lim_{\substack{r_{\ell,r} \rightarrow 1 \\ \varphi_{\ell,r} \rightarrow -\pi}} \rho_{\text{FP}}(E, x) = \rho_b + \sum_{n=1}^{\infty} \frac{4L_0}{a} \frac{1}{\sqrt{k_E^2 - (n \frac{\pi}{a})^2}} \sin^2(n \frac{\pi}{a} x) \Theta(k_E - n \frac{\pi}{a}), \quad (5.5)$$

which is exactly the result one calculates for infinite square barriers, i.e. the LDOS shows sharp non-analytical rises at energies $E_n = \hbar^2 k_n^2 / 2m^*$, where $k_n a = n\pi$ with $n = 1, 2, \dots$, followed by a $1/\sqrt{E - E_n}$ decay due to the fact that the electrons are free parallel to the steps. Finally, for $r_r \rightarrow 0$ one finds the LDOS at a single straight step edge given in Eq. (3.8).

Due to the translation symmetry the LDOS in the Fabry-Pérot resonator does only depend on one lateral coordinate, i.e. x . The 2D nature of the problem enters in Eq. (5.3) through the integration over all $k_x < k_E$ and the $1/\sqrt{k_E^2 - k_x^2}$ term. The integration leads to a broadening of the LDOS features of the corresponding 1D Fabry-Pérot resonator, which has to be taken into account when one is interested in the peak width of spectra taken in resonators.

In Fig. 5.3 $\rho_{\text{FP}}(E)|_x$ from Eq. (5.3) is plotted for a 100 Å wide *symmetric* resonator, i.e. $r_{\ell} = r_r = r$ and $\varphi_{\ell} = \varphi_r = \varphi$, at different lateral positions x and for various step reflection coefficients. $\rho_{\text{FP}}(E)|_x$ shows peaks at roughly the energies for which the denominator in Eq. (5.3) is minimal, i.e.

$$k_{E_n} a \approx \pi (n - 1 - \frac{\varphi_{\ell} + \varphi_r}{2}), \quad (5.6)$$

where $n = 1, 2, \dots$. Figure 5.3(a) and (c) clearly show that reduced step reflection amplitudes $r_{\ell,r}$ lead to increased peak width Γ , whereas the peak positions are hardly influenced by $r_{\ell,r}$. On the other hand, the phaseshifts $\varphi_{\ell,r}$ play a complementary role: the position of the peaks is strongly influenced by $\varphi_{\ell,r}$, but not the peak widths, as seen in Fig. 5.3(b). In a more quantitative manner this can be seen in Fig. 5.4. In (a) the energy of the $n = 5$ mode of a 100 Å wide symmetric resonator is plotted as a function of reflection phaseshift and amplitude. It is obvious that the peak positions are mainly determined by the phaseshift and they are very sensitive to deviations of φ from $-\pi$ especially in the case of narrow resonators (see Eq.(5.6)). Linewidths Γ of the model ρ_{FP} are shown as a function of the reflection amplitude in Fig. 5.4(b) ³. As

³ Γ is defined here as the full width at $(E_n + E_n^{\min})/2$ where E_n^{\min} is the minimum in $\rho_{\text{FP}}(E)|_x$ preceding the maximum at E_n .

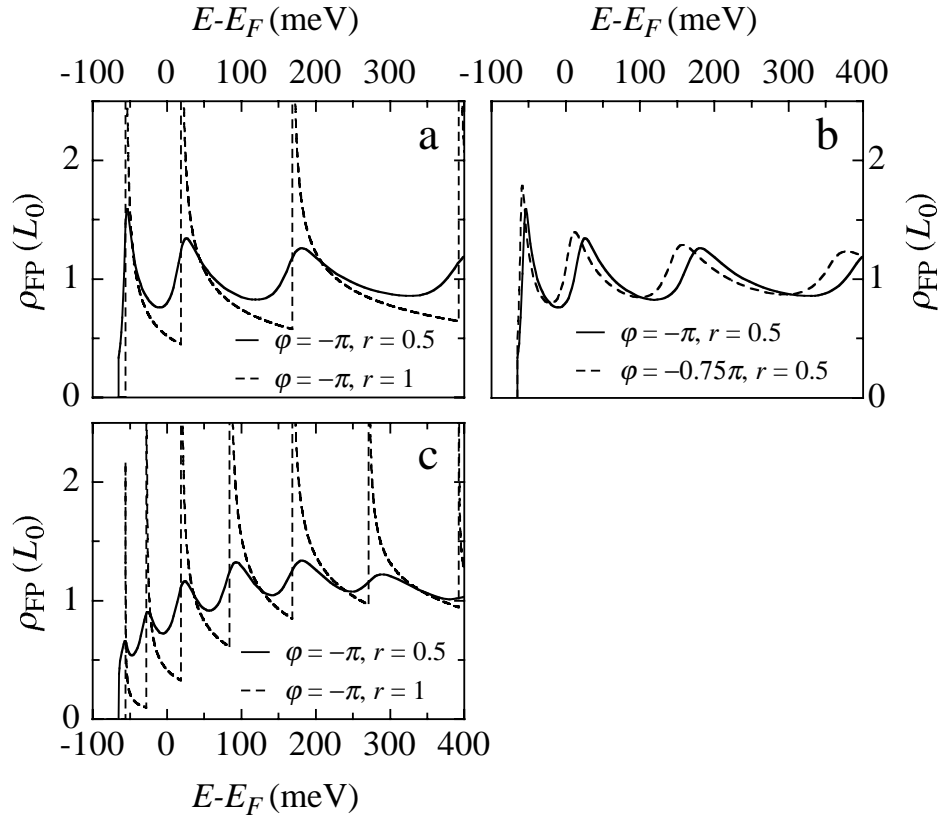


Figure 5.3: $\rho_{\text{FP}}(E)|_x$ from Eq. (5.3) for a symmetric 100 Å wide Fabry-Pérot resonator. ($\rho_b = 0$, Ag(111) parameters: $m^* = 0.4m_e$, $E_{\text{F}} = -65$ meV.) **(a)** In the center of the resonator, i.e. $x = 50$ Å, only modes of odd symmetry ($n = 1, 3, \dots$) contribute to the DOS. The broadening of the peaks for reduced coherent reflection amplitudes is clearly seen. **(b)** $x = 50$ Å. The peak positions depend crucially on the reflection phaseshifts. **(c)** At $x = 12$ Å even modes contribute as well.

seen in Fig. 5.4(b) peak widths depend crucially on the coherent reflection amplitudes of the step edges, and thus allow for an experimental estimate of r . For example, the linewidth measured for the $n = 3$ peak of a 67 Å wide (asymmetric) resonator on Ag(111) is 100 meV which corresponds to a reflection amplitude of $r \approx 0.5$ (Fig. 5.4(b)). We emphasize that a measured peak widths of the order of 100 meV must be dominated by reduced step reflection, since the linewidth due to e - e and e - ph scattering are smaller than 10 meV for the energies of interest ($|E| < 400$ meV), as outlined in Chapter 4. We now turn our attention to the x dependence of ρ_{FP} . As seen in Fig. 5.5(a) the amplitudes of the oscillations in $\rho_{\text{FP}}(x)|_E$ depend strongly on the reflection amplitudes. Positions of the maxima and peak widths of $\rho_{\text{FP}}(E)|_x$ are not sensitive to asymmetries in the step reflection properties of right and left hand side step, i.e. to $\Delta\varphi = \varphi_\ell - \varphi_r$ and $\Delta r = r_\ell - r_r$. They mainly depend on the average reflection properties, i.e. on $\varphi = 0.5(\varphi_\ell + \varphi_r)$ and $r = \sqrt{r_\ell r_r}$. Asymmetries in reflection properties rather manifest

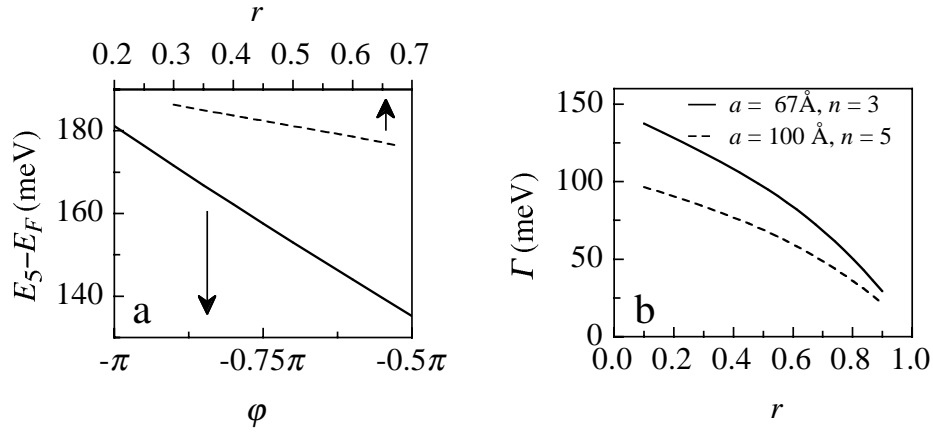


Figure 5.4: (a) $E_{n=5}$ of ρ_{FP} from Eq. (5.3) for a 100 Å wide symmetric resonator as a function of reflection phaseshift (full line, $r = 0.5$) and reflection amplitude (dashed line, $\varphi = -\pi$). (b) Linewidth of the $n = 3$ and $n = 5$ peak for symmetric resonators of 67 Å and 100 Å width, respectively, as a function of step reflection amplitude. The phaseshift φ is $-\pi$ (Ag(111) parameters: $m^* = 0.4 m_e$, $E_{\text{T}} = -65$ meV).

themselves in maxima positions and asymmetries in amplitudes of $\rho_{\text{FP}}(x)|_E$ (Figs. 5.5(b) and (c)). For example, from Eq. (5.3) one estimates a lateral shift of the maxima in $\rho_{\text{FP}}(x)|_E$ of $\Delta x \approx -\Delta\varphi/4k_E$ for a phase asymmetry $\Delta\varphi$, i.e. with Eq. (5.6):

$$\Delta x \approx \frac{-\Delta\varphi}{4n\pi} a. \quad (5.7)$$

One can readily show that $\rho_{\text{FP}}(E, x)$ of a resonator with reflectors at positions $x = 0$ and a and reflection properties φ_ℓ , r_ℓ , φ_r and r_r is identical to $\rho_{\text{FP}}(E, x)$ of a resonator with reflectors at $x = x_0$ and $a + \Delta a + x_0$ and reflection properties $\varphi_\ell + 2k_E x_0$, r_ℓ , $\varphi_r - 2k_E x_0 - 2k_E \Delta a$ and r_r . This confirms what has been stated above: the choice of the reflector positions is arbitrary, but the (energy dependent) phaseshifts depend on the choice and there usually is one distinguished set of positions for which the energy dependence of the phaseshifts is minimal.

To conclude this Section we would like to emphasize that the features of the LDOS $\rho_{\text{FP}}(E, x)$ in the resonator strongly depend on the step reflection properties. Whereas the average phaseshift φ determines the positions of the maxima in the DOS $\rho_{\text{FP}}(E)|_x$, the mean reflection amplitude governs the peak width of $\rho_{\text{FP}}(E)|_x$ and the oscillation amplitudes in $\rho_{\text{FP}}(x)|_E$. Differences in reflection properties of left and right hand step (reflector) lead to pronounced asymmetries in the LDOS features, i.e. $\rho_{\text{FP}}(x)|_E$. Due to their different role in influencing the LDOS of a resonator, reflection phaseshift and reflection amplitudes can be considered as independent (fit) parameters.

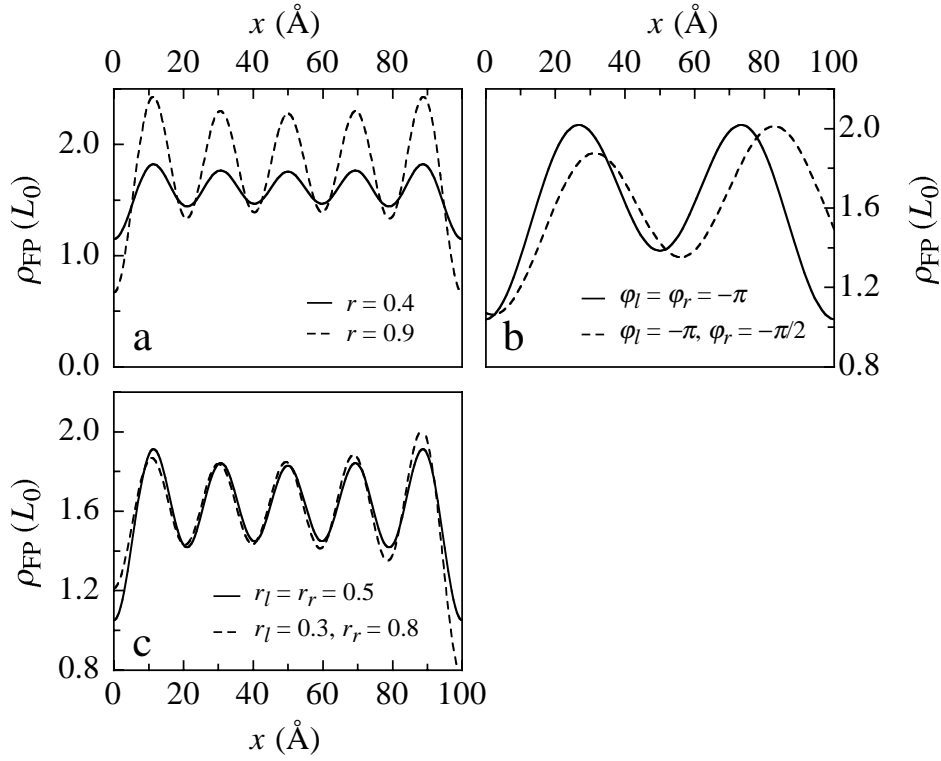


Figure 5.5: $\rho_{\text{FP}}(x)|_E$ from Eq. (5.3) for a 100 Å wide resonator. ($\rho_b = 0.56 L_0$, Ag(111) parameters: $m^* = 0.4 m_e$, $E_{\text{F}} = -65$ meV.) **(a)** Dependence of the amplitudes of $\rho_{\text{FP}}(x)|_{E=180 \text{ meV}}$ on r ($\varphi_\ell = \varphi_r = -\pi$). **(b)** An asymmetry in the phaseshifts, $\Delta\varphi$, leads to a lateral shift of peak positions of the order of 10 Å at $E = -24$ meV and for $\Delta\varphi = \pi/2$ ($r = 0.5$). **(c)** Asymmetries in reflection amplitudes lead to asymmetries in oscillation amplitudes ($E = 180$ meV, $\varphi_\ell = \varphi_r = -\pi$).

5.3 Ag(111)

Differential conductance maps $dI/dV(E, x)$ for Fabry-Pérot resonators have been acquired perpendicular to the step directions, at low temperatures and under open feedback loop conditions as described on page 35 (Figs. 5.6 and 5.8). Therefore, they can directly be interpreted in terms of the surface LDOS. In the following the model LDOS ρ_{FP} from Eq. (5.3) is used to analyze such dI/dV maps quantitatively. Note, that since we have determined $m^* = 0.4 m_e$, $E_{\text{F}} = -65$ meV as well as $\rho_b = 0.56 L_0$ in independent measurements earlier (Section 3.2), the number of free parameters (apart from a proportionality factor between dI/dV and ρ_{FP}) reduces to four, namely, the step reflection properties φ_ℓ , φ_r , r_ℓ and r_r . Fig. 5.6(b) shows a measured dI/dV map of a 56 Å wide symmetric Ag(111) resonator. The quantum nature of the LDOS due to electron confinement is evident. The “ground state” ($n = 1$) is located at $E_1 = -30$ meV, the first “excited state” ($n = 2$) with one node at $E_2 = 60$ meV and the second “excited state” ($n = 3$) with two nodes at $E_3 = 220$ meV. Around 290 meV, there is a location

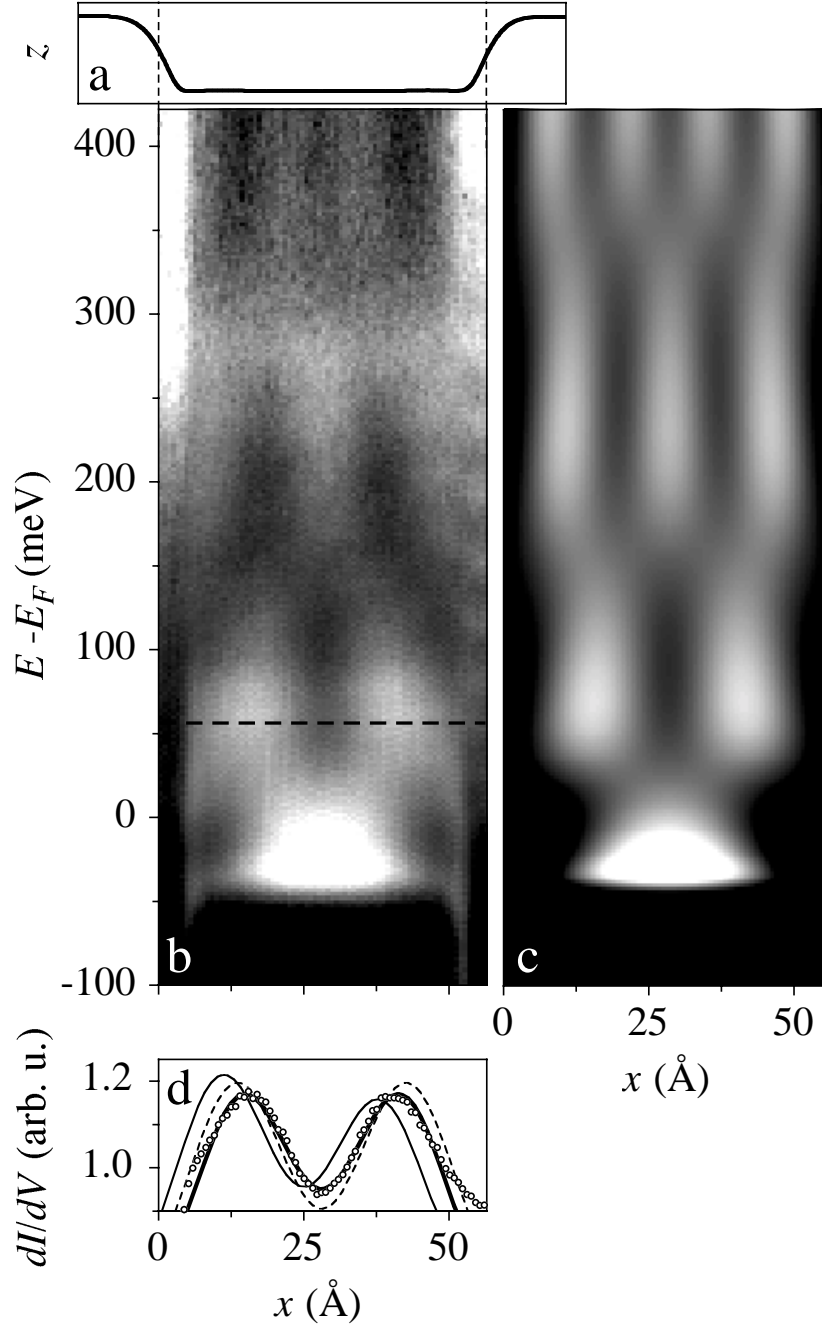


Figure 5.6: (a) Constant-current line scan over 56 Å wide symmetric Ag(111) resonator taken at $V_{\text{st}} = 303$ mV and $I = 2$ nA. The dashed lines indicate the electron mirrors, by definition located at the mid-height points of the constant-current line scan. (b) The corresponding differential conductance map clearly shows the confinement of the s - p surface-state electrons ($T = 4.9$ K, o.f., $\nu \approx 1$ kHz, $\Delta V = 20$ mV). (c) Model calculation of $\rho_{\text{FP}}(E, x)$ from Eq. (5.3) using the parameters: $a = 56$ Å, $\varphi_\ell = \varphi_r = -\pi$, $r_\ell = r_r = r_{\text{asc}}(E)$ of Fig. 5.9. (d) Constant energy cut through (b) at $E = 56.3$ meV (see dashed line) plotted as open circles. The thick line displays $\rho_{\text{FP}}(x)|_{E=56.3\text{ meV}}$ for $\varphi_\ell = \varphi_r = -\pi$. The sensitivity of the peak position to the choice of the phaseshifts is demonstrated by the thin full ($\varphi_\ell = -\frac{3}{4}\pi$, $\varphi_r = -\frac{5}{4}\pi$) and the dashed line ($\varphi_\ell = \varphi_r = -\frac{3}{4}\pi$). $r_\ell = r_r = 0.35$ for all three curves.

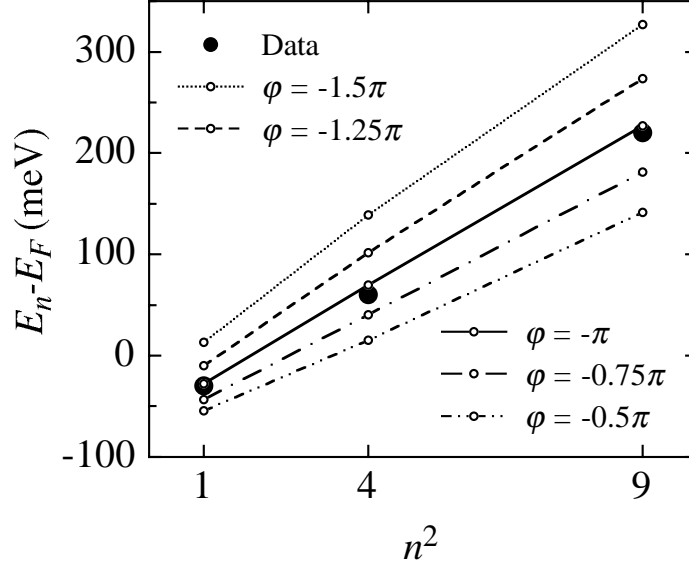


Figure 5.7: Measured peak positions E_n for the 56 Å wide symmetric Ag(111) resonator are compared to the maxima in the model ρ_{FP} from Eq. (5.3) ($r_\ell = r_r = 0.5$, Ag(111) parameters: $m^* = 0.4 m_e$, $E_{\text{T}} = -65$ meV). Clearly, a phaseshift of $\varphi = \varphi_\ell = \varphi_r = -\pi$ fits the data best.

independent enhancement of dI/dV due to an enhanced tip DOS at this energy.

First of all, by carefully inspecting the measured LDOS map for the symmetric resonator in Fig. 5.6(b) we observe no significant asymmetry in peak positions and amplitudes, leading to the conclusion that *A and B steps on Ag(111) reflect the s-p surface-state electrons on Ag(111) in the very same way*⁴, in contrast to previous results on Au(111) [78]. Thus, $\varphi_{\text{Aasc}} = \varphi_{\text{Basc}} =: \varphi_{\text{asc}}$ and $r_{\text{Aasc}} = r_{\text{Basc}} =: r_{\text{asc}}$ (see Fig. 5.1(c)). Please note that a phaseshift difference of $\pi/2$ between A and B steps, as claimed in Ref. [78], would lead to a 7 Å shift of the $n = 1$ maximum to either side of the 56 Å resonator (see Eq. (5.7)), which is clearly absent in Fig. 5.6(b).

Next, we analyze the positions of the maxima of $dI/dV(E)|_x$, E_n , for the 56 Å symmetric Ag(111) resonator. As discussed in Section 5.2, E_n are very sensitive to the absolute value of the phaseshift φ_{asc} . Since the reflection amplitude hardly influences the peak positions, φ_{asc} is the only essential parameter concerning E_n . From Fig. 5.7 we conclude $\varphi_{\text{asc}} = -\pi \pm 0.3$, independent of energy. A phaseshift of $-\pi$ is in perfect agreement with the lateral positions of the maxima in $dI/dV(x)|_E$ line cuts (see e.g. Fig. 5.6(d)). Now, the only remaining free parameter needed to fully describe the symmetric resonator is r_{asc} . Remember, the reflection amplitudes govern the amplitude of the oscillations in $\rho_{\text{FP}}(x)|_E$ (Fig. 5.5(a)). Thus, we determined r_{asc} by fitting constant energy line cuts $dI/dV(x)|_E$ with $\rho_{\text{FP}}(x)|_E$ from Eq. (5.3) for all energies, under use of

⁴As stated in Section 5.1 the symmetric resonator consists of an A and a B step (Fig. 5.1).

$\varphi_{\text{asc}} = -\pi$ and $\rho_b = 0.56 L_0$. The energy dependent reflection amplitudes for ascending steps, $r_{\text{asc}}(E)$, resulting from these fits are shown in Fig. 5.9(b) (open symbols) ⁵. In principle, since the reflection amplitudes are found to be energy dependent, the fit procedure should be repeated with a reflection amplitude $r'_{\text{asc}}(E) = r_{\text{asc}}(E) + \Delta r$, until self-consistency is reached, i.e. Δr converges to 0. It turns out that the Δr values found in a second fit sequence are less than 10 % of $r_{\text{asc}}(E)$, and thus we content ourselves with the $r_{\text{asc}}(E)$ values from the first fit sequence.

Now that all step reflection parameters of the symmetric resonator are determined, i.e. $\varphi_\ell = \varphi_r = \varphi_{\text{asc}} = -\pi$ and $r_\ell = r_r = r_{\text{asc}}(E)$, the model LDOS $\rho_{\text{FP}}(E, x)$ from Eq. (5.3) for these parameters can be plotted for comparison with the experimental data (Fig. 5.6(c)). The calculated map agrees well with the measured LDOS concerning peak positions, peak broadening and symmetric evolution of the maxima.

Our finding that ascending A and B steps have identical scattering properties with respect to *s-p* surface-state electrons strongly suggests that electron scattering will be identical for the two microfacets also at descending steps. Under this assumption, the asymmetric resonator can now be described with only two remaining free parameters within the Fabry-Pérot model, i.e. φ_{desc} , and r_{desc} . Fig. 5.8(b) displays the measured $dI/dV(E, x)$ for a 104 Å wide asymmetric resonator. In contrast to the symmetric resonator the maxima evolution is now clearly asymmetric. Maxima evolve from bottom right to top left, indicative for the different scattering behavior of descending and ascending steps.

The absence of an asymmetry in the lateral positions of the maxima for this asymmetric trough indicates that $\varphi_{\text{desc}} = \varphi_{\text{asc}}$. For comparison, a difference of $\Delta\varphi$ of $\pi/2$ in phaseshifts would imply a 13 Å shift of the $n = 1$ peak, which is clearly not observable in Fig. 5.8(b). Furthermore, analyzing E_n for 57 Å, 67 Å, 104 Å and 210 Å wide asymmetric resonators as in the symmetric case (Fig. 5.7, analysis not shown for asymmetric resonators) yields $\varphi_{\text{desc}} = -\pi \pm 0.4$. We are again left with only one parameter, and can extract $r_{\text{desc}}(E)$ from fitting $dI/dV(x)|_E$ for asymmetric resonators of different widths, just as in the case of the symmetric resonator. The result is depicted in Fig. 5.9(b).

$r_{\text{desc}}(E)$ is by about a factor of 1.5 - 2 larger than $r_{\text{asc}}(E)$, in accordance with oscillation amplitudes in constant-current line scans left and right from steps (Fig. 3.6). Furthermore, the reflection amplitudes from Fig. 5.9(b) agree well with the rough estimate

⁵Since the step electronic structure influences the spectra up to 5 Å off from its midpoints (see Fig. 5.6), only data outside this range were included into the fit. Furthermore, an influence of the measurement on the LDOS can be excluded since various stabilizing impedances showed identical differential conductance maps.

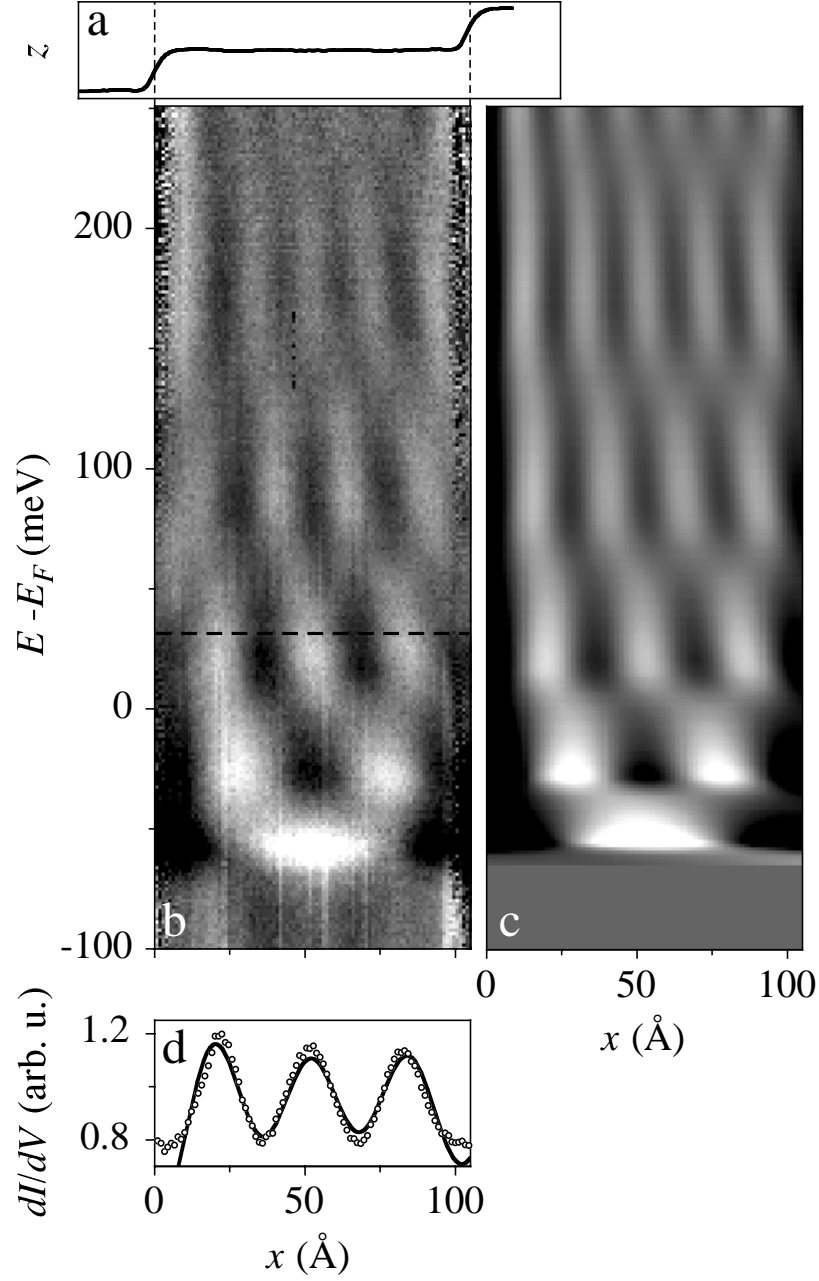


Figure 5.8: (a) Constant-current line scan over a 104 Å wide asymmetric resonator taken at $V_{st} = 115$ mV and $I = 1$ nA. The dashed lines indicate the location of the electron mirrors. (b) Corresponding differential conductance map ($T = 4.9$ K, o.f., $\nu = 1.2$ kHz, $\Delta V = 11$ mV). (c) Model $\rho_{FP}(E, x)$ from Eq. (5.3) with $a = 104$ Å, $\varphi_\ell = \varphi_r = -\pi$, $r_\ell = r_{desc}(E)$ and $r_r = r_{asc}(E)$ of Fig. 5.9 (Line-by-line constants have been subtracted horizontally to enhance contrast in (b) and (c)). (d) A constant energy cut of (b) at $E = 31.5$ meV (see dashed line) is plotted as open circles. The line depicts $\rho_{FP}(x)|_{E=31.5\text{meV}}$ for $\varphi_\ell = \varphi_r = -\pi$, $r_\ell = 0.70$ and $r_r = 0.37$.

of $r = 0.5$ necessary to explain the enhanced level width in dI/dV spectra (Section 5.2). The determined reflection amplitudes are, within the error margins, independent of the resonator width. This implies that inelastic scattering processes on the terrace, i.e. e - e and e - ph processes, can be neglected. In other words, the phase-relaxation length due to e - e and e - ph interaction is larger than the mean distance an electron travels in the resonators. Due to the reduced reflection at steps this mean distance is not much larger than the width of the resonator. Fig. 5.8(c) shows the model LDOS with reflection phaseshifts $-\pi$ and the amplitudes $r_{\text{desc}}(E)$ and $r_{\text{asc}}(E)$ from Fig. 5.9. There is excellent agreement between the measured conductance map and our simple Fabry-Pérot model. Note how well the asymmetric evolution of the peak amplitudes is explained by the different reflection amplitudes for ascending and descending steps. The amplitude asymmetry is clearly visible in the constant energy line cut in Fig. 5.8(d), reflecting the fact that $r_{\text{desc}} > r_{\text{asc}}$.

Our finding of a common phaseshift of $-\pi$ for the four different kinds of steps indicates a net repulsive interaction of s - p surface-state electrons with steps on Ag(111), in accordance with Refs. [76, 78, 81]. Together with the strongly reduced reflection amplitudes the phaseshifts of $-\pi$ imply *considerable absorption of surface-state electrons at steps*⁶. This is further supported by the fact that the measured LDOS outside the resonator cannot be distinguished from the LDOS of a single step edge and thus the resonator is decoupled from its surrounding through absorptive processes. We thus conclude that absorption at the step edge is the dominant process over transmission of the surface-state electrons to the neighboring terraces, in agreement with Refs. [127, 131]. The absorption process is most likely coupling to bulk states since the step allows for mixing of surface and bulk states [127, 131]. The difference between $r_{\text{desc}}(E)$ and $r_{\text{asc}}(E)$ is rationalized in geometric terms, i.e. the surface-state wave functions show a stronger overlap with bulk states at ascending steps, leading to a stronger coupling and hence absorption for this step type [82].

Fig. 5.9(a) clearly shows that the enhanced level widths compared to a quasi-infinite hard wall model (see dashed line) can only be rationalized by reduced reflection amplitudes. *We emphasize that reduced step reflection amplitudes are the dominant broadening mechanism above all other conceivable effects for energies not too close to the band edge $E_{\overline{\Gamma}}$.* For silver the peak broadening due to e - e and e - ph processes $\Gamma = \hbar(1/\tau_{e-e} + 1/\tau_{e-ph})$ is of the order of 10 meV for the energies of interest (Chapter 4) and comparable to experimental broadening $e\Delta V \approx 14$ meV due to the lock-in

⁶Neglecting absorption and modeling the step by a real δ -potential leads to the relation $r = 1/\sqrt{1 + \tan^2(\varphi + \pi)}$ [81], which is obviously not fulfilled in our case.

modulation (thermal broadening at 4.9 K can be completely neglected). Both effects cannot account for the measured level widths, which are of the order of 50 – 100 meV in all resonators (Figs. 5.6(b), 5.8(b) and 5.9(a)), at least for $E > E_F$. The situation is a little different for energies close to the band edge $E_{\overline{\Gamma}}$, where the reflection amplitudes approach unity (Fig. 5.9(b), [45, 127]), implying very small level width. Thus, for energies close to the band edge, i.e. $E < E_F$ on Ag(111), experimental and inelastic level width can become comparable to the measured peak width. Since we did not account for experimental and inelastic broadening in our model, the measured spectrum shown in Fig. 5.9(a) is broader than the model LDOS for energies below -20 meV. For the same reason, the experimentally determined reflection amplitudes $r_{\text{desc}}(E)$ and $r_{\text{asc}}(E)$ have to be considered as lower limits in the energy range $E_{\overline{\Gamma}} < E < E_F$. The last possible broadening effect we are aware of is the *finite* tip width. But a finite tip width as reason for reduced oscillation amplitudes in $dI/dV(x)|_E$, and thus reduced r , can be discarded, since different tips have yielded the same results and typical intermaxima distances of $\rho_{\text{FP}}(x)|_E$ are large compared to typical tip radii.

The coupling of surface-state electrons to the underlying bulk states is the most important process in causing imperfection of electron confinement. Former 1D Kronig-Penney models, employed for vicinal surfaces, disregarded this coupling as well as the difference between ascending and descending steps yielding unrealistic scattering phases [81, 86]. The coupling to bulk states was treated for scattering centers on Cu(111) [45, 127], with the result of monotonically decreasing reflection amplitudes with increasing energy for different kinds of scatterers. The data reproduced in Fig. 5.9(b) are an experimental confirmation of this prediction. The idea put forward by Heller *et al.* [131] to reduce scattering into bulk states, and thus enhance the reflection properties of step edges by using thin-film substrates, was doubted by Hörmandinger [45]. However, recent experiments for thin silver films on Si(111) are encouraging [145]. They clearly show the presence of standing wave patterns on these thin films. Since there are no bulk states in the Si substrate to couple to, absorption at scattering centers on these surfaces is expected to be very small.

A remark about the effect of reduced reflection amplitudes on the lifetimes of surface-state electrons is appropriate at this place. If reflection amplitudes are reduced due to finite coherent transmission of surface-state electrons to adjacent terraces, then, of course, the lifetime is not reduced. However, if the amplitudes are reduced because of absorptive processes at the steps, lifetimes of the electrons are affected and can be considerably shortened in the case of strong absorption.

Concluding this Section, we have measured the LDOS in quantum resonators for

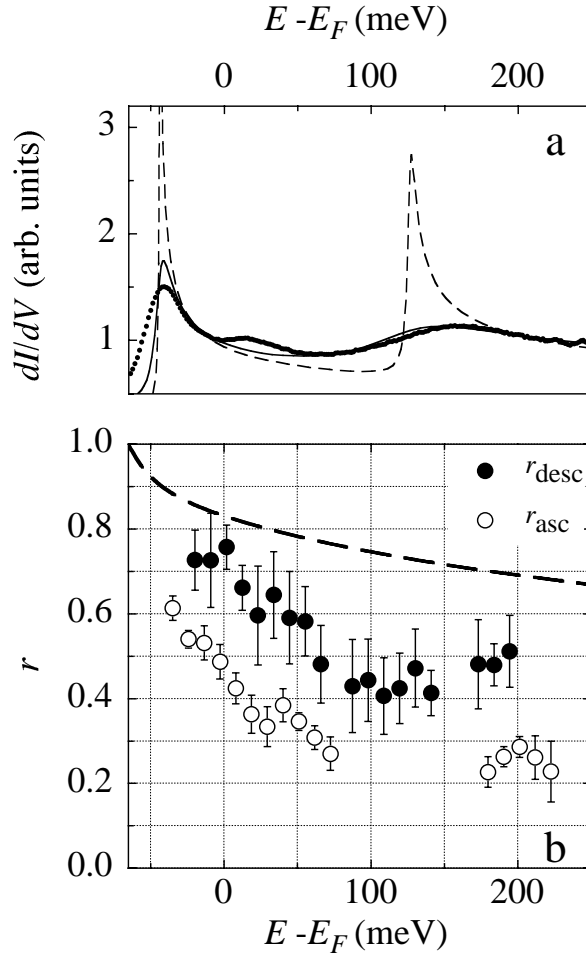


Figure 5.9: **(a)** Measured dI/dV spectrum in the center of a 67 Å wide asymmetric Ag(111) resonator (dots) showing peak broadening due to the reduced reflectivity of the boundaries ($T = 4.9$ K, o.f., $\nu = 1.2$ kHz, $\Delta V = 14$ mV). The shoulder around 25 meV is due to the finite tip width which thus collects signal from the $n = 2$ maxima even in the center. The full line displays the LDOS $\rho_{\text{FP}}(E)|_{x=a/2}$ from Eq. (5.3) with $\varphi_{\text{desc}} = \varphi_{\text{asc}} = -\pi$ and $r_{\text{desc}}(E)$ and $r_{\text{asc}}(E)$ given by the measured values represented in (b). The dashed line shows for comparison the quasi-ideal resonator ($r = 0.95$). **(b)** Energy dependent reflection amplitudes for descending and ascending step edges on Ag(111) determined as described in the text. For qualitative comparison the calculated reflection amplitude of two missing rows on Cu(111) is shown as a dashed line [45]. (The curve was shifted by 375 meV to adjust the surface-state band edges.)

s - p surface-state electrons realized by two parallel steps on a Ag(111) surface. The analogy to wave optics was employed to model the LDOS pattern in terms of the scattering properties of the resonator boundaries. *The electron reflectivity is found to be independent of the crystallographic step structure (A, B) but depends on the step morphology (ascending, descending).* With our method, $r(E)$ and φ can be quantified for any two parallel steps, enabling studies of electron scattering at modified (decorated) steps

and providing insight into the scattering mechanism. *In analogy to optics the quantum resonators could be employed as a sensitive tool to probe the electron interaction with magnetic and nonmagnetic atoms and nanostructures introduced into them.* Changes in the LDOS due to the presence of such “nano-samples” could be detected by comparing the measured LDOS with the well-characterized model LDOS for an empty resonator, and related to the interaction mechanism.

5.4 Au(111)

With the help of the $dI/dV(E, x)$ map in Fig. 3.10 we discuss the scattering properties of Au(111) step edges qualitatively in the following. As described on page 39 this map was taken over a line scan of Fig. 3.9 and thus contains in its left half the LDOS of the roughly 80 Å wide asymmetric resonator formed by the (not perfectly straight) descending and ascending steps. The resonator is labeled “Confinement” in Fig. 3.10. First of all, we remark an asymmetric evolution of the peaks in the LDOS of the resonator, as in the case of asymmetric resonators on Ag(111). The peaks evolve from bottom right to top left, and by comparing this with Fig. 5.8 we conclude that $r_{\text{asc}} < r_{\text{desc}}$ for Au(111) as well. Secondly, the $n = 1$ peak of the resonator LDOS in Fig. 3.10 is not shifted to either side of the resonator, implying that $\varphi_{\text{asc}} = \varphi_{\text{desc}}$. Furthermore, the broadening of the peaks seems to be even stronger than for resonators on Ag(111) (compare to Fig. 5.8) leading to the conclusion that step reflection amplitudes for Au(111) steps are at least as small as those for Ag(111) steps. Altogether, step scattering of s - p derived surface-state electrons on Au(111) is qualitatively the same as on Ag(111).

Chapter 6

Potential Mapping

6.1 Introduction

In 1998 the Nobel Prize in Chemistry was awarded to Walter Kohn for his development of density functional theory (DFT). DFT has for a long time been extensively used to determine the electronic structure of solids and is today also becoming a very important basis for theoretical studies of molecular systems. At the heart of DFT is the Hohenberg–Kohn theorem [146], which states that *the external (one-electron) potential $U(\mathbf{x})$ is determined, within a trivial additive constant, by the ground state electron density $n(\mathbf{x})$* . In other words, the Hamiltonian of the electronic system, and therefore all electronic properties, are completely determined by the ground state electron density. Unfortunately, there exists no exact recipe linking the potential with the electron density, and consequently approximations have been developed, e.g. Thomas–Fermi approximation or Lindhard theory [98].

If one was able to measure $n(\mathbf{x})$ one would in principle have the whole information about the electronic properties of the particular system. A method that offers an access to the electronic structure with high spatial resolution is STM. But STM is restricted to the surface and consequently will yield the 2D surface electron density at the most, and it is not possible to obtain the 3D $n(\mathbf{x})$ necessary to characterize bulk electrons. However, electronic surface states are quasi two-dimensional and their 2D electron density $n(\mathbf{x})$ is accessible to STM. Following the Hohenberg–Kohn theorem the two-dimensional potential landscape $U(\mathbf{x})$ such surface-state electrons are moving in can in principle be inferred from $n(\mathbf{x})$ measured with STM.

In this Chapter we use linear response theory to relate the measured 2D surface-state density to the potential $U(\mathbf{x})$. The theoretical background is outlined in Section 6.2. In Section 6.3 we apply the formalism to the *s-p* surface-state electrons on the reconstructed

Au(111) surface. Potential maps on Au(111) show that the reconstruction induces a complicated shallow superlattice: surface-state electrons are more strongly bound in hcp regions than in fcc regions and most strongly bound in the transition regions between fcc and hcp, where the surface atoms occupy bridge sites. Our results are in excellent agreement with the work by Chen *et al.*, and the Au(111) potential we find is a refinement of the extended Kronig–Penney potential used in Ref. [79].

6.2 Linear Response Theory

Any potential $U^{\text{tot}}(\mathbf{x})$ acting on an otherwise free electron gas of density n_0 will induce rearrangements in the electron density, i.e. the density in presence of $U^{\text{tot}}(\mathbf{x})$ reads $n(\mathbf{x}) = n_0 + n^{\text{ind}}(\mathbf{x})$ ¹.

If the potential $U^{\text{tot}}(\mathbf{x})$ varies slowly on the scale of the Fermi wavelength of the electron gas, Thomas–Fermi approximation can be used [98], i.e.

$$n_{\text{TF}}^{\text{ind}}(\mathbf{x}) = -\rho(E_F)U^{\text{tot}}(\mathbf{x}), \quad (6.1)$$

where $\rho(E_F)$ is the density of states of the electron gas at the Fermi level. However, in our experiments the assumption of Thomas–Fermi theory is not necessarily fulfilled as we will see below, and we have to go beyond Thomas–Fermi. A widely used approximation is linear response theory, where changes in the response function, e.g. n^{ind} , are calculated to within linear order of the perturbation, e.g. U^{tot} [98]:

$$n^{\text{ind}}(\mathbf{q}) = \chi(\mathbf{q}) U^{\text{tot}}(\mathbf{q}). \quad (6.2)$$

Here $\chi(\mathbf{q})$ is the susceptibility, and $n^{\text{ind}}(\mathbf{q})$ and $U^{\text{tot}}(\mathbf{q})$ are the Fourier transforms of $n^{\text{ind}}(\mathbf{x})$ and $U^{\text{tot}}(\mathbf{x})$, respectively. Solving the Schrödinger equation for electrons subjected to a potential U^{tot} in linear order perturbation theory leads to the Lindhard expression for the susceptibility, the so-called Lindhard function χ_L [147, 148]:

$$\chi_L(\mathbf{q}) = \frac{1}{\Omega} \lim_{\alpha \rightarrow 0} \sum_{\mathbf{k}, \sigma} \frac{f(E_{\mathbf{k}}) - f(E_{\mathbf{k}+\mathbf{q}})}{E_{\mathbf{k}} - E_{\mathbf{k}+\mathbf{q}} + i\hbar\alpha}. \quad (6.3)$$

The summation is taken over all one-electron states (σ characterizes the spin state), where $E_{\mathbf{k}}$ is their energy and f the Fermi–Dirac occupation probability, as usual. Ω is the sample volume (i.e. surface area in 2D). Since we are interested in 2D (surface-state) electrons, we restrict the discussion to two dimensions in the following. In 2D the

¹We only consider static potentials here.

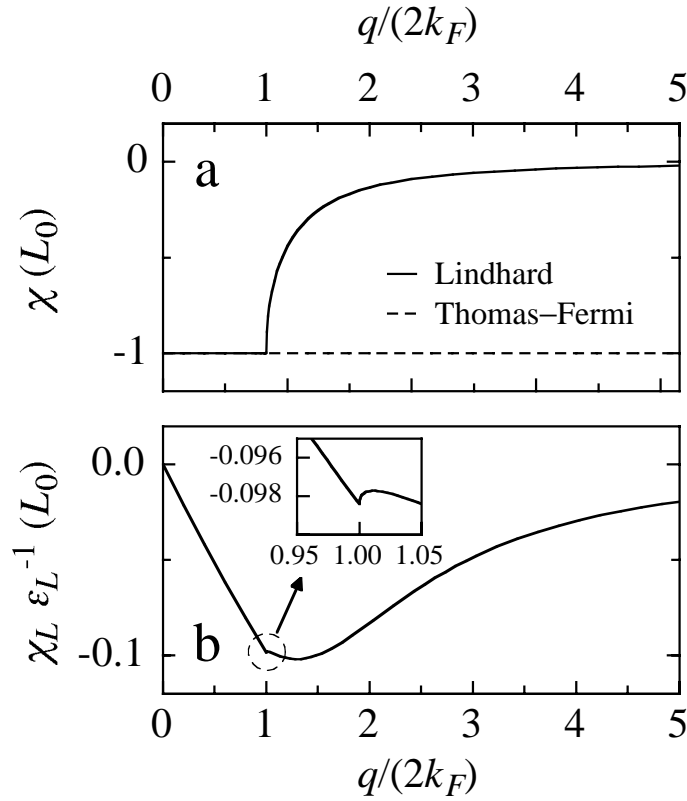


Figure 6.1: (a) 2D Lindhard function (full line) and Thomas-Fermi susceptibility (dashed). (b) 2D Lindhard function divided by the 2D Lindhard dielectric function for $\epsilon_b = 1$ and Ag(111) parameters: $m^* = 0.4 m_e$, $k_F = 0.083 \text{ \AA}^{-1}$.

Lindhard function is given by [99]

$$\chi_L(\mathbf{q}) = \begin{cases} -L_0 & \text{for } q \leq 2k_F \\ -L_0 \left(1 - \sqrt{1 - \frac{4k_F^2}{q^2}} \right) & \text{for } q > 2k_F, \end{cases} \quad (6.4)$$

where $q = |\mathbf{q}|$ and L_0 is the DOS of the free 2D electron gas, $L_0 = m^*/\pi\hbar^2$. As seen in Fig. 6.1(a) the 2D Lindhard function is non-analytic at $q = 2k_F$. This non-analyticity leads to the well known Friedel oscillations with wave vector $2k_F$ in the total electron density [93].

The susceptibility χ relates the induced density n^{ind} with the *total* potential U^{tot} . Since electrons are charged particles the total potential is the sum of the external potential U and the induced potential U^{ind} which is due to the redistribution of charge $-e n^{\text{ind}}(\mathbf{x})$, i.e.

$$U^{\text{tot}}(\mathbf{q}) = U(\mathbf{q}) + U^{\text{ind}}(\mathbf{q}). \quad (6.5)$$

Using the Poisson equation it is straightforward to show that in 2D [99]

$$U^{\text{ind}}(\mathbf{q}) = \frac{1}{2} \frac{e^2}{\epsilon_b \epsilon_0 q} n^{\text{ind}}(\mathbf{q}), \quad (6.6)$$

where ϵ_b is the dielectric constant of the medium surrounding the electron plane. The linear response dielectric function, relating external potential with total potential

$$U(\mathbf{q}) = \epsilon(\mathbf{q}) U^{\text{tot}}(\mathbf{q}), \quad (6.7)$$

is thus in 2D given by (Eqs. (6.2), (6.5) and (6.6))

$$\epsilon(\mathbf{q}) = 1 - \frac{1}{2} \frac{e^2}{\epsilon_b \epsilon_0 q} \chi(\mathbf{q}). \quad (6.8)$$

Introducing the Lindhard expression from Eq. (6.4) into Eq. (6.8) yields the widely used Lindhard dielectric function.

The quantity we are interested in is the *external potential* U acting on the 2D electrons. It is related to the electron density through (Eqs. (6.2) and (6.7))

$$n^{\text{ind}}(\mathbf{q}) = \frac{\chi(\mathbf{q})}{\epsilon(\mathbf{q})} U(\mathbf{q}). \quad (6.9)$$

$\chi(\mathbf{q})/\epsilon(\mathbf{q})$ in the Lindhard approximation is plotted in Fig. 6.1(b) for the case of a non-polarizable surrounding medium, i.e. $\epsilon_b = 1$. Compare this to the situation where the surrounding medium is highly polarizable ($\epsilon_b \rightarrow \infty$), e.g. a 3D electron gas with a very large Fermi wave vector, where $\epsilon(\mathbf{q}) = 1$ and thus $\chi(\mathbf{q})/\epsilon(\mathbf{q}) = \chi(\mathbf{q})$ as shown in Fig. 6.1(a).

By way of illustration we show in Fig. 6.2 the density in a 2D electron gas that results from an external repulsive square potential of width $a = 5 \text{ \AA}$ in Lindhard theory². The external potential (Fig. 6.2(a)) is Fourier transformed and then multiplied with $\chi_L(\mathbf{q})/\epsilon_L(\mathbf{q})$ to yield the Fourier transform of the electron density (Eq. (6.9)) shown in (b). The resulting electron density depends crucially on the polarizability of the surrounding medium. If this medium is highly polarizable, $\epsilon_b \rightarrow \infty$, the density shows pronounced Friedel oscillations [93] of the form $-x^{-1} J_1(2k_F x)$ around the mean value n_0 (dashed line). Since a highly polarizable surrounding medium screens the Coulomb field of the 2D electrons, they effectively can be treated as uncharged particles, i.e. $e \rightarrow 0$ in Eq. (6.8), and it is thus no surprise that the electron density for $\epsilon_b \rightarrow \infty$ shows the same behavior as the density calculated for a *non-interacting* 2D electron gas in the presence of a step edge in Section 3.2 (see e.g. Eq. (3.12)). Note that for $\epsilon_b \rightarrow \infty$ there is *no screening* due to the fact that the 2D electrons are “effectively uncharged” (Fig. 6.2(c)). If, on the other hand, the surrounding medium is not polarizable ($\epsilon_b = 1$), e.g. vacuum, the 2D electrons screen the surplus positive charge in the repulsive potential region through a net accumulation of negative charge carriers right outside this region (Fig. 6.2(b) full

² $U(x, y) = U_0[\Theta(x + \frac{a}{2}) - \Theta(x - \frac{a}{2})]$, where U_0 is the height and a the width of the potential.

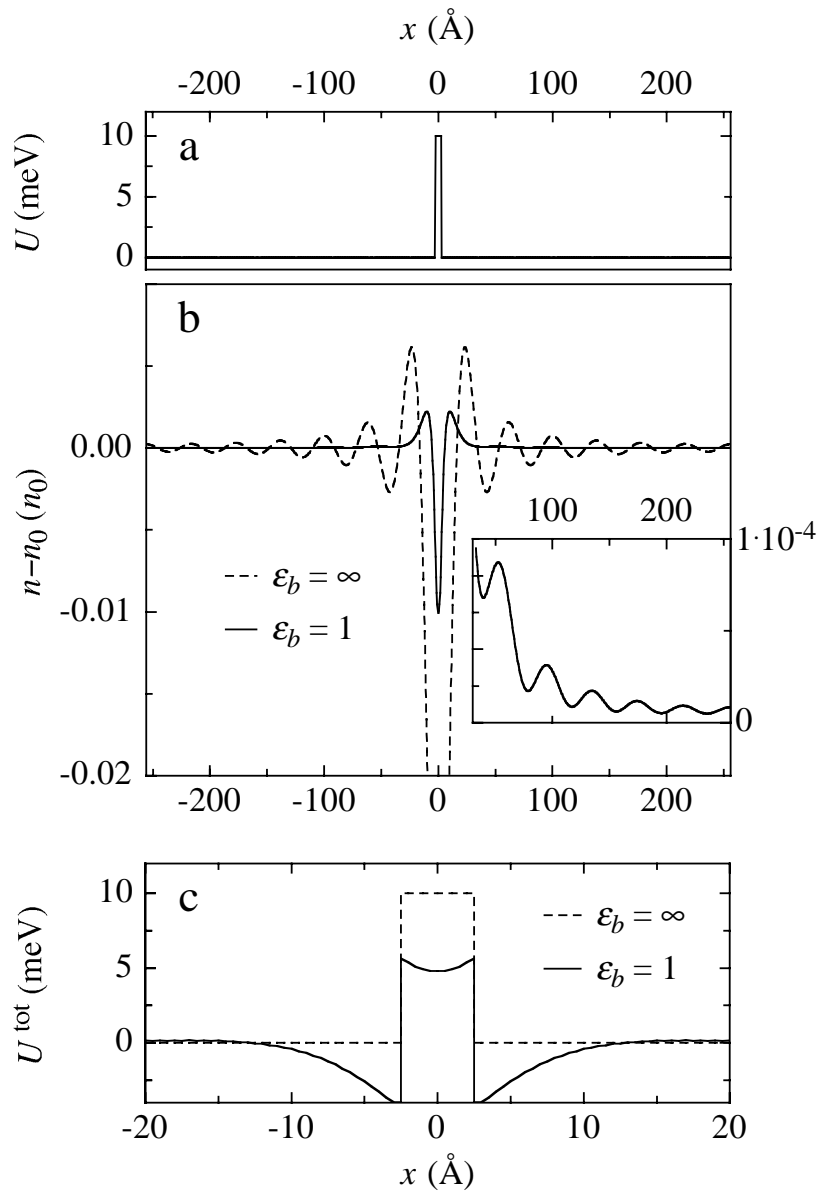


Figure 6.2: Using Eq. (6.9) and the 2D Lindhard function and dielectric function the density in a 2D electron gas is calculated for an (a) external $U_0 = 10$ meV high and $a = 5$ \AA wide square potential and plotted in (b) (Ag(111) parameters: $m^* = 0.4 m_e$, $k_F = 0.083$ \AA^{-1}). The full and dashed lines depict the density which results when the surrounding medium is not ($\epsilon_b = 1$) and highly polarizable ($\epsilon_b \rightarrow \infty$), respectively. The inset shows an enlargement for $\epsilon_b = 1$. (c) U^{tot} for the external potential from (a) calculated with Eq. (6.7) using the Lindhard dielectric function. (Note the different x range.) If $\epsilon_b \rightarrow \infty$ the external potential is not screened at all by the 2D electron gas.

line). Due to screening Friedel oscillations are much less pronounced in this case, as seen in the inset of Fig. 6.2(b). The total potential $U_{\epsilon_b=1}^{\text{tot}}$ is reduced with respect to the external potential in the region $-a/2 < x < a/2$ due to the surplus of positive charge (Fig. 6.2(c)). Outside this region the effective positive charge leads to an attractive total

potential which is exponentially screened [99]³.

Comparing the electron densities of Fig. 6.2(b) with the electron densities of *s-p* derived noble-metal surface states around scattering centers measured with STM (Chapter 3, Refs. [46,76,78]), which show pronounced Friedel oscillations much as the dashed curve in Fig. 6.2(b), leads to the conclusion, that these *surface-state electrons are surrounded by a highly polarizable medium*. The latter is of course nothing else than the bulk electron gas, which screens the Coulomb field of the surface-state electrons very efficiently (see also Chapters 3 and 4).

6.3 Reconstruction Induced Potential on Au(111)

In this Section direct potential mapping using the Lindhard approximation is illustrated by the *s-p* derived surface state on the reconstructed Au(111) surface. This surface state has its band edge at $E_{\overline{\Gamma}} = -510$ meV and an effective mass of $m^* = 0.27 m_e$ (Table 3.1). It has been outlined in Section 3.2 that the $22 \times \sqrt{3}$ “herringbone” reconstruction on Au(111) [102] induces a periodic potential acting on the surface-state electrons, and this system is particularly suited for our potential mapping since the potential modulations are *weak*. Furthermore, the Fermi wave vectors k_F of *s-p* derived noble-metal surface states are small and thus density modulations, taking place on length scales of the order of π/k_F , i.e. some 10 Å, can easily be resolved with STM.

The topography of the Au(111) surface in Fig. 6.3 clearly shows the “herringbone” reconstruction⁴. As it will be useful for the discussion of potential maps later on, we first of all discuss the differential conductance map $dI/dV(E, x)$ in Fig. 6.4, acquired as described on page 35. It shows the influence of the reconstruction on the electronic structure of the surface. The onset of the *s-p* derived surface state around $E_{\overline{\Gamma}} = -510$ meV is clearly visible. The tip used to perform the dI/dV map had a very structured DOS leading to the location independent horizontal stripes in Fig. 6.4. The striking features of the surface-state LDOS are the enhancement around -470 meV in the hcp regions and the broad maxima centered at -380 meV and situated close to the ridges of the reconstruction. They are due to the reconstruction induced potential acting on the surface-state electrons. As becomes clear from Fig. 6.4 the LDOS of the sample is almost independent of the lateral variable x for energies above -200 meV. Therefore we can directly conclude that the reconstruction induced potential variations

³See also e.g. Thomas–Fermi theory of screening in Ref. [98].

⁴When the Au(111) stayed at 4.9 K for several days, unknown adsorbates have been observed at the elbows, showing up as white spots in Fig. 6.3.

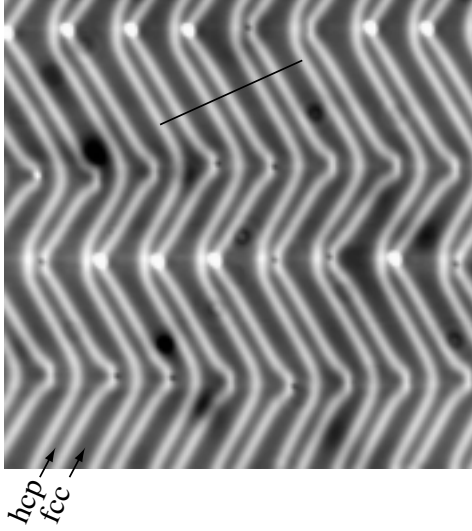


Figure 6.3: 588 Å×588 Å constant-current image of the reconstructed Au(111) surface ($V = -0.35$ V, $I = 2.2$ nA, $T = 4.9$ K). The hcp regions are with 25 Å considerably narrower and image roughly 0.05 Å higher than the 38 Å wide fcc regions. The ridges are formed by atoms occupying bridge sites and have a corrugation of about 0.2 Å independent of imaging conditions.

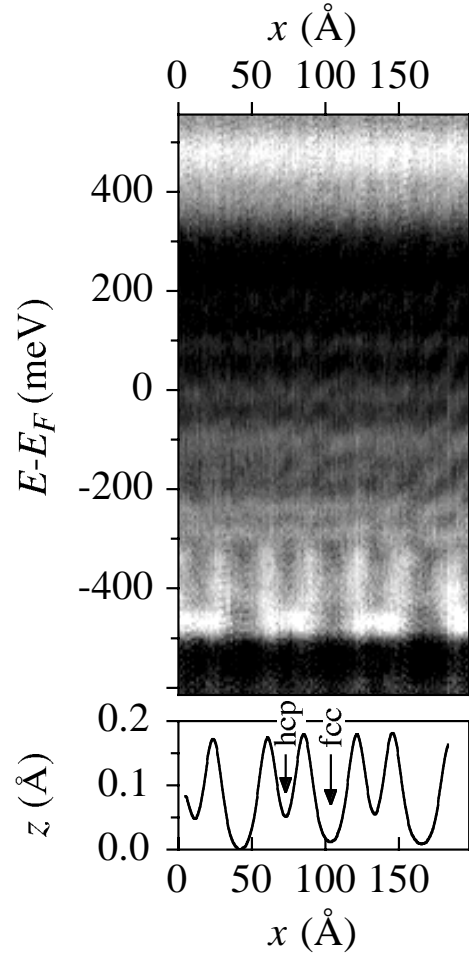


Figure 6.4: Differential conductance map dI/dV taken perpendicular to the reconstruction along the line depicted in Fig. 6.3 ($\Delta V = 20$ mV, $\nu = 1.4$ kHz, o.f., $V_{\text{st}} = 1$ V, $I = 2.1$ nA, $T = 4.9$ K). The stabilization constant-current line scan is shown in the lower graph.

are much smaller than $(-200 \text{ meV} - E_{\text{F}}) \approx 300 \text{ meV}$. Note also that the bulk LDOS ρ_b is almost not influenced by the reconstruction as seen in Fig. 6.4 for energies below the surface-state onset, i.e. $E < -510 \text{ meV}$. This is due to the fact that the wavelength of bulk electrons with energies close to the Fermi level is with typically 5 Å much shorter than the distance over which the potential varies. With regard to the bulk LDOS close to the Fermi level the weak potential modulations therefore lead to a mere shift of the bulk band edge (Thomas–Fermi theory), and since ρ_b is very flat at the Fermi energy, the weak reconstruction potential hardly influences the bulk LDOS at E_F ⁵.

In the following we outline how the total electron density of surface-state electron

⁵For the same reason the constant-current tip-sample distance taken at $V_{\text{st}} = 1$ V is at the most very weakly influenced by the potential associated with the reconstruction.

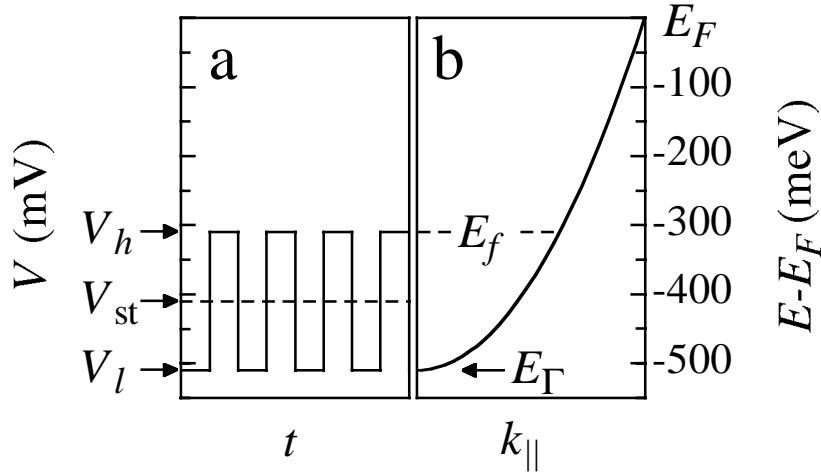


Figure 6.5: (a) Bias signal used for potential mapping (full line). Since the bias modulation frequency is chosen far above the bandwidth of the feedback loop, the tip height is effectively stabilized through the time-averaged current $\bar{I} = \frac{1}{2}(I(V_l) + I(V_h))$. (b) Sketch of the dispersion relation of the Au(111) s - p surface state. If $eV_l = E_T$ the lock-in signal yields the total density of surface-state electrons with $E_T < E < E_f = eV_h \leq E_F$ (see text).

gases, and in particular of the s - p surface state on reconstructed Au(111), can be measured using STM. Similar to dI/dV imaging we acquire the density image $\Sigma(\mathbf{x}, \Delta V_{\square})$ by lock-in technique under closed feedback loop conditions, but here we use a *rectangular* bias modulation around the mean value V_{st} of peak-to-peak amplitude ΔV_{\square} , i.e. the bias switches between $V_h = V_{st} + \frac{\Delta V_{\square}}{2}$ and $V_l = V_{st} - \frac{\Delta V_{\square}}{2}$ (Fig. 6.5(a)). Since the bias modulation frequency ν is chosen far above the bandwidth of the feedback loop, the tip is effectively stabilized through the time-averaged current value, i.e. $\bar{I} = \frac{1}{2}(I(V_l) + I(V_h))$, and the constant-current tip-sample distance $s(\mathbf{x})|_{\bar{I}}$ is not influenced by the bias modulation. For a rectangular bias modulation the lock-in output is proportional to the difference between the high and the low bias values of the current ⁶, i.e.

$$\Sigma(\mathbf{x}, \Delta V_{\square}) \propto I(V_h, \mathbf{x}) - I(V_l, \mathbf{x}). \quad (6.10)$$

At low temperatures, for the low bias values of interest here ($-510 \text{ meV} \leq E_T < eV < E_F$) Eq. (2.6) can be used, and assuming a constant tip DOS yields

$$\Sigma(\mathbf{x}, \Delta V_{\square}) \propto e^{-2s(\mathbf{x})|_{\bar{I}} \sqrt{\frac{m_F}{\hbar^2}} \sqrt{2W}} \int_{eV_l}^{eV_h} dE \rho_s(E, \mathbf{x}). \quad (6.11)$$

If the influence of electronic effects on the tip-sample distance can be disregarded, i.e.

⁶ $eV_h < E_F$ in our measurements.

$s(\mathbf{x})|_{\bar{f}} = s$ independent of \mathbf{x} , then

$$\Sigma(\mathbf{x}, \Delta V_{\square}) \propto \int_{eV_l}^{eV_h} dE (\rho_b + \rho_{2D}(E, \mathbf{x})) \quad (6.12)$$

where the surface LDOS $\rho_s(E, \mathbf{x})$ from Eq. (6.11) has been split into the constant bulk (background) LDOS ρ_b ⁷ and the contribution from the surface state, $\rho_{2D}(E, \mathbf{x})$. In our measurements we choose the lower bias value so that eV_l lies just below $E_{\bar{f}}$ and therefore

$$\Sigma(\mathbf{x}, \Delta V_{\square}) \propto \int_{eV_l}^{eV_h} dE (\rho_b + \rho_{2D}(E, \mathbf{x})) = e\Delta V_{\square} \rho_b + n_{2D}(E_f, \mathbf{x}). \quad (6.13)$$

$\Sigma(\mathbf{x}, \Delta V_{\square})$ is directly related to the total electron density $n_{2D}(E_f, \mathbf{x})$ of surface-state electrons with energy $E_{\bar{f}} < E < eV_h$, i.e the total density of the electron gas with a “fictitious Fermi level” $E_f = eV_h$ (see Fig. 6.5). Note that $\int_{eV_l}^{eV_h} dE \rho_{2D}(E, \mathbf{x})$ can be interpreted in terms of the electron density $n_{2D}(E_f, \mathbf{x})$ only because e - e interaction in the surface-state electron gas is screened efficiently by the bulk electrons (see Section 6.2). If many-body effects were relevant in the 2D gas, the presence of electrons in occupied states with energies in the interval $[eV_h, E_F]$ would alter the electronic states with $E < eV_h$ and thus $\int_{eV_l}^{eV_h} dE \rho_{2D}(E, \mathbf{x})$ could not directly be related to $n_{2D}(E_f, \mathbf{x})$, except for $E_f = E_F$. In the case of Au(111) we normally measured with $E_f < E_F - 300$ meV for the following reasons: if a narrow energy interval $[E_{\bar{f}}, E_f]$ is used, the assumption of a constant transmission factor is justified (Eq. (4.7)) and it is also easier to fulfill the requirement of a constant tip DOS (see below).

The quantity of interest, $n_{2D}(E_f, \mathbf{x})$, can directly be inferred from the measured $\Sigma(\mathbf{x}, \Delta V_{\square})$ (Eq. (6.13)):

$$n_{2D}(E_f, \mathbf{x}) = n_0 \left(\frac{\Sigma(\mathbf{x}, \Delta V_{\square})}{\bar{\Sigma}(\Delta V_{\square})} \left(1 + \frac{\rho_b}{L_0}\right) - \frac{\rho_b}{L_0} \right), \quad (6.14)$$

where $n_0 = L_0 (E_f - E_{\bar{f}}) = L_0 (eV_h - E_{\bar{f}})$ is the total density of the free electron gas in absence of any external potential and $\bar{\Sigma}(\Delta V_{\square})$ is the spatial average of the lock-in signal $\Sigma(\mathbf{x}, \Delta V_{\square})$.

Figure 6.6(b) shows the total density $n_{2D}(-320 \text{ meV}, \mathbf{x})$ for the reconstructed Au(111) surface. Note that in this case, with $V_{st} = -420$ mV and $\Delta V_{\square} = 200$ mV, $eV_l = -520$ meV lies just below the surface-state onset at $E_{\bar{f}} = -510$ meV. The total density in Fig. 6.6(b) has been obtained from the lock-in signal $\Sigma(\mathbf{x}, 200 \text{ mV})$ using Eq. (6.14)

⁷We outlined in the preceding paragraph why ρ_b can be considered constant for the system of interest.

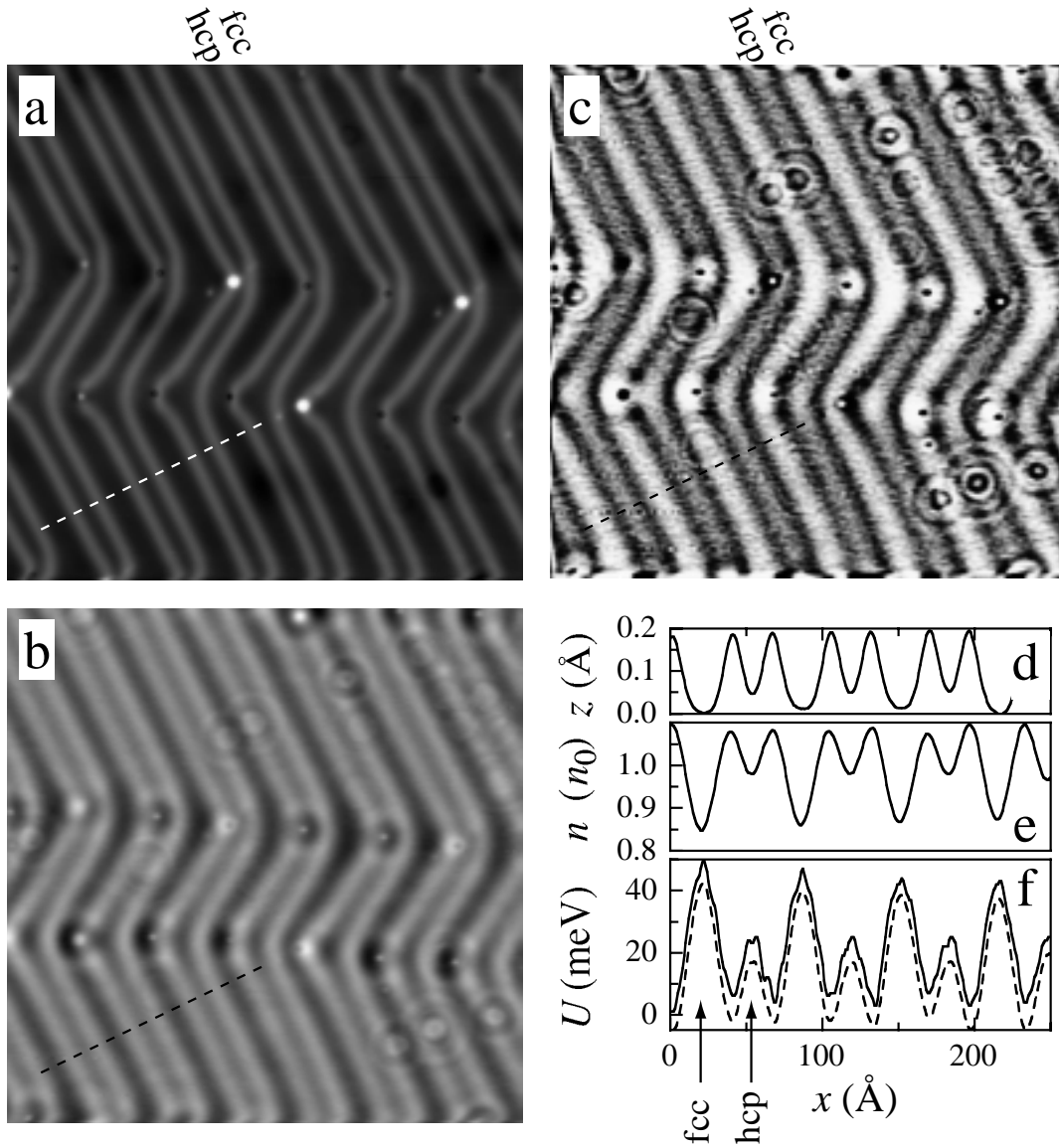


Figure 6.6: (a) $512 \text{ Å} \times 512 \text{ Å}$ constant-current image of the reconstructed Au(111) surface taken with $V_{\text{st}} = -420 \text{ mV}$ and $I = 0.87 \text{ nA}$ ($T = 4.9 \text{ K}$). The feedback bandwidth was set to 1 kHz . (b) Density map acquired simultaneously with (a) using lock-in technique under closed feedback loop conditions with a rectangular bias modulation of $\nu = 2.43 \text{ kHz}$ and $\Delta V_{\square} = 200 \text{ mV}$, i.e. $eV_l = -520 \text{ meV}$ and $eV_h = -320 \text{ meV}$ (see text for details). (c) External potential map obtained by applying the Lindhard procedure (see text) to the density of (b) ($k_f = 0.12 \text{ Å}^{-1}$). Dark levels correspond to more attractive potential regions. The reconstruction induced potential modulation can be clearly seen. (d)-(f) Data averaged over some linescans parallel to the dashed lines in (a)-(c), respectively. The dashed line in (f) shows the potential resulting from Thomas-Fermi theory applied to the total density in (e) (Eq. (6.1)).

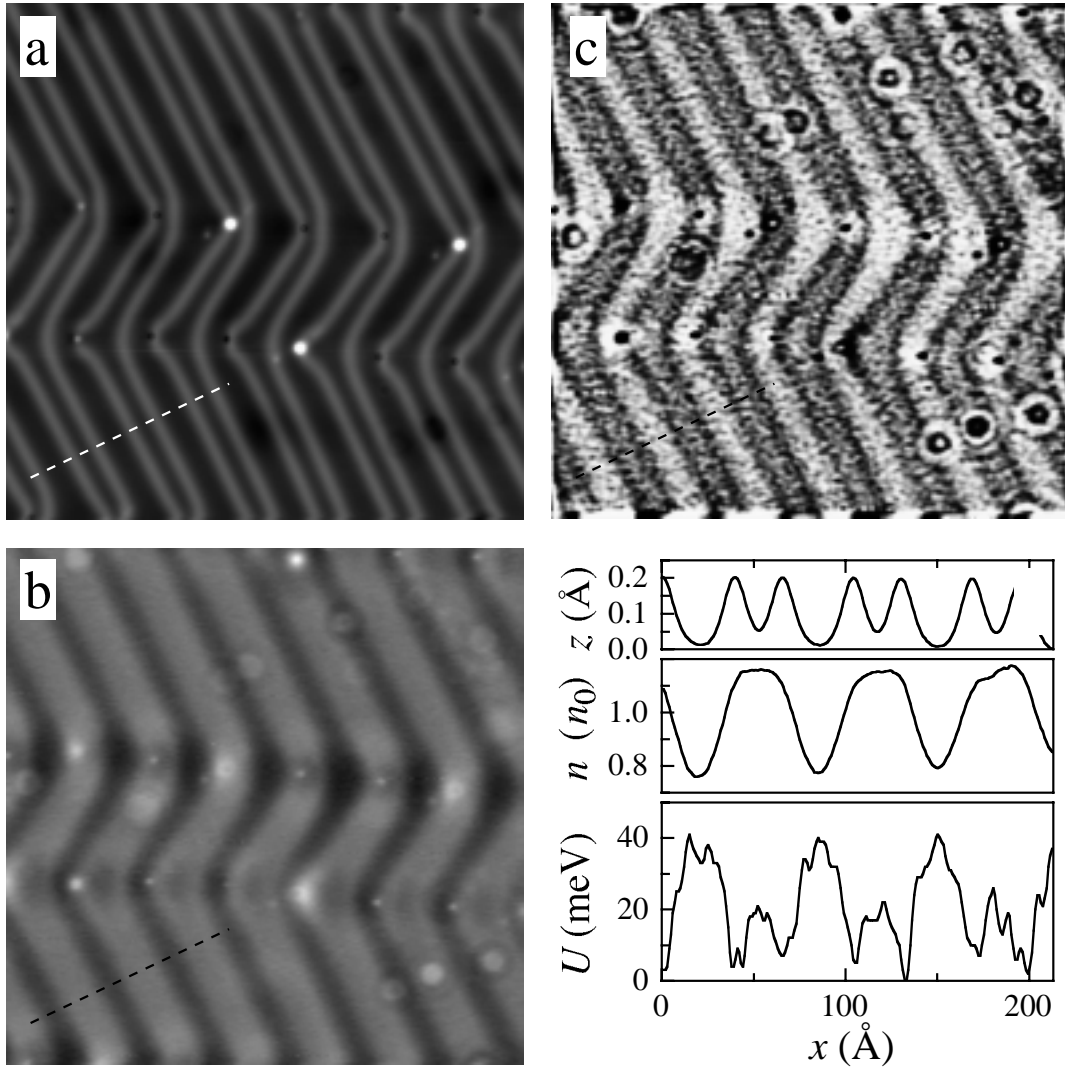


Figure 6.7: (a) 512 Å × 512 Å constant-current image of the reconstructed Au(111) surface taken with $V_{\text{st}} = -485$ mV and $I = 0.87$ nA ($T = 4.9$ K). The feedback bandwidth was set to 1 kHz. (b) Density map acquired simultaneously with (a) using lock-in technique (c.f.) with a rectangular bias modulation of $\nu = 2.43$ kHz and $\Delta V_{\square} = 70$ mV, i.e. $eV_l = -520$ meV and $eV_h = -450$ meV (see text for details). (c) External potential map obtained by applying the Lindhard procedure (see text) to the density of (b) ($k_f = 0.07$ Å⁻¹). The reconstruction induced potential modulation can be clearly seen. (d)-(f) Data averaged over some linescans parallel to the dashed lines in (a)-(c), respectively.

and the ratio ρ_b/L_0 determined by tunneling spectra taken on clean surface spots right before and after the acquirement of the density map (Fig. 6.8). A particular tip was only then used for potential mapping when the spectra taken on clean terraces proved to be reasonably flat above the surface-state onset, i.e. in the relevant energy interval $E_{\overline{\Gamma}} < E < E_f$ (see Fig. 6.8), ensuring that the assumption of a constant tip DOS is justified.

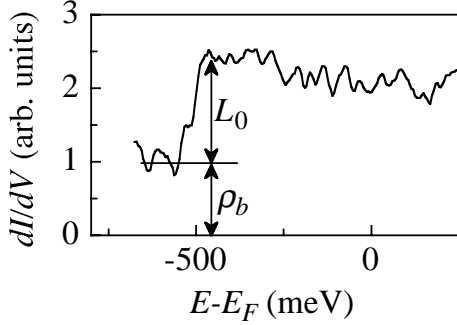


Figure 6.8: The spectrum taken on a clean spot on Au(111) right before having performed the measurement shown in Fig. 6.6 yields a ratio ρ_b/L_0 of 0.7 ($T = 4.9$ K, o.f., $\Delta V = 20$ mV, $\nu \approx 2.43$ kHz).

The total density of Fig. 6.6(b) shows minima in the fcc regions and maxima on the fcc side of the ridges (see also Figs. 6.6(d) and (e)). The distance between next neighbor maxima in the density is with 27 \AA about 2 \AA wider than the corresponding distance in the constant-current topograph. The measured total density $n_{2D}(-320 \text{ meV}, \mathbf{x})$ of Fig. 6.6(b) can very well be understood in terms of the LDOS displayed in Fig. 6.4. Integrating the LDOS of Fig. 6.4 over energies in the corresponding interval $[-520 \text{ meV}, -320 \text{ meV}]$ actually leads to a density very similar to the one displayed in Fig. 6.6(e). It is clear from

Fig. 6.4 that the maxima in the total density lying close to the ridges of the reconstruction are due to the broad LDOS peaks centered at -380 meV . It can also be inferred from Fig. 6.4 that the stabilizing current $\bar{I} = \frac{1}{2}(I(V_l) + I(V_h))$, which is proportional to the mean value of the integrals of the depicted LDOS from the Fermi level to $eV_h = -320 \text{ meV}$ and $eV_l = -520 \text{ meV}$, is only weakly influenced by the reconstruction induced LDOS features. Thus, the assumption of a constant tip-sample distance is justified. This is further supported by the similarity of the density inferred from Fig. 6.4 and the density of Fig. 6.6(e), which have been measured using different stabilizing bias voltages of $V_{st} = 1 \text{ V}$ and $V_{st} = -420 \text{ mV}$, respectively.

Starting with the total density of surface-state electrons with energies in $[E_{\overline{\Gamma}}, E_f]$ the potential has been determined using the formalism of Section 6.2. Since the medium surrounding the 2D surface-state electron gas, i.e. the 3D bulk electrons, is highly polarizable, we can set $\epsilon_b \rightarrow \infty$ in Eq. (6.8) and thus the external potential is related to the induced electron density through $n^{\text{ind}}(\mathbf{q}) = \chi_L(\mathbf{q}) U(\mathbf{q})$ (Eq. (6.9)), where we use the Lindhard susceptibility of Eq. (6.4). Note that in our case k_F entering the Lindhard function has to be replaced by the $k_f = \sqrt{2m^*(E_f - E_{\overline{\Gamma}})/\hbar^2}$. We wrote a computer program to map the potential. This program performs the fast Fourier transform of

the density image, divides this Fourier transform by the Lindhard susceptibility and then does an inverse Fourier transformation to yield the potential map. The program has been tested by applying the procedure to the total particle density in presence of weak square potentials, calculated using simple quantum mechanics. The potentials determined with our program for such test electron densities agree very well with the input potentials, minor discrepancies being due to the fact that our procedure relies on *linear* response theory.

Figure 6.6(c) shows the potential map of the Au(111) surface that results from the total electron density of Fig. 6.6(b). Since dividing the Fourier transform of the density by the Lindhard susceptibility (Fig. 6.1(a)) leads to an enhancement of high frequency noise, we usually low-pass filtered the resulting potentials. The potential modulation due to the herringbone reconstruction is clearly seen in Fig. 6.6(c). Furthermore, there are features in the potential maps that can be associated with surface and subsurface defects, i.e. white and black spots in Fig. 6.6(a). We believe that these features do not represent the real potential, since it is probable that the different chemical nature of the defects induces changes in the bulk LDOS, and the assumption of a constant ρ_b is not justified close to such defects. Therefore, we concentrate on the potential modulations induced by the reconstruction. In agreement with Chen *et al.* [79] we find that surface-state electrons are less bound in fcc than in hcp regions. Furthermore, the regions close to the reconstruction ridges are more attractive than fcc and hcp regions. As can be seen from the line cut in Fig. 6.6(f) the difference in binding energy between fcc and hcp region is of the order of 20 meV and close to the ridges electrons experience a potential energy that is roughly 15 meV reduced with respect to hcp regions. The dashed line in Fig. 6.6(f) shows the potential obtained using the Thomas–Fermi approach (Fig. 6.1(a)), i.e. by dividing the total density of Fig. 6.6(e) by $-L_0$. Since the fictitious Fermi wavelength $2\pi/k_f$ of the total density of Fig. 6.6 is with 54 Å comparable to the typical length over which the potential changes, Thomas–Fermi theory works well in this case.

Clearly, the total electron density $n_{2D}(E_f, \mathbf{x})$ depends on the choice of E_f , i.e. the bias modulation ΔV_{\square} used during the measurement. But of course, if our potential mapping is correct, the resulting external potential should be independent of the measuring conditions and therefore also independent of E_f . This is indeed what we observe in all our measurements: densities for E_f in the range of -450 meV to -320 meV yield essentially the same surface potential. This is illustrated by Fig. 6.7, which shows potential mapping performed on the very same surface area as the measurement of Fig. 6.6 but using a smaller bias modulation of $\Delta V_{\square} = 70$ mV, i.e. $E_f = -450$ meV as compared to

$E_f = -320$ meV in Fig. 6.6. The total density shown in Fig. 6.7(b) is less structured and clearly different from the density in Fig. 6.6(b) (compare also the linescans in (e)). This is due to the fact that k_f in Fig. 6.7(b) is by about a factor of two smaller than k_f in Fig. 6.6(b), and therefore the electron density, which can exhibit modulations on length scales not shorter than π/k_f , is smoother in Fig. 6.7(b). Note also that the electron density of Fig. 6.7(e) agrees well with the density obtained by integrating the LDOS of Fig. 6.4 from -520 meV to -450 meV. The maxima of the density in hcp regions are in this case due to the broad LDOS peaks at -470 meV seen in Fig. 6.4. Although the densities of Figs. 6.6(b),(e) and 6.7(b),(e) are significantly different, the resulting potentials shown in (c) and (f) are identical, except for noise⁸. This proves that our results do not depend on the chosen bias modulation ΔV_{\square} . In the about twenty independent potential measurements we performed the relative sensitivity of the tip to surface and bulk states, ρ_b/L_0 , ranged from 0.7 to 3. Nevertheless, the resulting potential maps proved to be independent of ρ_b/L_0 . We also emphasize that an uncertainty in the dispersion relation, i.e. an uncertainty in k_f , does not affect the deduced potentials crucially: varying k_f by ± 10 % leads to essentially identical potential maps.

Our measurements reveal the “herringbone” reconstruction induced potential as sketched in Fig. 6.9. The potential shows its minima between fcc and hcp regions, where surface atoms occupy bridge sites. In hcp regions electrons are less bound by $U_{\text{hcp}} = 15 \pm 5$ meV. The difference in binding energy between fcc and hcp regions amounts to $U_{\text{fcc}} - U_{\text{hcp}} = 22 \pm 5$ meV (Fig. 6.9). The potential we have found is in excellent agreement with the results of Chen *et al.* [79], if one takes into account that Chen *et al.* interpreted their STS data taken in fcc and hcp regions in the framework of an extended Kronig–Penney model with one single free parameter, namely the potential difference between hcp and fcc regions. The value they found for this difference is 25 ± 5 meV and compares very well with our $U_{\text{fcc}} - U_{\text{hcp}} = 22 \pm 5$ meV. Since we did not make any *a priori* assumptions on the form of the “herringbone” potential, our results constitute a refinement of the potential proposed by Chen *et al.* The schematics of the “herringbone” potential shown in Fig. 6.9 only holds for locations not too close to elbow regions of the reconstruction. Frequently, we observed impurities at the elbows themselves, showing up as black or white dots in Figs. 6.6(a) and 6.7(a). These impurities lead to features in the potential maps in Figs. 6.6(c) and 6.7(c) which probably do not represent the real potential, as outlined above. But apart from these “artifacts”, we can observe real potential changes at the elbows: there is a further enhancement of the potential energy in the fcc regions at those elbows which show a widening of the

⁸The larger the bias modulation ΔV_{\square} , the lower the noise.

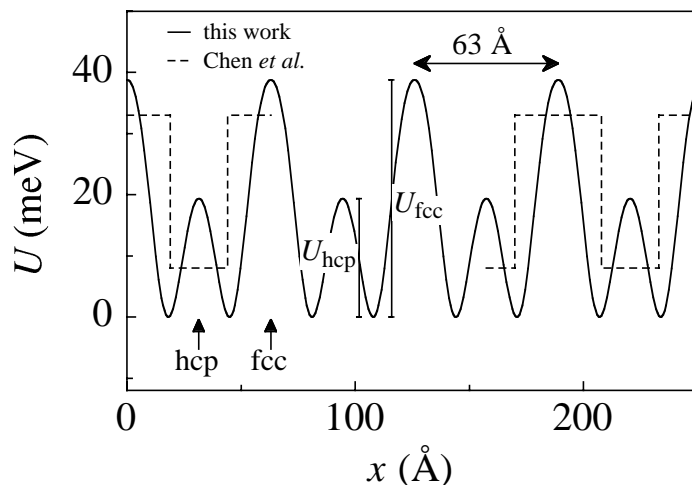


Figure 6.9: Electron potential perpendicular to the herringbone reconstruction lines on Au(111). The full line shows a fourth order Fourier series fit to the potential of Fig. 6.6(f) and is compared to the 25 meV deep extended Kronig–Penney potential of Chen *et al.* [79] (dashed line).

fcc region, i.e. the upper row of elbows in Figs. 6.6 and 6.7. Furthermore, for the other type of elbows, showing a narrowing of the fcc region (lower row of elbows in Figs. 6.6 and 6.7), we observe two additional shallow potential minima on the ridge sides of every hcp region.

It is natural to ask what could be the physical origin behind the potential modulations induced by the reconstruction. Based on the fact that the pseudopotential of noble metals, particularly that of s electrons, is unusually attractive, implying that regions of higher atom density should also be regions of lower potential for s - p electrons [149], Chen *et al.* suggested that the slightly higher concentration of atoms in hcp regions may be the cause for the observed potential well in these regions. However, Barth *et al.* found an enhanced atomic distance in the ridge regions between hcp and fcc stripes [102], and one would thus expect these regions to be less attractive for s - p electrons, in contrast to our results. Further investigations are thus needed to fully understand the physical origin of the reconstruction induced potential modulations on Au(111).

In conclusion of this Chapter, we have developed a *new method to directly image electron potential landscapes at surfaces, so-called potential mapping*. It has been applied to the s - p derived surface state on the reconstructed Au(111) surface. Excellent agreement between the measured Au(111) potential maps and previously published results obtained using traditional scanning tunneling spectroscopy [79] establishes potential mapping as a useful tool with applicability to many other surface systems.

Chapter 7

Conduction Through Single Metal Atoms

In this Chapter measurements of the electrical conductance of single-metal-atom constrictions are presented. One single or two metal atoms in series are contacted to two reservoirs: the STM tip on one side and a Cu(100) sample on the other. We prove that one single metal atom can open up one conduction channel, i.e. its conductance corresponds to one quantum of conductance $G_0 = 2e^2/h$. On the contrary to all previously reported works on metallic point contacts we observe a smooth transition between tunneling and contact, i.e. there is *no atomic rearrangement* associated with the contact formation in our measurements.

After a general introduction and an overview over the field of ballistic point contacts in Section 7.1 a short description of vertical STM manipulation of single metal atoms is given in Section 7.2, which is preparatory for the conductance measurements of single-metal-atom junctions presented in Section 7.3.

The measurements for this Chapter have been performed with the 4 K-STM in the laboratory of D. Eigler at IBM Almaden.

7.1 Quantized Conductance of Ballistic Point Contacts

The miniaturization of electronics has reached the stage where the discussion of devices with atomic-scale dimensions is becoming technologically relevant. One important question is how the behavior of existing electronic devices is altered as their size shrinks [80, 150, 151]. A second question is how the quantum behavior of ultrasmall

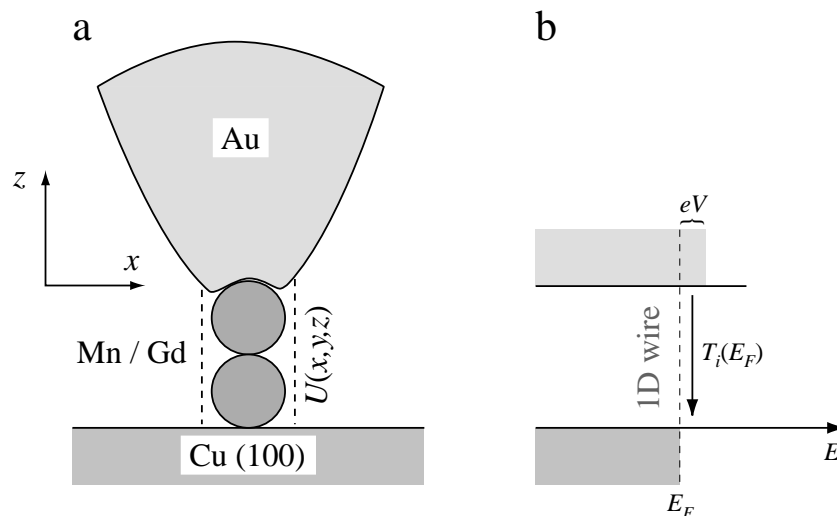


Figure 7.1: (a) Atomic wire between STM tip and substrate. Electrons experience the potential $U(x, y, z)$ in the wire. (b) Energy scheme for the situation depicted in (a). Applying a voltage difference V between the two electrodes leads to a net current which in the ideal case is equally distributed between the different transverse modes of the 1D wire. For a general potential $U(x, y, z)$ the transmission of electrons in a particular transverse mode i can be reduced from 1 and is given by $T_i(E_F)$.

structures might form the basis for new devices. As the scale of microelectronic engineering continues to shrink, interest has focused on the nature of electron transport through essentially one-dimensional nanometer-scale channels such as split gate confined 2DEGs in semiconductor heterostructures [152, 153], metallic point contacts [154] or carbon nanotubes [155–157].

For macroscopic conductors Ohm’s law is a well established fact, i.e. $G = \sigma A/L$ where G is the conductance, A the area, L the length of the conductor, and the conductivity σ is a material property of the sample independent of its dimensions. If this ohmic relation were to hold as the length L is reduced, then one would expect the conductance to grow indefinitely. However, it is found that the measured conductance approaches a limiting value when the dimension of the conductor becomes smaller than mean free path L_m and phase-relaxation length L_ϕ (so-called ballistic conductor) [152, 153, 158]. In other words, when the size of the conductor is so small to allow the current carrying electrons to travel through it *ballistically*, the rules of resistance have to be rewritten. The theoretical basis for the understanding of ballistic conductance was proposed by Landauer [159, 160], who introduced the notion that “conduction is transmission”.

To illustrate the behavior of the conductance in this ballistic regime let us consider the situation depicted in Fig. 7.1(a), where an atomic-sized wire is connected to two

electrodes (here STM tip and sample, as in our experiments). For the sake of simplicity let us assume that the wire potential is independent of z , i.e. $U = U(x, y)$, and that the wire is much longer than wide. In this case the electrons are completely ballistic since there is no scattering and the single electron Schrödinger equation separates: for every transverse mode i of the 2D confining potential $U(x, y)$ there is a one-dimensional free electron subband with dispersion $E = E_i + \hbar^2 k^2 / 2m_e$, where E_i is the transverse mode energy and the wave vector k characterizing the motion in z -direction is a good quantum number. When such a conductor is contacted to two ideal reservoirs (see Ref. [80]) of potential difference V , then a net current $I_i = e (eV \rho_i^\pm(E_F)) v_i(E_F)$ is flowing through each transverse mode with $E_i < E_F$. Here $\rho_i^\pm(E_F)$ is the DOS for electrons with either positive or negative k and $v_i(E_F)$ the group velocity in mode i at the Fermi energy. Since every mode accommodates a 1D electron gas one has $\rho_i^\pm(E_F) = 2/hv_i(E_F)$ (assuming spin degeneracy) and by summing over all modes we thus find for the conductance

$$G = \frac{1}{V} \sum_{\substack{i \\ E_i < E_F}} I_i = \frac{2e^2}{h} \sum_i \Theta(E_F - E_i) = \frac{2e^2}{h} N, \quad (7.1)$$

where N is the number of open transverse modes. Therefore, for an ideal 1D conductor the conductance is quantized and can take values that are an integer multiple of the so-called quantum of conductance $G_0 = 2e^2/h = (12.9 \text{ k}\Omega)^{-1}$. N depends on the effective area of the potential $U(x, y)$. Figure 7.2 illustrates this for the simplest case of an infinite square potential. A rough estimate of the number of transverse modes that can be accommodated in a constriction of area A is given by $N = \pi A / \lambda_F^2$ where λ_F is the electron's Fermi wavelength, and this leads to the Sharvin formula for the conductance of the constriction [158]:

$$G_{\text{Sharvin}} = \frac{2e^2}{h} \pi \frac{A}{\lambda_F^2}. \quad (7.2)$$

A striking feature of the expression for the conductance derived in Eq. (7.1) is the fact that *even in the absence of scattering in the conductor the conductance is finite*, i.e. the resistance is nonzero. The voltage drop associated with this finite resistance is localized at the contacts [80], and one thus speaks of the contact resistance. Note that since the electrons travel through the constriction ballistically there is no energy dissipation in the wire itself, the electrons being thermalized only in the reservoirs. Furthermore, the contact resistance does not depend on the conductor's length, which is in strong contrast with Ohm's law. Only when the length of the wire exceeds the mean free path of the electrons Ohm's law recovers [80]. Until now we did not allow for a z -dependence of the confining potential U , which of course is a major restriction. For a

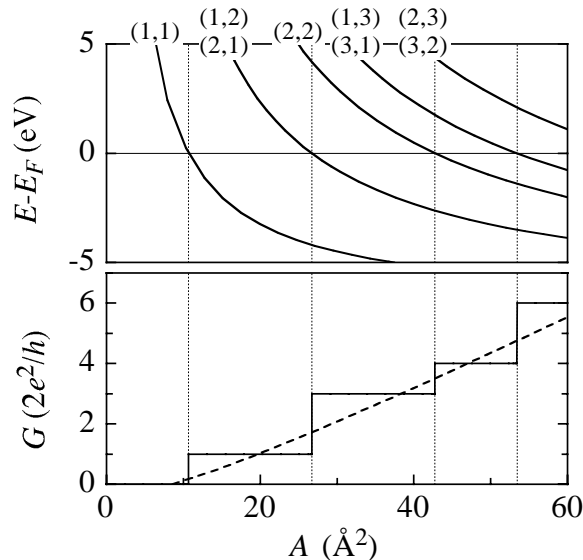


Figure 7.2: Conductance of a wire modeled by the infinite square potential, where the transverse mode energies are given by $E_{(r,s)} = E_0 + \hbar^2/(2m_e)(r^2 + s^2)\pi^2/A$. Here A is the area and (r,s) the transverse quantum numbers. Top: $E_{(r,s)}$ for the low-lying transverse modes (r,s) as a function of A (Cu parameters: $E_0 = -7$ eV, $\lambda_F = 4.6$ \AA). Bottom: the full line shows the corresponding conductance. Every time a transverse mode crosses the Fermi level a jump occurs in the conductance. Depending on the degeneracy of the particular mode it jumps by one or more quanta of conductance. The dashed line depicts the perimeter corrected Sharvin estimate (Eq. (7.2)) [161].

general potential $U(x, y, z)$ there is reflection by the potential leading to transmission factors for the individual modes, $T_i(E_F)$, that may be less than unity. Moreover there is coupling between different modes [80, 161–163]. In this more general case Eq. (7.1) takes the form

$$G = \frac{2e^2}{h} NT, \quad (7.3)$$

where T represents the average probability that an electron injected at one end of the conductor will transmit to the other end. So, for more general potentials the quantization of conductance is not that obvious, since T may take any value between 0 and 1. Astonishingly, the quantized nature survives even for rather rough confining potentials and a considerable amount of scattering in the constriction [161, 163–165]. The resistance G^{-1} of any ballistic conductor (Eq. (7.3)) can be viewed as two resistors in series, $G^{-1} = G_c^{-1} + G_s^{-1}$, where

$$G_c^{-1} = \frac{h}{2e^2} \frac{1}{N}, \quad G_s^{-1} = \frac{h}{2e^2} \frac{1}{N} \frac{1-T}{T}. \quad (7.4)$$

G_c^{-1} is the contact resistance as in the case of an ideal conductor and G_s^{-1} is the resistance

associated to scattering in the wire [80, 166]. The latter was introduced in this form by Landauer [159] and leads to ohmic behavior when the conductor's length exceeds the mean free path. The potential drop associated with the scattering resistance is localized around the individual scatterers.

To conclude this more “theoretical” discussion we would like to emphasize that contact resistance in ballistic conductors is a classical effect [158], and quantum mechanics manifests itself only through the quantized nature of this resistance. The quantization is normally only observable when the diameter of the conductor is of the same order as the Fermi wavelength λ_F , since for larger wires scattering tends to wash out the conductance steps.

The history of ballistic transport and contact resistance goes back to studies of Sharvin in 1965 [158]. But it was only in 1988 that the quantized conductance of point contacts in high-mobility two-dimensional electron gases, present at the interfaces of GaAs-AlGaAs heterostructures, was demonstrated experimentally in beautiful experiments by van Wees *et al.* and Wharam *et al.* [150–153]. Their results showed that the conductance changed in quantized steps of $2e^2/h$ when the constriction width, controlled by a voltage applied to a gate on top of the heterojunction, was varied. Since the Fermi wavelength in these semiconductor structures is of the order of 50 nm, the constriction width required to observe quantized conductance is large compared to atomic dimensions. On the other hand, the “large” constriction areas imply that the transverse mode energy separation is less than 1 meV, and thus the conductance steps in semiconductor heterojunctions can be clearly resolved only at temperatures below 1 K. Nowadays point contact experiments in semiconductors are focussed on sub-step conductance features, which reveal properties of 1D electron gases [167]. Remarkably, the optical analogue of quantized conductance of a point contact, which of course is a wave phenomenon, was discovered only after the findings of van Wees *et al.* and Wharam *et al.* in a very neat experiment by Montie *et al.* [168].

Because the Fermi wavelength of metals is of the same order of magnitude as the atomic separation, a *quantum point contact in a metal is necessarily of atomic dimensions* (see Eq. (7.2)), in contrast to semiconductor heterostructures. Therefore, it proved to be very difficult to realize a controlled metallic quantum point contact, and the variation of the constriction diameter suffers from the limits set by the size of the atoms. In 1987 Gimzewski and Möller studied the formation of a metallic quantum point contact by bringing an STM tip very close to the surface of a metal [169]. They observed a contact resistance comparable to $h/2e^2 = 12.9 \text{ k}\Omega$ and concluded that the contact was formed by one or two atoms. Because the transverse mode energy spacing for atomic

sized point contacts is several eV, measurements on quantized conductance in metals can be performed under ambient conditions and even simple classroom experiments showing quantized conductance can be performed [170, 171].

Mainly two techniques were used to study atomic-sized *metallic* point contacts: mechanically controllable break junctions (BJ) [154, 172–177], and STM [162, 178–187]. In BJ experiments the distance between two macroscopic pieces of metal can be adjusted with sub-atomic precision, allowing the formation of a contact constituted by a few atoms. By varying the distance between the two electrodes the area of the contact can be changed, but not in a controlled manner. STM point contacts in the experiments cited above were produced in basically the same way: the tip is pushed into a metallic sample and by pulling it out again, a neck forms, and before fracture occurs a nanosized constriction builds [163–165, 188, 189]. A very nice recent combined STM and transmission electron microscopy study shows the formation of such atomic bridges between Au tip and Au sample [187]. Common features in STM and BJ measurements of the conductance as a function of displacement of the electrodes are conductance plateaus separated by more or less sharp steps [162, 173–175, 178, 180, 184, 185, 187]. There are several ways how conductance trace data has been analyzed. One way is to measure the conductance values of the conductance plateaus. These data are accumulated for a large number of traces and the result is presented as a histogram. Histograms of this kind almost invariably show a relatively sharp peak just at one quantum of conductance ($G_0 = 2e^2/h$) for all investigated metals (Au, Cu, Na, Al, Pt, Ni, Fe, Co). A weaker bump is usually observed at $2 G_0$ and sometimes also at larger integers. On the other hand, a single conductance trace hardly ever presents series of steps located near integers (except for the last plateau before fracture at G_0): usually there are many more steps than expected. Furthermore, the steps are much sharper than what would be expected for non-perfect metal quantum constrictions when the constriction area is varied smoothly [161, 163]. Closer inspection shows that there are small steps on major plateaus. This effect is disconcerting and distracts from a picture of simply quantized conductance in these wires. A long debate about the origin of the steps in the conductance versus displacement curves started in the early nineties [180–182]. On one hand there is true quantization of conductance, i.e. almost perfect atomic-sized conductors with very little scattering. But this can not explain the non-integer plateaus, the sharpness of the steps and the hysteresis effects. On the other hand there is an explanation based on the atomic rearrangements in the junctions, which are always present when the area of an atomic-sized wire is changed [188, 189]. Such rearrangements necessarily cause steps of the order of G_0 in the conductance even for imperfect

conductors showing a lot of scattering (see Eq. (7.2)). The atomic rearrangement argument does not explain why there are pronounced peaks in the conductance histograms, and this is a major drawback of this reasoning. Later on, very nice combined STM and atomic force microscopy (AFM) studies showed that the stepwise variation of the conductance is always due to atomic rearrangements in the contact [184, 185]. The picture that has emerged since is one in which *the quantized conductance at integer values of G_0 is determined by the quantum modes, i.e. real quantization in more or less perfect conductors, but the jump between the different values are caused by abrupt atomic rearrangements* [163–165, 174, 190]. This picture was further supported by the work of de Heer *et al.* [176], who gave a very nice interpretation of the non-integer steps in single conductance traces in terms of quantum conductors in series. Thus the conductance is given by $G = (1/n + 1/m)^{-1}G_0$ ($n, m \in \mathbb{N}$) and could be interpreted in terms of contact and scattering resistances: $G^{-1} = G_0^{-1} 1/n (1 + n/m) = G_c^{-1} + G_s^{-1}$ (see Eq. (7.4)).

To conclude this Section, let us emphasize the following: there is a wealth of experimental evidence for true quantized conductance in atomic-sized metallic point contacts, i.e. the quality of a contact formed by a few atoms proved to be surprisingly good. Changes in conductance have been observed to be related to atomic rearrangements in the conductor and thus are abrupt. Finally, one single metal atom is believed to carry one quantum of conductance [173, 175, 177, 178, 187, 189].

7.2 Vertical Manipulation of Metal Atoms with an STM

The possibility of controlled vertical manipulation of single *metal* atoms with the STM tip is shown in this Section: a single metal adatom can be transferred from the surface to the apex of the tip, from where it subsequently can be put at another location on the surface. The results presented here are preparatory for Section 7.3 where we have used the pick-up mechanism to form two-metal-atom wires.

The adventure of controlled atomic-scale modification of surfaces became possible through STM and started in 1987 when Becker *et al.* reported of the transfer of atomic-sized bits (probably single Ge atoms) from the STM tip to a Ge(111) surface through a short voltage pulse [36]. Three years later a fabulous example of positioning single Xe atoms on a Ni(110) surface was given by Eigler and Schweizer [3]. Van der Waals interactions between tip and adsorbed xenon atoms allowed them to slide the atoms along the surface and fabricate the famous atomic IBM logo. Later on Avouris *et al.* succeeded in reproducibly transferring Si clusters from a Si(111) surface to the tip and vice versa [37],

and it was Eigler *et al.* who realized the first atomic switch, where a *single* xenon atom was *reversibly* switched between the tip and a Ni(110) surface [38]. Depending on adsorbate, sample and type of manipulation used, the dominating mechanisms behind these processes are electrostatic forces, Van der Waals interactions, exchange interactions, ionization followed by field evaporation, or electromigration [191]. Controlled manipulation with STM has since developed into a frequently used technique [192]. Probably its most exciting application is the synthesis of custom made structures giving access to phases of matter that are not normally accessible in the laboratory [33].

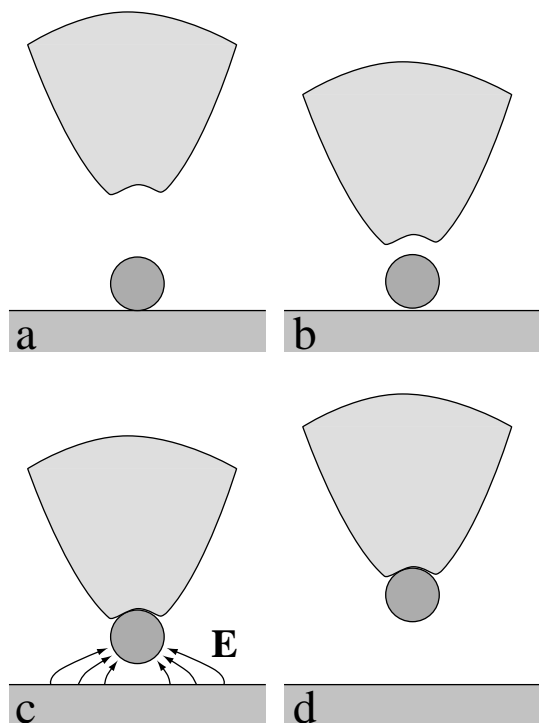


Figure 7.3: Metal-atom pick-up. **(a)** Centering over the adatom at imaging conditions ($R \approx 100 \text{ M}\Omega$). **(b)** Approaching to typically 30 - 40 k Ω . **(c)** The feedback loop is interrupted and a voltage pulse of typically +1.5 V is applied to the sample, leading to the transfer of the atom. **(d)** Going back to imaging conditions.

applied to the sample and results in the pick-up of the atom (c). This voltage difference leads to high electric fields \mathbf{E} of the order of $3 \cdot 10^{10} \text{ V/m}$. Note that the polarity of this pulse is so that the electrons flow from tip to sample, i.e. in the opposite direction than the metal atom, contrary to the case of rare gases (xenon) [38], as will be discussed

In the following it is demonstrated that even single *metal* adatoms (Mn or Gd) can be reversibly transferred between a metallic surface (Cu(100) or Nb(110)) and an STM tip (gold). Thus, the tip can be used not only to slide metal atoms [191], but also to carry them, for example from one terrace to another. In contrast to the vertical manipulation of physisorbed xenon this is rather surprising, since the binding energy of metal atoms is much larger. Figure 7.3 depicts the principle of the metal-atom pick-up. The tip is centered over the adatom of interest at imaging conditions (typically $V = 10 \text{ mV}$, $I = 0.1 \text{ nA}$), and then brought very close to the surface by asking for a higher feedback current, thus reducing the tunneling impedance to about 30 - 40 k Ω (b). This is close to the point of contact, which is defined by a conductance of $G_0 = 2e^2/h = (12.9 \text{ k}\Omega)^{-1}$. At this stage the feedback loop is interrupted and a voltage pulse of typically +1.5 V is applied to the sample and results in the pick-up of the atom (c). This voltage difference

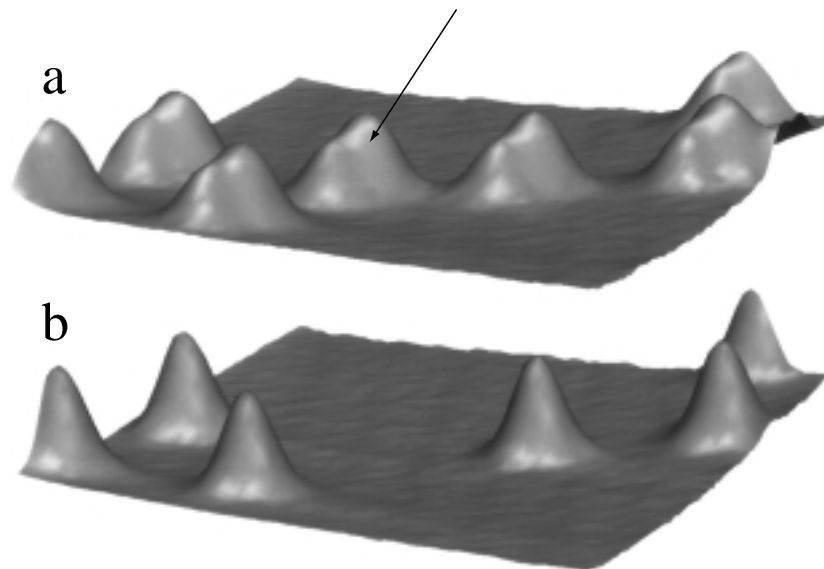


Figure 7.4: (a) $95 \text{ \AA} \times 95 \text{ \AA}$ constant-current image of 7 Mn atoms on Cu(100) ($V = 2.58 \text{ mV}$, $I = 0.1 \text{ nA}$). (b) The same surface spot after having picked up the Mn atom marked with the arrow in (a) by applying the procedure described in the text. The six remaining atoms are still at the very same position. Note the enhanced resolution in (b) due to the presence of the Mn atom at the very end of the tip. The tunneling current is then flowing mainly through this single atom ($T = 5.6 \text{ K}$).

below. Since the tunneling impedance depends crucially on the detailed structure of the two electrodes (tip and sample), it is not surprising that the conductance of the junction with the atom on the surface is different (generally higher) from the one of the junction with the atom transferred to the tip (Fig. 7.3(b) and (c), Fig. 7.5). Finally, the feedback loop is closed and the tip retracted to normal imaging conditions (Fig. 7.3(d)). Putting down the atom requires the inverse procedure: the tip with the atom at the very apex is approached even closer, i.e. to $20 - 30 \text{ k}\Omega$. Then the feedback is opened and a voltage pulse of 0 to -0.5 V is applied to the sample. Often no voltage pulse is needed at all to transfer the atom back on the surface. This can be rationalized in terms of a simple bond counting argument: it is very probable that the single atom has more next neighbors to bind to on the flat surface than on the curved tip. Thus, the configuration with the additional atom on the surface is energetically favored, and the atom jumps to the surface as soon as the energy barrier is reduced enough by bringing the tip very close to the surface.

Figure 7.4 shows an example of a Mn atom pick-up, i.e. the topography of Mn adatoms on Cu(100) right before (in (a)) and just after (in (b)) the transfer of the Mn atom marked with an arrow from the surface to the apex of the tip. The apparent shape

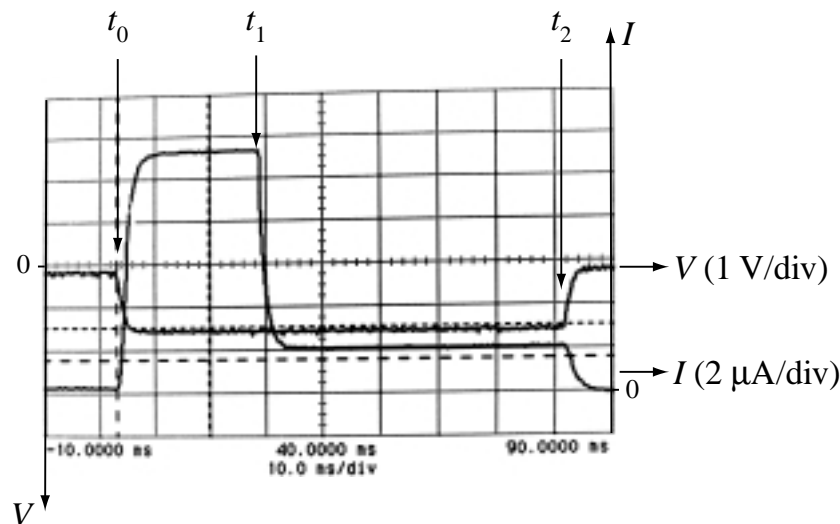


Figure 7.5: Tunneling current I and bias voltage V during a pick-up of a Mn atom. At time t_0 the bias pulse is switched on and leads to the jump of the atom from the surface to the tip apex at t_1 . At time t_2 the bias pulse is switched off. Due to a 1 ms time constant of the current pre-amplifier used for this experiments, the features are smeared out.

of the remaining 6 atoms has drastically changed in (b), due to “sharpening” of the tip induced by the additional Mn atom at the very apex of the Au tip. The pick-up shown in Fig. 7.4 is completely reversible, meaning that the Mn atom can subsequently be put down at a chosen position on the surface, and the whole procedure can be repeated at will. After the put-down of the atom the apparent shape of the adatoms turns out to be the same as before the pick-up, which is strong evidence for the fact that the tip itself recovered its initial state. Hence, the only atom affected is this single metal atom itself!

To reveal the driving mechanism of the metal-atom transfer we have tried to study the delay between the onset of the voltage pulse and the change of the conductance owing to the motion of a Mn atom from the Cu(100) surface to the STM tip. This has been done by tracing the tunneling current and bias voltage during the pick-up on an oscilloscope (see Fig. 7.5). At time t_0 the bias (of the sample) has been increased to +1.5 V and accordingly the current rises, since the feedback loop had been opened before. For a time interval $\Delta t = t_1 - t_0$ the atom remains on the surface site and jumps to the apex of the tip only at time t_1 , leading to a change in the conductance of the junction. At time t_2 the bias is finally decreased to its normal imaging value. For fixed tip height (i.e. initial tunneling impedance) and pulse voltage amplitude, the distribution of the delays Δt has been found to be exponential, which indicates a constant probability of transferring per unit time, characterized by the transfer rate τ^{-1} . For the sake of simplicity we plotted the number N of transfers with a time delay larger

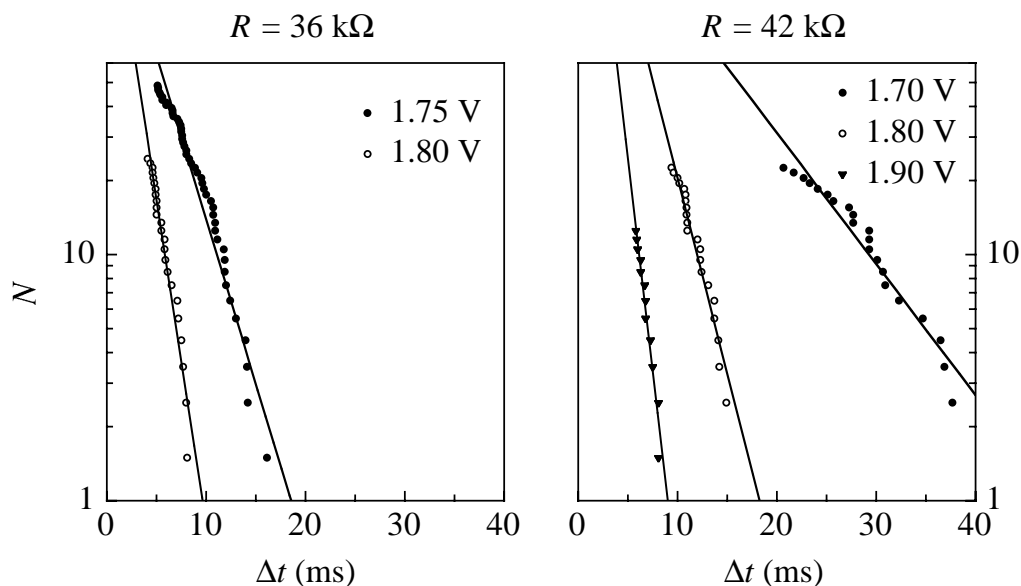


Figure 7.6: Determination of the characteristic transfer time τ for a Mn atom on Cu(100) as a function of tunneling impedance R and voltage pulse amplitude. N is the number of transfers with a time delay larger than Δt (0.5 has been added to N , which allows for a logarithmic display). The lines depict an exponential fit. It has been carefully checked that the tip did not change during the experiments at a particular tunneling impedance ($T = 5.6$ K).

than Δt as a function of Δt for different impedances and bias pulses (Fig. 7.6). If the probability to find the atom still on the surface after a delay Δt decays exponentially, then it is easy to show that N follows the same decay. The decay rates τ^{-1} given in Table 7.1 can therefore be determined by fitting an exponential to the data in Fig. 7.6¹. The transfer times in Table 7.1 reflect the expected tendencies: they decrease with increasing voltage pulse amplitude and decreasing tip-sample separation. The idea was to complete this table with τ values measured with the very same tip over an extended bias pulse and tunneling impedance range. Unfortunately, we did not succeed in doing that during my short stay at IBM Almaden.

From the presented data we conclude that: the transferring atom moves in the direction opposite to the direction of the tunneling electrons. Electromigration as the driving mechanism for the transfer of metal atoms can thus be ruled out [191], contrary to rare gases [38]. The time delay for an individual transfer is distributed exponentially, characterized by a time constant τ which depends strongly on the amplitude of the

¹The latter meander around the fit in a correlated way since N is not an independent quantity.

R (k Ω)	1.70 V	1.75 V	1.80 V	1.90 V
42	8.2 ms		2.7 ms	1.3 ms
36		3.3 ms	1.6 ms	

Table 7.1: Characteristic time constants τ for the transfer of a Mn atom as a function of tunneling impedance (i.e. distance) and voltage pulse amplitude.

applied bias pulse and the distance between tip and sample. The voltage dependence of τ is not linear, indicating the presence of a threshold voltage below which no transfer of metal atoms takes place (Table 7.1). The only mechanism which is consistent with these findings is positive ion formation followed by field evaporation. This mechanism was previously inferred for silicon by Lyo and Avouris [37].

7.3 Single-Metal-Atom Point Contacts

A major drawback of all but one (Ref. [187]) metallic point contact measurements described in Section 7.1 is the ignorance of the actual constriction geometry. Furthermore, all these experiments were not reversible in the sense that during the measurement of the properties of a particular point contact its atomic arrangement was changed irreversibly. Due to missing knowledge of the atomic configuration it is difficult to model such contacts theoretically. These facts were the motivation for us to think of a reversible metallic point contact experiment which allows for a better control and knowledge of the junction geometry. Our approach and results are discussed in this Section.

Our point contacts have been formed by single manganese or gadolinium atoms adsorbed on an atomically clean Cu(100) surface. The substrate forms one electrode whereas the STM gold tip serves as second electrode (Fig. 7.7). By means of the atom pick-up described in Section 7.2 it has been possible to form two-atom wires. Because the substrate and the adatom can be imaged with the STM prior to forming the point contact, the *junction geometry is partially known*.

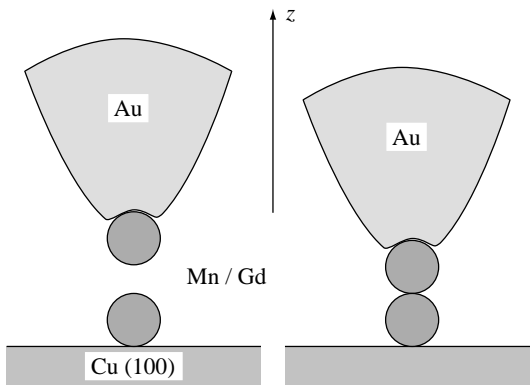


Figure 7.7: Schematic of the experiment. A single-atom point contact is formed by reducing the distance between an STM tip and an adatom on a metallic substrate.

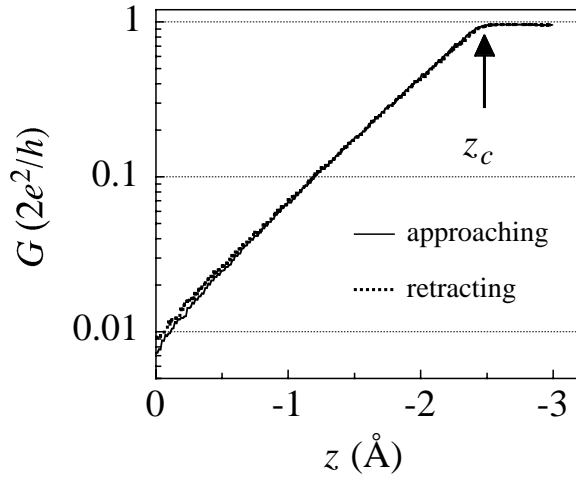


Figure 7.8: Conductance of a single-Mn-atom junction as a function of tip displacement. $z = 0$ Å is defined as the z -piezo expansion for which the tunneling impedance is 1.29 M Ω . The full line (dashed line) depicts the conductance curve taken during approaching (retracting) the tip ($T = 5.6$ K).

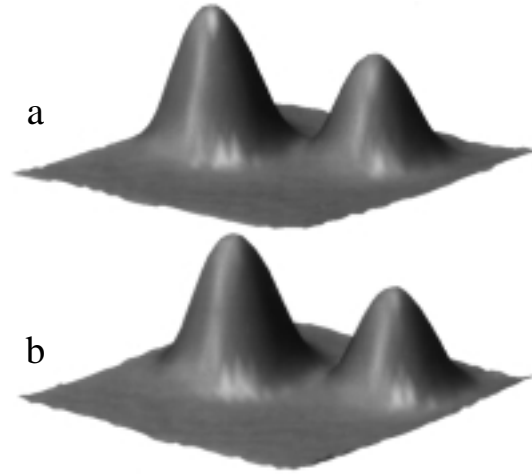


Figure 7.9: 36 Å \times 36 Å constant-current images of a Gd and a Mn adatom on Cu(100). They image as bumps of 2.2 Å and 1.5 Å height, respectively ($V = 100$ mV, $I = 1$ nA). The same surface spot is shown before in (a) and after the conductance measurements on both atoms (b) ($T = 5.6$ K).

This knowledge can be improved by picking up a well known atom at the very apex of the tip, whose chemical and configurational identity is a priori unknown. The conductance of the atomic wires has been measured as follows: the tip (with or without a defined atom at the very apex) has been centered over the adatom at a tunneling impedance of normally 1.29 M Ω ($V = 2.58$ mV, $I = 2$ nA). Then the feedback has been interrupted and the tip displaced towards the adatom by means of a controlled z -piezo expansion with a speed of typically 0.5 Å/s. During approaching the adatom we have kept the bias voltage constant and the current has been monitored, i.e. we have measured the conductance as a function of distance between tip and adatom at low bias. The resistance of the single-atom constrictions is in series with the finite input resistance of the current pre-amplifier (21 k Ω) and the values of the two resistances can become comparable in such contact measurements. Thus the pre-amplifier resistance has to be subtracted from the total resistance to yield the resistance of the atomic wire itself, i.e. the conductance of interest [101].

Single-Mn-Atom Contacts

Figure 7.8 shows a typical conductance measurement of a single-Mn-atom junction. The conductance is plotted on a logarithmic scale versus the z -piezo displacement towards the surface. Initially the conductance increases exponentially with decreasing z , as expected for the tunneling regime. In agreement with Ref. [101] we find an apparent barrier height $\overline{W} = [\frac{\sqrt{eV}\text{\AA}}{1.025} \frac{d}{dz} \ln(G \cdot \Omega)]^2$ which does not decrease upon approaching the surface and stays constant until the point of contact z_c is reached [169]. The apparent barrier heights we have found over Mn or Gd adatoms on Cu(100) all lie in the reasonable interval of 3 eV - 4 eV. At z_c the transition from tunneling to contact occurs. One could speak of the formation of contact at z_c . For $z < z_c$ the conductance takes a constant value which for Mn lies very close to $2e^2/h$ (Fig. 7.8). Driving the z -piezo further in than about -3 \AA eventually opens up a second or third conduction channel and leads to the corresponding conductance plateaus. But at the same time it leads to irreversible changes in the atomic arrangement. Since our goal has been reproducibility we have not measured beyond -3 \AA and thus we have only studied the formation of a first conduction plateau. I - V curves taken just beyond contact formation (e.g. at -2.8 \AA) showed perfect ohmic behavior from about -1 to $+1$ V. Applying larger bias values than 1 V leads to the destruction of the junction. Figure 7.9 illustrates the reproducibility of our experiments. The image taken after the conductance measurements (Fig. 7.9(b)) looks the very same as the one taken just before (Fig. 7.9(a)). No additional atoms are seen in Fig. 7.9(b), and the apparent shape of the Gd and Mn atoms in Fig. 7.9(b) are the very same as in Fig. 7.9(a). This is strong evidence that neither the tip nor the sample have changed during the conductance measurement. Together with the fact that the conductance curves shown in Fig. 7.8 are smooth (on a time scale of 1 ms which is the current pre-amplifier time constant), show no hysteresis and can be reproduced at will by repeating the measurement with the same tip, leads us to the conclusion that our experiment is completely *reversible*, i.e. that the atomic configuration does not change at all. To our knowledge our experiments show for the first time a smooth transition from tunneling to contact for metal point contacts. For all the experiments discussed in Section 7.1 this transition was always accompanied by an abrupt change in the atomic configuration called “jump to contact” [169, 173, 178, 185, 188, 189].

As seen in Fig. 7.10 the conductance of a one-Mn-atom point contact, measured with a supposedly “bare” tip, does depend on properties of the STM tip. Different tips have been prepared in-situ by field emission and controlled immersion into the sample. The general features of the conductance of a single atom of the 3d metal Mn, i.e. a tunneling regime which goes over to a conductance plateau smoothly, are present for all different

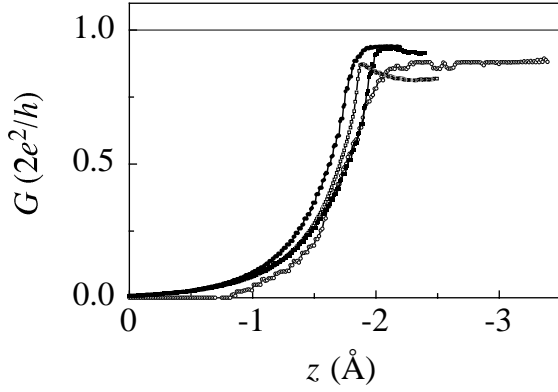


Figure 7.10: Conductance of a one-Mn-atom point contact measured with 4 different tips ($T = 5.6$ K).

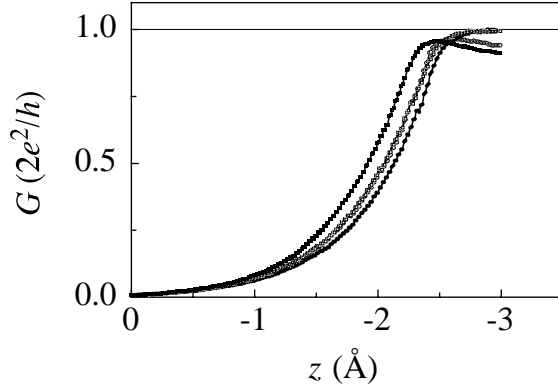


Figure 7.11: Conductance of two Mn atoms in series measured with different tips ($T = 5.6$ K).

tips. In all cases the conductance levels off at a value close to $2e^2/h$. But the apparent barrier height and the conductance value of the plateau depend on the tip properties (see Fig. 7.10). Furthermore, some tips show a shoulder in the conductance curve at the point of contact followed by a negative slope on the conductance plateau. We define the value at which a single trace levels off as the conductance value for which the derivative $\frac{d}{dG}$ of the number of sampled points of this trace with conductance smaller than G shows a maximum². We have found an average over 18 values of the conductance plateau for single Mn atoms measured with different tips of $G = (0.87 \pm 0.07)G_0$. The dependence of the conductance traces on the tip structure can be rationalized in terms of the constriction potential and thus the reflection and transmission amplitudes being different for different tips (Eq. (7.3)). Presumably we have used a variety of tip configurations to measure the conductance and thereby a large variety of different point contacts with different atomic arrangements on the tip electrode. It is thus rather surprising that the tip dependence of our experiment is so small [161,163]. We would like to mention that we have carefully tested the influence of not positioning the tip exactly over the center of the adatom before measuring the conductance: the conductance traces do not depend on misalignment up to a lateral distance between tip apex and adatom, Δx , of about 1 Å. Therefore, misalignment can be excluded as the reason for the difference in the conductance traces of Fig. 7.10. Furthermore, if the misalignment Δx is larger than 2 Å we observe an irreversible jump in the approaching branch of the conductance trace. After the jump the trace looks as if the tip was perfectly centered. This means that the adatom hops from one lattice site to another, right into the junction.

²In other words, the most frequently measured conductance value.

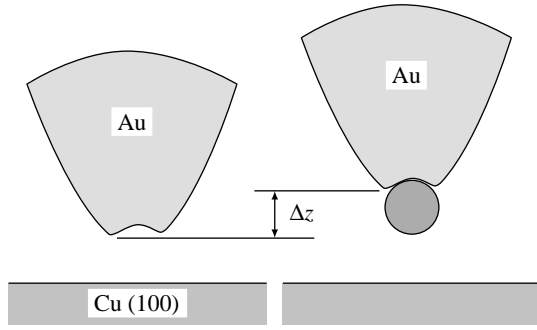


Figure 7.12: Characterizing the tip by the difference in z -piezo expansion Δz , measured with and without metal atom at the very apex.

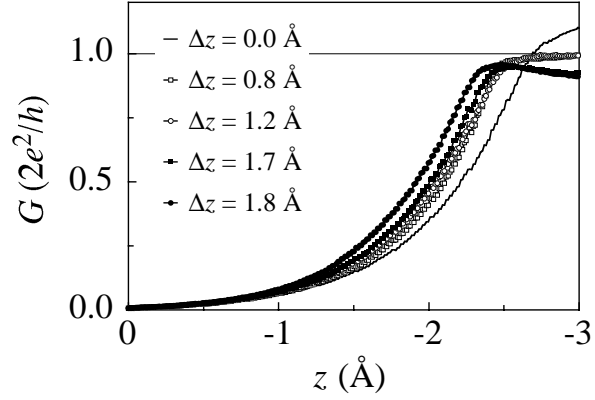


Figure 7.13: Conductance of two Mn atoms in series measured with tips of different Δz (see text) ($T = 5.6$ K).

Attractive lateral forces must therefore act on the adatom, which try to keep the atom as well centered in the junction as possible. The fact that for $\Delta x < 1$ Å the conductance traces do not depend on Δx may be due to a self adjusting elastic deformation of the junction. Actually, we can not rule out smooth lateral motion of the adatom during the experiment.

Two-Mn-Atom Contacts

To enhance the reproducibility of the tip configuration we profited from the metal-atom pick-up described in Section 7.2 and repeated the conductance measurement with a Mn-terminated tip. Figure 7.11 shows typical conductance traces of such two-Mn-atom wires. Compared to the single-atom point contact the two-atom wires level off at a conductance value which is closer to $2e^2/h$. The average over 20 traces is $(0.95 \pm 0.04)G_0$ and compares well with the calculated conductance for a stable single-metal-atom contact of $(0.93 \pm 0.05)G_0$ [189]. Furthermore, the tip dependence is reduced for the two-atom wire (Fig. 7.11). Thus, by picking up a Mn atom at the very apex of the tip, the measurement becomes more reproducible, i.e. we have a better control over the tip.

We have tried to characterize a particular tip even further by the difference Δz in tip height before and after the pick-up of a Mn atom (Fig. 7.12). This “geometrical” quantity tells us something about how far the picked up atom sticks out, i.e. how sharp the tip is. From our preliminary measurements shown in Fig. 7.13 we infer that Δz can be used to classify the conductance traces of two-Mn-atom wires: for “blunt” tips with a small Δz there is no clear plateau. Tips with a Δz of about 1 Å show a nice

plateau whereas “sharp” tips ($\Delta z \approx 2 \text{ \AA}$) exhibit a conductance shoulder followed by a negatively sloped plateau. We do not have the necessary amount of Δz -characterized conductance traces to draw final conclusions, but it seems that tips with similar Δz lead to similar conductance traces for the two-Mn-atom wires. Therefore, the easily accessible Δz appears to be a key quantity concerning the contact formation behavior of a particular tip. Altogether, with our single-Mn-atom point contact measurements we have reached a considerable amount of control and reproducibility.

A striking aspect of our measurement on Mn is the fact, that the plateaus in the conductance traces occur at a value so close to one quantum of conductance. According to Eq. (7.3) and since our wires are far from being perfect, we could expect that the product NT is not an integer, i.e. that there are strong reflection and tunneling effects [161, 163]. But we believe that the fact that the Mn point contacts show a plateau so close to $2e^2/h$ is not a coincidence, and we conclude that all but one channel are basically closed and that the only open channel shows almost no reflection. Recently, Scheer *et al.* found that the number of current-carrying modes of one-atom contacts is determined by the number of available valence orbitals [177], i.e. 7 in the case of Mn. But Scheer *et al.* defined a mode to contribute to the current as soon as its transmission is larger than 1 %. Our measurements show that for Mn atoms 6 of the 7 valences contribute very little to the total current, the other one being the main (and almost perfect) channel.

With our experiments we have the second (after Ref. [187]) direct experimental prove of what has been inferred from so many experiment described in Section 7.1: *a single-metal-atom point contact can provide one quantum of conductance*. The situation can be very different for atoms of non-metallic materials. For example the conductance of a single Xe atom is by a factor of 7 reduced compared to $2e^2/h$. This is due to the fact that the atomic resonances of the Xe atoms lie far away from the Fermi level of the electrodes and thus contribute only little to the DOS at E_F [193], and is in agreement with the conclusions by Scheer *et al.* [177].

Gd-Atom Contacts

In Fig. 7.14 we show the results of similar measurements for single-atom point contacts of the 4f metal Gd. One first of all notices that the results depend much more on the tip than in the case of Mn (compare with Fig. 7.10). Secondly, the traces level off at conductance values well below $2e^2/h$. The average over 10 traces is $(0.52 \pm 0.10)G_0$ and lies close to half a quantum of conductance. In addition, some traces show a pronounced maximum followed by a (negatively sloped) plateau. We have not yet a final explanation

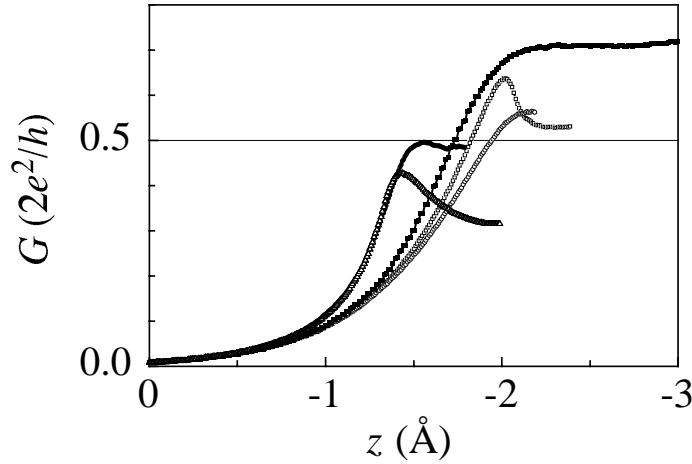


Figure 7.14: Conductance of a single-Gd-atom point contact. Different traces have been measured with different tips ($T = 5.6$ K).

for the conductance behavior of single-Gd-atom point contacts. In view of an average conductance of $G_0/2$, one could think of a possible lifting of the spin degeneracy induced by the $4f$ magnetism of Gd, leading to the closure of the channel for one spin species. But this of course is speculative, and we do not see how this effect could explain the strong tip dependence of our results. A more plausible and less exciting explanation would be the reduction of T in Eq. (7.3) due to reflection. Calculated conductance traces as a function of constriction width in the presence of scatterers and rough boundaries show the same features as our measured traces in Fig. 7.14: conductance shoulders and plateaus at values below $2e^2/h$ [163]. Since the presence of scatterers and the amount of roughness of the confining potential may depend much on the particular tip, this could explain the strong tip dependence. But we then would have to explain why Mn behaves so much better. What comes to our mind here are the covalent radii of the elements of interest: 1.17 Å, 1.34 Å, 1.17 Å, and 1.61 Å for Cu, Au, Mn and Gd, respectively (Gd atoms image as a larger bump in STM as seen in Fig. 7.9). The covalent radius of Mn is much closer to Cu and Au than Gd, and Gd may act more like a scatterer in a point contact formed between a Cu and an Au electrode than Mn. Again, this is speculation and *ab initio* calculations are needed to understand differences in the conductance behavior of Mn and Gd.

Conclusion

In conclusion, we have presented in this Section very controlled conductance measurements of single Mn and Gd-atom point contacts. Our junctions do not suffer from any

plastic deformation during contact formation, and thus the measurements have been reversible. Furthermore, since STM allows for atomic-scale imaging of sample electrode and constriction atom before the conduction through the latter is measured, and since the measurement is non-destructive, the point contact geometry is partially known. This constitutes an advantage for theoretical modeling. For both Mn and Gd we observe for the first time a smooth transition from tunneling to contact, not involving any atomic rearrangement called “jump to contact”. The value at which the conductance levels off after contact formation is very close to one quantum of conductance $2e^2/h$ in the case of a single-Mn-atom constriction. We interpret this as a direct experimental prove that *one single* metal atom can conduct a current corresponding to one quantum of conductance. Finally, we would like to mention that it might be interesting to investigate the conductance of single-metal-atom point contacts in high magnetic fields, which normally improve the quantization due to backscattering suppression [153, 167, 194, 195].

Chapter 8

Probing Magnetism with STM

A new approach to detect magnetic moments at surfaces with an STM is described in this Chapter. The basic idea is to make use of the strong influence of magnetism on superconductivity due to exchange interaction of magnetic moments with the conduction electrons. For example, single magnetic moments induce localized electronic excitations in a superconductor with excitation energies lying in the energy gap of the superconductor [4]. Thus, a superconducting STM tip could serve as a probe for magnetic moments at surfaces: by bringing the apex of such a tip very close to magnetic moments, its superconducting properties may be changed, i.e. electronic excitations in the gap can be induced by the moments, and by studying these excitations via tunneling spectra, information about the magnetic moments may be obtained.

After a survey of existing magnetization-sensitive techniques with high spatial resolution in Section 8.1 we present preliminary STM experiments with niobium tips in Section 8.2. Though not yet confirmed, the results are indeed promising. Close to magnetic moments we have observed sub-gap features in the DOS of the niobium tip which we believe are induced by the magnetic moments.

The measurements presented in this Chapter have been performed with the 4 K-STM in the laboratory of D. Eigler at IBM Almaden.

8.1 Towards Magnetism on the Atomic Scale

Magnetism in reduced dimensions is very interesting from both the technological and fundamental point of view. As an example, the physics of small magnetic particles and their magnetic coupling is relevant for data storage devices. On the other hand, understanding the magnetic behavior of low-dimensional systems is very challenging for experimentalists as well as for theorists. Many fascinating questions have been only

Technique	Lateral Resolution	Remarks
Scanning SQUID microscopy [200]	$> 1 \mu\text{m}$	high magnetic flux sensitivity
Scanning Kerr microscopy and Lorentz microscopy [198]	$\sim 1 \mu\text{m}$	non-destructive
Point contact Andreev reflection [201, 202]	$< 1 \mu\text{m}$	see text
Scanning Hall probe microscopy [200]	$> 100 \text{ nm}$	high magnetic field sensitivity of $\sim 0.1 \text{ G}$
Scanning near-field optical microscopy (SNOM) with polarization analysis [200]	$> 10 \text{ nm}$	non-destructive
Magnetic force microscopy (MFM) [200]	$\sim 20 \text{ nm}$	probes long-range magnetic dipole interaction
Scanning electron microscopy with polarization analysis (SEMPA) [198]	$\sim 10 \text{ nm}$	probing polarization of emitted secondary electrons
Spin-sensitive STM [203–208]	$< 10 \text{ nm}$	see text

Table 8.1: Magnetic-moment-sensitive techniques with high lateral resolution.

partially answered and will have to be addressed with always more powerful theories and experimental techniques in the future: how does the magnetic moment per atom evolve from the atomic limit via clusters to the bulk [19]? How does the presence of a matrix or substrate surface influence the magnetic properties of the imbedded or deposited cluster? What does the domain structure and dynamics of small magnetic particles and magnetic films look like [196]? Can magnetism in reduced dimensions be characterized by some few universality classes [197]? How is the particle size and shape related to its magnetic ordering [198]?

To address these and similar issues experimentally, magnetic-moment-sensitive techniques with high spatial resolution are required. Several techniques with resolution from the micrometer range down to several nanometers have been developed. In Table 8.1 we give a short overview of such techniques [199, 200].

Recently Soulen *et al.* and Upadhyay *et al.* simultaneously pioneered a beautiful technique to measure the spin polarization of metals [201, 202]. They formed a point contact between a superconducting material and the metal of interest of down to 3 nm

in diameter. Depending on the polarization of the normal metal conduction electrons at the Fermi level the enhancement of the differential conductance at low biases of such a point contact due to Andreev reflection is reduced. This reduction of the Andreev reflection then allows for a direct determination of the *magnitude* of spin polarization at the Fermi level. Since the point contact can in principle be of atomic size it would be interesting to use this method to investigate the spin polarization in nanosized magnetic particles. Using an STM with a superconducting tip would allow to image the particle of interest in a first step, and subsequently the tip could be used to form the point contact with this particle. We currently use a superconducting niobium tip in our laboratory and will attempt to realize such measurements. One major drawback of this method is of course the necessity to form a point contact and therefore the partial deformation of the object of interest. But the simplicity of the technique, the ease with which the polarization can be deduced from the measured data and the very high lateral resolution are of highest interest.

Since the invention of STM there have been quite a few attempts to make this technique sensitive to the electron spin and therefore to magnetic structures on the *atomic scale*. Its capability of local imaging and tunneling spectroscopy combined with spin sensitivity opens up the fascinating possibility of correlating structural and electronic properties with magnetic properties. As so often in the field of STM, the predecessors of spin-sensitive STM can be found in classical electron tunneling experiments of planar oxide tunnel junctions. Pioneering spin-dependent tunneling experiments were performed by Tedrow and Meservy in the seventies [209–211]. They used superconductor-oxide-ferromagnet junctions subjected to a high in-plane magnetic field. The magnetic field splits up the quasiparticle excitation spectrum of the superconductor in spin up and spin down branches, leading to a spin-polarized tunneling current which then could be used to determine the spin polarization in the counterelectrode. This method relies on the fact that the in-plane critical field in *thin* superconducting films is highly enhanced [212, 213], and thus, a magnetic field high enough to split the two spin states to a measurable extent but not destroying superconductivity altogether can be applied. To make use of this classical technique for STM one should therefore be capable of producing STM tips with small superconducting particles at the apex, which would show strongly enhanced critical fields compared to the bulk. This may be achieved by pushing a normal tip into a clean superconducting substrate and thereby picking up a superconducting cluster (see Section 8.2). Hence, although not yet realized for STM, this method may be extended to STM.

Another approach is based on the experiments by Jullière, which showed that the

conductance of ferromagnet-oxide-ferromagnet tunnel junctions depends on the relative magnetization of the two ferromagnetic electrodes [214]. In 1990 Wiesendanger *et al.* applied this so-called spin-valve effect to STM by using a ferromagnetic (CrO_2) tip [203]. With such tips they were able to probe the topological antiferromagnetic order of the $\text{Cr}(100)$ surface where terraces separated by a monoatomic step are magnetized in opposite directions. Recently Bode *et al.* refined the spin-valve STM by using 10 ML Fe coated tungsten tips and thereby reducing the magnetic stray field of the tip [204]. By tunneling into the exchange-split surface state of $\text{Gd}(0001)$ Bode *et al.* were able to separate topology and magnetism and could image the domain structure of the Gd films with high lateral resolution (10 nm). The spin-valve approach to spin-polarized tunneling is thus in principle possible, but it has drawbacks: it is difficult or even impossible to separate topology and magnetic information except for the case of exchange-split states for which the majority as well as the minority parts lie close enough to the Fermi level to be easily accessible to STS [204]. The magnetic structure of the tip apex, and thus the direction of the spin polarization is not known. Therefore, it is not possible to obtain quantitative values for the spin polarization in the sample. Furthermore, the signal-to-noise ratio for spin-valve STM is not large.

By optical means a spin selectivity can be achieved in a non-magnetic semiconductor due to the spin-orbit interaction. For that reason, also a III-V semiconductor material can be used in a spin-polarized tunneling experiment. For example, the injection of nonequilibrium spin-polarized carriers can be detected due to the emission of polarized radiation. On the other hand, spin-polarized carriers can be created by photoexcitation with circularly polarized light [215]. Optical spin-polarized tunneling with STM was pioneered by Alvarado and Renaud [205]. They used a ferromagnetic Ni tip to tunnel into a GaAs sample and analyzed the polarization of the emitted light which revealed the spin polarization of the tip. An important step towards using optical spin-polarized STM as a real tool was done by Prins *et al.* who used an optically pumped GaAs tip and showed that there is a light polarization dependent tunneling current contribution on Pt/Co multilayers [206]. Even for the commonly used tip material Pt/Ir the injection of spin-polarized tunneling electrons creates polarized light [207]. The first application of optical spin-polarized STM came from Suzuki *et al.* who succeeded in imaging magnetic domains in ultrathin Co films [208]. A major advantage of optical spin-polarized STM is the natural separation of magnetism and topography. Furthermore, there is no magnetic interaction between probe tip and sample. On the other hand, the technique of optical spin-polarized STM is quite demanding: the set-up is complicated and the magnetic signals are tiny.

8.2 Detecting Magnetism with a Superconducting Tip

Although optical spin-polarized STM as well as spin-valve STM work in principle, a lot of development will be needed until these two techniques can be used as standard tools to characterize magnetism on surfaces with atomic resolution. Therefore, we tried to take another approach to get magnetic information from an STM which relies on the strong influence of magnetism on superconductivity. It is well known that tiny amounts of magnetic impurities drastically suppress the transition temperature T_c of superconductors, can even lead to gapless superconductivity, and eventually destroy superconductivity altogether when the amount exceeds a critical concentration [27, 212, 213, 216, 217]. On the other hand, ordinary non-magnetic impurities do not alter superconductivity much [218]. This difference in behavior for magnetic and non-magnetic scatterers is due to the violation of time-reversal symmetry in the presence of magnetic moments [212]. On the microscopic level, the quasiparticle DOS of conventional low-temperature superconductors, described by BCS theory (Bardeen, Cooper and Schrieffer) in the absence of magnetic impurities [34, 212, 213, 217], is influenced by local magnetic moments, leading to an impurity band in the energy gap [219–221].

Electron tunneling experiments with planar oxide tunnel junctions give a direct experimental access to the DOS [26, 27]¹. The pioneering and beautiful tunneling experiments by Giaever directly confirmed the gap structure in the density of states, $\rho(E)$, of superconductors predicted by BCS theory [25, 225]:

$$\rho(E) \propto \begin{cases} \frac{|E|}{\sqrt{E^2 - \Delta^2}} & |E| > \Delta, \\ 0 & |E| < \Delta, \end{cases} \quad (8.1)$$

where in BCS theory the $T = 0$ K gap energy Δ is related to the critical superconducting temperature T_c by $\Delta = 1.764 k_B T_c$. The formation of impurity bands in the energy gap of superconductors due to magnetic impurities was subsequently investigated experimentally with classical tunneling experiments as well [226, 227].

With the STM it has become possible to look at superconductivity at the nanoscopic level through spatially resolved tunneling spectroscopy. The first to investigate superconductivity with STM were Lozanne *et al.* [228], and later on Hess *et al.* succeeded in beautifully mapping the Abrikosov flux lattice at the surface of NbSe₂ [229], which has to be viewed as a major breakthrough of low-temperature STM.

¹This holds even for superconducting electrodes, where one might think that coherence effects could alter the picture [222–224].

More recently, Yazdani *et al.* investigated the nature of the magnetically induced quasiparticle excitations around a single magnetic impurity on the atomic length scale by means of low-temperature STM [4]. These experiments form the basis for the detection of magnetism with a superconducting tip. Figure 8.1 sketches the experiment by Yazdani *et al.*

Single magnetic impurity atoms, Mn or Gd, were dosed on an atomically clean Nb(110) surface². The spectrum taken on a clean Nb spot at $T = 3.9$ K in Fig. 8.2(a) follows the temperature broadened BCS DOS (Eq. (8.1)). The influence of a single magnetic moment was studied by comparing the spectrum of clean Nb with spectra taken directly over (Fig. 8.2(a)) and in several distances from the magnets. The LDOS in the vicinity of magnetic adatoms is significantly modified as seen in Fig. 8.2(a). This is even clearer in the difference spectra shown in Fig. 8.2(b). Note that over

non-magnetic adatoms as Ag the LDOS of the superconductor in this small energy window around E_F is not altered at all (Fig. 8.2(b)). The additional features in the LDOS close to magnetic moments were shown to be localized within 10 Å of the adatom for both Mn and Gd. They can be understood in the framework of a model developed by Soda *et al.*, Shiba, and Sakurai [219–221], where the interaction of the conduction electrons of the superconductor with the localized magnetic moment is assumed to be of *s-d* exchange type. A low-lying excited state exists in this model with a wave function that is localized around the magnetic moment. The excitation energy lies in the energy gap of the superconductor and is given by

$$E = \Delta \left| \frac{1 - ((J/2)S\pi\rho)^2}{1 + ((J/2)S\pi\rho)^2} \right|, \quad (8.2)$$

where S is the impurity spin, J the magnitude of the *s-d* exchange interaction ($J > 0$ and $J < 0$ for ferromagnetic and antiferromagnetic coupling, respectively), and ρ the DOS. This excitation leads to additional sub-gap features observed in scanning tunneling spectra [4]. When $J^2 > 4/(S\pi\rho)^2$, as in the experiments discussed here, one favorable electronic spin is localized at the magnetic moment in the ground state [221]. In this

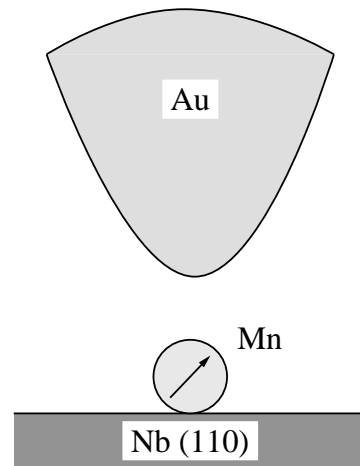


Figure 8.1: Schematics of the experiment by Yazdani *et al.* [4].

²Niobium is a classical type II superconductor with $T_c = 9.3$ K, a zero-temperature energy gap of $\Delta = 1.53$ meV, a 0 K upper critical induction B_{c2} of several Tesla (depending much on purity), and a coherence length $\xi(0 \text{ K}) \approx 39$ nm [230].

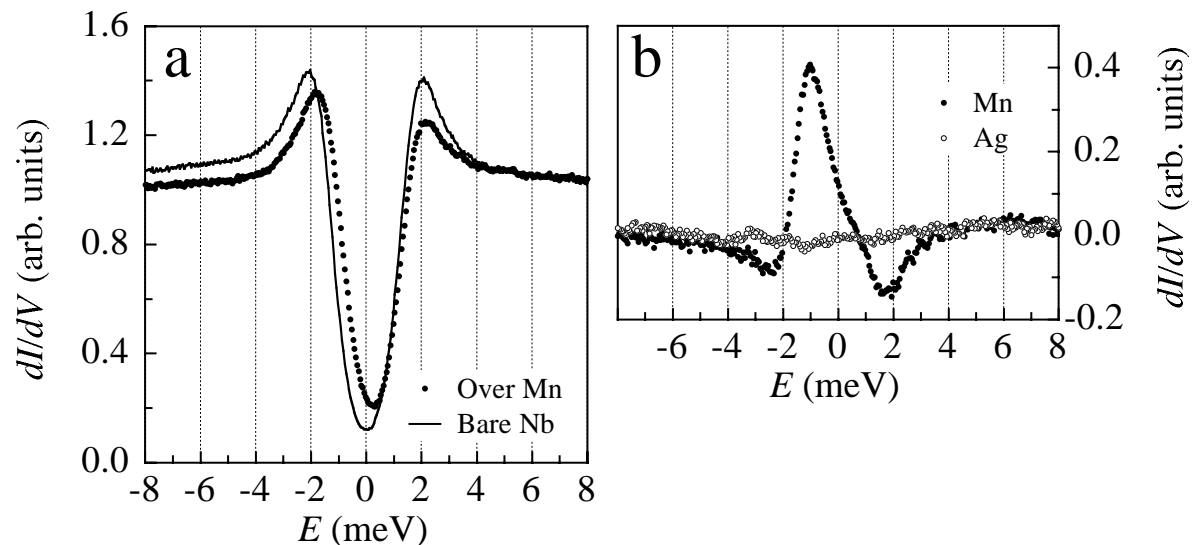


Figure 8.2: (a) Scanning tunneling spectra over the bare Nb surface and a single Mn atom taken at $T = 3.9$ K. (b) Difference spectra (spectrum over bare Nb was deduced from spectrum over atom) for single Mn and Ag atoms. (Reproduced from Ref. [4].)

case the spin of the localized excitation is antialigned with that of the impurity and the hole-like excitation is favored rather than the electron-like. Therefore, tunneling into the superconductor at the excitation energy involves a polarized electron of unfavorable spin, whereas tunneling out of the superconductor involves an electronic spin that is favorable.

By interchanging the role of probe and sample in the experiments by Yazdani *et al.*, i.e. by using a superconducting STM tip on normal metal samples, one could imagine the following: by bringing the apex of the superconducting tip very close to magnetic moments on the surface, these could induce sub-gap excitations in the tip via s - d exchange interaction, which in turn could be detected due to the additional features in scanning tunneling spectra. Since only magnetic moments induce such a sub-gap structure in the spectra, they would be clearly identifiable and due to the localized s - d exchange character of the coupling, the resolution of this technique should be better than 1 nm. This has to be compared to magnetic force microscopy where the resolution is limited to ~ 20 nm due to the long-ranged dipolar interaction.

In the following we present first results confirming the feasibility of this new approach. A Nb cluster large enough to show superconductivity has been picked up at the apex of the Au tip by pushing the tip into the Nb(110) sample. In a first step a Nb(110) substrate has been used. Gd adatoms have been dosed on this substrate at low temperature by evaporation from a current-heated Gd filament.

To check for the influence of magnetism on the superconducting tip, spectra taken at different tunneling impedances over the center of Gd trimers are compared to spectra taken on a clean spot of the Nb(110) surface (see Fig. 8.3). The Gd trimers have been assembled from Gd monomers by atomic manipulation: by bringing the tip close to an adatom (typically 100 k Ω tunneling impedance) the strong adatom-tip interactions make the atom follow the lateral tip movements, and thus the adatom can be positioned at a desired final spot [3]. Figure 8.4 illustrates the controlled assembly of multimers. Once formed, it is even possible to separate the multimers into monomers again. We have chosen Gd trimers for this experiment rather than single Gd atoms, since trimers have a larger effect on superconductivity, as seen in STS spectra taken with a normal-metal tip over Gd trimers assembled on Nb(110).

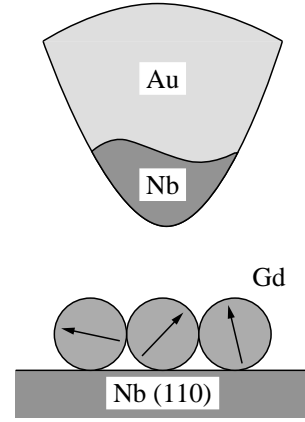


Figure 8.3: Schematics of the experiments using a superconducting tip.

Figure 8.5 shows spectra taken with a superconducting tip over the Nb(110) sub-

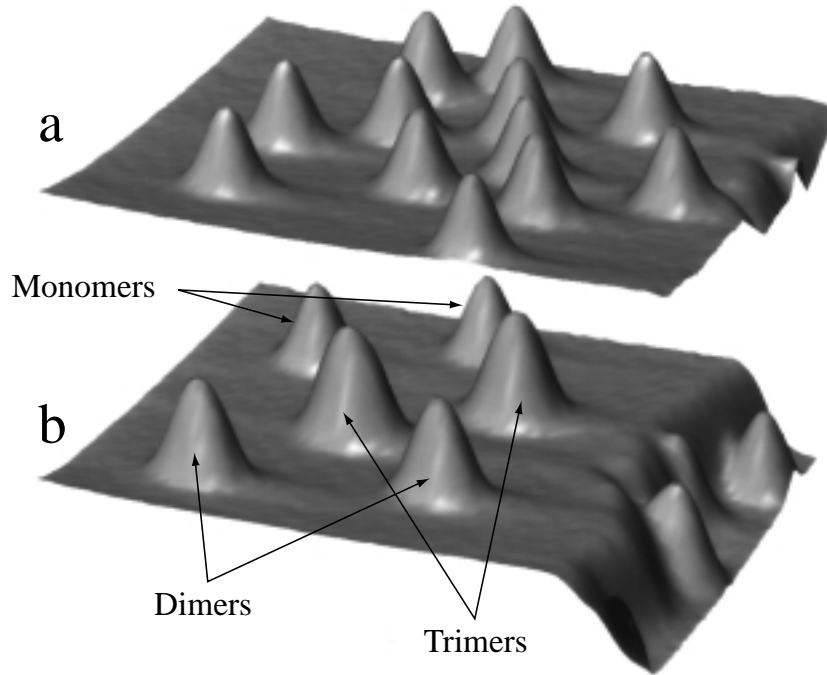


Figure 8.4: (a) 100 Å \times 100 Å STM topograph of Mn monomers on Cu(100). (b) Same surface spot after having assembled monomers to dimers and trimers by dragging the atoms together (two monomers are still present on the upper terrace). Note that the number of atoms on the upper terrace is 12 in (a) as well as in (b). The monomers, dimers and trimers image as bumps of 1.7 Å, 2.1 Å and 2.3 Å height, respectively ($T = 5.6$ K).

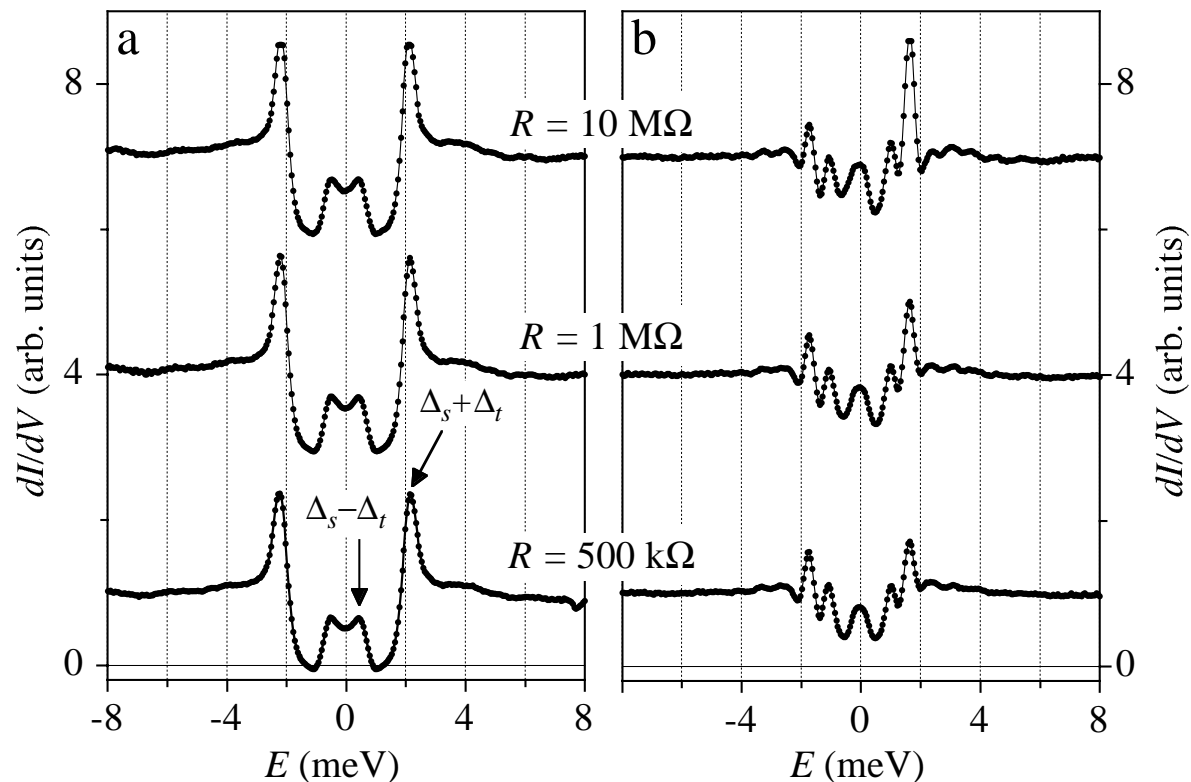


Figure 8.5: Spectra taken with a Nb-covered Au tip at different tunneling impedances R . **(a)** Spectra over a clean Nb surface spot. Data taken at different impedances are offset by 3 units for clarity. **(b)** Corresponding spectra over the center of a Gd trimer ($\Delta V = 350 \mu\text{V}$, $T = 5.6 \text{ K}$).

strate. Spectra taken over a clean spot (Fig. 8.5(a)) show the typical two-peak feature of a superconductor-insulator-superconductor (SIS) junction [27, 225]. Such spectra show maxima at $\Delta_s(T_s) - \Delta_t(T_t)$ and $\Delta_s(T_s) + \Delta_t(T_t)$, where $\Delta_s(T_s)$ and $\Delta_t(T_t)$ are the temperature dependent energy gaps of sample and tip, respectively. (The temperature T_s and T_t of sample and tip need not be the same.) From the spectra in Fig. 8.5(a) the sample and tip gaps are determined to $\Delta_s(5.7 \text{ K}) = 1.33 \text{ meV}$ and $\Delta_t(6.4 \text{ K}) = 0.88 \text{ meV}$. The temperatures of sample and tip are exactly known from BCS fits of spectra taken with a normal tip over the superconducting Nb(110) sample (Fig. 8.2(a)) and a superconducting tip over a normal metal (Fig. 8.7), respectively. Assuming BCS behavior, the zero temperature values of the energy gaps for Nb sample and Nb cluster on the tip can be extrapolated from their value at $T \neq 0 \text{ K}$ [231]: $\Delta_s = 1.47 \text{ meV}$ and $\Delta_t = 1.04 \text{ meV}$. The former agrees well with the bulk value of 1.53 meV reported for Niobium [230]. The gap energy of the tip is reduced by 30 % compared to bulk Nb. This may be due to the proximity of the normal metal Au, the so-called proximity effect [232], or due to size effects, e.g. change of phonon spectrum or electronic level quantization in small

clusters [233]. We now turn to the spectra taken over the Gd trimer (Fig. 8.5(b)). It is evident that the Gd trimer induces sub-gap features in these spectra. In addition, further away from the surface (at $R = 10 \text{ M}\Omega$) the spectrum is fairly asymmetric and gets more and more symmetric by bringing the apex of the tip closer and closer to the trimer. At $R = 500 \text{ k}\Omega$ it is almost symmetric. Note that the reference spectra over the bare Nb do not depend on the impedance at all (Fig. 8.5(a)). Therefore we believe that the increasing symmetry with decreasing tip-sample separation over the trimer is due to the exchange interaction felt by the tip. To illustrate this, let us assume that the sample density of states over the Gd trimer is given by $\rho_{\text{Trimer}}(E)$, which is the BCS density of states with additional features due to the presence of the magnetic moments (similar to Fig. 8.2). The tip LDOS, $\rho_t(E)$, on the other hand, may depend on the tip-sample separation, due to the exchange interaction with the magnetic moment of the trimer. Far away from the surface it is BCS-like (see below), but by getting closer and closer to the surface the magnetic moment of the trimer might induce sub-gap features in $\rho_t(E)$ as well. Let us assume that, by bringing the tip very close to the trimer, the magnetic moments influence the superconductivity of substrate and tip in the same way: $\rho_t(E) = \rho_{\text{Trimer}}(E)$. In this case the tunneling current over the trimer $I_{\text{Trimer}}(V)$ is an asymmetric function with respect to the tunneling voltage

$$\begin{aligned} I_{\text{Trimer}}(V) &\propto \int_0^{eV} dE \rho_{\text{Trimer}}(E) \rho_t(E - eV) = \int_0^{eV} dE \rho_{\text{Trimer}}(E) \rho_{\text{Trimer}}(E - eV) \\ &= - \int_0^{-eV} dE \rho_{\text{Trimer}}(E + eV) \rho_{\text{Trimer}}(E) \propto -I_{\text{Trimer}}(-V), \end{aligned} \quad (8.3)$$

i.e. the differential conductance dI/dV is symmetric. That is exactly what we observe, when the tip is very close ($500 \text{ k}\Omega$). This leads us to the interpretation that the strength of the exchange interaction between magnetic moments on the surface and the conduction electrons of the tip superconductor can be tuned by adjusting the tunneling impedance, i.e. the overlap of tip and surface wave functions. Altogether, we believe that the spectra of Fig. 8.5 are strong evidence for the fact that a magnetic moment on a surface can influence superconductivity of an STM tip brought into proximity.

A good tool for magnetic moment detection should of course not depend on the choice of the substrate, in particular it should not rely on superconductivity of the chosen substrate. We have therefore repeated the same experiments on a non-superconducting substrate, Cu(100) (Fig. 8.6). Figure 8.7 shows a reference spectrum taken with a Nb-coated Au tip over a clean spot of the Cu(100) surface. The BCS fit is very satisfactory and yields temperature and zero temperature energy gap of the tip: $T_t = 6.4 \text{ K}$, $\Delta_t =$

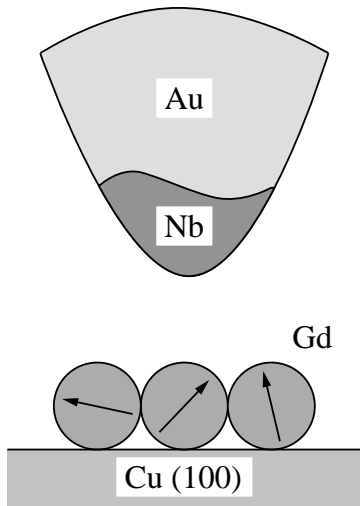


Figure 8.6: Schematics of the experiments using a superconducting tip and a normal metal substrate.

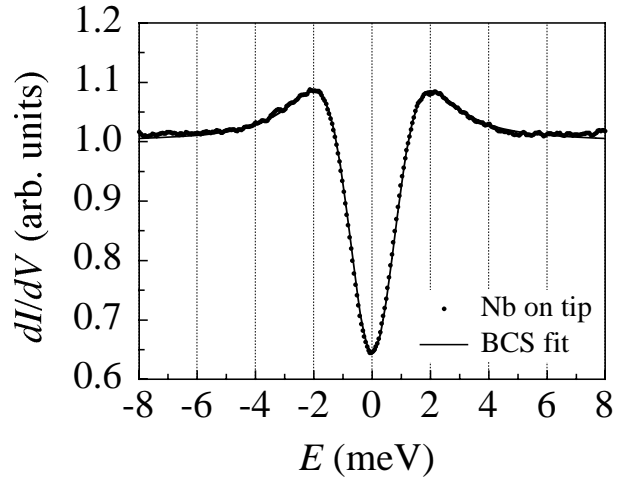


Figure 8.7: Spectrum taken with superconducting tip over bare Cu(100) surface. The full line depicts the BCS fit with the parameters $T_t = 6.4$ K and $\Delta_t = 1.2$ meV ($R = 1$ M Ω , $\Delta V = 350$ μ V).

1.2 meV. The tip energy gap naturally depends on shape and size of the superconducting cluster and thus the value determined here is different from the value extracted from SIS spectra above (1.04 meV), taken with a different Nb-coated tip. A spectrum taken over a Gd trimer is shown in Fig. 8.8(a) together with its reference spectra performed on the non-superconducting Cu(100) substrate. There is an overall decrease in the spectrum over the trimer which is probably due to a resonance lying close to the Fermi energy in the density of states of the trimer. To check for the presence of trimer-induced sub-gap excitations in the superconducting tip we divided the spectrum over the trimer by the reference spectrum (Fig. 8.8(b)). This normalized spectrum shows sub-gap features at -0.7 meV and +1.0 meV, which we believe are induced by the exchange interaction with the magnetic moments of the trimer. But the effect is small ($< 5\%$) in these spectra. By reducing the distance between tip and trimer (going to lower impedances) it could be enhanced. It would be a good test for our hypothesis to take similar spectra at different tunneling impedances and see if the effect scales with the overlap of tip and surface wave functions. Unfortunately, the tip lost superconductivity right when we were doing these experiments, postponing such checks to a future session. Furthermore, it is absolutely necessary to test the absence of sub-gap features in the tip DOS over non-magnetic structures.

We conclude, that although we have evidence for the possibility of detecting magnetic moments as small as a few Bohr magnetons with a superconducting tip, much work has to be done to confirm these first results in a systematic manner. Furthermore, it is not

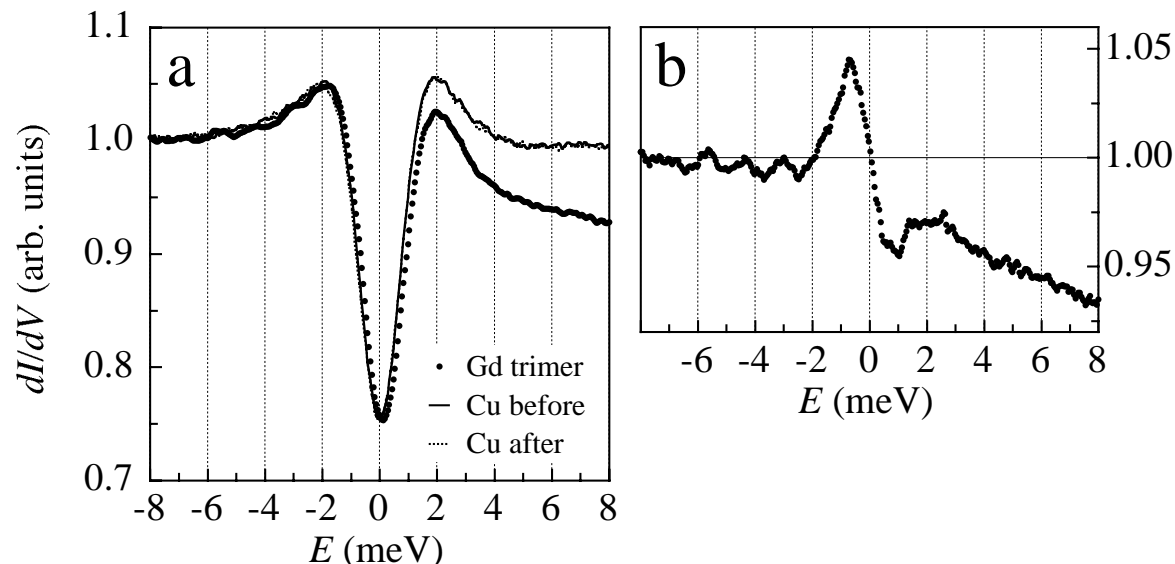


Figure 8.8: (a) Spectrum taken with a superconducting Nb cluster at the apex of an Au tip over a Gd trimer. The full and dashed lines depict the reference spectra over a clean Cu(100) spot taken right before and after the spectrum on the trimer. Since we are interested in sub-gap excitations of the *tip*, electron (hole) excitations of the tip are exceptionally characterized by positive (negative) energies here ($E = -eV$). (b) Spectrum over Gd trimer divided by reference spectrum ($R = 2 \text{ M}\Omega$, $\Delta V = 350 \text{ }\mu\text{V}$, $T = 5.6 \text{ K}$).

yet clear, which physical quantity our technique is sensitive to: are we looking at the net magnetic moment of the trimer or is a single localized spin responsible for the effect? In other words, it is unclear what the spatial resolution is. The advantages of spin-sensitive STM with a superconducting tip would be the simplicity with which magnetic information can be acquired, the possibility to completely separate topography from magnetism and the high spatial resolution due to the fact that it relies on short-ranged exchange interactions. On the other hand, considering the poor mechanical properties of high- T_c superconductors, spin-sensitive STM with superconducting tips will be restricted to low-temperature STM. As a second and major disadvantage, magnet detection via the sub-gap features in a superconducting tip is not sensitive to the direction of the magnetic moments on the surface.

To close this Chapter, we would like to sketch an idea how the technique described here could be extended to become spin-direction sensitive (Fig. 8.9). As described in Section 7.2, several magnetic atoms could be picked up from the surface to form a magnetic cluster at the very apex of a superconducting tip. This magnetic cluster induces sub-gap excitations in the superconductor of the tip [4]. The electronic spin of these excitations is either aligned or antialigned with respect to the magnetic moment

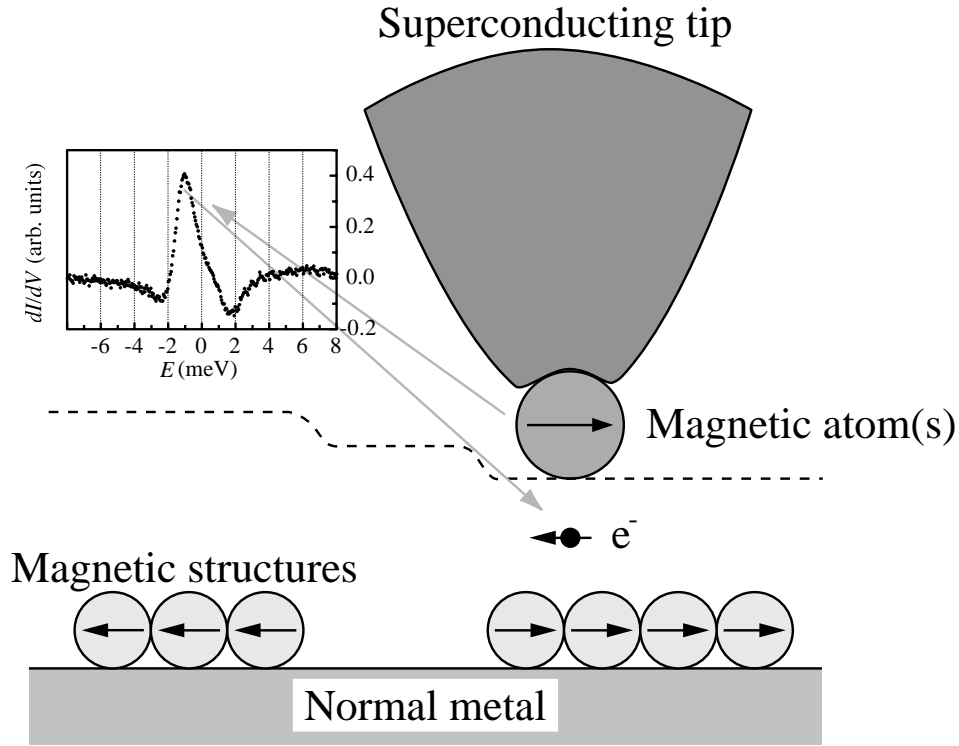


Figure 8.9: Spin-polarized electrons tunnel out of the sub-gap feature induced by the magnetic cluster at the very apex of the superconducting tip. The dashed line shows the trajectory of the tip apex. Due to the spin-polarization of the tunneling electrons, different magnetic domains of the magnetic structures on the surface are imaged with different heights.

of the cluster [219–221]. Thus, if the moment was coupled strong enough to the cluster (spin-orbit interaction) to suppress fluctuations at the temperature of the microscope, electrons tunneling out of (into) that excitation would be polarized. Theoretically, the polarization of the tunneling beam would be 100 %. This would bring us back to spin-valve STM with the advantage of a highly polarized tunneling current and very low magnetic stray fields [203, 204].

Bibliography

- [1] D. C. Ralph, C. T. Black, and M. Tinkham, Phys. Rev. Lett. **74**, 3241 (1995).
- [2] C. T. Black, D. C. Ralph, and M. Tinkham, Phys. Rev. Lett. **76**, 688 (1996).
- [3] D. M. Eigler and E. K. Schweizer, Nature **344**, 524 (1990).
- [4] A. Yazdani *et al.*, Science **275**, 1767 (1997).
- [5] J. Li, W.-D. Schneider, R. Berndt, and B. Delley, Phys. Rev. Lett. **80**, 2893 (1998).
- [6] V. Madhavan *et al.*, Science **280**, 567 (1998).
- [7] B. C. Stipe, M. A. Rezaei, and W. Ho, Science **280**, 1732 (1998).
- [8] B. C. Stipe, M. A. Rezaei, and W. Ho, Phys. Rev. Lett. **82**, 1724 (1999).
- [9] T. M. Rice, Nature **389**, 916 (1997).
- [10] E. Bertel and M. Donath, *Electronic Surface and Interface States on Metallic Systems* (World Scientific Publishing, Singapore, 1995).
- [11] N. Memmel and E. Bertel, Physikalische Blätter **53**, 323 (1997).
- [12] E. Bertel, P. Roos, and J. Lehmann, Phys. Rev. B **52**, R14384 (1995).
- [13] E. Bertel, Phys. Stat. Sol. A **159**, 235 (1997).
- [14] N. Memmel, Surface Science Reports **32**, 91 (1998).
- [15] K. H. Lau and W. Kohn, Surface Science **75**, 69 (1978).
- [16] N. Memmel and E. Bertel, Phys. Rev. Lett. **75**, 485 (1995).
- [17] N. García and P. A. Serena, Surface Science **330**, L665 (1995).
- [18] S. Crampin, J. Phys.: Condens. Matter **6**, L613 (1994).

- [19] I. M. L. Billas, A. Châtelain, and W. A. de Heer, *Science* **265**, 1682 (1994).
- [20] K. Wildberger *et al.*, *Phys. Rev. Lett.* **75**, 509 (1995).
- [21] J. W. Gadzuk, *Phys. Rev. Lett.* **76**, 4234 (1996).
- [22] C. J. Chen, *Introduction to Scanning Tunneling Microscopy* (Oxford University Press, New York, 1993).
- [23] G. Binnig, H. Rohrer, C. Gerber, and E. Weibel, *Phys. Rev. Lett.* **49**, 57 (1982).
- [24] G. Binnig and H. Rohrer, *Helvetica Physica Acta* **55**, 726 (1982).
- [25] I. Giaever, *Phys. Rev. Lett.* **5**, 147 (1960).
- [26] J. Bardeen, *Phys. Rev. Lett.* **6**, 57 (1961).
- [27] E. L. Wolf, *Principles of Electron Tunneling Spectroscopy* (Oxford University Press, New York, 1985).
- [28] G. Hörmandinger, *Phys. Rev. B* **49**, 13897 (1994).
- [29] J. Tersoff and D. R. Hamann, *Phys. Rev. Lett.* **50**, 1998 (1983).
- [30] A. Selloni, P. Carnevali, E. Tosatti, and C. D. Chen, *Phys. Rev. B* **31**, 2602 (1985).
- [31] N. D. Lang, *Phys. Rev. B* **34**, 5947 (1986).
- [32] S. Park and R. C. Barrett, Design Considerations for an STM System, in *Scanning Tunneling Microscopy* (Eds.: J. A. Stroscio and W. J. Kaiser, Academic Press, San Diego, 1993).
- [33] M. F. Crommie, C. P. Lutz, and D. M. Eigler, *Science* **262**, 218 (1993).
- [34] J. Bardeen, L. N. Cooper, and J. R. Schrieffer, *Phys. Rev.* **108**, 1175 (1957).
- [35] J. Buisset, *Tieftemperatur Rastertunnelmikroskopie* (Wissenschaft und Technik Verlag, Berlin, 1996).
- [36] R. S. Becker, J. A. Golovchenko, and B. S. Swartzentruber, *Nature* **325**, 419 (1987).
- [37] I.-W. Lyo and P. Avouris, *Science* **253**, 173 (1991).
- [38] D. M. Eigler, C. P. Lutz, and W. E. Rudge, *Nature* **352**, 600 (1991).

- [39] P. S. Weiss and D. M. Eigler, NATO Proceedings **E235**, 213 (1993).
- [40] A. Hirstein, Ph.D. thesis, Ecole Polytechnique Fédérale de Lausanne, 1998.
- [41] H. Brune, Surface Science Reports **31**, 121 (1998).
- [42] J. Frohn, J. F. Wolf, K. Besocke, and M. Teske, Rev. Sci. Instrum. **60**, 1200 (1989).
- [43] K. Besocke, Surf. Sci. **181**, 145 (1987).
- [44] S. Behler, M. K. Rose, D. F. Ogletree, and M. Salmeron, Rev. Sci. Instrum. **68**, 124 (1997).
- [45] G. Hörmandinger and J. B. Pendry, Phys. Rev. B **50**, 18607 (1994).
- [46] J. Li, W.-D. Schneider, and R. Berndt, Phys. Rev. B **56**, 7656 (1997).
- [47] J. A. Vergés and E. Louis, Solid State Communications **22**, 663 (1977).
- [48] H. Lüth, *Surfaces and Interfaces of Solid Materials* (Springer, Berlin, 1995).
- [49] A. Zangwill, *Physics at Surfaces* (Cambridge University Press, New York, 1988).
- [50] S. G. Davison and M. Stęślicka, *Basic Theory of Surface States* (Oxford University Press, New York, 1992).
- [51] I. Tamm, Z. Phys. **76**, 849 (1932).
- [52] W. Shockley, Phys. Rev. **56**, 317 (1939).
- [53] S. G. Davison and J. D. Levine, Surface States, in *Solid State Physics* (Eds.: H. Ehrenreich, F. Seitz and D. Turnbull, Academic Press, New York, 1970).
- [54] W. E. Meyerhof, Phys. Rev. **71**, 727 (1947).
- [55] J. Bardeen, Phys. Rev. **71**, 717 (1947).
- [56] W. H. Brattain and W. Shockley, Phys. Rev. **72**, 345 (1947).
- [57] W. Shockley and G. L. Pearson, Phys. Rev. **74**, 232 (1948).
- [58] L. W. Swanson and L. C. Crouser, Phys. Rev. Lett. **16**, 389 (1966).
- [59] L. W. Swanson and L. C. Crouser, Phys. Rev. **163**, 622 (1967).
- [60] B. Feuerbacher, B. Fitton, and R. F. Willis, *Photoemission and the Electronic Properties of Surfaces* (John Wiley, Chichester, 1978).

- [61] S. D. Kevan and R. H. Gaylord, Phys. Rev. B **36**, 5809 (1987).
- [62] R. Courths and S. Hüfner, Physics Reports **112**, 53 (1984).
- [63] R. Matzdorf, G. Meister, and A. Goldmann, Phys. Rev. B **54**, 14807 (1996).
- [64] R. Matzdorf, Surf. Sci. Rep. **30**, 153 (1998).
- [65] P. O. Gartland and B. J. Slagsvold, Phys. Rev. B **12**, 4047 (1975).
- [66] J. Tersoff and S. D. Kevan, Phys. Rev. B **28**, 4267 (1983).
- [67] T. C. Hsieh, T. Miller, and T.-C. Chiang, Phys. Rev. Lett. **55**, 2483 (1985).
- [68] Z. Qu *et al.*, J. Vac. Sci. Technol. A **12**(4), 2187 (1994).
- [69] R. Paniago, R. Matzdorf, G. Meister, and A. Goldmann, Surf. Sci. **336**, 113 (1995).
- [70] B. A. McDougall, T. Balasubramanian, and E. Jensen, Phys. Rev. B **51**, 13891 (1995).
- [71] S. LaShell, B. A. McDougall, and E. Jensen, Phys. Rev. Lett. **77**, 3419 (1996).
- [72] S. L. Hulbert *et al.*, Phys. Rev. B **31**, 6815 (1985).
- [73] S. L. Hulbert, P. D. Johnson, N. G. Stoffel, and N. V. Smith, Phys. Rev. B **32**, 3451 (1985).
- [74] D. P. Woodruff, W. A. Royer, and N. V. Smith, Phys. Rev. B **34**, 764 (1986).
- [75] A. Goldmann, V. Dose, and G. Borstel, Phys. Rev. B **32**, 1971 (1985).
- [76] M. F. Crommie, C. P. Lutz, and D. M. Eigler, Nature **363**, 524 (1993).
- [77] O. Jeandupeux *et al.*, Phys. Rev. B **59**, 15926 (1999).
- [78] Y. Hasegawa and P. Avouris, Phys. Rev. Lett. **71**, 1071 (1993).
- [79] W. Chen, V. Madhavan, T. Jamneala, and M. F. Crommie, Phys. Rev. Lett. **80**, 1469 (1998).
- [80] S. Datta, *Electronic Transport in Mesoscopic Systems* (Cambridge University Press, Cambridge, 1995).
- [81] L. C. Davis, M. P. Everson, R. C. Jaklevic, and W. Shen, Phys. Rev. B **43**, 3821 (1991).

- [82] P. Avouris and I.-W. Lyo, *Science* **264**, 942 (1994).
- [83] P. Avouris, I.-W. Lyo, R. E. Walkup, and Y. Hasegawa, *J. Vac. Sci. Technol. B* **12(3)**, 1447 (1994).
- [84] G. Hörmandinger, *Phys. Rev. Lett.* **73**, 910 (1994).
- [85] P. Avouris, I.-W. Lyo, and P. Molinàs-Mata, *Chem. Phys. Lett.* **240**, 423 (1995).
- [86] O. Sánchez *et al.*, *Phys. Rev. B* **52**, 7894 (1995).
- [87] L. Petersen *et al.*, *Phys. Rev. B* **57**, R6858 (1998).
- [88] J. Li, W.-D. Schneider, R. Berndt, and S. Crampin, *Phys. Rev. Lett.* **80**, 3332 (1998).
- [89] L. Petersen, P. Laitenberger, E. Lægsgaard, and F. Besenbacher, *Phys. Rev. B* **58**, 7361 (1998).
- [90] J. Li *et al.*, *Phys. Rev. Lett.* **81**, 4464 (1998).
- [91] L. Bürgi *et al.*, *Phys. Rev. Lett.* **81**, 5370 (1998).
- [92] L. Bürgi, O. Jeandupeux, H. Brune, and K. Kern, *Phys. Rev. Lett.* **82**, 4516 (1999).
- [93] J. Friedel, *Del Nuovo Cimento* **7**, 287 (1958).
- [94] H. Brune, J. Wintterlin, G. Ertl, and R. J. Behm, *Europhys. Lett.* **13**, 123 (1990).
- [95] M. C. M. M. van der Wielen, A. J. A. van Roij, and H. van Kempen, *Phys. Rev. Lett.* **76**, 1075 (1996).
- [96] P. T. Sprunger *et al.*, *Science* **275**, 1764 (1997).
- [97] B. G. Briner *et al.*, *Europhysics News* **28**, 148 (1997).
- [98] N. W. Ashcroft and N. D. Mermin, *Solid State Physics* (Saunders College, Philadelphia, 1976).
- [99] F. Stern, *Phys. Rev. Lett.* **18**, 546 (1967).
- [100] I. Adawi, *Phys. Rev.* **146**, 379 (1966).
- [101] L. Olesen *et al.*, *Phys. Rev. Lett.* **76**, 1485 (1996).

- [102] J. V. Barth, H. Brune, G. Ertl, and R. J. Behm, Phys. Rev. B **42**, 9307 (1990).
- [103] C. Kittel, *Introduction to Solid State Physics* (John Wiley, New York, 1986).
- [104] S. D. Kevan, Phys. Rev. Lett. **50**, 526 (1983).
- [105] J. A. Appelbaum and D. R. Hamann, Solid State Communications **27**, 881 (1978).
- [106] P. M. Echenique and J. B. Pendry, Progress in Surface Science **32**, 111 (1989).
- [107] D. Kalkstein and P. Soven, Surface Science **26**, 85 (1971).
- [108] L. Dobrzynski, *Handbook of Surfaces and Interfaces* (Garland STPM Press, New York, 1978).
- [109] D. Pines and P. Nozières, *The Theory of Quantum Liquids* (Benjamin, New York, 1966).
- [110] J. J. Quinn, Physical Review **126**, 1453 (1962).
- [111] G. Grimvall, *The Electron-Phonon Interaction in Metals* (North- Holland, New York, 1981).
- [112] A. Yacoby, U. Sivan, C. P. Umbach, and J. M. Hong, Phys. Rev. Lett. **66**, 1938 (1991).
- [113] S. Q. Murphy, J. P. Eisenstein, L. N. Pfeiffer, and K. W. West, Phys. Rev. B **52**, 14825 (1995).
- [114] G. F. Giuliani and J. J. Quinn, Phys. Rev. B **26**, 4421 (1982).
- [115] L. Zheng and S. Das Sarma, Phys. Rev. B **53**, 9964 (1996).
- [116] A. Goldmann, R. Matzdorf, and F. Theilmann, Surface Science **414**, L932 (1998).
- [117] R. Paniago, R. Matzdorf, G. Meister, and A. Goldmann, Surface Science **331-333**, 1233 (1995).
- [118] C. A. Schmuttenmaer, M. Aeschlimann, H. E. Elsayed-Ali, and R. J. D. Miller, Phys. Rev. B **50**, 8957 (1994).
- [119] M. Aeschlimann, M. Bauer, and S. Pawlik, Chemical Physics **205**, 127 (1996).
- [120] T. Hertel, E. Knoesel, M. Wolf, and G. Ertl, Phys. Rev. Lett. **76**, 535 (1996).
- [121] E. Knoesel *et al.*, Surface Science **368**, 76 (1996).

- [122] S. Xu *et al.*, Phys. Rev. Lett. **76**, 483 (1996).
- [123] W. Wallauer and T. Fauster, Surface Science **374**, 44 (1997).
- [124] S. Ogawa, H. Nagano, and H. Petek, Phys. Rev. B **55**, 10869 (1997).
- [125] M. Bauer, Ph.D. thesis, Eidgenössische Technische Hochschule Zürich, 1998.
- [126] E. Knoesel, A. Hotzel, and M. Wolf, Phys. Rev. B **57**, 12812 (1998).
- [127] S. Crampin, M. H. Boon, and J. E. Inglesfield, Phys. Rev. Lett. **73**, 1015 (1994).
- [128] S. Crampin and O. R. Bryant, Phys. Rev. B **54**, R17367 (1996).
- [129] J. Li, W.-D. Schneider, S. Crampin, and R. Berndt, Surface Science **422**, 95 (1999).
- [130] J. J. Paggel, T. Miller, and T.-C. Chiang, Science **283**, 1709 (1999).
- [131] E. J. Heller, M. F. Crommie, C. P. Lutz, and D. M. Eigler, Nature **369**, 464 (1994).
- [132] R. Smoluchowski, Phys. Rev. **60**, 661 (1941).
- [133] M. Rocca, L. Yibing, F. Buatier de Mongeot, and U. Valbusa, Phys. Rev. B **52**, 14947 (1995).
- [134] P. M. Echenique, J. M. Pitarke, E. V. Chulkov, and A. Rubio, Chemical Physics, to be published .
- [135] P. M. Echenique, Private communication .
- [136] M. Schmid, W. Hebenstreit, P. Varga, and S. Crampin, Phys. Rev. Lett. **76**, 2298 (1996).
- [137] E. Wahlström, I. Ekvall, H. Olin, and L. Wallden, Appl. Phys. A **66**, S1107 (1998).
- [138] F. Theilmann, R. Matzdorf, G. Meister, and A. Goldmann, Phys. Rev. B **56**, 3632 (1997).
- [139] T. Balasubramanian, E. Jensen, X. L. Wu, and S. L. Hulbert, Phys. Rev. B **57**, R6866 (1998).
- [140] M. Hengsberger *et al.*, Phys. Rev. Lett. **83**, 592 (1999).
- [141] J.-Y. Marzin and J.-M. Gérard, Phys. Rev. Lett. **62**, 2172 (1989).

- [142] G. Salis *et al.*, Phys. Rev. Lett. **79**, 5106 (1997).
- [143] H. K. Harbury and W. Porod, Phys. Rev. B **53**, 15455 (1996).
- [144] M. Born and E. Wolf, *Principles of Optics* (Pergamon, New York, 1980).
- [145] N. Sato and S. Takeda, Phys. Rev. B **59**, 2035 (1999).
- [146] P. Hohenberg and W. Kohn, Phys. Rev. **136**, B 864 (1964).
- [147] J. Lindhard, Kgl. Danske Videnskab. Selskab, Mat.-Fys. Medd. **28**, 1 (1954).
- [148] J. M. Ziman, *Principles of the Theory of Solids* (Cambridge University Press, London, 1972).
- [149] V. Heine and L. D. Marks, Surface Science **165**, 65 (1986).
- [150] M. Pepper and D. Wharam, Physics World **October**, 45 (1988).
- [151] H. van Houten and C. Beenakker, Physics Today **49(7)**, 22 (1996).
- [152] B. J. van Wees *et al.*, Phys. Rev. Lett. **60**, 848 (1988).
- [153] D. A. Wharam *et al.*, J. Phys. C **21**, L209 (1988).
- [154] C. J. Muller, J. M. van Ruitenbeek, and L. J. de Jongh, Phys. Rev. Lett. **69**, 140 (1992).
- [155] S. J. Tans *et al.*, Nature **386**, 474 (1997).
- [156] S. Frank, P. Poncharal, Z. L. Wang, and W. A. de Heer, Science **280**, 1744 (1998).
- [157] C. Dekker, Physics Today **52**, 22 (1999).
- [158] Y. V. Sharvin, Sov. Phys. JETP **21**, 655 (1965).
- [159] R. Landauer, IBM J. Res. Dev. **1**, 223 (1957).
- [160] R. Landauer, Z. Phys. B **68**, 217 (1987).
- [161] J. A. Torres, J. I. Pascual, and J. J. Sáenz, Phys. Rev. B **49**, 16581 (1994).
- [162] M. Brandbyge *et al.*, Phys. Rev. B **52**, 8499 (1995).
- [163] M. Brandbyge, K. W. Jacobsen, and J. K. Nørskov, Phys. Rev. B **55**, 2637 (1997).
- [164] J. A. Torres and J. J. Sáenz, Phys. Rev. Lett. **77**, 2245 (1996).

- [165] T. N. Todorov and A. P. Sutton, Phys. Rev. B **54**, R14234 (1996).
- [166] Y. Imry, Physics of Mesoscopic Systems, in *Directions in Condensed Matter Physics* (Eds.: G. Grinstein and G. Mazenko, World Scientific Publishing, Philadelphia, 1986).
- [167] K. J. Thomas *et al.*, Phys. Rev. Lett. **77**, 135 (1996).
- [168] E. A. Montie *et al.*, Nature **350**, 594 (1991).
- [169] J. K. Gimzewski and R. Möller, Phys. Rev. B **36**, 1284 (1987).
- [170] J. L. Costa-Krämer, N. García, P. García-Mochales, and P. A. Serena, Surface Science **342**, L1144 (1995).
- [171] K. Hansen, E. Lægsgaard, I. Stensgaard, and F. Besenbacher, Phys. Rev. B **56**, 2208 (1997).
- [172] C. J. Muller, J. M. van Ruitenbeek, C. W. J. Beenakker, and R. de Bruyn Ouboter, Physica B **189**, 225 (1993).
- [173] J. M. Krans *et al.*, Phys. Rev. B **48**, 14721 (1993).
- [174] J. M. Krans *et al.*, Nature **375**, 767 (1995).
- [175] D. P. E. Smith, Science **269**, 371 (1995).
- [176] W. A. de Heer, S. Frank, and D. Ugarte, Z. Phys. B **104**, 469 (1997).
- [177] E. Scheer *et al.*, Nature **394**, 154 (1998).
- [178] N. Agraït, J. G. Rodrigo, and S. Vieira, Phys. Rev. B **47**, 12345 (1993).
- [179] J. I. Pascual *et al.*, Phys. Rev. Lett. **71**, 1852 (1993).
- [180] L. Olesen *et al.*, Phys. Rev. Lett. **72**, 2251 (1994).
- [181] J. M. Krans *et al.*, Phys. Rev. Lett. **74**, 2146 (1995).
- [182] L. Olesen *et al.*, Phys. Rev. Lett. **74**, 2147 (1995).
- [183] J. I. Pascual *et al.*, Science **267**, 1793 (1995).
- [184] N. Agraït, G. Rubio, and S. Vieira, Phys. Rev. Lett. **74**, 3995 (1995).
- [185] G. Rubio, N. Agraït, and S. Vieira, Phys. Rev. Lett. **76**, 2302 (1996).

- [186] J. L. Costa-Krämer, Phys. Rev. B **55**, R4875 (1997).
- [187] H. Ohnishi, Y. Kondo, and K. Takayanagi, Nature **395**, 780 (1998).
- [188] U. Landman, W. D. Luedtke, N. A. Burnham, and R. J. Colton, Science **248**, 454 (1990).
- [189] T. N. Todorov and A. P. Sutton, Phys. Rev. Lett. **70**, 2138 (1993).
- [190] J. M. Krams, J. M. van Ruitenbeek, and L. J. de Jongh, Physica B **218**, 228 (1996).
- [191] J. A. Stroscio and D. M. Eigler, Science **254**, 1319 (1991).
- [192] L. Bartels, G. Meyer, and K.-H. Rieder, Phys. Rev. Lett. **79**, 697 (1997).
- [193] A. Yazdani, D. M. Eigler, and N. D. Lang, Science **272**, 1921 (1996).
- [194] B. J. van Wees *et al.*, Phys. Rev. B **38**, 3625 (1988).
- [195] V. Marigliano Ramaglia and F. Ventriglia and G. P. Zucchelli, Phys. Rev. B **48**, 2445 (1993).
- [196] R. Allenspach, Journal of Magnetism and Magnetic Materials **129**, 160 (1994).
- [197] C. H. Back *et al.*, Nature **378**, 597 (1995).
- [198] C. Stamm *et al.*, Science **282**, 449 (1998).
- [199] R. J. Celotta and D. T. Pierce, Science **234**, 333 (1986).
- [200] R. Wiesendanger, J. Vac. Sci. Technol. B **12(2)**, 515 (1994).
- [201] R. J. Soulen Jr. *et al.*, Science **282**, 85 (1998).
- [202] S. K. Upadhyay, A. Palanisami, R. N. Louie, and R. A. Buhrman, Phys. Rev. Lett. **81**, 3247 (1998).
- [203] R. Wiesendanger *et al.*, Phys. Rev. Lett. **65**, 247 (1990).
- [204] M. Bode, M. Getzlaff, and R. Wiesendanger, Phys. Rev. Lett. **81**, 4256 (1998).
- [205] S. F. Alvarado and P. Renaud, Phys. Rev. Lett. **68**, 1387 (1992).
- [206] M. W. J. Prins, R. Jansen, and H. van Kempen, Phys. Rev. B **53**, 8105 (1996).
- [207] Z. Wu, T. Nakayama, M. Sakurai, and M. Aono, Surface Science **386**, 311 (1997).

- [208] Y. Suzuki, W. Nabhan, and K. Tanaka, Appl. Phys. Lett. **71**, 3153 (1997).
- [209] R. Meservey, P. M. Tedrow, and P. Fulde, Phys. Rev. Lett. **25**, 1270 (1970).
- [210] P. M. Tedrow and R. Meservey, Phys. Rev. Lett. **26**, 192 (1971).
- [211] P. M. Tedrow and R. Meservey, Phys. Rev. B **7**, 318 (1973).
- [212] P. G. De Gennes, *Superconductivity of Metals and Alloys* (W. A. Benjamin, Inc., New York, 1966).
- [213] M. Tinkham, *Introduction to Superconductivity* (Robert E. Krieger Publishing Company, Inc., Malabar, 1980).
- [214] M. Jullière, Physics Letters **54A**, 225 (1975).
- [215] F. Meier and B. P. Zakharchenya, *Optical Orientation* (Elsevier Science Publishers B. V., Amsterdam, 1984).
- [216] M. B. Maple, Appl. Phys. **9**, 179 (1976).
- [217] D. R. Tilley and J. Tilley, *Superfluidity and Superconductivity* (Adam Hilger Ltd, Bristol, 1986).
- [218] P. W. Anderson, J. Phys. Chem. Solids **11**, 26 (1959).
- [219] T. Soda, T. Matsuura, and Y. Nagaoka, Progress of Theoretical Physics **38**, 551 (1967).
- [220] H. Shiba, Progress of Theoretical Physics **40**, 435 (1968).
- [221] A. Sakurai, Progress of Theoretical Physics **44**, 1472 (1970).
- [222] M. H. Cohen, L. M. Falicov, and J. C. Phillips, Phys. Rev. Lett. **8**, 316 (1962).
- [223] J. Bardeen, Phys. Rev. Lett. **9**, 147 (1962).
- [224] J. R. Schrieffer and J. W. Wilkins, Phys. Rev. Lett. **10**, 17 (1963).
- [225] I. Giaever, Phys. Rev. Lett. **5**, 464 (1960).
- [226] M. A. Woolf and F. Reif, Phys. Rev. **137**, A 557 (1965).
- [227] W. Bauriedl, P. Ziemann, and W. Buckel, Phys. Rev. Lett. **47**, 1163 (1981).
- [228] A. L. de Lozanne, S. A. Elrod, and C. F. Quate, Phys. Rev. Lett. **54**, 2433 (1985).

- [229] H. F. Hess *et al.*, Phys. Rev. Lett. **62**, 214 (1989).
- [230] C. P. Poole, H. A. Farach, and R. J. Creswick, *Superconductivity* (Academic Press, San Diego, 1995).
- [231] B. Mühlischlegel, Zeitschrift für Physik **155**, 313 (1959).
- [232] L. N. Cooper, Phys. Rev. Lett. **6**, 689 (1961).
- [233] B. G. Orr, H. M. Jaeger, and A. M. Goldman, Phys. Rev. Lett. **53**, 2046 (1984).

Curriculum vitae

Name:	Lukas Bürgi
Date of Birth:	June 6, 1970
Nationality	Swiss
1985–1989	High School at the Kantonsschule im Lee in Wintherthur, Switzerland
1990–1993	Undergraduate studies in physics at the University of Bern, Switzerland
1993–1995	Diploma studies in physics at the Swiss Federal Institute of Technology in Zürich
May 1995–Sept 1995	Diploma thesis in the group of Prof Dr D. Pescia at the Laboratory for Solid State Physics of the Swiss Federal Institute of Technology in Zürich: “Magnetische Anisotropie von Cu/Co/Cu(100) und Fe/Co/Cu(100), Antiferromagnetismus in Fe/Cu(100)”
1996–1999	Research and teaching assistant in the group of Prof Dr K. Kern at the Institute for Experimental Physics of the Swiss Federal Institute of Technology in Lausanne
Oct 1996–Dec 1996	Joint research studies with the group of Dr D. Eigler at the IBM Almaden Research Center in San Jose, USA
1999	PhD thesis: “Scanning Tunneling Microscopy as Local Probe of Electron Density, Dynamics, and Transport at Metal Surfaces”

Remerciements

J'aimerais remercier tous ceux qui, d'une façon ou d'une autre, ont contribué à l'élaboration de ma thèse. En particulier:

Le professeur **Klaus Kern**, mon directeur de thèse, pour m'avoir donné l'opportunité de réaliser ce travail et pour m'avoir guidé avec optimisme et engagement tout au long de ma thèse. Ensuite **Andreas Hirstein**, mon prédécesseur avec qui j'ai travaillé pendant 2 ans sur le microscope à basse température. Il a effectué un travail difficile, la construction du microscope avec lequel j'ai pu récolter les fruits présentés dans cette thèse. Avec son calme et sa patience il a beaucoup contribué au succès de la manip. Pendant certaines périodes de montage, Andreas était le seul à croire à la réussite du projet. Et, en fin de compte, il a eu raison. Merci! Puis j'aimerais remercier **Olivier Jeandupeux**, mon post-doc, avec qui j'ai passé des heures à discuter les résultats présentés dans ce travail. Un grand merci aussi à Olivier pour sa généreuse disponibilité à résoudre tout de sorte de problèmes informatiques! Ensuite, **Harald Brune** a toujours été présent en cas de problèmes et a pris le temps pour trouver des solutions. Ses compétences dans le domaine de la microscopie à effet tunnel ont été un grand atout pour mon projet.

Pendant ma thèse j'ai eu l'unique opportunité de faire un stage de trois mois dans le laboratoire de Don Eigler au centre de recherche d'IBM à San Jose. Je tiens à remercier son équipe, **Chris Lutz**, **Ali Yazdani** et **Don Eigler**, pour leur accueil chaleureux et pour avoir pu profiter de leurs connaissances exceptionnelles. Puis **Lars Petersen** de l'Université d'Aarhus au Danemark qui a effectué des mesures dans notre laboratoire pendant plusieurs mois. Les heures qu'on a passées ensemble devant la manip ont toujours été très animées.

Je remercie aussi MM. les membres du jury: Dr. **D. Eigler**, Prof. **A. Goldmann** et Prof. **L. Zuppiroli** pour avoir bien voulu juger ce travail.

Ce travail n'aurait pas pu être effectué sans l'aide très importante de tout l'équipe du secrétariat, de l'atelier de mécanique et d'électronique de l'IPE. J'aimerais surtout remercier **André Guisolan** pour son engagement tout au long du projet; **Philippe**

Zürcher pour toutes les pièces qu'il nous a fabriquées; **Philippe Cordey** pour sa contribution à l'optimisation des signaux électriques; **Claire-Lise Bandelier** pour avoir numérisé et traité des quantités d'images; **Martial Doy** pour tout ce qu'il a fait pour surmonter mes lacunes en informatique; **Michel Fazan** pour les travaux délicats et finalement **André Schläfli** pour les petits cadeaux en forme de courrier qu'il nous a apportés chaque matin (et qui malheureusement étaient plus souvent pour Hannes Kind que pour moi).

Au-delà du projet j'aimerais remercier tout le group Kern pour l'ambiance très agréable et amicale. En particulier, je tiens à remercier **Hannes Kind** et **Jens Weckesser** pour leur amitié et les heures inoubliables que nous avons vécues ensemble, soit autour d'une table d'un bistrot lausannois, ou dans une cabane perdue dans les alpes.

Puis je tiens à remercier mes **parents** pour tout ce qu'il m'ont donné (et me donnent encore). Finalement, le plus grand merci à ma femme **Elisabeth** pour son amour et à **Moritz**, qui est né le jour même de mon examen oral de thèse, pour la joie immense qu'il m'apporte!